Proceedings of the 3rd World Summit on Exploring the Dark Side of the Universe (EDSU2020)

March 9–13, 2020
Guadeloupe Islands

Edited by
Alexander Novikov, Pierre Pétroff, Christophe Royon

Proceedings of the 3rd World Summit on Exploring the Dark Side of the Universe (EDSU 2020)

March 9–13, 2020
Guadeloupe Islands

Edited by
Alexander Novikov, Pierre Pétroff, Christophe Royon

Published by the University of Kansas Libraries
Lawrence, KS 66045

Contents

Images

Preface: 3rd World Summit on Exploring the Dark Side of the Universe 2020

The 3rd World Summit on Exploring the Dark Side of the Universe (EDSU2020) (https://indico.cern.ch/event/801461/overview) took place from March 9 to 13 in the Guadeloupe Islands, a picturesque French archipelago in the Caribbean. This was the 3rd meeting in this series of workshops, with previous editions held in the Galapagos Islands and Guadeloupe. EDSU2020 was one of the major venues of interaction between cosmologists and particle physicists. The discussed topics included Cosmological Microwave Background, Large Scale Structure, Inflation and Early Universe, Particle Astrophysics, Dark Matter and Dark Energy, and Particle Physics.

The workshop was attended by 89 participants from 27 countries, including a large fraction of students. During the entire workshop, more than 60 talks were presented and many discussion sessions were held. The workshop was very active and efficient despite the fact that a few talks had to be given virtually because of the COVID-19 epidemic situation.

Group photo of EDSU2020 participants

As editors of these proceedings, we wish to thank all participants and speakers for their highly valuable contributions, as well as the French Physique-Outremer non-profit association that took care of the practical organization. We owe everyone who participated in the organization and all the sponsors our very warm thanks. We also express our deepest gratitude to the prestigious physicists, among them three Nobel Laureates, who agreed to serve on the international advisory committee. We also thank the members of the organizing committee and more particularly the conveners who did a great job in preparing the scientific sessions of the conference. We also appreciate the efforts of all participants who had decided to travel and attend the conference in Guadeloupe in person despite the threats of the COVID-19 pandemic. Last but not least, EDSU2020 could not have been held without the very efficient financial support of the Guadeloupe Regional Council and its President Mr. Ary Chalus, of the French Ministry of Overseas Territories and its former Minister Mrs. Annick Girardin, and the Institute of Astrophysics of Paris and its Director Prof. Francis Bernardeau. Thanks also to Prof. Eustase Janky, President of the University of Antilles who kindly agreed to host the conference at the University. We would also like to thank all speakers who wrote their proceedings on time! Finally, our great and very warm thanks to the staff of the University of Kansas who provided support for editing of the EDSU2020 proceedings.

The Editors Alexander Novikov, Pierre Pétroff and Christophe Royon

Last Results and Questions From Planck

Silvia Galli

e-mail: gallis@iap.fr

IAP

Presented at the 3rd World Summit on Exploring the Dark Side of the Universe
Guadeloupe Islands, March 9-13 2020

Abstract

Planck is an ESA satellite aimed at the observation of the Cosmic Microwave Background. The Planck collaboration has recently published its last legacy release. In this talk I shortly reviewed the main Planck results on cosmological parameters, highlighted some of the curious features present in the data and the Planck point of view on tensions with a few other astrophysical probes, notably with the Hubble constant measurements from local distance measurements.

1 Introduction

One of the main driving forces behind the phenomenal progress of cosmology in the last twenty years has been the observation of the cosmic microwave background (CMB). Europe has played a leading role in CMB science in the last 10 years through the success of ESA's Planck satellite, which provided the ultimate measurement of the CMB temperature anisotropies up to up to multipoles smaller than about $\ell \sim 1500$ [1]. Moreover, Planck has provided powerful measurements of the CMB polarization anisotropies, and the first full-sky measurement of the CMB lensing potential [2]. Furthermore, Figure 1 shows the angular power spectra as measured by Planck.

One of the legacy results of Planck is that the standard model of cosmology, the ΛCDM, works astonishingly well to describe the CMB anisotropies, as well as a large number of other observations. Planck measured cosmological parameters with percent level accuracy, in agreement with other probes, ranging from Baryon Acoustic Oscillations (BAO) to measurements of primordial elements combined with Big-Bang Nucleosynthesis calculations [1]. Nevertheless, the Planck results feature a number of outstanding inconsistencies which might hint towards cracks in this very successful model.

2 The H_0 problem.

In 2019 the ΛCDM model reached a remarkable milestone. The difference between early-time and late-time probes measuring the expansion rate of the universe, i.e. the Hubble constant, reached an unexplained discrepancy of 5.3σ. Indeed, distance-ladder measurements using cepheids and supernovae Ia yield H_0=74.22 $\pm$ 1.82 Km/s/Mpc [3]. Combined with data of time delays of multiply imaged strongly lensed quasars, they measure H_0= 73.8$\pm$1.1 Km/s/Mpc [4], as also shown in Figure 2. On the contrary, observations of the CMB anisotropies performed by the Planck satellite yield H_0=67.36$\pm$ 0.54 Km/s/Mpc [1], in agreement with BAO plus primordial deuterium abundance measurements. This difference appeared in the first release of the Planck data at the 2.5σ level, and in

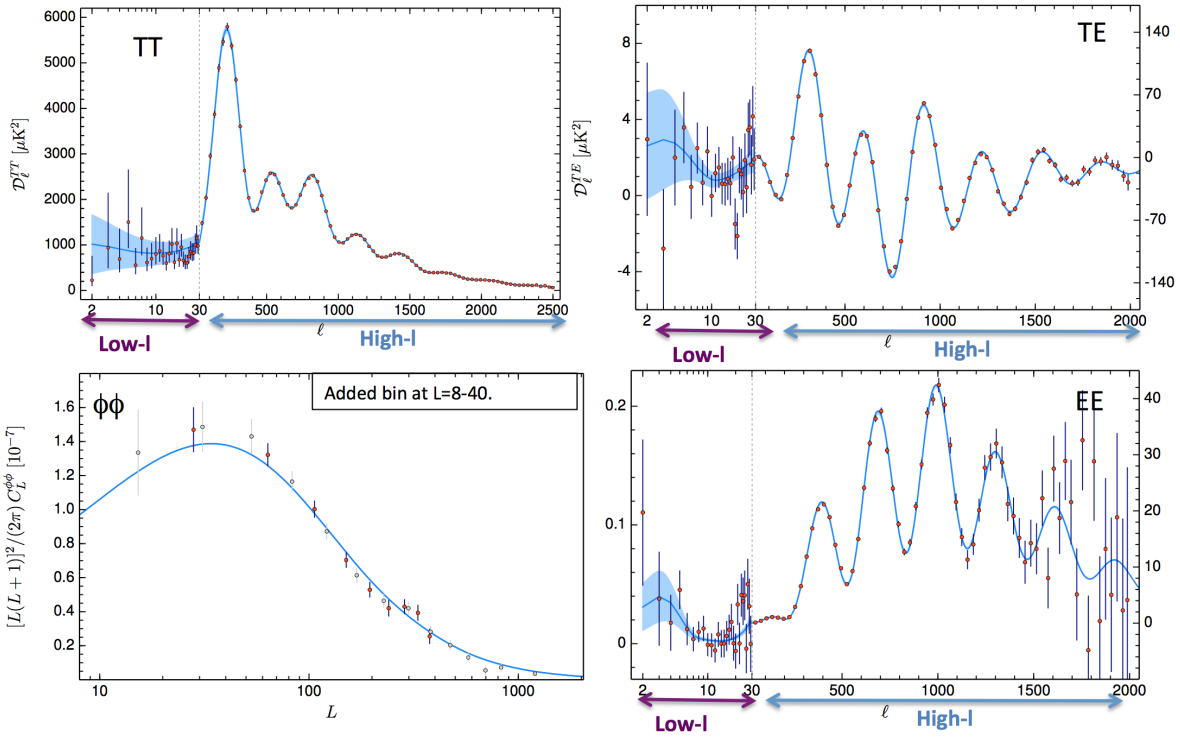

Figure 1: Planck angular power spectra for intensity (TT), E-mode polarization (EE), temperature polarization cross-correlation (TE) and the lensing reconstruction (PP). The red points are the data, while blue lines are the best-fit spectra assuming a ΛCDM model. Taken from [1]

spite of all of the efforts trying to identify systematic effects which could explain it, it has only grown in statistical significance over the years. Recently, distance-ladder measurements using the tip of the red giant branch to calibrate supernovae Ia provided measurements which are for the moment consistent with both, as well as other probes [5]. If one could completely exclude statistical and systematic effects as the source of such a discrepancy, the implications of this tension could potentially be revolutionary. In effect, distance-ladder measurements are direct, i.e. they directly test the local expansion of the universe today. Conversely, CMB and BAO are indirect, i.e. they are probes which require a model in order to infer the Hubble rate today. Thus, the most fascinating hypothesis is that the solution of this tension lies in a change of the cosmological model, implying evidence for the existence of new physics [6]. As of today, a number of possible extensions of the ΛCDM model has been proposed to solve this issue, although none of them are so-far able to completely explain it. Most of these focus on changing the physics of the early universe, in particular the calculation of the sound horizon [6]. Examples are models with new physics in the neutrino sector [7] or early dark energy [8]. On the other hand, changing the physics of the universe at late-times such as e.g. with dark energy, decaying dark matter or interacting dark matter-dark energy was already proved to be in disagreement with current data.

3 The σ_8 and beyond the standard model problem.

The H_0 problem is not the only one related to the Planck measurements. There is a series of inconsistencies at lower statistical significance, and likely all related to each other. These have triggered a huge interest in the cosmology community due to their potentially pivotal consequences.

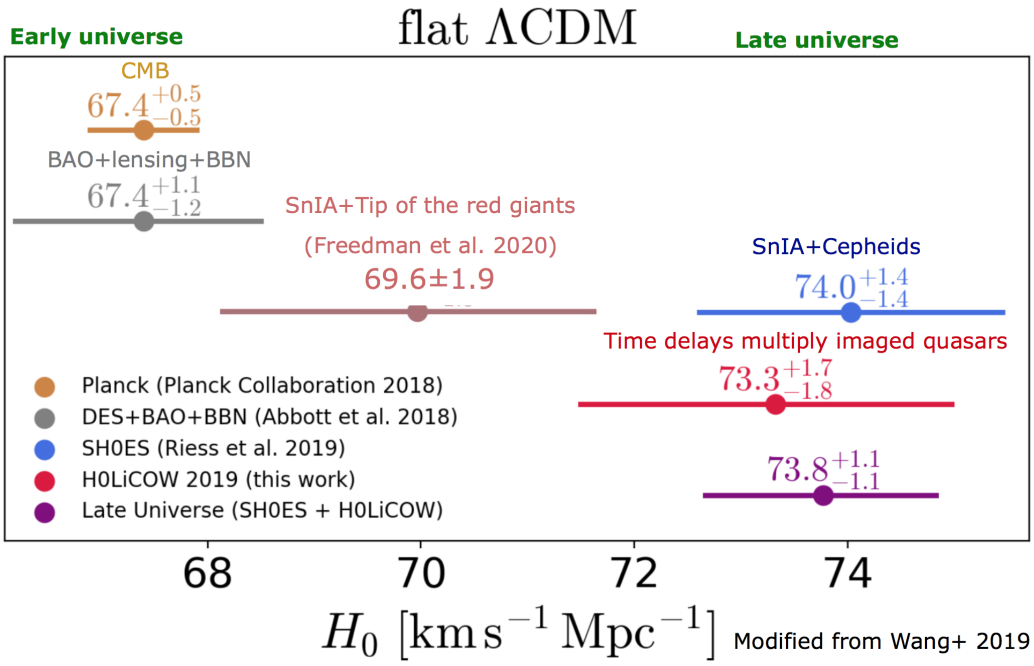

Figure 2: Measurements of the Hubble constant from different probes. Modified from [4]

3.1 The σ_8 problem

There is a long-standing, persistent discrepancy on combinations of the amplitude of matter density perturbations today, σ_8, and matter density, ω_m, as measured by Planck on the one hand or by counts of galaxy clusters and weak lensing observations [9] on the other hand. The latest Planck CMB data yield e.g. σ_8=0.8111±0.0060 (Planck TT,TE,EE+lowE+lensing, ΛCDM) [1], while late-time probes measure values lower by 2-3σ (with error bars typically 3 times larger than Planck). This subject has triggered a large literature, investigating the possibility that part of this discrepancy might be due to astrophysical uncertainties in the lower-redshift probes (e.g. the hydrodynamical mass-bias of galaxy clusters). However, the possibility that this could also be due to something unusual in the CMB spectra, either it be statistical, systematic or physical, is still viable, and requires a deeper investigation.

3.2 Extensions of the vanilla ΛCDM model

Models beyond the vanilla one, such as those with large non-zero curvature of the universe or modified gravity, which increase the predicted amplitude of lensing in the CMB power spectra, provide marginally better fits to the Planck CMB anisotropy data at the 2-3σ level [1]. However, such findings are in disagreement with the observed amplitude of the reconstructed CMB lensing potential as measured e.g. by Planck itself, and BAO data. The discrepancies on the measurement of these extensions between different probes suggest that if these are indeed signs of new physics, the existing models are unlikely to provide the correct answer yet.

3.3 Planck inconsistencies

The Planck data marginally passes two internal consistency tests. The first evaluates cosmological parameters from two ranges of multipoles, the low ones (ℓ800) and the high ones (ℓ800), finding ΛCDM

parameters which are different at the $\sim 2\sigma$ level [10]. The second measures the amplitude of lensing as measured in the anisotropy power spectra via the phenomenological lensing parameter A_L, which is expected to be equal to unity in the standard model of cosmology. Unexpectedly, Planck measures this parameter to be higher, $A_L = 1.180 \pm 0.065$ (68% confidence level, Planck TT,TE,EE+lowE) [1]. However, it is already known this cannot be the sign of an anomalous, physical excess of lensing in the universe. In fact, while this effect is measured at $\sim 15\sigma$ in the anisotropy spectra, it is much better measured (at $\sim 33\sigma$ when marginalizing over uncertainties of the theoretical model) by the lensing potential reconstructed from the non-gaussian signatures it leaves in the CMB maps. The reconstructed CMB lensing from Planck itself does not show an equivalent excess in amplitude. All these three families of anomalies and inconsistencies are likely sourced by the same features of the Planck power spectra. These look like a preference for an extra-smoothing of the peaks and troughs of the small scale Planck CMB temperature anisotropy power spectrum at $\ell \sim 1000$, and a preference for lower power at large scales (at $\ell 30$), as shown in [10]. This is also shown in Figure 3, where we plot the Planck residuals of the TT temperature power spectrum with respect to the ΛCDM model, together with extended models which can better fit the remaining residuals. We underline here that although these models provide marginally better chi-squares, the ΛCDM is already an excellent fit to the data.

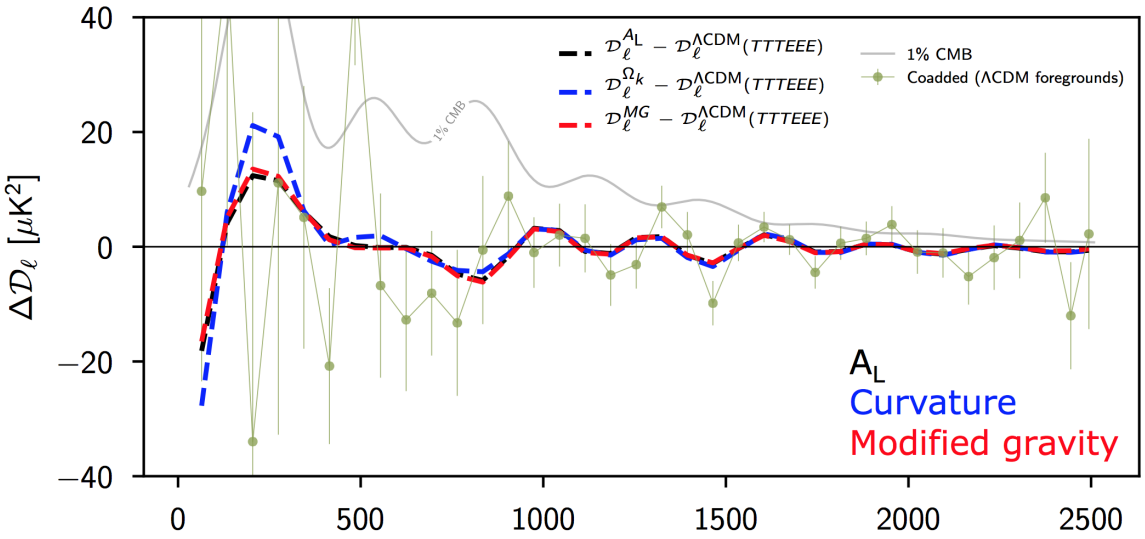

Figure 3: Figure 2: Residuals of the Planck TT CMB anisotropy power spectrum with respect to the ΛCDM best-fit (gray data points). The dashed lines show extended ΛCDM models which marginally better fit the data at the $2-3\sigma$ level, and which all fit the same features in the power spectra. We show the case of extra-lensing, (ΛCDM+A_L green), curvature (ΛCDM+Ω_k, blue), modified gravity (ΛCDM+MG, red [1]) and electron mass (ΛCDM+ m_e, green, [11]).

We showed that as-of-today there is no evidence that these residuals can be caused by a known systematic (see summary in Section 3.10 of [12],. Thus, these anomalies, whether they are due to a statistical fluctuation, unknown systematics or the signature of new physics, still lack a correct interpretation, despite many years of intense scrutiny. If further confirmed, they would impact the interpretation of some of the most interesting fundamental physics parameters that only cosmology can provide, including the curvature of the universe, the sum of the neutrino masses, dark energy and modified gravity.

4 Conclusions

The Planck results have marked a milestone in our knowledge of the universe. They have demonstrated that the ΛCDM model is a remarkably good fit to the current data. However, they have also opened new questions. The most remarkable one is about the value of the Hubble constant, which Planck measures to be in disagreement with more direct observations at more than the 4σ level. Future observations of the CMB at high resolution in polarization, as well as of plenty of other probes, will certainly shed new light on these issues, possibly confirming or refuting the need of a new paradigm in the standard model of cosmology.

References

[1] **Planck** Collaboration, N. Aghanim et al., *Planck 2018 results. VI. Cosmological parameters*, arXiv:1807.06209.

[2] **Planck** Collaboration, N. Aghanim et al., *Planck 2018 results. VIII. Gravitational lensing*, , *in press* (2018) [arXiv:1807.06210].

[3] A. G. Riess, S. Casertano, W. Yuan, L. M. Macri, and D. Scolnic, *Large Magellanic Cloud Cepheid Standards Provide a 1% Foundation for the Determination of the Hubble Constant and Stronger Evidence for Physics beyond ΛCDM*, **876** (May, 2019) 85, [arXiv:1903.07603].

[4] K. C. Wong et al., *H0LiCOW XIII. A 2.4% measurement of H_0 from lensed quasars: 5.3σ tension between early and late-Universe probes*, (June, 2020) [arXiv:1907.04869].

[5] W. L. Freedman, B. F. Madore, D. Hatt, T. J. Hoyt, I. S. Jang, R. L. Beaton, C. R. Burns, M. G. Lee, A. J. Monson, J. R. Neeley, M. M. Phillips, J. A. Rich, and M. Seibert, *The Carnegie-Chicago Hubble Program. VIII. An Independent Determination of the Hubble Constant Based on the Tip of the Red Giant Branch*, **882** (Sept., 2019) 34, [arXiv:1907.05922].

[6] L. Knox and M. Millea, *Hubble constant hunter's guide*, **101** (Feb., 2020) 043533, [arXiv:1908.03663].

[7] C. D. Kreisch, F.-Y. Cyr-Racine, and O. Doré, *Neutrino puzzle: Anomalies, interactions, and cosmological tensions*, **101** (June, 2020) 123505, [arXiv:1902.00534].

[8] V. Poulin, T. L. Smith, T. Karwal, and M. Kamionkowski, *Early Dark Energy can Resolve the Hubble Tension*, **122** (June, 2019) 221301, [arXiv:1811.04083].

[9] S. Joudaki, H. Hildebrandt, D. Traykova, N. E. Chisari, C. Heymans, A. Kannawadi, K. Kuijken, A. H. Wright, M. Asgari, T. Erben, H. Hoekstra, B. Joachimi, L. Miller, T. Tröster, and J. L. van den Busch, *KiDS+VIKING-450 and DES-Y1 combined: Cosmology with cosmic shear*, **638** (June, 2020) L1, [arXiv:1906.09262].

[10] **Planck** Collaboration, N. Aghanim et al., *Planck intermediate results. LI. Features in the cosmic microwave background temperature power spectrum and shifts in cosmological parameters*, **607** (Nov., 2017) A95, [arXiv:1608.02487].

[11] L. Hart and J. Chluba, *New constraints on time-dependent variations of fundamental constants using Planck data*, **474** (Feb., 2018) 1850–1861, [arXiv:1705.03925].

[12] **Planck** Collaboration, N. Aghanim et al., *Planck 2018 results. V. CMB power spectra and likelihoods*, *arXiv e-prints* (July, 2019) arXiv:1907.12875, [arXiv:1907.12875].

Hubble Constant at the Late Universe

Sherry H. Suyu

e-mail: suyu@mpa-garching.mpg.de

Max-Planck-Institut für Astrophysik, Karl-Schwarzschild-Str. 1, 85748 Garching, Germany
Physik-Department, Technische Universität München, James-Franck-Straße 1, 85748 Garching, Germany
Academia Sinica Institute of Astronomy and Astrophysics (ASIAA), 11F of ASMAB, No.1, Section 4, Roosevelt Road, Taipei 10617, Taiwan

Presented at the 3rd World Summit on Exploring the Dark Side of the Universe
Guadeloupe Islands, March 9-13 2020

Abstract

The tension between measurements of the Hubble constant from different cosmological probes has been much debated in recent years. If it is not resolved by measurement errors, then it necessitates new physics beyond the standard flat ΛCDM model. In order to assess the significance of the tension, having independent probes of the Hubble constant is crucial. In this presentation, I describe various late-Universe probes for measuring the Hubble constant: the cosmic distance ladder, megamasers, standard sirens and strong lensing. Focussing on strongly lensed quasars and supernovae, I show that they have the potential to deliver a 1% measurement of the Hubble constant in the upcoming years.

1 Introduction

In the past decade, the so-called flat Λ cold dark matter (ΛCDM) cosmological model consisting of dark energy (with density characterised by the cosmological constant Λ) and CDM in a spatially flat Universe has emerged as the standard cosmological model. This model has provided excellent fits to various cosmological observations, especially the temperature anisotropies in the cosmic microwave background (CMB).

Despite the successes of the ΛCDM model, there is currently an intriguing tension in the measurements of the Hubble constant (H_0) from independent probes. In particular, the measurement from observations of the CMB by [1] under the flat ΛCDM model is more than 4σ lower than the local measurement from the Cepheid distance ladder by the "Supernovae, H_0, for the Equation of State of Dark Energy" (SH0ES) programme [2] . This tension, if not explained by yet unaccounted-for measurement uncertainties, has great implications for cosmology, requiring new physics beyond the standard flat ΛCDM model. By using a separate distance calibrator, the tip of the red giants (instead of Cepheids), [3] measured H_0 that is in between the values from [1] and [2] through the Carnegie-Chicago Hubble Program (CCHP) [4]. There is ongoing debate about the method, e.g. [5, 6], and the results from CCHP and SH0ES are not fully independent due to calibrating sources/data that are common among the two distance ladders. This highlights the value of having independent probes for the Hubble constant. In the following sections, we provide an overview of the various late-Universe probes of the Hubble constant.

2 Distance Ladder

The distance ladder has a long history in providing measurements of H_0. In fact, the *Hubble Space Telescope* (*HST*) Key Project was based on this method and yielded a measurement of H_0 with 10% uncertainty [7], resolving the multi-decade "factor-of-two" controversy in H_0.

By measuring distances (d) to objects in the Hubble flow (with negligible peculiar velocities) and their recessional velocities (v) via redshifts, H_0 can be inferred through the Hubble-Lemaître law $v = H_0 d$. However, direct distance measurements to such faraway objects are difficult to acquire. Thus, a practical way is to measure absolute distances to nearby objects (through e.g. parallax), and then use methods to measure relative distances (such as supernovae) to further away objects. This builds a "ladder" to obtain distances to faraway object in the Hubble flow.

In the SH0ES programme, [2] used Milky Way parallax, detached eclipsing binaries (DEB) in the Large Magellanic Cloud [8] and the maser galaxy NGC4258 to calibrate the Cepheid distance scale, that are in turn calibrating the supernova distance scale. Using all three anchors (parallax, DEB and NGC4258), [2] measured $H_0 = 74.03 \pm 1.42\,\mathrm{km\,s^{-1}\,Mpc^{-1}}$.

In the CCHP, [3] calibrated the supernova distance scale using the tip of the red giant branch instead of Cepheids, and measured $H_0 = 69.8 \pm 0.8(\pm 1.1\%\ \mathrm{stat}) \pm 1.7(\pm 2.4\%\ \mathrm{sys})\,\mathrm{km\,s^{-1}\,Mpc^{-1}}$. This measurement is in between the discrepant Planck and SH0ES results, and is within 2σ of either one.

3 Megamasers

Water masers in orbit around supermassive black holes (SMBH) at centers of galaxies provide a geometric approach for measuring H_0. One could measure the velocity v_r of the masers in orbit around the SMBH (through observations of the Doppler shifts in the maser lines), and their angular positions θ_r from the central SMBH. In addition, observations of the change in velocities of the "systemic masers" (which are the masers located in front of the SMBH for nearly edge-on maser disks), the acceleration a_r could be measured. This provides a determination of the physical size of the disk r, since $a_\mathrm{r} = v_\mathrm{r}^2/r$. This physical size could then be compared to the angular size, to derive the angular diameter distance to the maser: $D = r/\theta_\mathrm{r} = v_\mathrm{r}^2/(a_\mathrm{r}\theta_\mathrm{r})$. For disks that are not viewed edge-on, there is an additional $\sin i$ factor in the numerator. Through the distance-redshift relation, the angular diameter distance then provides a measurement of H_0.

The Megamaser Cosmology Project (MCP) [9, 10] aims to determine H_0 precisely via measurements of geometric distances to galaxies in the Hubble flow. The Hubble constant based on the analysis of six megamaser galaxies in the MCP is $H_0 = 73.9 \pm 3.0\,\mathrm{km\,s^{-1}\,Mpc^{-1}}$ [11], assuming a fixed uncertainty for the velocities of 250 $\mathrm{km\,s^{-1}}$ due to peculiar motions. Peculiar motions of galaxies are currently the dominant source of uncertainty in deriving H_0 from the megamasers. Nonetheless, different peculiar velocity corrections performed by [11] do not change H_0 by more than 1σ.

4 Standard Sirens

GW170817 is the first gravitational wave (GW) source detected with electromagnetic (EM) counterpart [12], providing the first opportunity to measure H_0 through the "standard sirens" approach proposed by [13]. The gravitational wave of GW170817 originates from the merger of a binary neutron-star system. Through observations of the gravitational wave signal with the Advanced Laser Interferometer Gravitational-wave Observatory (LIGO) [14] and Virgo [15] detectors, the luminosity distance to the binary system is determined. From the EM observations, the galaxy that hosted the binary system is identified as NGC 4993. Optical observations of NGC4993 subsequently allow the determination of the recessional velocity (incorporating peculiar motion of the galaxy). By combining the luminosity distance from the GW and the recessional velocity from the EM counterpart and

using the Hubble-Lemaître law, [16] made the first measurement of $H_0 = 70^{+12}_{-8}\,\mathrm{km\,s^{-1}\,Mpc^{-1}}$ from this standard siren.

While the measurement is statistically consistent with both the SH0ES and Planck results given its uncertainties, this very first measurement has started the era of standard sirens. The current uncertainties in GW170817 are dominated by the unknown inclination of the binary orbit of the neutron stars, since the inclination is highly degenerate with H_0. Additional gravitational wave detectors in the future would be able to constrain better the inclination. Furthermore, more sirens are expected from future observations of GW sources, providing a completely independent route of measuring H_0.

5 Strongly Lensed Quasars and Supernovae

Strong gravitational lensing occurs when there is a chance alignment of a massive object along the line of sight to a background source. The foreground massive object acts like a lens, and deflects the light rays from the background source such that multiple images of the background source appear around the foreground lens galaxy. When the source is one that varies in its luminosity, such as an activie galactic nucleus or supernova, the variability of the source manifests in each of the multiple images but delayed in time due to the different light paths. [17] proposed to use such time delays to measure H_0. This requires (1) measurements of the time delays by monitoring the lens systems over time, (2) model of the lens mass distribution, and (3) characterisation of mass distributions along the line of sight to the background source.

The H0LiCOW collaboration [18] obtained exquisite imaging and spectroscopic observations of lensed quasars with time delays from the COSMOGRAIL collaboration [19, 20] and radio monitoring [21, 22]. Through the blind analyses of 6 strongly lensed quasars[1] from the H0LiCOW and SHARP collaborations [23, 24, 25, 26, 27, 28, 29], [30] measured $H_0 = 73.3^{+1.7}_{-1.8}\,\mathrm{km\,s^{-1}\,Mpc^{-1}}$. The newly formed TDCOSMO collaboration has performed a detailed investigations of systematic uncertainties of 7 lensed quasars [31], including a seventh lens system analysed by the STRIDES collaboration [32] in addition to the 6 H0LiCOW lenses. In contrast to [33], [31] finds no evidence of bias or errors larger than the current statistical uncertainties reported by H0LiCOW/SHARP/STRIDES.

In addition to lensed quasars, the first lensed supernovae (envisioned by [17]) are being discovered in recent years [34, 35]. Given the exciting prospects of discovering more lensed supernovae, [36] have launched the HOLISMOKES programme to study cosmology and stellar physics with lensed supernovae. With the hundreds of new lens systems expected from current and future surveys, a 1% measurement of H_0 from lensing time delays will be achievable [37, 38].

6 Conclusions

The current tension in the H_0 measurements from Planck and the SH0ES collaborations poses an exciting opportunity for potential discovery of new physics beyond the standard cosmological model. In order to verify that the tension is not due to measurement errors, it is crucial to have multiple independent probes. In this presentation, I have outlined four late-Universe methods that are promising to yield independent measurements of H_0 with uncertainties reaching 1% to address the H_0 tension in the coming years.

Acknowledgements

SHS thanks the organisers for the wonderful conference, and the Max Planck Society for support through the Max Planck Research Group. The HOLISMOKES programme has received funding from

[1] The analysis of the first lens system was not blind, but subsequent analyses of the other lenses were blind.

the European Research Council (ERC) under the European Union's Horizon 2020 research and innovation programme (LENSNOVA: grant agreement No 771776).

References

[1] **Planck** Collaboration, N. Aghanim et al., *Planck 2018 results. VI. Cosmological parameters*, *arXiv e-prints* (July, 2018) arXiv:1807.06209, [arXiv:1807.06209].

[2] A. G. Riess, S. Casertano, W. Yuan, L. M. Macri, and D. Scolnic, *Large Magellanic Cloud Cepheid Standards Provide a 1% Foundation for the Determination of the Hubble Constant and Stronger Evidence for Physics beyond ΛCDM*, *ApJ* **876** (May, 2019) 85, [arXiv:1903.07603].

[3] W. L. Freedman, B. F. Madore, D. Hatt, T. J. Hoyt, I. S. Jang, R. L. Beaton, C. R. Burns, M. G. Lee, A. J. Monson, J. R. Neeley, M. M. Phillips, J. A. Rich, and M. Seibert, *The Carnegie-Chicago Hubble Program. VIII. An Independent Determination of the Hubble Constant Based on the Tip of the Red Giant Branch*, *ApJ* **882** (Sept., 2019) 34, [arXiv:1907.05922].

[4] R. L. Beaton, W. L. Freedman, B. F. Madore, G. Bono, E. K. Carlson, G. Clementini, M. J. Durbin, A. Garofalo, D. Hatt, I. S. Jang, J. A. Kollmeier, M. G. Lee, A. J. Monson, J. A. Rich, V. Scowcroft, M. Seibert, L. Sturch, and S.-C. Yang, *The Carnegie-Chicago Hubble Program. I. An Independent Approach to the Extragalactic Distance Scale Using Only Population II Distance Indicators*, *ApJ* **832** (Dec., 2016) 210, [arXiv:1604.01788].

[5] W. Yuan, A. G. Riess, L. M. Macri, S. Casertano, and D. M. Scolnic, *Consistent Calibration of the Tip of the Red Giant Branch in the Large Magellanic Cloud on the Hubble Space Telescope Photometric System and a Redetermination of the Hubble Constant*, *ApJ* **886** (Nov., 2019) 61, [arXiv:1908.00993].

[6] W. L. Freedman, B. F. Madore, T. Hoyt, I. S. Jang, R. Beaton, M. G. Lee, A. Monson, J. Neeley, and J. Rich, *Calibration of the Tip of the Red Giant Branch*, *ApJ* **891** (Mar., 2020) 57, [arXiv:2002.01550].

[7] W. L. Freedman, B. F. Madore, B. K. Gibson, L. Ferrarese, D. D. Kelson, S. Sakai, J. R. Mould, J. Kennicutt, Robert C., H. C. Ford, J. A. Graham, J. P. Huchra, S. M. G. Hughes, G. D. Illingworth, L. M. Macri, and P. B. Stetson, *Final Results from the Hubble Space Telescope Key Project to Measure the Hubble Constant*, *ApJ* **553** (May, 2001) 47–72, [astro-ph/0012376].

[8] G. Pietrzyński, D. Graczyk, A. Gallenne, W. Gieren, I. B. Thompson, B. Pilecki, P. Karczmarek, M. Górski, K. Suchomska, M. Taormina, B. Zgirski, P. Wielgórski, Z. Kołaczkowski, P. Konorski, S. Villanova, N. Nardetto, P. Kervella, F. Bresolin, R. P. Kudritzki, J. Storm, R. Smolec, and W. Narloch, *A distance to the Large Magellanic Cloud that is precise to one per cent*, *Nature* **567** (Mar., 2019) 200–203, [arXiv:1903.08096].

[9] M. J. Reid, J. A. Braatz, J. J. Condon, L. J. Greenhill, C. Henkel, and K. Y. Lo, *The Megamaser Cosmology Project. I. Very Long Baseline Interferometric Observations of UGC 3789*, *ApJ* **695** (Apr., 2009) 287–291, [arXiv:0811.4345].

[10] J. A. Braatz, M. J. Reid, E. M. L. Humphreys, C. Henkel, J. J. Condon, and K. Y. Lo, *The Megamaser Cosmology Project. II. The Angular-diameter Distance to UGC 3789*, *ApJ* **718** (Aug., 2010) 657–665, [arXiv:1005.1955].

[11] D. W. Pesce, J. A. Braatz, M. J. Reid, A. G. Riess, D. Scolnic, J. J. Condon, F. Gao, C. Henkel, C. M. V. Impellizzeri, C. Y. Kuo, and K. Y. Lo, *The Megamaser Cosmology Project. XIII. Combined Hubble Constant Constraints*, *ApJL* **891** (Mar., 2020) L1, [arXiv:2001.09213].

[12] **LIGO and Virgo** Collaboration, B. P. Abbott et al., *Gw170817: Observation of gravitational waves from a binary neutron star inspiral*, *Phys. Rev. Lett.* **119** (Oct, 2017) 161101.

[13] B. F. Schutz, *Determining the Hubble constant from gravitational wave observations*, *Nature* **323** (Sept., 1986) 310–311.

[14] **LIGO** Collaboration, J. Aasi et al., *Advanced LIGO*, *Classical and Quantum Gravity* **32** (mar, 2015) 074001.

[15] F. Acernese et al., *Advanced Virgo: a second-generation interferometric gravitational wave detector*, *Classical and Quantum Gravity* **32** (Jan., 2015) 024001, [arXiv:1408.3978].

[16] **LIGO and Virgo** Collaboration, B. P. Abbott et al., *A gravitational-wave standard siren measurement of the Hubble constant*, *Nature* **551** (Nov., 2017) 85–88, [arXiv:1710.05835].

[17] S. Refsdal, *On the possibility of determining Hubble's parameter and the masses of galaxies from the gravitational lens effect*, *MNRAS* **128** (Jan., 1964) 307.

[18] S. H. Suyu, V. Bonvin, F. Courbin, C. D. Fassnacht, C. E. Rusu, D. Sluse, T. Treu, K. C. Wong, M. W. Auger, X. Ding, S. Hilbert, P. J. Marshall, N. Rumbaugh, A. Sonnenfeld, M. Tewes, O. Tihhonova, A. Agnello, R. D. Blandford, G. C. F. Chen, T. Collett, L. V. E. Koopmans, K. Liao, G. Meylan, and C. Spiniello, *H0LiCOW - I. H_0 Lenses in COSMOGRAIL's Wellspring: program overview*, *MNRAS* **468** (July, 2017) 2590–2604, [arXiv:1607.00017].

[19] F. Courbin, V. Chantry, Y. Revaz, D. Sluse, C. Faure, M. Tewes, E. Eulaers, M. Koleva, I. Asfand iyarov, S. Dye, P. Magain, H. van Winckel, J. Coles, P. Saha, M. Ibrahimov, and G. Meylan, *COSMOGRAIL: the COSmological MOnitoring of GRAvItational Lenses. IX. Time delays, lens dynamics and baryonic fraction in HE 0435-1223*, *A&A* **536** (Dec., 2011) A53, [arXiv:1009.1473].

[20] M. Tewes, F. Courbin, G. Meylan, C. S. Kochanek, E. Eulaers, N. Cantale, A. M. Mosquera, P. Magain, H. Van Winckel, D. Sluse, G. Cataldi, D. Vörös, and S. Dye, *COSMOGRAIL: the COSmological MOnitoring of GRAvItational Lenses. XIII. Time delays and 9-yr optical monitoring of the lensed quasar RX J1131-1231*, *A&A* **556** (Aug., 2013) A22, [arXiv:1208.6009].

[21] C. D. Fassnacht, T. J. Pearson, A. C. S. Readhead, I. W. A. Browne, L. V. E. Koopmans, S. T. Myers, and P. N. Wilkinson, *A Determination of H_0 with the CLASS Gravitational Lens B1608+656. I. Time Delay Measurements with the VLA*, *ApJ* **527** (Dec., 1999) 498–512, [astro-ph/9907257].

[22] C. D. Fassnacht, E. Xanthopoulos, L. V. E. Koopmans, and D. Rusin, *A Determination of H_0 with the CLASS Gravitational Lens B1608+656. III. A Significant Improvement in the Precision of the Time Delay Measurements*, *ApJ* **581** (Dec., 2002) 823–835, [astro-ph/0208420].

[23] S. H. Suyu, P. J. Marshall, M. W. Auger, S. Hilbert, R. D. Blandford, L. V. E. Koopmans, C. D. Fassnacht, and T. Treu, *Dissecting the Gravitational lens B1608+656. II. Precision Measurements of the Hubble Constant, Spatial Curvature, and the Dark Energy Equation of State*, *ApJ* **711** (Mar., 2010) 201–221, [arXiv:0910.2773].

[24] S. H. Suyu, T. Treu, S. Hilbert, A. Sonnenfeld, M. W. Auger, R. D. Blandford, T. Collett, F. Courbin, C. D. Fassnacht, L. V. E. Koopmans, P. J. Marshall, G. Meylan, C. Spiniello, and M. Tewes, *Cosmology from Gravitational Lens Time Delays and Planck Data*, *ApJL* **788** (June, 2014) L35, [arXiv:1306.4732].

[25] K. C. Wong, S. H. Suyu, M. W. Auger, V. Bonvin, F. Courbin, C. D. Fassnacht, A. Halkola, C. E. Rusu, D. Sluse, A. r. Sonnenfeld, T. Treu, T. E. Collett, S. Hilbert, L. V. E. Koopmans, P. J. Marshall, and N. Rumbaugh, *H0LiCOW - IV. Lens mass model of HE 0435-1223 and blind measurement of its time-delay distance for cosmology*, *MNRAS* **465** (Mar., 2017) 4895–4913, [arXiv:1607.01403].

[26] S. Birrer, T. Treu, C. E. Rusu, V. Bonvin, C. D. Fassnacht, J. H. H. Chan, A. Agnello, A. J. Shajib, G. C. F. Chen, M. Auger, F. Courbin, S. Hilbert, D. Sluse, S. H. Suyu, K. C. Wong, P. Marshall, B. C. Lemaux, and G. Meylan, *H0LiCOW - IX. Cosmographic analysis of the doubly imaged quasar SDSS 1206+4332 and a new measurement of the Hubble constant*, *MNRAS* **484** (Apr., 2019) 4726–4753, [arXiv:1809.01274].

[27] I. Jee, S. H. Suyu, E. Komatsu, C. D. Fassnacht, S. Hilbert, and L. V. E. Koopmans, *A measurement of the Hubble constant from angular diameter distances to two gravitational lenses*, *Science* **365** (Sept., 2019) 1134–1138, [arXiv:1909.06712].

[28] G. C. F. Chen, C. D. Fassnacht, S. H. Suyu, C. E. Rusu, J. H. H. Chan, K. C. Wong, M. W. Auger, S. Hilbert, V. Bonvin, S. Birrer, M. Millon, L. V. E. Koopmans, D. J. Lagattuta, J. P. McKean, S. Vegetti, F. Courbin, X. Ding, A. Halkola, I. Jee, A. J. Shajib, D. Sluse, A. r. Sonnenfeld, and T. Treu, *A SHARP view of H0LiCOW: H_0 from three time-delay gravitational lens systems with adaptive optics imaging*, *MNRAS* **490** (Dec., 2019) 1743–1773, [arXiv:1907.02533].

[29] C. E. Rusu, K. C. Wong, V. Bonvin, D. Sluse, S. H. Suyu, C. D. Fassnacht, J. H. H. Chan, S. Hilbert, M. W. Auger, A. Sonnenfeld, S. Birrer, F. Courbin, T. Treu, G. C. F. Chen, A. Halkola, L. V. E. Koopmans, P. J. Marshall, and A. J. Shajib, *H0LiCOW XII. Lens mass model of WFI2033-4723and blind measurement of its time-delay distance and H_0*, *MNRAS* (June, 2020) [arXiv:1905.09338].

[30] K. C. Wong, S. H. Suyu, G. C. F. Chen, C. E. Rusu, M. Millon, D. Sluse, V. Bonvin, C. D. Fassnacht, S. Taubenberger, M. W. Auger, S. Birrer, J. H. H. Chan, F. Courbin, S. Hilbert, O. Tihhonova, T. Treu, A. Agnello, X. Ding, I. Jee, E. Komatsu, A. J. Shajib, A. Sonnenfeld, R. D. Bland ford, L. V. E. Koopmans, P. J. Marshall, and G. Meylan, *H0LiCOW XIII. A 2.4% measurement of H_0 from lensed quasars: 5.3σ tension between early and late-Universe probes*, *MNRAS* (June, 2020) [arXiv:1907.04869].

[31] M. Millon, A. Galan, F. Courbin, T. Treu, S. H. Suyu, X. Ding, S. Birrer, G. C. F. Chen, A. J. Shajib, D. Sluse, K. C. Wong, A. Agnello, M. W. Auger, E. J. Buckley-Geer, J. H. H. Chan, T. Collett, C. D. Fassnacht, S. Hilbert, L. V. E. Koopmans, V. Motta, S. Mukherjee, C. E. Rusu, A. Sonnenfeld, C. Spiniello, and L. Van de Vyvere, *TDCOSMO. I. An exploration of systematic uncertainties in the inference of H_0 from time-delay cosmography*, *A&A* **639** (July, 2020) A101, [arXiv:1912.08027].

[32] A. J. Shajib et al., *STRIDES: a 3.9 per cent measurement of the Hubble constant from the strong lens system DES J0408-5354*, *MNRAS* **494** (Mar., 2020) 6072–6102, [arXiv:1910.06306].

[33] C. S. Kochanek, *Overconstrained gravitational lens models and the Hubble constant*, *MNRAS* **493** (Apr., 2020) 1725–1735, [arXiv:1911.05083].

[34] P. L. Kelly, S. A. Rodney, T. Treu, R. J. Foley, G. Brammer, K. B. Schmidt, A. Zitrin, A. Sonnenfeld, L.-G. Strolger, O. Graur, A. V. Filippenko, S. W. Jha, A. G. Riess, M. Bradac, B. J. Weiner, D. Scolnic, M. A. Malkan, A. von der Linden, M. Trenti, J. Hjorth, R. Gavazzi, A. Fontana, J. C. Merten, C. McCully, T. Jones, M. Postman, A. Dressler, B. Patel, S. B. Cenko, M. L. Graham, and B. E. Tucker, *Multiple images of a highly magnified supernova formed by an early-type cluster galaxy lens*, *Science* **347** (Mar., 2015) 1123–1126, [arXiv:1411.6009].

[35] A. Goobar, R. Amanullah, S. R. Kulkarni, P. E. Nugent, J. Johansson, C. Steidel, D. Law, E. Mörtsell, R. Quimby, N. Blagorodnova, A. Brand eker, Y. Cao, A. Cooray, R. Ferretti, C. Fremling, L. Hangard, M. Kasliwal, T. Kupfer, R. Lunnan, F. Masci, A. A. Miller, H. Nayyeri, J. D. Neill, E. O. Ofek, S. Papadogiannakis, T. Petrushevska, V. Ravi, J. Sollerman, M. Sullivan, F. Taddia, R. Walters, D. Wilson, L. Yan, and O. Yaron, *iPTF16geu: A multiply imaged, gravitationally lensed type Ia supernova*, *Science* **356** (Apr., 2017) 291–295, [arXiv:1611.00014].

[36] S. H. Suyu, S. Huber, R. Cañameras, S. Schuldt, S. Taubenberger, A. Yıldırım, V. Bonvin, J. H. H. Chan, F. Courbin, M. Kromer, U. Nöbauer, S. A. Sim, and D. Sluse, *HOLISMOKES – I. Highly Optimised Lensing Investigations of Supernovae, Microlensing Objects, and Kinematics of Ellipticals and Spirals*, *arXiv e-prints* (Feb., 2020) arXiv:2002.08378, [arXiv:2002.08378].

[37] I. Jee, E. Komatsu, S. H. Suyu, and D. Huterer, *Time-delay cosmography: increased leverage with angular diameter distances*, *JCAP* **2016** (Apr., 2016) 031, [arXiv:1509.03310].

[38] A. J. Shajib, T. Treu, and A. Agnello, *Improving time-delay cosmography with spatially resolved kinematics*, *MNRAS* **473** (Jan., 2018) 210–226, [arXiv:1709.01517].

How to Resolve the Hubble Tension

Vivian Poulin

e-mail: vivian.poulin@umontpellier.fr

Laboratoire Univers & Particules de Montpellier (LUPM), CNRS & Université de Montpellier

Presented at the 3rd World Summit on Exploring the Dark Side of the Universe
Guadeloupe Islands, March 9-13 2020

Abstract

The 'Hubble tension' is a $\sim 5\sigma$ discrepancy – in the ΛCDM context – between the H_0 value derived from early- and late-universe observations. I discuss guidelines to resolving this long-standing mystery, arguing that our best shot is through modification of the pre-recombination physics, right around matter-radiation equality. I introduce a toy model dubbed 'Early Dark Energy' (EDE) in which a frozen scalar-field contributing a fraction $f_{\rm EDE}(z_c) \sim 10\%$ of the energy density of the universe around $z_c \simeq 3500$ and diluting as or faster than radiation afterwards can accomodate CMB, Baryon Acoustic Oscillation (BAO), growth function (FS), Supernova Ia (SNIa) and the latest SH0ES measurement of H_0. I discuss some potential challenges that this model is facing in light of the latest weak lensing surveys, but argue that the level of tension between weak lensing surveys and Planck within ΛCDM does not allow to make robust conclusions about the status of EDE. Future CMB and LSS measurements will provide a definitive test to this scenario.

1 Introduction

In recent years, a strong mismatch between the prediction of the current expansion rate of the universe (known as Hubble constant) in the Λ cold dark matter (ΛCDM) model calibrated onto Planck CMB data, and its direct measurement using low redshift data (i.e., the classical distance ladder) [1, 2] has emerged. Originally, this "Hubble tension" was limited to the determination of the Hubble constant using type Ia supernovae by the SH0ES collaboration, whose latest *determination* is $H_0 = 74.03 \pm 1.42$ km/s/Mpc [3], while the *prediction* from the ΛCDM model inferred from Planck CMB data is $H_0 = 67.4 \pm 0.5$ km/s/Mpc [4]. Tremendous progress have been made in measuring H_0 with alternative methods, such that nowadays there exist five other methods[1] to measure H_0 with few percent accuracy. Remarkably, various averages over these measurements (excluding correlated data) leads to H_0 values that ranges from 72.8 ± 1.1 and 74.3 ± 1.0, in 4.5 to 6.3σ discrepancy with the prediction from ΛCDM [1, 2]. A number of possible systematic effects affecting some of these measurements have been discussed (see e.g. [11, 12, 13, 14, 15]), yet the existence of several vastly different methods – none of which giving a value of H_0 smaller than ~ 70 km/s/Mpc – have triggered a wide range of theoretical activities to resolve the Hubble tension (see in particular [16] for a recent review). This tension between different measurements of the Hubble constant could point to a major failure of the ΛCDM scenario, and hence to a new cosmological paradigm: that would be a new and unexpected breakthrough in cosmology.

[1] These include strong-lens time delays of quasars [5], Tip of the red giant branch from the 'CCHP' [6, 7] (and re-evaluation by the SH0ES team [8]), SNIa calibrated on Miras (an alternative to Cepheids) [9], water masers (sources of microwave stimulated emission) in four galaxies at great distances [10] and Surface Brightness Fluctuations of distant galaxies [1].

There have been many attempts to find extensions of the standard cosmological model, ΛCDM, which bring these estimates into agreement. However, theoretical explanations for the Hubble tension are not easy to come by. It has been found that the most promising solution lies in modifying physics in the pre-recombination era ($10000 > z > 1000$) [16]. At first sight, given the precision measurements of the CMB from Planck, this might appear to be even more constraining than the late-time probes of the expansion rate. Excitingly, there are a few early-time resolutions which do not spoil the fit to current CMB temperature measurements [17, 18, 19, 20, 21], sometimes even *improving it* over ΛCDM.

In this talk, I show that a constant Early Dark Energy (EDE) component contributing a fraction $f_{\rm EDE}(z_c) \sim 10\%$ of the energy density of the universe around $z_c \simeq 3500$ and diluting as or faster than radiation afterwards can resolve the Hubble tension. After introducing generic guidelines to resolving this tension, I introduce the EDE model and show through a MCMC analysis that incorporates the latest CMB, BAO, SN1a and SH0ES data that this model can resolve the tension. I then discuss some potential challenges that this model is facing in light of the latest weak lensing surveys, before drawing my conclusions.

2 Guidelines to resolving the Hubble tension

CMB data do not provide an absolute measurement of H_0. Rather, the value of H_0 is inferred within a given cosmological model from a measurement of the angular scale of sound horizon $\theta_s \equiv r_s(z_*)/d_A(z_*)$, where $r_s(z_*)$ is the sound horizon at recombination and $d_A(z_*)$ is the angular diameter distance to recombination. The great challenge lies in that θ_s is nowadays measured at sub-percent-level accuracy with the latest CMB data [4]. This suggests two main ways of resolving the Hubble tension through new physics – based on the requirement to keep the key angular scale θ_s fixed – usually called *late-* and *early*-universe solutions.

- The first way boils down to changing the redshift evolution of the angular diameter distance in the late-universe, i.e. $z < z_*$, so as to force a higher H_0, *without* changing $d_A(z_*)$ nor $r_s(z_*)$. To that end, a large number of proposed scenarios invoked modification of the late-time dynamics of dark matter and/or dark energy. This includes (but is not limited to) models of dynamical dark energy [22], decaying dark matter [23] and interacting dark matter-dark energy [24]. Late-time observables, especially BAO and luminosity-distance to SNIa, place severe limitations on modifications to the late-time ($0 \leq z \leq 2$) expansion history [25, 26, 27, 28, 29, 30, 31, 32, 33, 34, 35, 36].

- The second way amounts in reducing $r_s(z_*)$ in the early-universe, which automatically requires to reduce $d_A(z_*)$ by the same amount to keep θ_s fixed, that is most naturally done by increasing the value of H_0. This can be done through additional relativistic species from various sources [32, **?**], exotic recombination [37, 38, 21], a time-varying Newton constant [39, 40] or the presence of dark energy at early times [41, 17, 42, 43, 44, 19]. However, most of these models are constrained by the details of the CMB acoustic peaks and in particular by the fact that the additional energy density lead to a different angular diffusion damping scale [16].

- A final, more subtle, way of resolving the H_0 tension comes from the fact that the position of the peaks receives an additional phase-shift from various effects, in particular from the gravitational pulling of CMB photons out of the potential wells by free-streaming neutrinos [45, 46, 47]. Suppressing this phase-shift can change the value of θ_s deduced from a CMB power spectra analysis and in turn significantly increase H_0.

3 Early Dark Energy resolution to the Hubble tension

The possible presence of a dark energy component before last-scattering has been studied for more than a decade [48, 49]. These alternative cosmological realizations have little to do with that under study here, as they typically assume tracking equation of state at early times. The idea of an anomalous era of expansion triggered by a frozen scalar field as a resolution to the Hubble tension was introduced in Ref. [41], where a background-only computation was shown to alleviate the Hubble tension. However, it is the work of Ref. [17] that showed through a fluid approximation the key role played by perturbations in the scalar field to allow for a resolution of the Hubble tension. Since this work, the treatment of the EDE component has been improved [42, 43, 44], and augmented to deal with alternative potentials and better motivated underlying fundamental models [50, 42, 44, 51, 52, 53, 40, 19, 54]. In particular, it has been shown that Planck data not only provide a detection of the background dynamics of the EDE component, but also severely restricts the dynamics of perturbations [44, 43]. As such, Planck data allows for pinning down directly properties of the EDE, making the choice of model crucial. They favor either non-canonical kinetic term whereby the equation of state w is approximately equal to the effective sound speed c_s^2 [44], or potential that flattens close to the initial field value [43].

In this talk, I study the modified axion potential introduced in Refs. [55, 41, 56, 17, 43],

$$V_n(\Theta) = m^2 f^2 [1 - \cos(\Theta)]^n, \tag{1}$$

where m represent the axion mass, f the decay constant and $\Theta \equiv \phi/f$ is a re-normalized field variable, so that $-\pi \leq \Theta \leq \pi$. It is assumed that the field always starts in slow-roll the background dynamics and without loss of generality $0 \leq \Theta_i \leq \pi$.

This potential is a phenomenological generalization of the well motivated axion-like potential (which can be recovered by setting $n = 1$) that arise generically in string theory [57, 58, 59, 60, 60]. Such a potential may be generated by higher-order instanton corrections [61], but taken at face values would suffer from a strong fine-tuning issues necessary to the cancelling of the lowest orders instantons. Therefore, it should not be interpreted beyond a phenomenological description. Note that similar forms of potential, with power law minima and flattened "wings" have been used in the context of inflationary physics, as well as dark energy (see, e.g., Refs. [62, 63, 64]). Still, this form was devised to allow for flexibility in the background dynamics after the field becomes dynamical, and it also provides an excellent fit to both Planck and SH0ES data. It corresponds to the EDE scenario that leads to the best combined χ^2 of the cosmological data-sets under study (although the better theoretically motivated model studied in Ref. [19, 54] seems to perform equally well).

Refer to Refs. [56, 43] for all necessary details about the model. The key features can be summarized as follows: at early times the scalar field is frozen due to Hubble friction, until the Hubble rate drops below its mass value; the field then starts moving in the potential, and eventually oscillating around the minimum, at which point the energy density dilutes at a rate dictated by the asymptotic equation of state $w(n) = (n-1)/(n+1)$ (e.g., Refs. [65, 66, 56]).

One can trade three out of the four model parameters $\{m, f, n, \Theta_i\}$ for phenomenological parameters: the first two of them describing the fractional energy density $f_{\rm EDE}(z_c)$ at the critical redshift z_c where the field becomes dynamical and the asymptotic equation of states after the field becomes dynamical $w(n) = (n-1)/(n+1)$, respectively; the last degree of freedom lies in the dynamics of linear perturbations, whose phenomenology is captured by the effective sound speed c_s^2. However, within the EDE scalar field scenario under study, such freedom is intrinsically encoded in the choice of the initial field value[2] Θ_i, once the other phenomenological parameters have been fixed.

To perform the analyses, the modified version of the Einstein-Boltzmann code CLASS [67, 68] presented in Ref. [43] is used. The code is publicly available at https://github.com/PoulinV/AxiCLASS (the latest version, used for this study, can be found in the "merge2.9" branch).

[2] In practice, it is the curvature of the potential, $\partial^2 V(\Theta)/\partial^2\Theta$, close to the initial field value Θ_i that dictates the last of degree of freedom in the perturbation dynamics [56, 43].

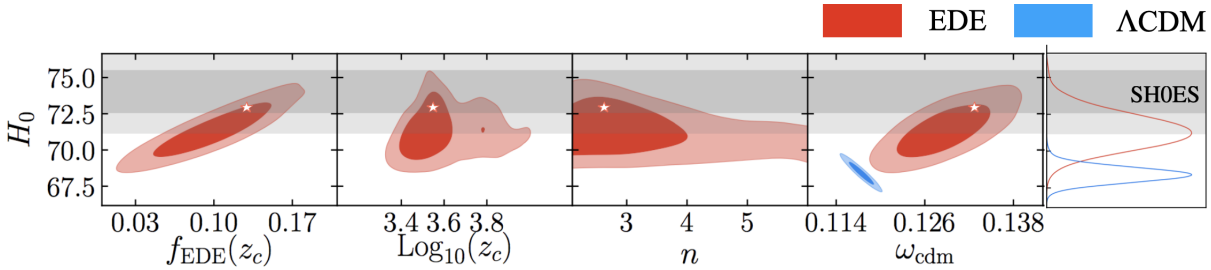

Figure 1: 2D posterior distribution of H_0 vs $\{f_{\rm EDE}(z_c), \log_{10}(z_c), n_{\rm EDE}, \omega_{\rm cdm}\}$ reconstructed from the analysis of Planck+BAO+SN1a+SH0ES data.

The results of a Markov-chain Monte Carlo (MCMC) taken from Ref. [43] and using the public code MontePython-v3[3] [69, 70], interfaced with the modified version of CLASS, is shown in Fig. 1. The analysis is performed with a Metropolis-Hasting algorithm, assuming flat priors on

$$\{\omega_b, \omega_{\rm cdm}, \theta_s, A_s, n_s, \tau_{\rm reio}, \log_{10}(z_c), f_{\rm EDE}(z_c), \Theta_i, n\}.$$

A shooting method to map a choice of $\{\log_{10}(z_c), f_{\rm EDE}\}$ to the theory parameters $\{m, f\}$ was used[43]. We adopt the Planck collaboration convention and model free-streaming neutrinos as two massless species and one massive with $M_\nu = 0.06$ eV [71]. The data set includes Planck 2015 high-ℓ and low-ℓ TT,TE,EE and lensing likelihood [72]; the latest SH0ES measurement of the present-day Hubble rate $H_0 = 74.03 \pm 1.42$ km/s/Mpc [3]; the isotropic BAO measurements from 6dFGS at $z = 0.106$ [25] and from the MGS galaxy sample of SDSS at $z = 0.15$ [26]; the anisotropic BAO and the growth function $f\sigma_8(z)$ measurements from the CMASS and LOWZ galaxy samples of BOSS DR12 at $z = 0.38, 0.51,$ and 0.61 [31]; the Pantheon[4] supernovae dataset [73], which includes measurements of the luminosity distances of 1048 SNe Ia in the redshift range $0.01 < z < 2.3$. Chains are considered to be converged using the Gelman-Rubin [74] criterion $R - 1 < 0.1$.

In the EDE cosmology, it is found that $H_0 = 71.5 \pm 1.2$ km/s/Mpc, with $f_{\rm EDE} = 0.1 \pm 0.03$ and $\log_{10}(z_c) = 3.56^{+0.05}_{-0.1}$. For comparison, the same analysis within ΛCDM yields $H_0 = 68.4 \pm 0.5$. The $\Delta\chi^2_{\rm min} = \chi^2_{\rm min}(\Lambda{\rm CDM}) - \chi^2_{\rm min}({\rm EDE}) = -20.33$ strongly favors EDE over ΛCDM (even when accounting for the extra degrees of freedom e.g. through a bayesian model comparison [17]). However, it is worth noting that Planck itself only mildly favors EDE, with a $\Delta\chi^2_{\rm min} \simeq= -6$ and most of the $\chi^2_{\rm min}$ difference is driven by SH0ES. The inability of Planck to distinguish EDE from ΛCDM is particularly visible in the CMB power spectra residual plot shown in fig. 2, where the two models are basically indistinguishable given current error bars. However, as shown in Fig. 3, an experiment like CMB-S4 [75] would be able to unambiguously detect the presence of EDE, regardless of the inclusion of SH0ES measurement of H_0 in the analysis.

As illustrated in the left panel of fig. 4, Planck polarization data also puts a strong constraint on the initial field value Θ_i. This is because the shape of the potential close to the initial field value, which flatten for a cosine (see the right panel of fig. 4) at high field value, plays a crucial role in the dynamics of EDE perturbations. One can thus conclude that, the very accurate measurement of CMB polarization data restricts not only the background dynamics but also that of perturbations. This was also shown in a model independent way in Ref. [44] and for a different EDE model in Ref. [19].

Finally, one can see in Fig. 1, that the EDE cosmology has $\omega_{\rm cdm} = 0.1290 \pm 0.0045$, a significant increase from the ΛCDM value $\omega_{\rm cdm} = 0.1175 \pm 0.0012$. This is due to the effect of the EDE perturbations on the gravitational potential wells, which is compensated for by a higher $\omega_{\rm cdm}$. This has interesting (and potentially dramatic) consequences for the growth of structure- the predicted matter power spectrum shows somewhat more power than in ΛCDM, as attested by the higher value of

[3] https://github.com/brinckmann/montepython_public
[4] https://github.com/dscolnic/Pantheon

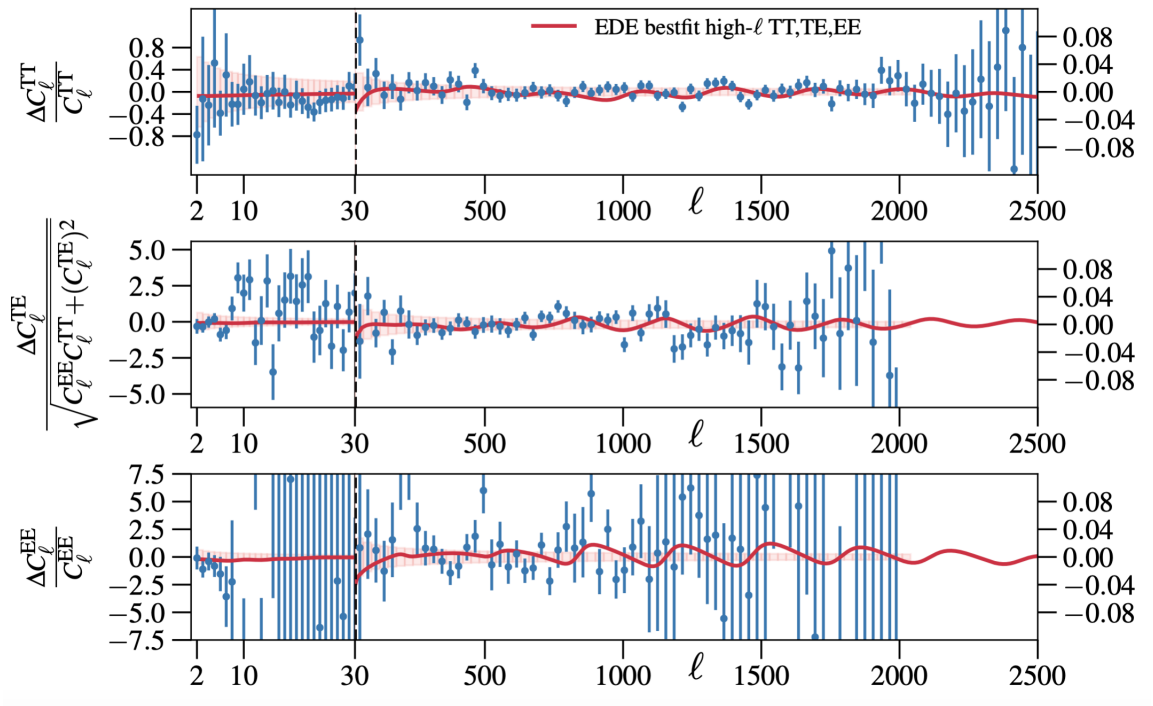

Figure 2: Residual of the CMB power spectra between ΛCDM and the bestfit EDE cosmology. The small differences, indistinguishable by Planck, can be measured by future experiment such as CMB-S4 [75].

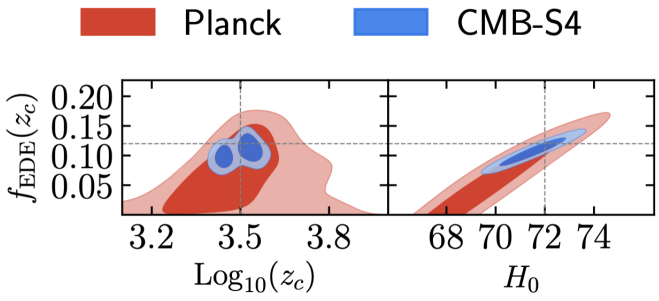

Figure 3: Posterior distributions of $\{\log(10)(z_c), f_{\rm EDE}(z_c)\}$ and $H_0, f_{\rm EDE}(z_c)\}$ reconstructed from a fit to simulated Planck data and CMB-S4. The fiducial model has $\{H_0 = 72$ km/s/Mpc, $f_{\rm EDE}(zc) = 0.115, \log_{10}(z_c) = 3.53.\}$

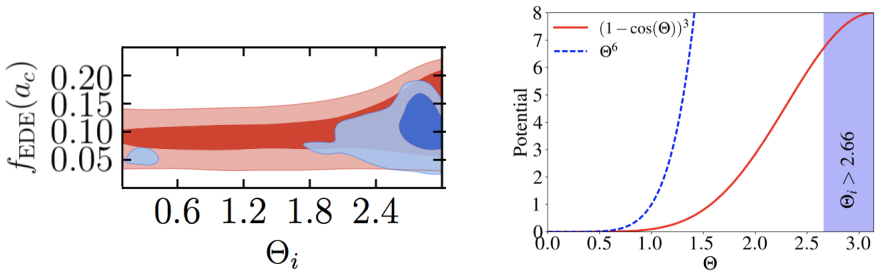

Figure 4: Left panel− 2D posterior distribution of $f_{\rm EDE}$ vs Θ_i reconstructed from Planck TT data (red) or TT+TE+EE data (blue), in combination with BAO, SN1a and SH0ES. Right panel − the potential as a function of the field value. The shape of the potential close to the initial field value plays a crucial role in the success of the solution, translating into a strong constraints on Θ_i.

$S_8 \equiv \sigma_8(\Omega_m/0.3)^{0.5} = 0.840 \pm 0.015$ – where σ_8 measures the amplitude of fluctuations in a sphere of radius 8 Mpc/h – than in ΛCDM, $S_8 = 0.820 \pm 0.012$. This opens up the possibility of constraining EDE with weak lensing data measuring S_8 to high accuracy, as done for instance in Ref. [76]. Indeed, a number of cosmic shear surveys (CFHTLenS [77], KiDS/Viking [78], DES [79], HSC [80]) have provided measurements of S_8 which are systematically lower than the ΛCDM prediction. The significance of this "S_8 tension" oscillates between 2 and 4σ depending on the experiments, such that the discrepancy cannot easily be attributed to a statistical fluke. In Ref. [76], it was for instance shown that the joint KiDS+Viking+DES data can constrain $f_{\rm EDE} < 0.057$ at 95% C.L.. However, the apparent constraining power on EDE is entirely driven by a $\sim 3\sigma$ statistical inconsistency that is already present between joint KiDS+Viking+DES data [81] and the ΛCDM model inferred from *Planck* data, which makes it hard to properly interpret constraints to beyond-ΛCDM models when using these data.

4 Conclusions

I have presented an early-dark energy model able to resolve the $4-6\sigma$ discrepancy between the prediction of Hubble constant in the Λ cold dark matter (ΛCDM) model calibrated onto Planck CMB data, and its direct measurement using a variety of low redshift data. In this model, it is found that a maximal fraction of early dark energy $f_{\rm EDE} = 0.1 \pm 0.03$ at the redshift $\log_{10}(z_c) = 3.56^{+0.05}_{-0.1}$ allows to reach $H_0 = 71.5 \pm 1.2$ km/s/Mpc. Taken at face value, this model suffers from a coincidence problem as the fluid needs to become dynamical around a key era of the universe. This is not without reminding the standard coincidence problem of DE that such models were originally introduced to resolve. However, this coincidence might be the sign of a very specific dynamics to be uncovered; in fact there exist models in which the field becomes dynamical precisely around matter-radiation equality, either because of a phase-transition triggered by some other process (e.g. the neutrino mass becoming of the order of the neutrino bath temperature [51] or the dynamics of a trigger field [19]) or because of a non-minimal coupling to the Ricci curvature [82]. An important follow-up to these studies will be to see whether the new ACT data [83], compatible with Planck (although see Ref. [84]), support – or restrict – the EDE resolution to the Hubble tension. Looking forward, future CMB experiment (such as Simons Observatory [71] and CMB-S4 [75]) and LSS data (from Euclid [85], LSST [86], JWST and DESI [87]) will be crucial in testing prediction of the EDE cosmology (and its potential extensions) [43, 88] and firmly confirm – or exclude – the presence of EDE.

Acknowledgements

VP warmly thanks the organizers of the EDSU 2020 Conference for their effort in keeping the conference going despite the extremely difficult situation due to the world wide pandemic.

References

[1] L. Verde, T. Treu, and A. G. Riess, *Tensions between the Early and the Late Universe*, in *Nature Astronomy 2019*, 2019. arXiv:1907.10625.

[2] A. G. Riess, *The expansion of the Universe is faster than expected*, *Nature Reviews Physics* **2** (Dec., 2019) 10–12, [arXiv:2001.03624].

[3] A. G. Riess, S. Casertano, W. Yuan, L. M. Macri, and D. Scolnic, *Large Magellanic Cloud Cepheid Standards Provide a 1% Foundation for the Determination of the Hubble Constant and Stronger Evidence for Physics beyond ΛCDM*, *Astrophys. J.* **876** (2019), no. 1 85, [arXiv:1903.07603].

[4] **Planck** Collaboration, N. Aghanim et al., *Planck 2018 results. VI. Cosmological parameters*, arXiv:1807.06209.

[5] K. C. Wong et al., *H0LiCOW XIII. A 2.4% measurement of H_0 from lensed quasars: 5.3σ tension between early and late-Universe probes*, arXiv:1907.04869.

[6] W. L. Freedman et al., *The Carnegie-Chicago Hubble Program. VIII. An Independent Determination of the Hubble Constant Based on the Tip of the Red Giant Branch*, arXiv:1907.05922.

[7] W. L. Freedman, B. F. Madore, T. Hoyt, I. S. Jang, R. Beaton, M. G. Lee, A. Monson, J. Neeley, and J. Rich, *Calibration of the Tip of the Red Giant Branch (TRGB)*, arXiv:2002.01550.

[8] W. Yang, S. Pan, E. Di Valentino, R. C. Nunes, S. Vagnozzi, and D. F. Mota, *Tale of stable interacting dark energy, observational signatures, and the H_0 tension*, *JCAP* **1809** (2018), no. 09 019, [arXiv:1805.08252].

[9] C. D. Huang, A. G. Riess, W. Yuan, L. M. Macri, N. L. Zakamska, S. Casertano, P. A. Whitelock, S. L. Hoffmann, A. V. Filippenko, and D. Scolnic, *Hubble Space Telescope Observations of Mira Variables in the SN Ia Host NGC 1559: An Alternative Candle to Measure the Hubble Constant*, *Astrophys. J.* **889** (Jan., 2020) 5, [arXiv:1908.10883].

[10] D. W. Pesce, J. A. Braatz, M. J. Reid, A. G. Riess, D. Scolnic, J. J. Condon, F. Gao, C. Henkel, C. M. V. Impellizzeri, C. Y. Kuo, and K. Y. Lo, *The Megamaser Cosmology Project. XIII. Combined Hubble Constant Constraints*, *ApJ Letters* **891** (Mar., 2020) L1, [arXiv:2001.09213].

[11] M. Rigault et al., *Confirmation of a Star Formation Bias in Type Ia Supernova Distances and its Effect on Measurement of the Hubble Constant*, *Astrophys. J.* **802** (2015), no. 1 20, [arXiv:1412.6501].

[12] **Nearby Supernova Factory** Collaboration, M. Rigault et al., *Strong Dependence of Type Ia Supernova Standardization on the Local Specific Star Formation Rate*, arXiv:1806.03849.

[13] K. Blum, E. Castorina, and M. Simonović, *Could Quasar Lensing Time Delays Hint to a Core Component in Halos, Instead of H_0 Tension?*, *Astrophys. J. Lett.* **892** (2020), no. 2 L27, [arXiv:2001.07182].

[14] M. Millon et al., *TDCOSMO. I. An exploration of systematic uncertainties in the inference of H_0 from time-delay cosmography*, *Astron. Astrophys.* **639** (2020) A101, [arXiv:1912.08027].

[15] S. Birrer et al., *TDCOSMO IV: Hierarchical time-delay cosmography – joint inference of the Hubble constant and galaxy density profiles*, arXiv:2007.02941.

[16] L. Knox and M. Millea, *The Hubble Hunter's Guide*, arXiv:1908.03663.

[17] V. Poulin, T. L. Smith, T. Karwal, and M. Kamionkowski, *Early Dark Energy Can Resolve The Hubble Tension*, *Phys. Rev. Lett.* **122** (2019), no. 22 221301, [arXiv:1811.04083].

[18] C. D. Kreisch, F.-Y. Cyr-Racine, and O. Dor[U+FFFD], arXiv:1902.00534.

[19] F. Niedermann and M. S. Sloth, *New Early Dark Energy*, arXiv:1910.10739.

[20] M. Escudero and S. J. Witte, *Could the Hubble Tension be Pointing Towards the Neutrino Mass Mechanism?*, *arXiv e-prints* (Apr., 2020) arXiv:2004.01470, [arXiv:2004.01470].

[21] K. Jedamzik and L. Pogosian, *Relieving the Hubble tension with primordial magnetic fields*, *arXiv e-prints* (Apr., 2020) arXiv:2004.09487, [arXiv:2004.09487].

[22] **CORE** Collaboration, E. Di Valentino et al., *Exploring cosmic origins with CORE: Cosmological parameters*, *JCAP* **1804** (2018) 017, [arXiv:1612.00021].

[23] V. Poulin, P. D. Serpico, and J. Lesgourgues, *A fresh look at linear cosmological constraints on a decaying dark matter component*, *JCAP* **1608** (2016), no. 08 036, [arXiv:1606.02073].

[24] E. Di Valentino, A. Melchiorri, O. Mena, and S. Vagnozzi, *Interacting dark energy after the latest Planck, DES, and H_0 measurements: an excellent solution to the H_0 and cosmic shear tensions*, arXiv:1908.04281.

[25] F. Beutler, C. Blake, M. Colless, D. H. Jones, L. Staveley-Smith, L. Campbell, Q. Parker, W. Saunders, and F. Watson, *The 6dF Galaxy Survey: Baryon Acoustic Oscillations and the Local Hubble Constant*, *Mon. Not. Roy. Astron. Soc.* **416** (2011) 3017–3032, [arXiv:1106.3366].

[26] A. J. Ross, L. Samushia, C. Howlett, W. J. Percival, A. Burden, and M. Manera, *The clustering of the SDSS DR7 main Galaxy sample ? I. A 4 per cent distance measure at $z = 0.15$*, *Mon. Not. Roy. Astron. Soc.* **449** (2015), no. 1 835–847, [arXiv:1409.3242].

[27] A. G. Riess et al., *A 2.4% Determination of the Local Value of the Hubble Constant*, *Astrophys. J.* **826** (2016), no. 1 56, [arXiv:1604.01424].

[28] E. Di Valentino, A. Melchiorri, E. V. Linder, and J. Silk, *Constraining Dark Energy Dynamics in Extended Parameter Space*, *Phys. Rev. D* **96** (2017), no. 2 023523, [arXiv:1704.00762].

[29] G. E. Addison, D. J. Watts, C. L. Bennett, M. Halpern, G. Hinshaw, and J. L. Weiland, *Elucidating ΛCDM: Impact of Baryon Acoustic Oscillation Measurements on the Hubble Constant Discrepancy*, *Astrophys. J.* **853** (2018), no. 2 119, [arXiv:1707.06547].

[30] E. Di Valentino, A. Melchiorri, and O. Mena, *Can interacting dark energy solve the H_0 tension?*, *Phys. Rev. D* **96** (2017), no. 4 043503, [arXiv:1704.08342].

[31] **BOSS** Collaboration, S. Alam et al., *The clustering of galaxies in the completed SDSS-III Baryon Oscillation Spectroscopic Survey: cosmological analysis of the DR12 galaxy sample*, *Mon. Not. Roy. Astron. Soc.* **470** (2017), no. 3 2617–2652, [arXiv:1607.03155].

[32] J. L. Bernal, L. Verde, and A. G. Riess, *The trouble with H_0*, *JCAP* **1610** (2016), no. 10 019, [arXiv:1607.05617].

[33] G.-B. Zhao et al., *Dynamical dark energy in light of the latest observations*, *Nature Astron.* **1** (2017), no. 9 627–632, [arXiv:1701.08165].

[34] V. Poulin, K. K. Boddy, S. Bird, and M. Kamionkowski, *Implications of an extended dark energy cosmology with massive neutrinos for cosmological tensions*, *Phys. Rev.* **D97** (2018), no. 12 123504, [arXiv:1803.02474].

[35] K. Aylor, M. Joy, L. Knox, M. Millea, S. Raghunathan, and W. L. K. Wu, *Sounds Discordant: Classical Distance Ladder & ΛCDM -based Determinations of the Cosmological Sound Horizon*, *Astrophys. J.* **874** (2019), no. 1 4, [arXiv:1811.00537].

[36] M. Raveri, *Reconstructing gravity on cosmological scales*, *Phys. Rev. D* **101** (Apr., 2020) 083524, [arXiv:1902.01366].

[37] C.-T. Chiang and A. Slosar, *Inferences of H_0 in presence of a non-standard recombination*, arXiv:1811.03624.

[38] L. Hart and J. Chluba, *Updated fundamental constant constraints from Planck 2018 data and possible relations to the Hubble tension*, *Mon. Not. Roy. Astron. Soc.* **493** (2020), no. 3 3255–3263, [arXiv:1912.03986].

[39] M. Zumalacarregui, *Gravity in the Era of Equality: Towards solutions to the Hubble problem without fine-tuned initial conditions*, *Phys. Rev. D* **102** (2020), no. 2 023523, [arXiv:2003.06396].

[40] M. Braglia, M. Ballardini, W. T. Emond, F. Finelli, A. E. Gumrukcuoglu, K. Koyama, and D. Paoletti, *A larger value for H_0 by an evolving gravitational constant*, arXiv:2004.11161.

[41] T. Karwal and M. Kamionkowski, *Dark energy at early times, the Hubble parameter, and the string axiverse*, *Phys. Rev.* **D94** (2016), no. 10 103523, [arXiv:1608.01309].

[42] P. Agrawal, F.-Y. Cyr-Racine, D. Pinner, and L. Randall, *Rock 'n' Roll Solutions to the Hubble Tension*, arXiv:1904.01016.

[43] T. L. Smith, V. Poulin, and M. A. Amin, *Oscillating scalar fields and the Hubble tension: a resolution with novel signatures*, arXiv:1908.06995.

[44] M.-X. Lin, G. Benevento, W. Hu, and M. Raveri, *Acoustic Dark Energy: Potential Conversion of the Hubble Tension*, *Phys. Rev.* **D100** (2019), no. 6 063542, [arXiv:1905.12618].

[45] S. Bashinsky and U. Seljak, *Signatures of relativistic neutrinos in CMB anisotropy and matter clustering*, *Phys. Rev. D* **69** (Apr., 2004) 083002, [astro-ph/0310198].

[46] B. Follin, L. Knox, M. Millea, and Z. Pan, *First Detection of the Acoustic Oscillation Phase Shift Expected from the Cosmic Neutrino Background*, *Phys. Rev. Lett.* **115** (2015), no. 9 091301, [arXiv:1503.07863].

[47] D. Baumann, D. Green, J. Meyers, and B. Wallisch, *Phases of New Physics in the CMB*, *JCAP* **01** (2016) 007, [arXiv:1508.06342].

[48] M. Doran, M. J. Lilley, J. Schwindt, and C. Wetterich, *Quintessence and the separation of CMB peaks*, *Astrophys. J.* **559** (2001) 501–506, [astro-ph/0012139].

[49] C. Wetterich, *Phenomenological parameterization of quintessence*, *Phys. Lett. B* **594** (2004) 17–22, [astro-ph/0403289].

[50] N. Kaloper, *Dark energy, H_0 and weak gravity conjecture*, *Int. J. Mod. Phys. D* **28** (2019), no. 14 1944017, [arXiv:1903.11676].

[51] J. Sakstein and M. Trodden, *Early dark energy from massive neutrinos – a natural resolution of the Hubble tension*, arXiv:1911.11760.

[52] K. V. Berghaus and T. Karwal, *Thermal Friction as a Solution to the Hubble Tension*, arXiv:1911.06281.

[53] S. Alexander and E. McDonough, *Axion-Dilaton Destabilization and the Hubble Tension*, *Phys. Lett. B* **797** (2019) 134830, [arXiv:1904.08912].

[54] F. Niedermann and M. S. Sloth, *Resolving the Hubble Tension with New Early Dark Energy*, arXiv:2006.06686.

[55] M. Kamionkowski, J. Pradler, and D. G. E. Walker, *Dark energy from the string axiverse*, *Phys. Rev. Lett.* **113** (2014), no. 25 251302, [arXiv:1409.0549].

[56] V. Poulin, T. L. Smith, D. Grin, T. Karwal, and M. Kamionkowski, *Cosmological implications of ultralight axionlike fields*, *Phys. Rev.* **D98** (2018), no. 8 083525, [arXiv:1806.10608].

[57] P. Svrcek and E. Witten, *Axions In String Theory*, *JHEP* **06** (2006) 051, [hep-th/0605206].

[58] M. R. Douglas and S. Kachru, *Flux compactification*, *Rev. Mod. Phys.* **79** (2007) 733–796, [hep-th/0610102].

[59] A. Arvanitaki, S. Dimopoulos, S. Dubovsky, N. Kaloper, and J. March-Russell, *String Axiverse*, *Phys. Rev. D* **81** (2010) 123530, [arXiv:0905.4720].

[60] D. J. E. Marsh, *Axion Cosmology*, *Phys. Rept.* **643** (2016) 1–79, [arXiv:1510.07633].

[61] R. Kappl, H. P. Nilles, and M. W. Winkler, *Modulated Natural Inflation*, *Phys. Lett. B* **753** (2016) 653–659, [arXiv:1511.05560].

[62] X. Dong, B. Horn, E. Silverstein, and A. Westphal, *Simple exercises to flatten your potential*, *Phys. Rev. D* **84** (2011) 026011, [arXiv:1011.4521].

[63] R. Kallosh and A. Linde, *Universality Class in Conformal Inflation*, *JCAP* **07** (2013) 002, [arXiv:1306.5220].

[64] J. J. M. Carrasco, R. Kallosh, and A. Linde, *α-Attractors: Planck, LHC and Dark Energy*, *JHEP* **10** (2015) 147, [arXiv:1506.01708].

[65] K. Griest, *Toward a possible solution to the cosmic coincidence problem*, *Phys. Rev.* **D66** (2002) 123501, [astro-ph/0202052].

[66] D. J. Marsh and P. G. Ferreira, *Ultra-Light Scalar Fields and the Growth of Structure in the Universe*, *Phys. Rev. D* **82** (2010) 103528, [arXiv:1009.3501].

[67] J. Lesgourgues, *The Cosmic Linear Anisotropy Solving System (CLASS) I: Overview*, arXiv:1104.2932.

[68] D. Blas, J. Lesgourgues, and T. Tram, *The Cosmic Linear Anisotropy Solving System (CLASS) II: Approximation schemes*, *JCAP* **1107** (2011) 034, [arXiv:1104.2933].

[69] B. Audren, J. Lesgourgues, K. Benabed, and S. Prunet, *Conservative Constraints on Early Cosmology: an illustration of the Monte Python cosmological parameter inference code*, *JCAP* **1302** (2013) 001, [arXiv:1210.7183].

[70] T. Brinckmann and J. Lesgourgues, *MontePython 3: boosted MCMC sampler and other features*, arXiv:1804.07261.

[71] **Simons Observatory** Collaboration, P. Ade et al., *The Simons Observatory: Science goals and forecasts*, *JCAP* **02** (2019) 056, [arXiv:1808.07445].

[72] **Planck** Collaboration, N. Aghanim et al., *Planck 2015 results. XI. CMB power spectra, likelihoods, and robustness of parameters*, *Astron. Astrophys.* **594** (2016) A11, [arXiv:1507.02704].

[73] D. M. Scolnic et al., *The Complete Light-curve Sample of Spectroscopically Confirmed SNe Ia from Pan-STARRS1 and Cosmological Constraints from the Combined Pantheon Sample*, *Astrophys. J.* **859** (2018), no. 2 101, [arXiv:1710.00845].

[74] A. Gelman and D. B. Rubin, *Inference from Iterative Simulation Using Multiple Sequences*, *Statist. Sci.* **7** (1992) 457–472.

[75] **CMB-S4** Collaboration, K. N. Abazajian et al., *CMB-S4 Science Book, First Edition*, arXiv:1610.02743.

[76] J. C. Hill, E. McDonough, M. W. Toomey, and S. Alexander, *Early Dark Energy Does Not Restore Cosmological Concordance*, arXiv:2003.07355.

[77] C. Heymans et al., *CFHTLenS tomographic weak lensing cosmological parameter constraints: Mitigating the impact of intrinsic galaxy alignments*, *Mon. Not. Roy. Astron. Soc.* **432** (2013) 2433, [arXiv:1303.1808].

[78] H. Hildebrandt et al., *KiDS+VIKING-450: Cosmic shear tomography with optical+infrared data*, *Astron. Astrophys.* **633** (2020) A69, [arXiv:1812.06076].

[79] T. Abbott, F. Abdalla, A. Alarcon, J. Aleksi?, S. Allam, S. Allen, A. Amara, J. Annis, J. Asorey, S. Avila, and et al., *Dark energy survey year 1 results: Cosmological constraints from galaxy clustering and weak lensing*, *Physical Review D* **98** (Aug, 2018).

[80] C. Hikage, M. Oguri, T. Hamana, S. More, R. Mandelbaum, M. Takada, F. Khlinger, H. Miyatake, A. J. Nishizawa, H. Aihara, and et al., *Cosmology from cosmic shear power spectra with subaru hyper suprime-cam first-year data*, *Publications of the Astronomical Society of Japan* **71** (Mar, 2019).

[81] M. Asgari et al., *KiDS+VIKING-450 and DES-Y1 combined: Mitigating baryon feedback uncertainty with COSEBIs*, *Astron. Astrophys.* **634** (2020) A127, [arXiv:1910.05336].

[82] M. Braglia, M. Ballardini, W. T. Emond, F. Finelli, A. E. Gümrükçüoğlu, K. Koyama, and D. Paoletti, *Larger value for H_0 by an evolving gravitational constant*, *Phys. Rev. D* **102** (July, 2020) 023529, [arXiv:2004.11161].

[83] **ACT** Collaboration, S. Aiola et al., *The Atacama Cosmology Telescope: DR4 Maps and Cosmological Parameters*, arXiv:2007.07288.

[84] W. Handley and P. Lemos, *Quantifying the global parameter tensions between ACT, SPT and Planck*, arXiv:2007.08496.

[85] L. Amendola et al., *Cosmology and fundamental physics with the Euclid satellite*, *Living Rev. Rel.* **21** (2018), no. 1 2, [arXiv:1606.00180].

[86] **LSST Dark Energy Science** Collaboration, D. Alonso et al., *The LSST Dark Energy Science Collaboration (DESC) Science Requirements Document*, arXiv:1809.01669.

[87] **DESI** Collaboration, A. Aghamousa et al., *The DESI Experiment Part I: Science,Targeting, and Survey Design*, arXiv:1611.00036.

[88] A. Klypin, V. Poulin, F. Prada, J. Primack, M. Kamionkowski, V. Avila-Reese, A. Rodriguez-Puebla, P. Behroozi, D. Hellinger, and T. L. Smith, *Clustering and Halo Abundances in Early Dark Energy Cosmological Models*, arXiv:2006.14910.

Is the Tension between Clusters and CMB resolved?

Laura Salvati

e-mail: laura.salvati@inaf.it

INAF - Osservatorio Astronomico di Trieste, via G. B. Tiepolo 11, I-34143 Trieste, Italy
IFPU - Institute for Fundamental Physics of the Universe, Via Beirut 2, 34014 Trieste, Italy

Presented at the 3rd World Summit on Exploring the Dark Side of the Universe
Guadeloupe Islands, March 9-13 2020

Abstract

We provide a novel cosmological analysis of galaxy clusters detected through the thermal Sunyaev-Zeldovich (tSZ) effect. We perform the first combination of tSZ cluster counts and power spectrum and we show how to solve the tension with CMB primary anisotropies on the σ_8 parameter. We highlight that the combination of tSZ cluster counts and power spectrum is fundamental to constrain extensions to the ΛCDM scenario. We focus on the problem of the cluster mass calibration, as the main source of systematic uncertainties in current cluster cosmology. We show the need of a proper mass and redshift evolution in the model for the scaling relations, in order to correctly take into account the interplay between astrophysics and cosmology in the cluster formation and evolution.

1 Introduction

Galaxy clusters are the largest structures gravitationally bound in the Universe and are associated with peaks in the matter density field on megaparsec scales. The abundance of clusters provides constraints on cosmological parameters, in particular on the total matter density Ω_m and the amplitude of the matter power spectrum, described by the σ_8 parameter.

Galaxy clusters can be observed at different wavelengths. In this analysis, we focus on clusters detected in the mm-wavelengths, through the thermal Sunyaev-Zeldovich (tSZ) effect [1], which is the inverse Compton scattering between photons of the cosmic microwave background (CMB hereafter) radiation and hot electrons in the intra-cluster medium. We make use of observations of the Planck satellite [2, 3, 4]. In particular, we perform the first cosmological analysis of the combination of galaxy cluster number counts and angular power spectrum of warm-hot gas seen with tSZ. We compare our results with cosmological constraints inferred from CMB measured by the Planck satellite [5, 6], discussing the discrepancy in the results between the different observables.

In extracting cosmological information from galaxy clusters, a key issue is related to the evaluation of the total cluster mass, through the calibration of the scaling relations. In particular, for tSZ observations the main uncertainty is related to the calibration of the mass bias $(1-b)$, i.e. the relation between the mass evaluated assuming hydrostatic equilibrium and the real mass of the cluster. In this analysis, we also focus on the impact of a mass and redshift evolution for the mass bias on the cosmological parameters inferred from galaxy clusters. The results presented here are based on [7, 8].

2 Method

We perform the first combination of tSZ number counts ($\mathrm{NC}^{\mathrm{tSZ}}$) and power spectrum ($C_\ell^{\mathrm{tSZ}}$). Since these two probes show different dependencies on cosmological and scaling relation parameters ($\mathrm{NC}^{\mathrm{tSZ}} \propto \sigma_8^9\,\Omega_m^3\,(1-b)^{3.6}$ and $C_\ell^{\mathrm{tSZ}} \propto \sigma_8^{8.1}\,\Omega_m^{3.2}\,(1-b)^{3.2}$ as described in [7]]), the combination of the two is useful in reducing the impact of systematic uncertainties and improve the understanding of the nature of the tension with CMB data. We consider the cluster sample provided by [2, 3], consisting of 439 clusters in the redshift range $z = [0, 1]$. For the power spectrum, we use Planck results from [4] and an estimate of the angular power spectrum from SPT at $\ell = 3000$ [9]. In performing this combination, we follow the analysis shown in [10] and neglect any correlation between the two probes. In building the tSZ cluster likelihood, we adopt the same baseline as in [3]. In detail, for the calibration of the mass bias we consider at first a constant value, i.e. the prior from the Canadian Cluster Comparison Project (CCCP) analysis [11], $(1-b) = 0.780 \pm 0.092$. We then adopt the following mass and redshift evolution

$$(1-b)_{\mathrm{var}}(M,z) = (1-\mathcal{B}) \cdot \left(\frac{M}{M_*}\right)^{\alpha_b} \cdot \left(\frac{1+z}{1+z_*}\right)^{\beta_b}, \tag{1}$$

where $(1-\mathcal{B})$ is an amplitude, $M_* = 4.82 \cdot 10^{14} M_\odot$ is the mean mass value of the Planck cluster sample and $z_* = 0.22$ is the median value of the cluster catalog that we are considering. For this new formulation, we consider the different calibrations reported in Table 1, applied at the given (M, z).

Since tSZ number counts and power spectrum are not able to constrain the full set of cosmological parameters alone, we also added baryonic acoustic oscillations (BAO hereafter) measurements from [12]. Finally, we consider also the new value of the optical depth released in [13], i.e. $\tau = 0.055 \pm 0.009$.

	$(1-b)_{\mathrm{var}}(M,z)$	M	z
WtG [14]	0.688 ± 0.072	$13.08\,10^{14} M_\odot$	0.31
CCCP [11]	0.780 ± 0.092	$14.83\,10^{14} h^{-1} M_\odot$	0.246
BIFFI [15]	0.877 ± 0.015	$10.53\,10^{14} M_\odot$	0

Table 1: Mass bias calibrations for different analysis, with the corresponding mass and redshift pivot.

3 Results

We first analyse the case with a constant value for the mass bias. In the ΛCDM scenario, the fundamental result is that the discrepancy on the σ_8 parameter between tSZ number counts and CMB is reduced from almost $2.4\,\sigma$ in [3] to $1.5\,\sigma$. This is mainly due to the shift in the CMB results because of the new value of the optical depth. When combining tSZ number counts and power spectrum, we obtain a small improvement in the constraining power, within 10% on individual error bars, with results being driven by tSZ counts. The results are reported in Table 2, upper panel.

We then consider extensions to the standard cosmological model. The most interesting results are obtained when varying the total mass of neutrinos. Results are reported in Table 2, lower panel, and in Figure 1 we show the two-dimensional probability distributions in the $(\sigma_8, \sum m_\nu)$ parameter plane. In this case, the addition of tSZ power spectrum helps in substantially improving the constraints from number counts, in particular on the mass of neutrinos. When comparing with CMB results, we see that the discrepancy is completely solved, mainly because of the enlargement in the constraints from CMB primary anisotropies along the (Ω_m, σ_8) degeneracy line.

We stress that, even if in general the discrepancy between tSZ observables and CMB is reduced, when combining them we still find a value of the mass bias, as reported in Table 2, that is lower than

	$\mathrm{NC}^{\mathrm{tSZ}} + \mathrm{BAO}$	$C_\ell^{\mathrm{tSZ}} + \mathrm{NC}^{\mathrm{tSZ}} + \mathrm{BAO}$	CMB	$\mathrm{CMB} + \mathrm{C}_\ell^{\mathrm{tSZ}} + \mathrm{NC}^{\mathrm{tSZ}} + \mathrm{BAO}$
Ω_m	$0.314^{+0.020}_{-0.024}$	$0.322^{+0.020}_{-0.022}$	$0.321^{+0.012}_{-0.014}$	0.311 ± 0.007
σ_8	$0.768^{+0.028}_{-0.035}$	$0.762^{+0.027}_{-0.034}$	0.817 ± 0.010	0.810 ± 0.008
$(1-b)$	0.754 ± 0.093	0.755 ± 0.091	-	$0.646^{+0.034}_{-0.039}$
Ω_m	$0.337^{+0.027}_{-0.031}$	$0.335^{+0.023}_{-0.024}$	$0.353^{+0.020}_{-0.037}$	0.315 ± 0.008
σ_8	$0.728^{+0.032}_{-0.038}$	$0.737^{+0.028}_{-0.037}$	$0.772^{+0.049}_{-0.024}$	$0.792^{+0.020}_{-0.013}$
$(1-b)$	0.749 ± 0.091	0.741 ± 0.089	-	$0.673^{+0.037}_{-0.047}$
$\sum m_\nu$	$< 2.84\,\mathrm{eV}$	$< 1.88\,\mathrm{eV}$	$< 0.68\,\mathrm{eV}$	$< 0.23\,\mathrm{eV}$

Table 2: 68% confidence level constraints for cosmological and scaling relation parameters. *Upper panel*: ΛCDM scenario. *Lower panel*: Varying neutrino mass scenario. For the $\sum m_\nu$ parameter we report the 95% upper limit.

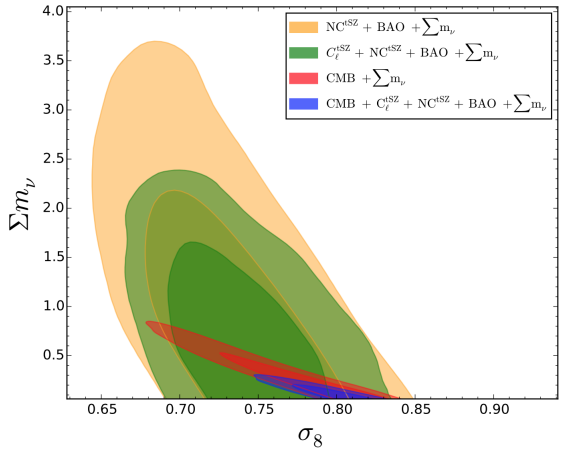

Figure 1: Two-dimensional probability distributions for $(\sigma_8, \sum m_\nu)$ for varying neutrino mass scenario. We report results for number counts (orange), the combination of number counts and power spectrum (green); we add also CMB data (blue) and we show results for CMB alone (red).

what is obtained from numerical simulations and weak lensing observations, see e.g. a collection of results in [7].

In order to further understand the remaining discrepancy on the mass bias between tSZ probes and CMB, we analyse results when adding the mass and redshift evolution reported in Eq. 1.

We start analysing the results when considering only the tSZ probes. For this dataset combination, we find a hint for the redshift evolution of the mass bias, with $\beta_b > 0$. This implies that the total mass bias is increasing with redshift, as shown in Figure 2, left panel. In this case, the addition of the tSZ power spectrum is not improving the constraining power. These results are reported in Table 3, upper panel. When performing the full combination of tSZ probes with CMB primary anisotropies, results are consistent with the standard scenario discussed above: we find no evidence for any mass or redshift variation for the mass bias, with $(1-b)_{\mathrm{var}} \sim 0.6$.

In order to further understand the increasing trend of the mass bias when analysing the tSZ

probes, we perform a series of consistency tests. For the tests, we focus only on the analysis of cluster number counts $\mathrm{NC^{tSZ}}$, but we check that we obtain consistent results when considering also the tSZ power spectrum. We first compare the impact of the different mass bias calibrations reported in Table 1. In this case, independently of the choice of the calibration (and therefore of the mass and redshift pivot), we always find the same hint for redshift evolution, with $\beta_b > 0$. The results are shown in Table 3, middle-upper panel. We then analyse a discrete redshift dependence for the mass bias, dividing the redshift range $z = [0, 1]$ in three bins, bin 1: $z = [0, 0.2]$, bin 2: $z = [0.2, 0.5]$, bin 3: $z = [0.5, 1.0]$. The results are reported in Table 3, lower panel. Also in this case, we find a clear hint for a redshift evolution of the mass bias, with the value in the first bin, $(1-b)_1$, being lower than the ones obtained in the second and third bin, $(1-b)_2$ and $(1-b)_3$.

As a final check, we test the stability of our results against selection effects. In particular, we analyse the mass and redshift evolution of the mass bias on a subsample of the total cluster catalog, considering only the redshift range $z = [0.2, 1.0]$. For this final case, we find that selecting a subsample of clusters changes the results with respect to the previous analysis: we do not find any evidence for a redshift evolution of the mass bias, with the β_b parameter being fully consistent with 0. The results are reported in Table 3, middle-lower panel and in the right panel of Figure 2, where we label the total cluster sample as "PSZ2 cosmo" and the subsample as "PSZ2 C". We stress therefore that our results are fully dependent on the selection of the cluster sample that we are considering.

Dataset	Ω_m	σ_8	$(1-\mathcal{B})$	α_b	β_b
$C_\ell^{\mathrm{tSZ}} + \mathrm{NC^{tSZ}} + \mathrm{BAO} + (1-\mathcal{B}) + \alpha_\mathrm{b} + \beta_\mathrm{b}$	$0.380^{+0.048}_{-0.032}$	$0.751^{+0.024}_{-0.032}$	0.63 ± 0.10	$0.141^{+0.083}_{-0.092}$	$0.20^{+0.20}_{-0.16}$
$C_\ell^{\mathrm{tSZ}} + \mathrm{NC^{tSZ}} + \mathrm{CMB} + (1-\mathcal{B}) + \alpha_\mathrm{b} + \beta_\mathrm{b}$	0.316 ± 0.009	0.812 ± 0.008	$0.614^{+0.045}_{-0.052}$	$0.017^{+0.064}_{-0.085}$	$0^{+0.14}_{-0.13}$
CCCP: $\mathrm{NC^{tSZ}} + \mathrm{BAO} + (1-\mathcal{B}) + \alpha_\mathrm{b} + \beta_\mathrm{b}$	$0.374^{+0.065}_{-0.035}$	$0.752^{+0.033}_{-0.040}$	$0.66^{+0.10}_{-0.14}$	0.10 ± 0.10	$0.24^{+0.24}_{-0.18}$
WtG: $\mathrm{NC^{tSZ}} + \mathrm{BAO} + (1-\mathcal{B}) + \alpha_\mathrm{b} + \beta_\mathrm{b}$	$0.385^{+0.060}_{-0.032}$	$0.765^{+0.026}_{-0.035}$	$0.597^{+0.077}_{-0.094}$	0.11 ± 0.10	$0.26^{+0.23}_{-0.17}$
BIFFI: $\mathrm{NC^{tSZ}} + \mathrm{BAO} + (1-\mathcal{B}) + \alpha_\mathrm{b} + \beta_\mathrm{b}$	$0.362^{+0.044}_{-0.023}$	$0.699^{+0.020}_{-0.033}$	0.845 ± 0.063	$0.11^{+0.08}_{-0.10}$	$0.27^{+0.22}_{-0.17}$
$z = [0.2, 1.0]$: $\mathrm{NC^{tSZ}} + \mathrm{BAO} + (1-\mathcal{B}) + \alpha_\mathrm{b} + \beta_\mathrm{b}$	$0.378^{+0.048}_{-0.036}$	$0.740^{+0.034}_{-0.044}$	$0.74^{+0.12}_{-0.15}$	0.04 ± 0.10	$-0.09^{+0.23}_{-0.17}$
Dataset	Ω_m	σ_8	$(1-b)_1$	$(1-b)_2$	$(1-b)_3$
z bins: $\mathrm{NC^{tSZ}} + \mathrm{BAO} + (1-\mathrm{b})_\mathrm{i}$	$0.371^{+0.028}_{-0.034}$	$0.733^{+0.028}_{-0.037}$	0.655 ± 0.078	0.775 ± 0.092	0.751 ± 0.095

Table 3: 68% confidence level constraints for cosmological and scaling relation parameters. *Upper panel*: Full analysis. *Middle-upper panel*: Comparison between different mass bias calibrations. *Middle-lower panel*: Cluster subsample in $z = [0.2, 1.0]$. *Lower panel*: Analysis with redshift bins.

4 Conclusions

We perform a novel cosmological analysis of the tSZ signal detected by the Planck satellite. We provide the first combination of tSZ cluster counts and power spectrum, solving the tension with CMB primary anisotropies on the σ_8 parameter. Furthermore, we analyse the remaining discrepancy on the evaluation of the total cluster mass, quantified through different constraints on the mass bias parameter $(1-b)$. We find hint for a redshift evolution of the mass bias, even though these results depend on the considered cluster sample. This analysis highlights the impact of mass calibration in cluster cosmology and the necessity to provide mass evaluation on large and representative cluster samples.

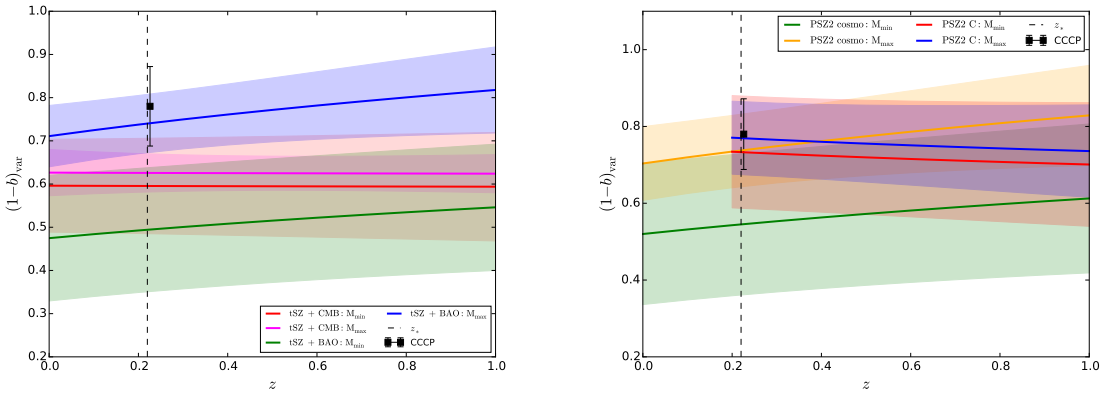

Figure 2: Redshift variation of $(1-b)_{\rm var}$ at fixed values of mass. *Left panel*: We show results for the combinations $C_\ell^{\rm tSZ} + {\rm NC}^{\rm tSZ} + {\rm BAO} + (1-\mathcal{B}) + \alpha_{\rm b} + \beta_{\rm b}$ (labelled as "tSZ + BAO", green and blue) and $C_\ell^{\rm tSZ} + {\rm NC}^{\rm tSZ} + {\rm CMB} + (1-\mathcal{B}) + \alpha_{\rm b} + \beta_{\rm b}$ (labelled as "tSZ+CMB", red and magenta). *Right panel*: We show results for the combination ${\rm NC}^{\rm tSZ} + {\rm BAO} + (1-\mathcal{B}) + \alpha_{\rm b} + \beta_{\rm b}$ for the total cluster sample (labelled as "PSZ2 cosmo", green and yellow) and for the subsample in $z = [0.2, 1.0]$ (labelled as "PSZ2 C", red and blue).

References

[1] R. A. Sunyaev and Ya. B. Zeldovich, *The Interaction of matter and radiation in the hot model of the universe*, *Astrophys. Space Sci.* **7** (1970) 20–30.

[2] Planck Collaboration, *Planck 2015 results. XXVI. The Second Planck Catalogue of Compact Sources*, *Astron. Astrophys.* **594** (Sept., 2016) A26, [arXiv:1507.02058].

[3] Planck Collaboration, *Planck 2015 results. XXIV. Cosmology from Sunyaev-Zeldovich cluster counts*, *Astron. Astrophys.* **594** (Sept., 2016) A24, [arXiv:1502.01597].

[4] Planck Collaboration, *Planck 2015 results. XXII. A map of the thermal Sunyaev-Zeldovich effect*, *Astron. Astrophys.* **594** (Sept., 2016) A22, [arXiv:1502.01596].

[5] **Planck** Collaboration, Planck Collaboration, *Planck 2015 results. XIII. Cosmological parameters*, *Astron. Astrophys.* **594** (2016) A13, [arXiv:1502.01589].

[6] **Planck** Collaboration, N. Aghanim et al., *Planck 2018 results. VI. Cosmological parameters*, arXiv:1807.06209.

[7] L. Salvati, M. Douspis, and N. Aghanim, *Constraints from thermal Sunyaev-Zeldovich cluster counts and power spectrum combined with CMB*, *Astron. Astrophys.* **614** (2018) A13, [arXiv:1708.00697].

[8] L. Salvati, M. Douspis, A. Ritz, N. Aghanim, and A. Babul, *Mass bias evolution in tSZ cluster cosmology*, *Astron. Astrophys.* **626** (2019) A27, [arXiv:1901.03096].

[9] E. M. George et al., *A measurement of secondary cosmic microwave background anisotropies from the 2500-square-degree SPT-SZ survey*, *Astrophys. J.* **799** (2015), no. 2 177, [arXiv:1408.3161].

[10] G. Hurier and F. Lacasa, *Combined analysis of galaxy cluster number count, thermal Sunyaev-Zel'dovich power spectrum, and bispectrum*, *Astron. Astrophys.* **604** (2017), no. 604 A71, [arXiv:1701.09067].

[11] H. Hoekstra, R. Herbonnet, A. Muzzin, A. Babul, A. Mahdavi, M. Viola, and M. Cacciato, *The Canadian Cluster Comparison Project: detailed study of systematics and updated weak lensing masses*, *Mon. Not. Roy. Astron. Soc.* **449** (2015), no. 1 685–714, [arXiv:1502.01883].

[12] **BOSS** Collaboration, L. Anderson et al., *The clustering of galaxies in the SDSS-III Baryon Oscillation Spectroscopic Survey: baryon acoustic oscillations in the Data Releases 10 and 11 Galaxy samples*, *Mon. Not. Roy. Astron. Soc.* **441** (2014), no. 1 24–62, [arXiv:1312.4877].

[13] **Planck** Collaboration, Planck Collaboration, *Planck intermediate results. XLVI. Reduction of large-scale systematic effects in HFI polarization maps and estimation of the reionization optical depth*, *Astron. Astrophys.* **596** (2016) A107, [arXiv:1605.02985].

[14] A. von der Linden et al., *Robust Weak-lensing Mass Calibration of Planck Galaxy Clusters*, *Mon. Not. Roy. Astron. Soc.* **443** (2014), no. 3 1973–1978, [arXiv:1402.2670].

[15] V. Biffi, S. Borgani, G. Murante, E. Rasia, S. Planelles, G. L. Granato, C. Ragone-Figueroa, A. M. Beck, M. Gaspari, and K. Dolag, *On the nature of hydrostatic equilibrium in galaxy clusters*, *Astrophys. J.* **827** (2016), no. 2 112, [arXiv:1606.02293].

Cosmology with DES Year-1 data: from 3x2pt analyses to the CMB imprint of cosmic voids

Pauline Eva Vielzeuf

e-mail: pvielzeu@sissa.if

Scuola Internazionale Superiore di Studi Avanzati (SISSA)

Presented at the 3rd World Summit on Exploring the Dark Side of the Universe
Guadeloupe Islands, March 9-13 2020

Abstract

New generation of photometric galaxy surveys are mapping large volumes of the Universe, measuring the angular positions and shapes of hundreds of millions (or billions) of galaxies. This will allow cosmological measurements with an unprecedented level of precision, leading to a considerable step forward in our understanding of cosmology and particularly of the nature of dark energy. In this perspective, here will be present two different aspects of the cosmological results obtained by the Dark Energy Survey (DES) first year of observation. More specifically we present the results coming form combination lensing of galaxies statistics and galaxy clustering information. In a second part we will exposed the correlations of DES observations that can be measured using external probes and more specifically the imprint of cosmic voids on the lensing measurement of the cosmic microwave background (CMB).

1 Introduction

The Dark Energy Survey ([1]) is a photometric galaxy survey, that has for main objective to understand the physics behind the accelerating expansion of our universe. After 6 years of observations (2013-2019) DES have observed about 300 million of galaxies in and area of about 5000 sq. deg. of the southern sky through 5 photometric filters (grizY) with a nominal limiting magnitude iAB$\simeq$24. We will focus on the main cosmological constrained perform by the DES collaboration using the data collected after the first year of observations DESY1 which are covering about 1300 square degree survey area. More specifically we will start in section 2 to present the results obtained combining both gravitational lensing and galaxy clustering. We will then follow in section 3 by presenting a specific example of possible correlation of DESY1 observations with external observation, namely the imprint of cosmic voids with the lensing signal extracted from the Planck CMB observations.

2 First cosmological results with the Dark Energy first year of oberservation (DESY1)

2.1 Methodology and samples

As mentioned above, the first analysis of the DESY1 galaxy samples have allowed the collaboration to provide cosmological constraints using a combination of various probes. Here will be presented the first cosmological results from the first year of observation using and combining three different two-point statistic signal (3X2pt analysis) :

- Galaxy clustering : correlation signal of galaxy positions as a function of their angular separation ($\propto b^2\sigma_8^2$) [2],
- Cosmic shear : correlations between galaxy shapes as a function of their angular separation ($\propto \Omega_m^2\sigma_8^2$) [3],
- Galaxy-galaxy lensing : correlations between the shape of background galaxy (source galaxies) with the position of foreground ones (lenses) as a function of their angular separation ($\propto b\Omega_m\sigma_8^2$) [4].

In order to proceed to the analysis, one had to in one hand define optimal galaxy catalog and on the other hand measure with the highest precision possible galaxy property such as galaxy 3D position and galaxy shape. To be more robust, two different approaches have been used to evaluate the shape of the DESY1 galaxy sample the (`METACALIBRATION` ([5, 6]) and `IM3SHAPE` ([7])) catalog. While for clustering statistics the *redMaGiC*code identified red luminous galaxies (LRG) with high-quality photometric redshift. that have been measured using treecorr **[?]** in 20 log-spaced bins of angular separation $2.5^{'}<\theta<250^{'}$.

While cosmic shear measurements, can be used alone to infer cosmological constraints, galaxy clustering and galaxy-galaxy lensing will have to be combined to break the degeneracy due to their dependance on galaxy bias.

2.2 Results

Cosmic shear being mostly sensitive to the clustering amplitude (S_8 parameter) and the matter parameter (Ω_m), it is possible to make an estimation of these parameter marginalizing over the other ones. The results obtained in [3], are, for ΛCDM: $\sigma_8(\Omega_m/0.3)^{0.5} = 0.782^{+0.027}_{-0.027}$ and $\Omega_m = 0.260^{+0.065}_{-0.037}$ at 68 % C.L. These values have improved by a factor of three the results obtained in the cosmic shear measurement of previous science DES science verification measurement. The main results of the combined analysis described above are shown in Figure (1). In the left panel of the figure we can see the comparison of the results obtained weather one combines the different probes or not. As it can be seen in the figure, the results here are showing a good agreement between clustering statistics and lensing statistics in cosmological parameter inference. Moreover, the combination of the three different probes shows to improve our constraints on cosmological parameters. The main constraints obtained by combining the three two-point statistics are for ΛCDM: $\sigma_8(\Omega_m/0.3)^{0.5} = 0.783^{+0.021}_{-0.025}$ and $\Omega_m = 0.264^{+0.032}_{-0.019}$ at 68 % C.L. On the other hand, the right panel of the figure shows the 68% confidence levels of S_8 and Ω_m in the ΛCDM parametrization for DESY1 alone and combined to external datasets. Thus one can see that first cosmological analysis made by DESY1 studying large scale structures at low redshift are in fair agreement with the CMB measurements at $z = 1100$ and second that the DESY1 analysis is actually reaching a level where the accuracy of cosmological parameter estimation is competitive with the one inferred by CMB experiments.

3 Correlation of the DESY1 underdensed regions with the CMB lensing signal

Similarly to galaxy shape distortions due to the foreground matter field in cosmic shear analysis, one expects the light coming from the cosmic microwave background (CMB) towards us to be also lensed by the large structures it crosses aloneg its path. Correlations is then expected between the foreground structures of our universe and the CMB radiation. In [9], using a stacking methodology, we developed a methodology to optimize and evaluate the imprint of cosmic voids, these large ($\sim$ tens of Mpc/h) underdensed region of the cosmic web, identified in the DESY1 observed galaxy in the reconstructed CMB lensing map provide by the Planck collaboration.

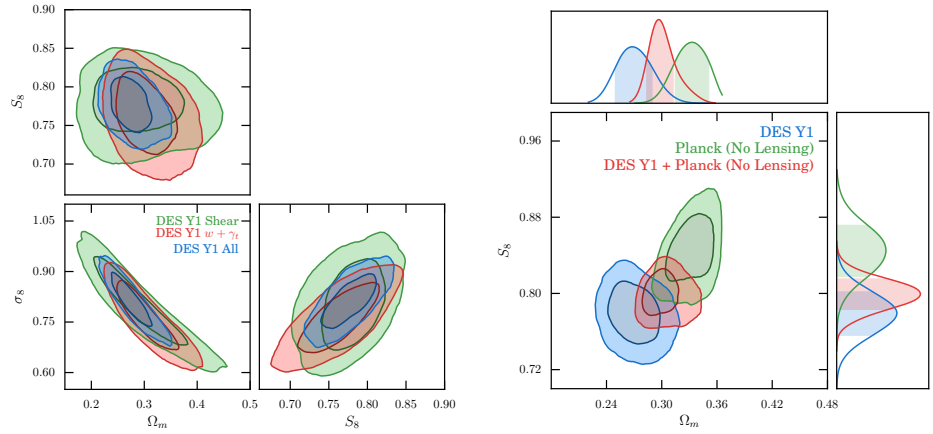

Figure 1: *Left panel:* constraints from DESY1 on Ω_m, σ_8 and S_8 from cosmic shear (green), *redMaGiC*galaxy clustering plus galaxy– galaxy lensing (red), and their combination (blue). Here, and in all such 2D plots below, the two sets of contours depict the 68% and 95% confidence levels. *Right panel :* ΛCDM constraints from the three combined probes in DES Y1 (blue), Planck with no lensing (green), and their combination (red). The agreement between DES and Planck can be quantified via the Bayes factor, which indicates that in the full, multi-dimensional parameter space, the two data sets are consistent. (Figures from [8])

3.1 Methodology

In order to be less affected by photometric redshift bias that is known to be a source of error in the void finding procedure, we have identified underdensed region of the DESY1 catalog in the high-precision photometric redshift *redMaGiC*luminous red galaxy sample.[10]. We have identified cosmic void in the DESY1 *redMaGiC*sample using the 2D void finder presented in [11]. The void finder is identifying voids in the following way: (1) Divide the sample in redshift slices 100Mpc/h slices are shown to be a good compromise considering *redMaGiC*redshift accuracy, (2) Compute the density field for each slice by counting the galaxy number in each pixel and smoothing the field with a Gaussian with a predefined smoothing scale, (3) Select the most underdense pixel and grow around it the void until it reaches the mean density, (4) Save the void, erase it from the density map and iterate the process with the following underdense pixel. The finder have been run two different *redMaGiC*catalogs, probing different smoothing parameter for the void finder ($\sigma = 10Mpc/h$ and $\sigma = 20Mpc/h$) in both DESY1 observed galaxies, and MICE ([12, 13, 14]) simulated galaxies. In order to be more complete, we have also considered a different definition of voids to probe the effect on the CMB lensing signal, the 3 dimensional voids identified with the VIDE toolkit ([15]).

To detect the imprint of cosmic voids in the CMB lensing maps, we have used a stacking methodology which consist in cutting out patches of the smoothed CMB map (different smoothing kernel have been probe) centered at superstructure position using `healpix` maps ([16]), re-scale the patches given the angular size of the structure, stack all patches and finally measure the average signal in different concentric radius bins around the center.

3.2 Results

Along the analysis, we observed good agreement between the simulated MICE ΛCDM results and the our observations. As a measure of the signal-to-noise (S/N) of simulated and observed signals given the measurement errors and their covariance, we aim to constrain an amplitude A (and its error

σ_A) as a ratio of DES Y1 and MICE signals using the full profile up to $R/R_v = 5$ in 16 radial bins. We expect $A = 1$ if the DESY1 and MICE ΛCDM results are in close agreement and we aim to test this hypothesis. In order to estimate the value of A, we have followed the statistic :

$$\chi^2 = \sum_{ij} (\kappa_i^{DES} - A\kappa_i^{MICE}) C_{ij}^{-1} (\kappa_j^{DES} - A\kappa_j^{MICE}) \quad (1)$$

where κ_i is the mean lensing signal in the radius bin i, and C is the covariance matrix computed using the variance of the lensing signal measured by rotating randomly 500 times the MICE lensing map to which we have add a *Planck*-like noise.

The final results of the detection level achieved for each void sample and the three different smoothing approaches studied can be seen in Fig.(2), from the figure, we can see that we robustly detected imprints at the 3σ significance level with most of our analysis choices, reaching $S/N \approx 4$ in the best predicted measurement configurations using DES Y1 high luminosity *redMaGiC*data.

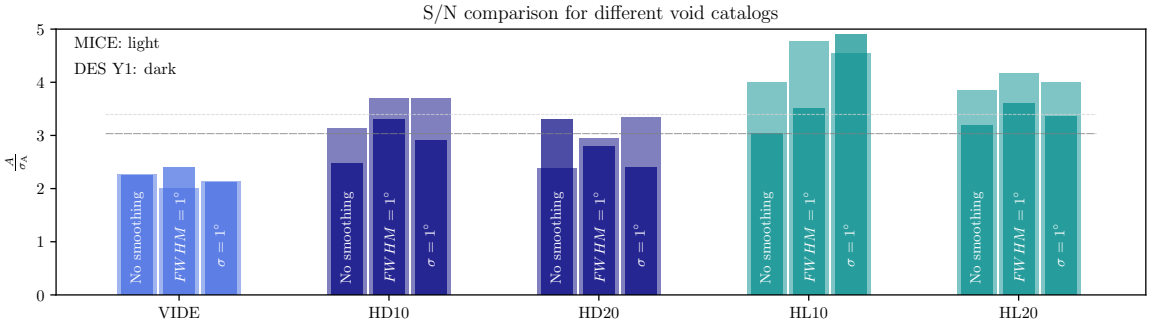

Figure 2: Measurement significance in the form of A/σ_A. The conservative VIDE sample also provides useful consistency tests in agreement with our 2D analyses. The dashed horizontal lines mark the mean of the DES Y1 (dark) and the MICE (light) significances with values 3.03 and 3.39, respectively

4 Conclusions

In this presentation, have been presented first the main cosmological results inferred from the DESY1 galaxy catalog, using the three different 2-point statistics probes after one year of observations. The Dark Energy survey has now collected 6 years of data and we saw its abilities after this first observation year, to be competitive in cosmological inference, more in particular, it has been shown that by combining different probes, DES have been able for the first time after one year of observation to infer cosmological parameter constraints at the level of accuracy of CMB experiments. So far, no significant deviations from the ΛCDM model have been found. In the future months, the Dark Energy Survey will present the analysis coming from the second and third year of observation, during this period DES has already covered the full expected final area (up to a given magnitude). The analysis will thus be realised in an area more than three times larger than the DESY1.

In a second part, we have shown that we have now entering the era where large and precise sample will allow us to use cosmic voids as cosmological probe. We robustly detected imprints at the 3σ significance level with most of our analysis choices, reaching S/N ≈ 4 in the best predicted measurement configurations using DES Y1 high luminosity *redMaGiC*data. Our goal for the future is to create a bigger catalogue of voids, and potentially superclusters, using galaxy catalogues from three years of observed DES data (DES Y3). These presumably more accurate future detections with more voids will most probably allow cosmological parameter constraints

References

[1] The Dark Energy Survey Collaboration, *The Dark Energy Survey*, *arXiv e-prints* (Oct., 2005) astro–ph/0510346, [astro-ph/0510346].

[2] J. Elvin-Poole and DES Collaboration, *Dark Energy Survey year 1 results: Galaxy clustering for combined probes*, **98** (Aug., 2018) 042006, [arXiv:1708.01536].

[3] M. A. Troxel and DES Collaboration, *Dark Energy Survey Year 1 results: Cosmological constraints from cosmic shear*, **98** (Aug., 2018) 043528, [arXiv:1708.01538].

[4] J. Prat and DES Collaboration, *Dark Energy Survey year 1 results: Galaxy-galaxy lensing*, **98** (Aug., 2018) 042005, [arXiv:1708.01537].

[5] E. Huff and R. Mandelbaum, *Metacalibration: Direct Self-Calibration of Biases in Shear Measurement*, *ArXiv e-prints* (Feb., 2017) [arXiv:1702.02600].

[6] E. S. Sheldon and E. M. Huff, *Practical Weak-lensing Shear Measurement with Metacalibration*, **841** (May, 2017) 24, [arXiv:1702.02601].

[7] J. Zuntz, T. Kacprzak, L. Voigt, M. Hirsch, B. Rowe, and S. Bridle, *IM3SHAPE: a maximum likelihood galaxy shear measurement code for cosmic gravitational lensing*, **434** (Sept., 2013) 1604–1618, [arXiv:1302.0183].

[8] Dark Energy Survey Collaboration, *Dark Energy Survey year 1 results: Cosmological constraints from galaxy clustering and weak lensing*, **98** (Aug., 2018) 043526, [arXiv:1708.01530].

[9] P. Vielzeuf and DES Collaboration, *Dark Energy Survey Year 1 Results: the lensing imprint of cosmic voids on the Cosmic Microwave Background*, *arXiv e-prints* (Nov., 2019) arXiv:1911.02951, [arXiv:1911.02951].

[10] E. Rozo and DES Collaboration, *redMaGiC: selecting luminous red galaxies from the DES Science Verification data*, **461** (Sept., 2016) 1431–1450, [arXiv:1507.05460].

[11] C. Sánchez and DES Collaboration, *Cosmic voids and void lensing in the Dark Energy Survey Science Verification data*, **465** (Feb., 2017) 746–759, [arXiv:1605.03982].

[12] P. Fosalba, E. Gaztañaga, F. J. Castander, and M. Crocce, *The MICE Grand Challenge light-cone simulation - III. Galaxy lensing mocks from all-sky lensing maps*, **447** (Feb., 2015) 1319–1332, [arXiv:1312.2947].

[13] M. Crocce, F. J. Castander, E. Gaztañaga, P. Fosalba, and J. Carretero, *The MICE Grand Challenge lightcone simulation - II. Halo and galaxy catalogues*, **453** (Oct., 2015) 1513–1530, [arXiv:1312.2013].

[14] P. Fosalba, M. Crocce, E. Gaztañaga, and F. J. Castander, *The MICE grand challenge lightcone simulation - I. Dark matter clustering*, **448** (Apr., 2015) 2987–3000, [arXiv:1312.1707].

[15] P. M. Sutter, G. Lavaux, B. D. Wandelt, D. H. Weinberg, M. S. Warren, and A. Pisani, *Voids in the SDSS DR9: observations, simulations, and the impact of the survey mask*, *Monthly Notices of the Royal Astronomical Society* **442** (06, 2014) 3127–3137, [https://academic.oup.com/mnras/article-pdf/442/4/3127/4168371/stu1094.pdf].

[16] K. M. Górski, E. Hivon, A. J. Banday, B. D. Wandelt, F. K. Hansen, M. Reinecke, and M. Bartelmann, *HEALPix: A Framework for High-Resolution Discretization and Fast Analysis of Data Distributed on the Sphere*, **622** (Apr., 2005) 759–771, [astro-ph/0409513].

Observing the Universe from Underground Gravitational Wave Telescope KAGRA

Keiko Kokeyama on behalf of the KAGRA collaboration

e-mail: kokeyama@icrr.u-tokyo.ac.jp

Institute for Cosmic Ray Research, The University of Tokyo

Presented at the 3rd World Summit on Exploring the Dark Side of the Universe
Guadeloupe Islands, March 9-13, 2020

Abstract

The underground and cryogenic gravitational-wave telescope, KAGRA, had its first observation run in the spring of 2020. The KAGRA is based on a complex laser interferometer with a number of signal enhancement techniques and state-of-the-art noise reduction technologies to detect gravitational wave signals. The first formal observation was performed from February 25 to March 10, 2020, and its first joint observation with the gravitational-wave detector GEO600 was performed from April 7–21, 2020, which is called O3GK. This article reviews the status of the KAGRA detector in O3GK.

1 Introduction

Gravitational-wave (GW) astronomy commenced with the discovery of a binary black-hole merger detected by Advanced LIGO (aLIGO) in 2015 in their first scientific observation run, O1 [1]. In 2017, the Advanced VIRGO (aVIRGO) detector in Europe joined the second operation of aLIGO (O2), and the detector network discovered a neutron-star merger [2]. Using the three detectors (two aLIGO detectors and one aVIRGO detector), the angular resolution of the signal direction in the sky (sky localization) was sufficiently improved for other types of telescopes to observe and discover corresponding object [3]. This initiated multi-messenger astrophysics where various science cases have been developed [4]. The Kamioka Gravitational Wave Detector (KAGRA) is the first underground and cryogenic GW detector built in Gifu, Japan. Adding a fourth detector to the network can improve sky localization further and the duty factor to enhance discovery in fundamental physics and astrophysics [5]. In addition, KAGRA is a pioneer in detector technologies with unique underground and cryogenic features.

2 KAGRA Project

The KAGRA project is an international scientific collaboration for GW science and astrophysics. As of August 2020, it consists of 130 groups with more than 400 members from 14 regions. The co-host institutions are the University of Tokyo, National Astronomical Observatory of Japan, and High Energy Accelerator Research Organization. The KAGRA project started in 2010 with funds from the Japanese funding agency. The excavation of the KAGRA tunnel started in May 2012 in Ikenoyama Mountain,

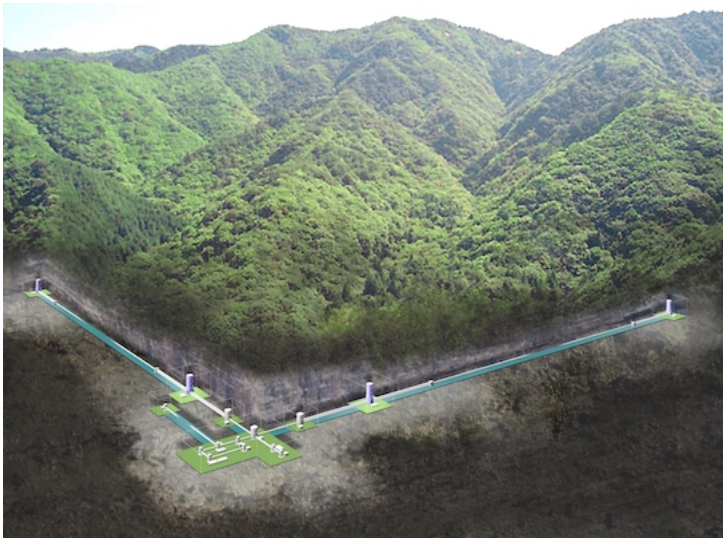

Figure 1: Image of the KAGRA underground site in Gifu prefecture, Japan. Although Ikenoyama Mountain was a heavy metal mining site, it is currently used for conducting several underground experiments related to fundamental physics. The KAGRA tunnels were newly excavated for the KAGRA experiment. Each tunnel has an L-shaped structure with a length of 3 km. Photo courtesy: KAGRA Observatory, ICRR, The University of Tokyo.

where underground experiment facilities, such as Super-Kamiokande, are located. After the completion of the excavation in early 2014, essential infrastructure such as power lines, network lines, clean booths, and vacuum enclosures were installed. While large-scale principal instruments, such as sapphire mirrors, large suspensions, and cryogenic instruments (see Sec. 3), were being installed and assembled in the tunnel, two engineering operations using temporary detector configurations were performed as project milestones in April 2016 (iKAGRA operation) [6] and April 2018 (bKAGRA phase-1 operation). In the bKAGRA phase-1 operation, cryogenic technology and the performance of the large vibration isolation systems of KAGRA were demonstrated [7]. In the summer of 2019, the major installation of the instruments was completed. Expeditiously, the commissioning of the detector was initiated. This continued until March 2020, when the first scientific operation began.

3 Detector

3.1 Optical Configuration

Similar to aLIGO and aVIRGO, KAGRA is a large-scale laser interferometer used to investigate subtle space-time displacements caused by the GWs. Fig. 2 shows the design of the interferometer configuration of the KAGRA detector. In addition to the 3 km Fabry-Perot arm cavities, the power-recycling mirrors (PRM, PR2, and PR3) constitute the power recycling cavity on the input side, and the signal-recycling mirrors (SRM, SR2, and SR3) constitute the signal recycling cavity on the output side. This optical configuration is a standard design in second-generation GW detectors (i.e., aLIGO, aVIRGO, and KAGRA), called the dual-recycled Fabry-Perot Michelson interferometer (DRFPMI). For the initial joint observation with GEO600 [9] (O3GK), owing to limited time and resources, the interferometer was operated in a simplified configuration without a signal recycling cavity. This configuration is called a power-recycled Fabry-Perot Michelson interferometer (PRFPMI) where the SRM is misaligned to prevent forming an optical cavity.

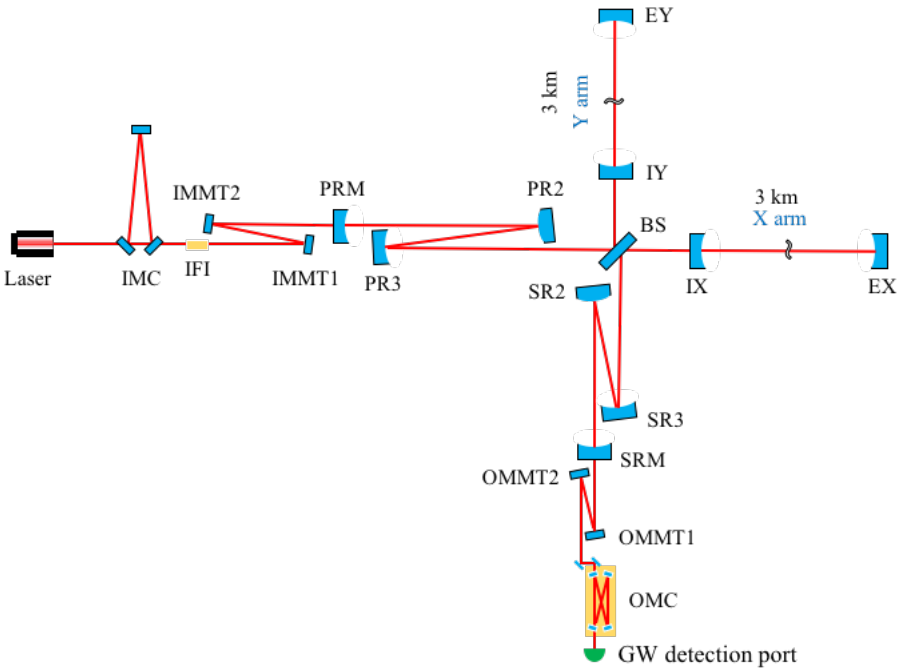

Figure 2: Conceptual optical configuration of the KAGRA interferometer. During an observation in the year 2020, one of the main mirrors, which is the signal recycling mirror and indicated as SRM, was not used for simplicity of interferometer controls. Abbreviations: Input mode cleaner (IMC), input Faraday isolator (IFI), input mode-matching telescope (IMMT), power-recycling mirror (PRM), beam splitter (BS), input test mass X (IX), input test mass Y (IY), end test mass X (EX), end test mass Y (EY), signal-recycling mirror (SRM), output mode-matching telescope (OMMT), and output mode cleaner (OMC).

To isolate the interferometer mirrors from seismic activities, the interferometer mirrors are held by vibration isolation systems that are significantly large suspensions. The test masses (EX, IX, EY, and IY mirrors forming the X and Y arm cavities) are made of sapphire [10] and suspended by the type-A suspensions (see Fig. 3). These are the largest among the KAGRA suspensions; they are at a height of 13.5 m and demonstrate the largest isolation performance for seismic motions. They consist of nine vibration isolation stages. The bottom four stages comprise the cryo-payload and are designed for operations at 20 K [11] to reduce thermal noise. During the observation run conducted in the year 2020, the test masses were preserved at room temperature because the sensitivity did not reach the thermal noise level.

The remaining suspensions are designed to be used at room temperature. The beam splitter and signal-recycling mirrors (SRM, SR2, and SR3) are suspended by type-B suspensions that have similar structures on the top part and have fewer vertical isolation stages in the middle compared to the type-A suspensions. The power-recycling mirrors (PRM, PR2, and PR3) are suspended by the type-Bp suspensions [8] that are adapted to smaller vacuum chambers. The three mirrors of the input mode cleaner (IMC), IMMT1, IMMT2, OMMT1, and OMMT2 shown in Fig. 2 are suspended by the simplest suspensions, which are the type-C suspensions. They are simple double pendulums for suspending small mirrors with ϕ=100 mm, whose design is based on the former GW project, TAMA300 [12].

For the laser source, the seed laser was a non-planar ring oscillator, Mephisto 500 NEFC (Coherent, Inc.) and the fiber-laser amplifier was a PSFA-10 mw-40 W-1064 (Coherent/Nufern, Inc.). The intensity and frequency of the laser were stabilized to prevent contamination of the GW sensitivity.

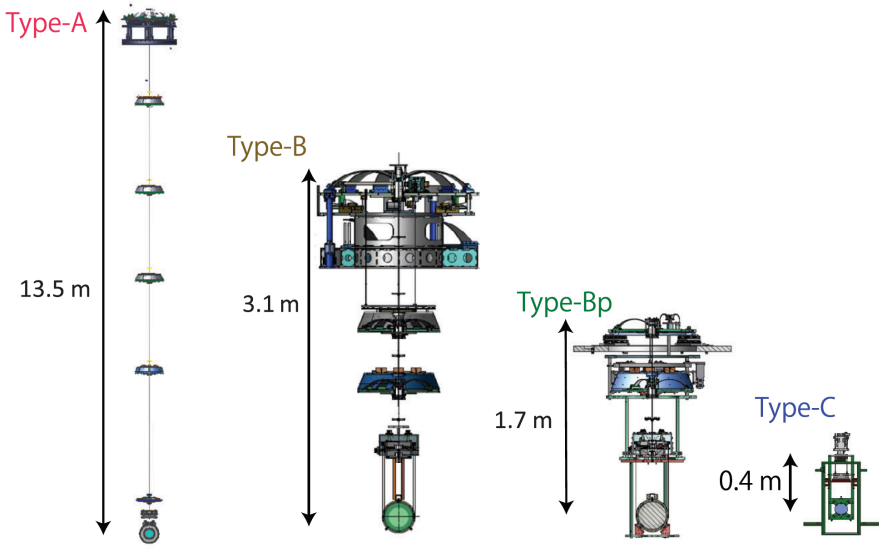

Figure 3: Types of KAGRA vibration isolation systems. This figure is acquired from Ref.[8]. The type-A large suspensions were used for the sapphire test masses, with the bottom four stages designed to be cryogenic. The type-B suspensions support the beam splitter and three signal-recycling mirrors. The type-Bp suspensions are meant for the three power-recycling mirrors. The other small ϕ=100 mm optics were held by the type-C suspensions.

The input mode cleaner (IMC) is a triangular cavity with a round-trip length of 53.3 m. The IMC rejects unwanted spatial higher-order modes and beam jitters from the input laser, and its length serves as a reference for the laser frequency [13]. A typical laser power injected into the main interferometer during O3GK was approximately 5 W.

The output mode cleaner (OMC) is a bow-tie cavity used to eliminate unwanted spatial higher-order modes and RF frequency sidebands used for interferometer controls that contaminate the GW detection port [14]. The final design of KAGRA OMC is semi-monolithic fused silica with four silica mirrors bonded on the silica breadboard. The OMC used for the KAGRA observation run in 2020 was a temporary design with a metal breadboard and four mirrors glued on metal mounts, bolted on the breadboard. The breadboard is suspended by three single-stage suspensions with blade springs for isolation of vertical seismic motion. The GW signals are extracted by the DC power readout of the OMC transmitting beam.

The data in the KAGRA tunnel, including the GW channel which is calibrated in rea-time, interferometer control signals and other auxiliary channels, e.g., environmental monitor channels, are transferred every 32 s to the main computer cluster system at the Institute for Cosmic Ray Research, Kashiwa, and Osaka City University. Data are also distributed from the Kashiwa computer system to the other KAGRA data tiers, that is, to Korea Institute of Science and Technology Information located in Korea and to Academia Sinica in Taiwan, with latencies of the order of several hours. GW searches and detector characterizations are performed there. The detecter sensitivities shown in this article use this real-time calibrated GW data.

For rapid GW searches, a chunk of data that is of duration 1 s is shared by the international detector networks. It is transmitted to Kashiwa and Osaka City University at a latency of approximately 3.5 s, then, transmitted to the computer centers at aLIGO (Caltech) at a latency of approximately 15 s. This low-latency pipeline contains only selected important channels.

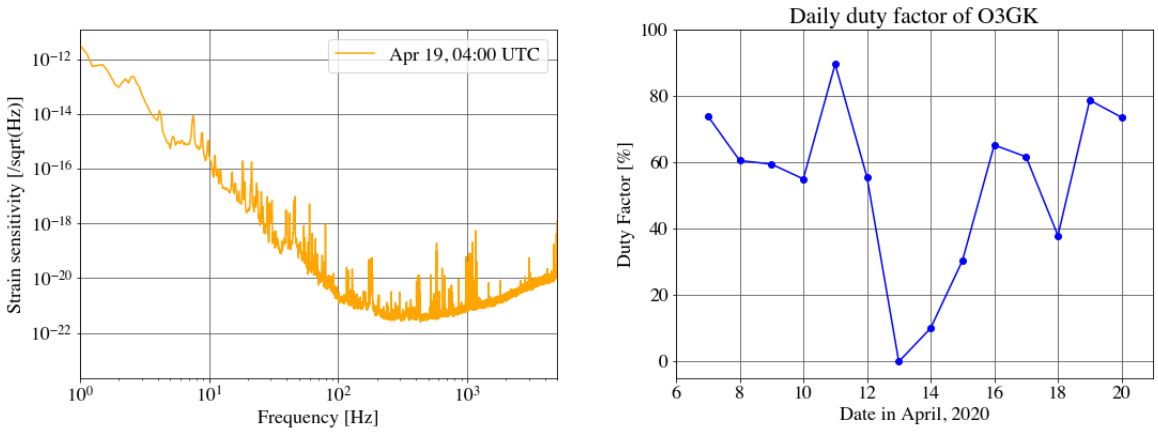

Figure 4: Left: Typical amplitude spectral density of the detector sensitivity in O3GK. Right: Daily duty factor of the KAGRA detector in O3GK. The mean duty factor of the period was 54%.

3.2 Interferometer Commissioning

As discussed, the large-scale interferometer is significantly complex. It requires considerable effort to integrate various instruments and parts until the interferometer can operate as a GW detector. First, the interferometer mirrors must be appropriately controlled for the complex optical cavities to resonate (or to be in anti-resonance) [15]. Without this, the interferometer will not respond to the GW signals. This is called as *lock acquisition*. Particularly, the first lock acquisition to establish the control and lock sequences persists for several months (this is why KAGRA operated in the simpler PRFPMI for this operation owing to limited time). Then, the complex procedures of the lock acquisition are automated. Once the interferometer is stably locked, every noise contaminating the detector sensitivity must be eliminated. This is called *noise hunting*. Based on the target sensitivity, noise hunting also requires several months or even years. This is why all large-scale interferometric GW detectors repeat the observation periods and offline periods to steadily upgrade the detector sensitivity in offline phases. The KAGRA sensitivity and limiting noise during O3GK are discussed in Sec. 4.2.

4 O3GK, the Joint Run with GEO600

4.1 Background

KAGRA's first joint observation with the GEO600 detector started at 08:00:00 UTC on April 7, 2020, UTC, and terminated at 00:00:00 on April 21, 2020, UTC. GEO600 is the GW detector in Germany with 600 m delay-line arm cavities [9]. Initially, KAGRA aimed to join the LIGO–VIRGO third observation (O3) once it achieves a certain sensitivity. However, owing to the COVID-19 pandemic, LIGO–VIRGO suspended O3 early on March 27, 2020, when KAGRA was still working for noise hunting. Furthermore, because GEO600, which had a sensitivity similar to that of KAGRA, was online when KAGRA began its observation in April, the GEO600-KAGRA joint observation was established.

4.2 Detector Sensitivity

The left panel of Fig. 4 shows a typical sensitivity of the KAGRA detector in strain [$/\sqrt{\text{Hz}}$] in the frequency domain in O3GK. The high-frequency region above 400 Hz is limited by the shot noise,

which is the photon-counting noise at the photodetector. The low-frequency region below 50 Hz is limited by the control noise from the resonance damping and controls of the type-A suspensions. Some spikes at approximately 180 Hz were from the suspension violin mode, which is a fundamental vibration mode of the suspension fibers that are thermally excited. Currently, the noise limiting the mid-frequency at approximately 100 Hz is unknown. Because the sensitivity of this region fluctuates significantly depending on the arm alignment, we assume that there are some noise coupling mechanisms related to the interferometer alignment. It can also arise from the scattered light as it is a typical non-stationary noise source. Details of the noise budget are being discussed and reports addressing this aspect are under preparation.

This sensitivity corresponds to a binary neutron-star (BNS) inspiral range of approximately 600 kpc. The BNS range is a figure of merit of GW detector we often use, describing how far (volume- and orientation-averaged) the single detector can detect the GW signals from a 1.4 $M_\odot$ neutron-star coalescence at a signal-to-noise ratio of 8 [16]. The BNS range in the 2-week O3GK is shown in the top panel of Fig. 5. The mean sensitivity in the science mode was 500 kpc, with a standard deviation of 170 kpc. The calibration error of this BNS range is assumed to be relatively large, possibly 30% or 40% because the real-time calibration pipeline does not include any optical gain alterations that are typically introduced by the alignment drifts. An offline analysis for more accurate calibration is in progress.

4.3 Duty Factor

The duty factor, which is the ratio between the period of the science mode (observation mode) and the total operation period, was 54%. The right panel in Fig. 4 shows the daily duty factor in O3GK. The duty factor on April 13 was zero because the interferometer was not operational owing to the so-called microseismic motion, i.e., the seismic motion between 0.1 Hz and 0.3 Hz, typically caused by ocean waves. The microseismic motion was significantly high owing to bad weather on April 13, as shown in the bottom panel in Fig. 5. It is band-filtered RMS seismometer data, filtered from 0.1 Hz and 0.3 Hz. The high microseismic motion continued until April 14, and the duty factor on that day was also degraded. The plot indicates that if the microseismic level was beyond approximately 1 [μm/s] RMS, the interferometer could not be operated. In future observations, suspension controls must be improved to isolate the seismic motion better, so that the interferometer locking can tolerate bad weather.

Compared with the performance of the aLIGO and aVIRGO detectors, the mean duty factor of 54% is low. A lock-loss occurred at hourly intervals because of the degradation of the global interferometer alignment. During the observation, no global active alignment control was implemented. Also, the large variations in the BNS range in the science mode are likely due to alignment drifts.

Furthermore, the lock-losses can be due to earthquakes. The middle plot in Fig. 5 shows the data from a seismometer at the EY station in the vertical direction to the ground. The data are band-filtered RMS, filtered from 30 mHz to 100 mHz, which is the typical frequency band of earthquakes. Compared to the top plot, some large spikes corresponding to earthquakes are coincident with some lock-loss times. A detector characterization study to investigate the relationship between the interferometer lock-losses and earthquakes is ongoing [17].

Data analysis of O3GK along with the GEO600 data for GW signal search is underway and will be presented in a future work.

5 Future Prospects of the Detector

KAGRA aims to join the next observation of LIGO–VIRGO (their fourth observation, O4). For KAGRA, the BNS sensitivity and duty factor must be significantly improved to contribute to GW astrophysics. The target sensitivity of KAGRA for O4 is 25 Mpc for BNS. To achieve the sensitivity, the

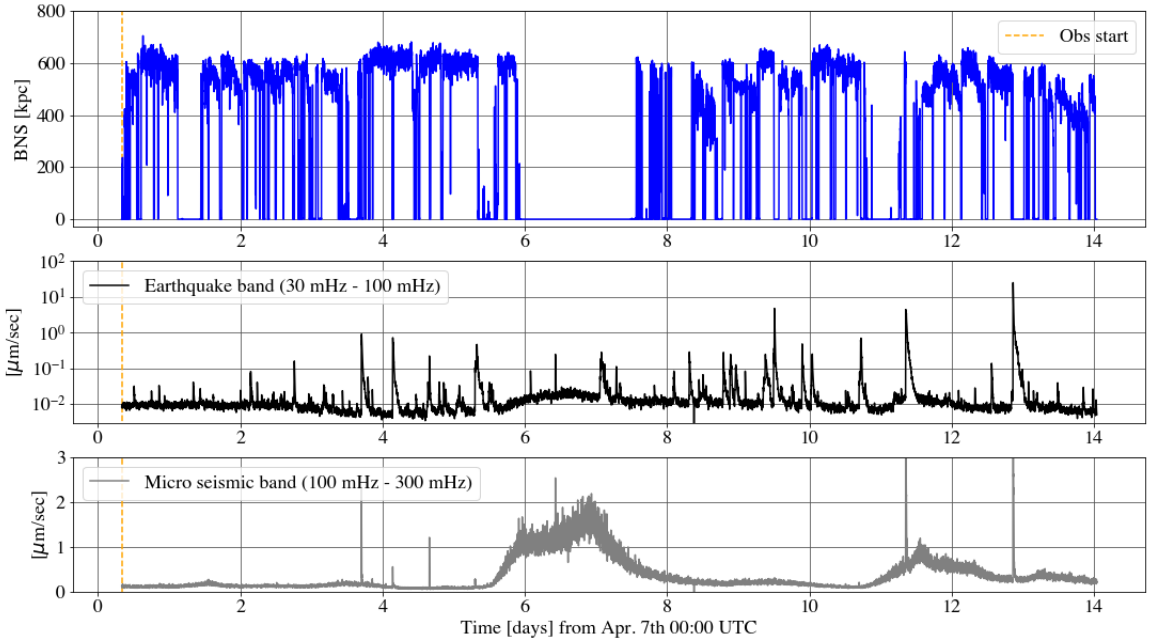

Figure 5: Top: BNS range in O3GK, April 7-21, 2020, UTC. The mean value of the sensitivity was 500 kpc. These data indicate a minute trend generated by the real-time calibration pipeline which have a relatively large calibration error. Middle: Seismic activity level at the earthquake frequency band (from 30 to 100 mHz). Note that the y-axis is on a log scale. Bottom: Seismic activity level at the microseismic frequency band (from 100 mHz to 300 mHz).

following hardware upgrades are planned: (i) Upgrading the interferometer configuration to DRFPMI. (ii) Improving the suspension damping and control schemes. (iii) Increasing the laser power to lower the shot noise. (iv) Improving the laser intensity and frequency stabilizations. (v) Reducing scattered light with more shrouds installed in vacuum.

6 Conclusions

The gravitational-wave detector, KAGRA, completed its first formal scientific observation in the spring of 2020. The last half of the observation was a joint observation with GEO600. Furthermore, KAGRA detector's mean BNS range was 500 kpc, with a duty factor of 54%. The obtained data are being analyzed for astrophysical searches. Currently, the KAGRA detector is offline for major upgrades to improve the sensitivity, thus aiming to join the next LIGO–VIRGO observation run.

Acknowledgements

This work was supported by MEXT, JSPS Leading-edge Research Infrastructure Program, JSPS Grant-in-Aid for Specially Promoted Research 26000005, JSPS Grant-in-Aid for Scientific Research on Innovative Areas 2905: JP17H06358, JP17H06361 and JP17H06364, JSPS Core-to-Core Program A. Advanced Research Networks, JSPS Grant-in-Aid for Scientific Research (S) 17H06133, the joint research program of the Institute for Cosmic Ray Research, University of Tokyo, National Research Founda-

tion (NRF), and Computing Infrastructure Project of KISTI-GSDC in Korea, Academia Sinica (AS), AS Grid Center (ASGC), and the Ministry of Science and Technology (MoST) in Taiwan under grants including AS-CDA-105-M06, the LIGO project, and the VIRGO project.

References

[1] B.P. Abbott et al. Observation of Gravitational Waves from a Binary Black Hole Merger. *Phys. Rev. Lett.*, 116(6):061102, 2016.

[2] B.P. Abbott et al. GW170817: Observation of Gravitational Waves from a Binary Neutron Star Inspiral. *Phys. Rev. Lett.*, 119(16):161101, 2017.

[3] B.P. Abbott et al. Multi-messenger Observations of a Binary Neutron Star Merger. *Astrophys. J. Lett.*, 848(2):L12, 2017.

[4] B.P. Abbott et al. A gravitational-wave standard siren measurement of the Hubble constant. *Nature*, 551(7678):85–88, 2017.

[5] T. Akutsu et al. Overview of KAGRA : KAGRA science. *PTEP*, 2020(1):PTAA120, 8 2020.

[6] T. Akutsu et al. Construction of KAGRA: an Underground Gravitational Wave Observatory. *PTEP*, 2018(1):013F01, 2018.

[7] T. Akutsu et al. First cryogenic test operation of underground km-scale gravitational-wave observatory KAGRA. *Class. Quant. Grav.*, 36(16):165008, 2019.

[8] Y. Akiyama et al. Vibration isolation system with a compact damping system for power recycling mirrors of KAGRA. *Class. Quant. Grav.*, 36(9):095015, 2019.

[9] J. Abadie et al. A Gravitational wave observatory operating beyond the quantum shot-noise limit: Squeezed light in application. *Nature Phys.*, 7:962–965, 2011.

[10] Eiichi Hirose, GariLynn Billingsley, Liyuan Zhang, Hiroaki Yamamoto, Laurent Pinard, Christoph Michel, Danièle Forest, Bill Reichman, and Mark Gross. Characterization of core optics in gravitational-wave detectors: Case study of kagra sapphire mirrors. *Phys. Rev. Applied*, 14:014021, Jul 2020.

[11] Cryogenic suspension design for a kilometer-scale gravitational-wave detector. *In preparation*.

[12] Akiteru Takamori et al. Mirror suspension system for the TAMA SAS. *Class. Quant. Grav.*, 19:1615–1621, 2002.

[13] T Akutsu et al. Input optics systems for the KAGRA observations in 2020. *In preparation*.

[14] Junko Kasuya, John Winterflood, Ju Li, and Kentaro Somiya. Optical design and suspension system of the KAGRA output mode-cleaner. *J. Phys. Conf. Ser.*, 957(1):012009, 2018.

[15] A. Staley et al. Achieving resonance in the Advanced LIGO gravitational-wave interferometer. *Class. Quant. Grav.*, 31(24):245010, 2014.

[16] Lee Samuel Finn and David F. Chernoff. Observing binary inspiral in gravitational radiation: One interferometer. *Phys. Rev. D*, 47:2198–2219, Mar 1993.

[17] A Fujikawa. Development of cause estimation system for interferometer lock loss in large-scale cryogenic gravitational waves telescope. Presented at the IEICE society meeting, 2020.

Testing the no-hair theorem with LIGO and Virgo

Maximiliano Isi [1]

e-mail: maxisi@mit.edu

LIGO Laboratory, Massachusetts Institute of Technology,
Cambridge, Massachusetts 02139, USA

Presented at the 3rd World Summit on Exploring the Dark Side of the Universe
Guadeloupe Islands, March 9-13 2020

Abstract

The no-hair theorem predicts that a perturbed Kerr black hole should emit gravitational waves as damped sinusoids with characteristic frequencies and damping rates depending only on the hole's mass and spin. Analyzing the spectrum of such quasinormal modes can provide a direct probe of the black-hole spacetime, distinguishing it from other compact objects and enabling tests of general relativity. Considering the two least-damped components of the dominant angular mode ($\ell = m = 2$, $n \leq 1$), we find that the first LIGO detection (GW150914) already encoded clues about the black-hole spectrum. A two-mode ringdown model allows us to measure the final mass and spin of the remnant exclusively from postinspiral data, obtaining an estimate in agreement with that from the full signal. We also find that an independent measurement of the frequency of the second mode yields agreement with the no-hair hypothesis at the $\sim 20\%$ level. Improved detectors on the ground, as well as future missions in space, will provide even stronger tests. *This is a summary of Isi, Giesler, Farr, Scheel, and Teukolsky (2020) [1].*

1 Introduction

The last portion of the gravitational waves (GWs) from a binary black hole (BH) coalescence corresponds to the ringdown of the remnant object. In general relativity (GR), this ringdown radiation takes the form of superposed damped sinusoids, corresponding to the quasinormal modes (QNMs) of the final Kerr BH [2, 3, 4, 5]. The frequencies and decay rates of these damped sinusoids are uniquely determined by the final hole's mass M_f and dimensionless spin magnitude χ_f. This follows from the *no-hair theorem*—the statement that mass and spin are the only two properties of astrophysical black holes in GR. Teasing out the QNMs from GW observations could allow us to test GR, and distinguish Kerr remnants from possible mimickers by testing the no-hair theorem [6, 7, 8, 9, 10, 11, 12, 13, 14].

In [1], we analyze LIGO [15] data from the GW150914 event [16] to perform a multimodal spectroscopic analysis of a BH ringdown. Following [17], we rely on tones of the $\ell = m = 2$ angular mode to measure M_f and χ_f from data starting at the peak of the signal, assuming first that QNMs are as predicted by perturbation theory for a Kerr BH. This measurement agrees with that from the longest-lived mode alone beginning $3\,\mathrm{ms}$ after the waveform peak amplitude [18], as well as that obtained from the full waveform using fits to numerical relativity. We also consider a two-tone model that allows deviations from the Kerr prediction for any given mass and spin. From data starting at

[1] NHFP Einstein fellow

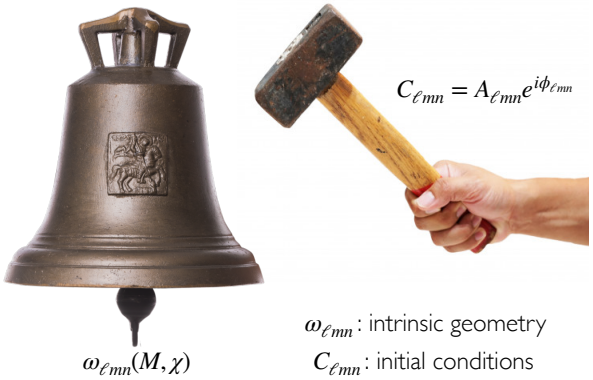

Figure 1: A perturbed BH rings just like a struck bell. The frequency $\omega_{\ell mn}$ and damping rate (pitch and duration) encode information about the intrinsic geometry of the object: mass and spin for a Kerr BH, shape and material for a bell. The complex amplitudes $C_{\ell mn} = A_{\ell mn} e^{i\phi_{\ell mn}}$, on the other hand, carry information about the origin of the perturbation. (*Image source:* bell [33], hammer [34].)

peak strain, we find the spectrum to be in agreement with the no-hair hypothesis to within $\sim 20\%$, with 68% credibility. This is a test of the no-hair theorem based purely on the postinspiral regime.

Previous analyses had looked for the ringdown in data at late times after the signal peak, where the QNMs are too weak to confidently characterize with current instruments [19, 20, 21, 22, 23, 24, 25]. This was motivated by concerns about potential nonlinearities surrounding the BH merger [9, 26, 27, 21, 22, 24, 25]. However, the linear description can be extended to the full waveform following the peak of the gravitational wave strain: times around the peak are dominated by ringdown *overtones*—the QNMs with the fastest decay rates [17, 28]. Indications of this can be found in the waveform modeling literature, with overtones an integral part of early equivalent one-body models [29, 30, 31]. Yet, with a few exceptions [13, 23], previous ringdown analyses have neglected overtones [9, 19, 32, 20, 21, 22, 24, 25]. As a consequence, these studies ignored were unable to extract multiple ringdown modes.

The remaining sections of these Proceedings summarize the method and results of [1] as presented at the *3rd World Summit on Exploring the Dark Side of the Universe*, and conclude with a brief discussion on future perspectives.

2 Method

Each QNM has a frequency $\omega_{\ell mn}$ and a damping time $\tau_{\ell mn}$, where n is the overtone index and (ℓ, m) are indices of spin-weighted angular harmonics that describe the angular structure of the mode. The overtone index n orders the modes with a given (ℓ, m) by increasing damping rate, so that $n = 0$ denotes the longest-lived ("fundamental") mode. Unlike elsewhere in physics, a higher n does not imply a higher frequency ω_n; rather, the opposite is generally true.

Our analysis targets the fundamental and overtones of the $\ell = m = 2$ spin-weighted spherical harmonic of the strain, as this is the only angular harmonic expected to be relevant for GW150914 [35, 36, 25]. We drop the ℓ and m indices, and write the $\ell = m = 2$ mode of the ringdown strain ($h = h_+ - ih_\times$) as a sum of damped sinusoids [2, 3, 4, 5],

$$h_{22}^N(t) = \sum_{n=0}^{N} A_n \exp\left[-i\left(\omega_n t + \phi_n\right) - t/\tau_n\right], \tag{1}$$

for times t greater than some start time t_0, where $\Delta t = t - t_0$. N is the index of the highest overtone included in the model, which for us will always be $N \leq 2$. For a Kerr BH, all the ω_n's and

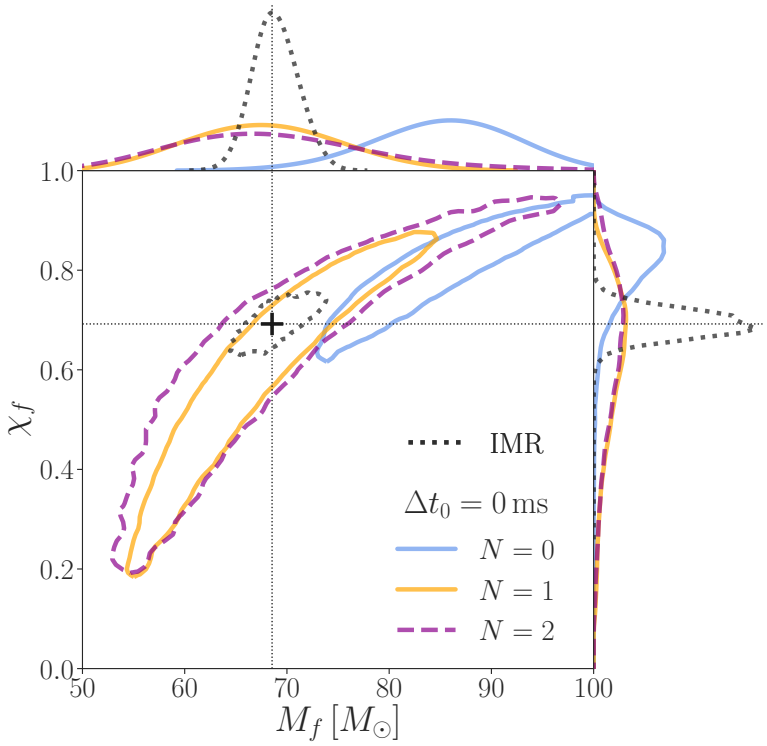

Figure 2: Contours represent 90%-credible regions on the remnant mass (M_f) and dimensionless spin magnitude (χ_f), obtained from the analysis of the GW150914 ringdown starting at peak strain amplitude ($\Delta t_0 = t_0 - t_{\rm peak} = 0$). Color encodes the number of overtones N in the model: 0 (solid blue), 1 (solid yellow), 2 (dashed purple) The dotted black contour is obtained from the full IMR waveform, assuming GR; the crosshairs mark the peak of this distribution ($M_f = 68.5 M_\odot$, $\chi_f = 0.69$). The top and right panels show marginal posteriors for M_f and χ_f respectively. This is Fig. 1 in [1].

τ_n's are implicit functions of the remnant mass and spin magnitude (M_f, χ_f), and can be computed from perturbation theory [37, 38, 39]. The amplitudes A_n and phases ϕ_n cannot be computed within perturbation theory, so we treat them as free parameters (Fig. 1).

We carry out a Bayesian analysis of LIGO Hanford and LIGO Livingston data for GW150914 [16, 40, 41]. For a choice of N and start time t_0, we compute the joint posterior probability over M_f, χ_f, A_n and ϕ_n. We first do so assuming a Kerr spectrum, but then relax the $N = 1$ model to test the no-hair theorem: in this non-GR model, we write

$$\omega_1 = 2\pi f_1^{(\rm GR)}\,(1 + \delta f_1)\,, \tag{2}$$

$$\tau_1 = \tau_1^{(\rm GR)}\,(1 + \delta \tau_1)\,, \tag{3}$$

with δf_1 and $\delta \tau_1$ fractional deviations away from the Kerr values $f_1^{(\rm GR)}$ and $\tau_1^{(\rm GR)}$ for any given M_f and χ_f. In all cases, we parametrize start times via $\Delta t_0 = t_0 - t_{\rm peak}$, where $t_{\rm peak} = 1126259462.423$ GPS refers to the signal peak at the LIGO Hanford detector [42, 19]. We define the likelihood in the time domain in order to explicitly exclude all data before t_0. See the Supplement to [1] for details.

We compare our ringdown-only measurements to the expectation from the full inspiral-merger-ringdown (IMR) signal. We use fitting formulas based on numerical relativity [43, 44] to predict the remnant parameters from publicly-available posterior samples on the binary parameters [40, 45].

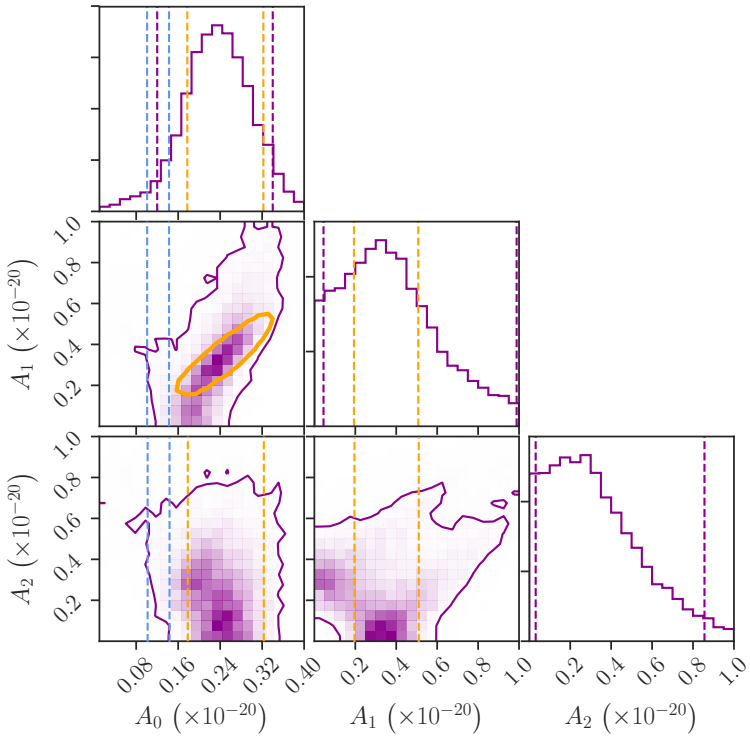

Figure 3: Measured QNM amplitudes for ringdown analyses with different number of overtones N, starting at peak strain: the joint posterior for A_0, A_1 and A_2 recovered by the $N = 2$ model (purple); the 90%-credible measurement of A_0 and A_1 obtained with $N = 1$ (yellow); and the same for A_0 obtained with $N = 0$ (blue). Solid curves and vertical dashed lines enclose 90% of the probability mass. Values have been rescaled by a constant to correspond to the strain measured by the LIGO Hanford detector. This is Fig. 2 in [1].

3 Results

Fig. 2 shows the 90%-credible regions for M_f and χ_f, obtained assuming a Kerr spectrum ($\delta f_n = \delta\tau_n = 0$) by analyzing data starting at $t_{\rm peak}$ with different numbers of overtones ($N = 0, 1, 2$) in the ringdown template of Eq. (1). Under GR, the ringdown and IMR measurements should agree. As expected for $\delta t_0 = 0$, this is only the case for the overtone results ($N \geq 1$), and not for the fundamental alone. Adding a second overtone ($N = 2$) does not improve agreement with IMR, which is expected given the network SNR of GW150914 [17].

The fact that the analysis is unable to unequivocally identify the second overtone in the data is reflected in the amplitude posteriors of Fig. 3. The $N = 2$ result supports a range of values for A_1 and A_2, but excludes $A_1 = A_2 = 0$ with 90% credibility (bottom center in Fig. 3). The joint posterior distribution on A_1 and A_2 tends to favor the first overtone at the expense of the second, favoring a value of A_1 in agreement with the $N = 1$ posterior (yellow traces in Fig. 3). Assuming $N = 1$, $A_1 = 0$ is disfavored at 3.6σ; assuming $N = 2$, $A_1 = A_2 = 0$ is disfavored with 90% credibility.

We next compare measurements carried out with overtones at the peak to those without overtones after the peak. Fig. 4 shows 90%-credible regions for the remnant mass and spin magnitude obtained with $N = 0$ at different times after $t_{\rm peak}$ ($\Delta t_0 \in [1,\ 3,\ 5]$ ms). As the overtones die out, the fundamental mode becomes a better model for the signal, and we find that the $N = 0$ contour coincides with the IMR measurement $\sim$3 ms after the peak, in agreement with [19].

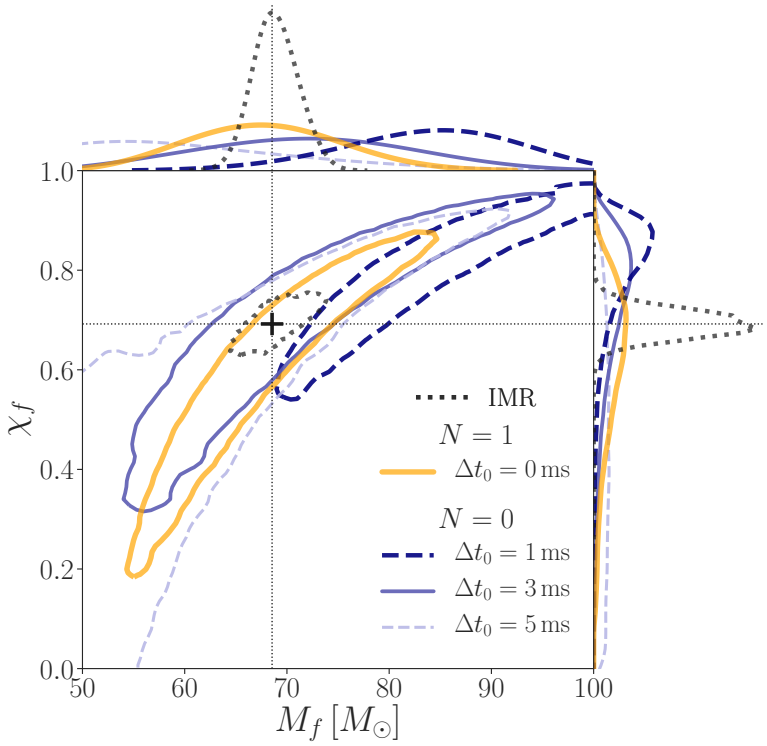

Figure 4: Contours represent 90%-credible regions on the remnant mass (M_f) and dimensionless spin magnitude (χ_f), obtained from the analysis of the GW150914 ringdown with $N = 0$ at different times after the peak (blue), compared to $N = 1$ at the peak. The dotted black contour is obtained from the full IMR waveform, assuming GR; the crosshairs mark the peak of this distribution ($M_f = 68.5M_\odot$, $\chi_f = 0.69$). The top and right panels show marginal posteriors for M_f and χ_f respectively. Around $\Delta t_0 = 3\,\mathrm{ms}$, the overtones have become unmeasurable and only the fundamental mode remains; consequently, at that time, the $N = 0$ result starts being consistent with both the full IMR waveform and the $N \geq 1$ models at the peak, in agreement with GR. This is Fig. 3 in [1].

Finally, we allow the first-overtone frequency and damping time to float around the no-hair values in the $N = 1$ model, starting the analysis at peak strain. Fig. 5 shows the resulting posterior over the δf_1 and $\delta\tau_1$. With 68% credibility, we measure $\delta f_1 = -0.05 \pm 0.2$, establishing agreement with the no-hair hypothesis ($\delta f_1 = 0$) at the 20% level. The damping time is largely unconstrained in the $-0.06 \lesssim \delta\tau_1 \lesssim 1$ range.

4 Conclusion

Making use of overtones, we extracted information about the GW150914 remnant using only postinspiral data, starting at the peak of the signal (Fig. 2). We found evidence of the fundamental mode plus at least one overtone (Fig. 3), and measured the remnant mass and spin in agreement with that the full waveform analysis. This result is also consistent with the one obtained using solely the fundamental mode at a later time (Fig. 4).

The agreement between all measurements (IMR, $N = 0$, $N \geq 1$) is evidence that, beginning as early as the signal peak, a far-away observer cannot distinguish the source from a linearly perturbed Kerr background, i.e., we do not observe nonlinearities in this regime. The agreement between the IMR and postmerger estimates implies that the data conform to the full GR prediction, as in the IMR

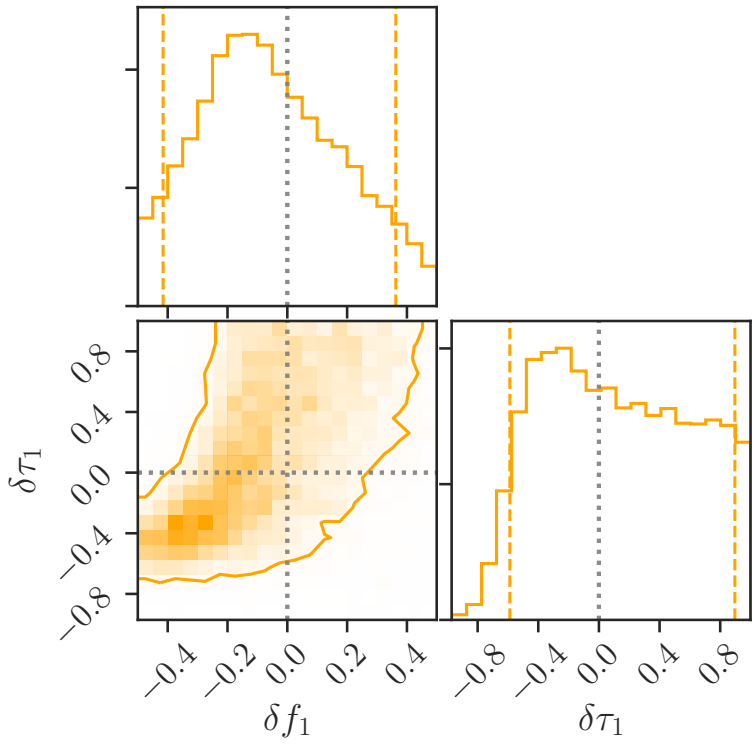

Figure 5: Posterior distribution of the fractional deviations δf_1 and $\delta\tau_1$ away from the no-hair value $\delta f_1 = \delta\tau_1 = 0$ (gray dotted lines), measured at peak strain with $N = 1$. The solid contour and dashed vertical lines enclose 90% of the posterior probability. Fixing $\delta f_1 = \delta\tau_1 = 0$ recovers the $N = 1$ analysis in Figs. 2 and 4. This is Fig. 4 in [1].

consistency test described in [46, 47].

With the identification of multiple ringdown modes, we took a step toward the goal of black hole spectroscopy. We constrained deviations away from the no-hair spectrum by allowing the overtone frequency and damping time to vary freely (Fig. 5). This is equivalent to independently measuring the frequencies of the fundamental and first overtone, and establishing their consistency with the Kerr hypothesis.

Future overtone measurements could potentially allow us to identify BH mimickers, and probe the applicability of the no-hair theorem with high precision. As the sensitivity of GW instruments improves, we will be able to leverage the increased quantity and quality of the detected signals to test the no-hair theorem in richer and more accurate ways.

Acknowledgements

These Proceedings summarized [1], as presented by M.I. at the *3rd World Summit on Exploring the Dark Side of the Universe* (Guadeloupe Islands, March 9-13 2020). Besides M.I., the authors of this work were Matthew Giesler, Will M. Farr, Mark A. Scheel, and Saul A. Teukolsky. M.I. is supported by NASA through the NASA Hubble Fellowship grant No. HST-HF2-51410.001-A awarded by the Space Telescope Science Institute, which is operated by the Association of Universities for Research in Astronomy, Inc., for NASA, under contract NAS5-26555. M.I. is a member of the LIGO Laboratory. LIGO was constructed by the California Institute of Technology and Massachusetts Institute

of Technology with funding from the National Science Foundation and operates under cooperative agreement PHY-0757058. M.G. and M.S. are supported by the Sherman Fairchild Foundation and NSF grants PHY-1708212 and PHY-1708213 at Caltech. S.T. is supported in part by the Sherman Fairchild Foundation and by NSF Grants PHY-1606654 and ACI-1713678 at Cornell. The Flatiron Institute is supported by the Simons Foundation. This research has made use of data, software and/or web tools obtained from the Gravitational Wave Open Science Center [48, 41], a service of the LIGO Laboratory, the LIGO Scientific Collaboration and the Virgo Collaboration.

References

[1] M. Isi, M. Giesler, W. M. Farr, M. A. Scheel, and S. A. Teukolsky, *Testing the no-hair theorem with GW150914*, *Phys. Rev. Lett.* **123** (2019), no. 11 111102, [arXiv:1905.00869].

[2] C. V. Vishveshwara, *Stability of the schwarzschild metric*, *Phys. Rev. D* **1** (May, 1970) 2870–2879.

[3] W. H. Press, *Long Wave Trains of Gravitational Waves from a Vibrating Black Hole*, *Astrophys. J.* **170** (1971) L105–L108.

[4] S. A. Teukolsky, *Perturbations of a Rotating Black Hole. I. Fundamental Equations for Gravitational, Electromagnetic, and Neutrino-Field Perturbations*, ApJ **185** (Oct., 1973) 635–648.

[5] S. Chandrasekhar and S. Detweiler, *The quasi-normal modes of the schwarzschild black hole*, *Proc. R. Soc. A* **344** (1975), no. 1639 441–452.

[6] F. Echeverria, *Gravitational Wave Measurements of the Mass and Angular Momentum of a Black Hole*, *Phys. Rev.* **D40** (1989) 3194–3203.

[7] O. Dreyer, B. J. Kelly, B. Krishnan, L. S. Finn, D. Garrison, and R. Lopez-Aleman, *Black hole spectroscopy: Testing general relativity through gravitational wave observations*, *Class. Quant. Grav.* **21** (2004) 787–804, [gr-qc/0309007].

[8] E. Berti, V. Cardoso, and C. M. Will, *On gravitational-wave spectroscopy of massive black holes with the space interferometer LISA*, *Phys. Rev.* **D73** (2006) 064030, [gr-qc/0512160].

[9] S. Gossan, J. Veitch, and B. S. Sathyaprakash, *Bayesian model selection for testing the no-hair theorem with black hole ringdowns*, *Phys. Rev.* **D85** (2012) 124056, [arXiv:1111.5819].

[10] J. Meidam, M. Agathos, C. Van Den Broeck, J. Veitch, and B. S. Sathyaprakash, *Testing the no-hair theorem with black hole ringdowns using TIGER*, *Phys. Rev.* **D90** (2014), no. 6 064009, [arXiv:1406.3201].

[11] E. Berti et al., *Testing General Relativity with Present and Future Astrophysical Observations*, *Class. Quant. Grav.* **32** (2015) 243001, [arXiv:1501.07274].

[12] E. Berti, A. Sesana, E. Barausse, V. Cardoso, and K. Belczynski, *Spectroscopy of Kerr black holes with Earth- and space-based interferometers*, *Phys. Rev. Lett.* **117** (2016), no. 10 101102, [arXiv:1605.09286].

[13] V. Baibhav, E. Berti, V. Cardoso, and G. Khanna, *Black Hole Spectroscopy: Systematic Errors and Ringdown Energy Estimates*, *Phys. Rev.* **D97** (2018), no. 4 044048, [arXiv:1710.02156].

[14] V. Baibhav and E. Berti, *Multimode black hole spectroscopy*, *Phys. Rev.* **D99** (2019), no. 2 024005, [arXiv:1809.03500].

[15] J. Aasi et al., *Advanced LIGO*, *Class. Quant. Grav.* **32** (2015) 074001.

[16] **LIGO Scientific Collaboration, Virgo Collaboration** Collaboration, B. P. Abbott et al., *Observation of Gravitational Waves from a Binary Black Hole Merger*, *Phys. Rev. Lett.* **116** (feb, 2016) 061102.

[17] M. Giesler, M. Isi, M. A. Scheel, and S. Teukolsky, *Black Hole Ringdown: The Importance of Overtones*, *Phys. Rev. X* **9** (2019), no. 4 041060, [arXiv:1903.08284].

[18] **LIGO Scientific Collaboration, Virgo Collaboration** Collaboration, B. P. Abbott et al., *Tests of general relativity with GW150914*, *Phys. Rev. Lett.* **116** (2016) 221101, [arXiv:1602.03841].

[19] **LIGO Scientific Collaboration, Virgo Collaboration** Collaboration, B. P. Abbott et al., *Tests of General Relativity with GW150914*, *Phys. Rev. Lett.* **116** (may, 2016) 221101.

[20] W. Del Pozzo and A. Nagar, *Analytic family of post-merger template waveforms*, *Phys. Rev.* **D95** (2017), no. 12 124034, [arXiv:1606.03952].

[21] M. Cabero, C. D. Capano, O. Fischer-Birnholtz, B. Krishnan, A. B. Nielsen, A. H. Nitz, and C. M. Biwer, *Observational tests of the black hole area increase law*, *Phys. Rev.* **D97** (2018), no. 12 124069, [arXiv:1711.09073].

[22] E. Thrane, P. D. Lasky, and Y. Levin, *Challenges testing the no-hair theorem with gravitational waves*, *Phys. Rev.* **D96** (2017), no. 10 102004, [arXiv:1706.05152].

[23] R. Brito, A. Buonanno, and V. Raymond, *Black-hole Spectroscopy by Making Full Use of Gravitational-Wave Modeling*, *Phys. Rev.* **D98** (2018), no. 8 084038, [arXiv:1805.00293].

[24] G. Carullo et al., *Empirical tests of the black hole no-hair conjecture using gravitational-wave observations*, *Phys. Rev.* **D98** (2018), no. 10 104020, [arXiv:1805.04760].

[25] G. Carullo, W. Del Pozzo, and J. Veitch, *Observational Black Hole Spectroscopy: A time-domain multimode analysis of GW150914*, *Phys. Rev.* **D99** (2019), no. 12 123029, [arXiv:1902.07527].

[26] I. Kamaretsos, M. Hannam, S. Husa, and B. S. Sathyaprakash, *Black-hole hair loss: learning about binary progenitors from ringdown signals*, *Phys. Rev.* **D85** (2012) 024018, [arXiv:1107.0854].

[27] L. London, J. Healy, and D. Shoemaker, *Modeling Ringdown: Beyond the Fundamental Quasi-Normal Modes*, *Phys. Rev. D* **90** (2014) 124032, [arXiv:1404.3197].

[28] A. Buonanno, G. B. Cook, and F. Pretorius, *Inspiral, merger and ring-down of equal-mass black-hole binaries*, *Phys. Rev.* **D75** (2007) 124018, [gr-qc/0610122].

[29] Y. Pan, A. Buonanno, A. Taracchini, L. E. Kidder, A. H. Mroue, et al., *Inspiral-merger-ringdown waveforms of spinning, precessing black-hole binaries in the effective-one-body formalism*, *Phys. Rev. D* **89** (2013) 084006, [arXiv:1307.6232].

[30] A. Taracchini, A. Buonanno, Y. Pan, T. Hinderer, M. Boyle, D. A. Hemberger, L. E. Kidder, G. Lovelace, A. H. Mroue, H. P. Pfeiffer, M. A. Scheel, B. Szilagyi, N. W. Taylor, and A. Zenginoglu, *Effective-one-body model for black-hole binaries with generic mass ratios and spins*, *Phys. Rev. D* **89 (R)** (2014), no. 6 061502, [arXiv:1311.2544].

[31] S. Babak, A. Taracchini, and A. Buonanno, *Validating the effective-one-body model of spinning, precessing binary black holes against numerical relativity*, arXiv:1607.05661.

[32] S. Bhagwat, D. A. Brown, and S. W. Ballmer, *Spectroscopic analysis of stellar mass black-hole mergers in our local universe with ground-based gravitational wave detectors*, *Phys. Rev.* **D94** (2016), no. 8 084024, [arXiv:1607.07845]. [Erratum: Phys. Rev.D95,no.6,069906(2017)].

[33] Koudounia, "Church bell 6500gr." https://koudounia.com/en/product/bells/church-bell/church-bell-3/. Accessed: 2020-01-30.

[34] freepik, "Hammer closeup." https://www.freepik.com/premium-photo/close-up-hand-holding-big-hammer-against-white-background_2744259.htm. Accessed: 2020-01-30.

[35] **LIGO Scientific Collaboration, Virgo Collaboration** Collaboration, B. P. Abbott et al., *Directly comparing GW150914 with numerical solutions of Einstein's equations for binary black hole coalescence*, *Phys. Rev. D* **94** (2016) 064035, [arXiv:1606.01262].

[36] **LIGO Scientific Collaboration, Virgo Collaboration** Collaboration, B. P. Abbott et al., *Effects of waveform model systematics on the interpretation of GW150914*, *Class. Quant. Grav.* **34** (2017), no. 10 104002, [arXiv:1611.07531].

[37] E. W. Leaver, *An Analytic representation for the quasi normal modes of Kerr black holes*, *Proc. Roy. Soc. Lond.* **A402** (1985) 285–298.

[38] E. Berti, V. Cardoso, and A. O. Starinets, *TOPICAL REVIEW: Quasinormal modes of black holes and black branes*, *Class. Quantum Grav.* **26** (Aug., 2009) 163001, [arXiv:0905.2975].

[39] http://pages.jh.edu/~eberti2/ringdown.

[40] **LIGO Scientific, Virgo** Collaboration, B. P. Abbott et al., *GWTC-1: A Gravitational-Wave Transient Catalog of Compact Binary Mergers Observed by LIGO and Virgo during the First and Second Observing Runs*, arXiv:1811.12907.

[41] https://www.gw-openscience.org.

[42] **LIGO Scientific Collaboration, Virgo Collaboration** Collaboration, B. P. Abbott et al., *Properties of the Binary Black Hole Merger GW150914*, *Phys. Rev. Lett.* **116** (jun, 2016) 241102, [arXiv:1602.03840].

[43] V. Varma, D. Gerosa, L. C. Stein, F. Hebert, and H. Zhang, *High-accuracy mass, spin, and recoil predictions of generic black-hole merger remnants*, *Phys. Rev. Lett.* **122** (2019), no. 1 011101, [arXiv:1809.09125].

[44] J. Blackman, S. E. Field, M. A. Scheel, C. R. Galley, C. D. Ott, M. Boyle, L. E. Kidder, H. P. Pfeiffer, and B. Szilágyi, *Numerical relativity waveform surrogate model for generically precessing binary black hole mergers*, *Phys. Rev.* **D96** (2017), no. 2 024058, [arXiv:1705.07089].

[45] LIGO Scientific Collaboration and Virgo Collaboration, "GWTC-1." https://doi.org/10.7935/82H3-HH23, 2018.

[46] A. Ghosh et al., *Testing general relativity using golden black-hole binaries*, *Phys. Rev. D* **94** (2016), no. 2 021101(R), [arXiv:1602.02453].

[47] A. Ghosh, N. K. Johnson-McDaniel, A. Ghosh, C. K. Mishra, P. Ajith, W. Del Pozzo, C. P. L. Berry, A. B. Nielsen, and L. London, *Testing general relativity using gravitational wave signals from the inspiral, merger and ringdown of binary black holes*, *Classical Quantum Gravity* **35** (2018), no. 1 014002, [arXiv:1704.06784].

[48] M. Vallisneri, J. Kanner, R. Williams, A. Weinstein, and B. Stephens, *The LIGO Open Science Center*, *J. Phys. Conf. Ser.* **610** (2015), no. 1 012021, [arXiv:1410.4839].

Dark Gravity confronted to SN, BAO and the CMB

Frederic Henry-Couannier

e-mail: henry@cppm.in2p3.fr

CPPM and Aix-Marseille University

Presented at the 3rd World Summit on Exploring the Dark Side of the Universe
Guadeloupe Islands, March 9-13 2020

Abstract

After a brief reminder of the Dark Gravity theory foundations the confrontation to the main cosmological probes is carried out. A complete, regularly updated, review of the theory and full references can be found in [1].

1 Introduction

Dark Gravity (DG) is a background dependent bimetric and semi-classical extension of General Relativity with an anti-gravitational sector. DG follows from a crucial observation: in the presence of a flat non dynamical background $\eta_{\mu\nu}$, it turns out that the usual gravitational field $g_{\mu\nu}$ has a twin, the "inverse" metric $\tilde{g}_{\mu\nu}$. The two being linked by :

$$\tilde{g}_{\mu\nu} = \eta_{\mu\rho}\eta_{\nu\sigma}\left[g^{-1}\right]^{\rho\sigma} = [\eta^{\mu\rho}\eta^{\nu\sigma}g_{\rho\sigma}]^{-1} \tag{1}$$

are just the two faces of a single field (no new degrees of freedom) that we called a Janus field.

The action treating our two faces of the Janus field on the same footing is achieved by simply adding to the usual action, the similar action with $\tilde{g}_{\mu\nu}$ in place of $g_{\mu\nu}$ everywhere.

$$\int d^4x(\sqrt{g}R + \sqrt{\tilde{g}}\tilde{R}) + \int d^4x(\sqrt{g}L + \sqrt{\tilde{g}}\tilde{L}) \tag{2}$$

where R and $\tilde{R}$ are the familiar Ricci scalars respectively built from $g_{\mu\nu}$ and $\tilde{g}_{\mu\nu}$ as usual and L and $\tilde{L}$ the Lagrangians for respectively SM F type fields propagating along $g_{\mu\nu}$ geodesics and $\tilde{F}$ fields propagating along $\tilde{g}_{\mu\nu}$ geodesics. This theory symmetrizing the roles of $g_{\mu\nu}$ and $\tilde{g}_{\mu\nu}$ is Dark Gravity (DG) and the field equation satisfied by the Janus field derived from the minimization of the action is:

$$\sqrt{g}\eta^{\mu\sigma}g_{\sigma\rho}G^{\rho\nu} - \sqrt{\tilde{g}}\eta^{\nu\sigma}\tilde{g}_{\sigma\rho}\tilde{G}^{\rho\mu} = -8\pi G(\sqrt{g}\eta^{\mu\sigma}g_{\sigma\rho}T^{\rho\nu} - \sqrt{\tilde{g}}\eta^{\nu\sigma}\tilde{g}_{\sigma\rho}\tilde{T}^{\rho\mu}) \tag{3}$$

with $T^{\mu\nu}$ and $\tilde{T}^{\mu\nu}$ the energy momentum tensors for F and $\tilde{F}$ fields respectively and $G^{\mu\nu}$ and $\tilde{G}^{\mu\nu}$ the Einstein tensors (e.g. $G^{\mu\nu} = R^{\mu\nu} - 1/2g^{\mu\nu}R$).

The minus signs in the field equation obviously imply that we have ghost interactions between the gravitational field and matter fields however our Janus field is not understood to be a quantum field insuring that the theory is free of quantum instabilities. The classical instabilities are completely harmless (their coupling is reduced by a huge power of the cosmological scale factor) for weak fields whereas for strong fields the theory also has it's own natural mechanism to insure the stability of the interactions (see [1]).

2 The homogeneous and isotropic case

We found that an homogeneous and isotropic solution is necessarily spatially flat because the two sides of the Janus field about our flat Minkowski background are required to be both homogeneous and isotropic. The conjugate homogeneous and isotropic spatially flat metrics are then assumed to take the form $g_{\mu\nu} = a(t)\eta_{\mu\nu}$ and $\tilde{g}_{\mu\nu} = a^{-1}(t)\eta_{\mu\nu}$. In this section the time variable t is the conformal time and the Hubble parameters H and $\tilde{H}$ are understood to be conformal Hubble parameters. Then the two Friedman type equations the conformal scale factor should satisfy are:

$$a^2(2\dot{H} + H^2) - \tilde{a}^2(2\dot{\tilde{H}} + \tilde{H}^2) = -6K(a^4 p - \tilde{a}^4\tilde{p}) \tag{4}$$

$$a^2H^2 - \tilde{a}^2\tilde{H}^2 = 2K(a^4\rho - \tilde{a}^4\tilde{\rho}) \tag{5}$$

with $K = \frac{4\pi G}{3}$. This has no solution except that of an empty static universe which is not surprising since our theory has no equivalent of the Bianchi identities resulting in two functionally independent cosmological equations for only one degree of freedom, the scale factor. However following an original idea by Prigogin (see for instance [2] and multi-references therein) let's allow the gravitationally induced adiabatic creation or annihilation of particles on either side. Our conservation equations then get modified:

$$\frac{\dot{\rho}}{H} = (\frac{\Gamma}{H} - 3)(\rho + p) \tag{6}$$

$$\frac{\dot{\tilde{\rho}}}{\tilde{H}} = -\frac{\dot{\tilde{\rho}}}{H} = (\frac{\tilde{\Gamma}}{\tilde{H}} - 3)(\tilde{\rho} + \tilde{p}) \tag{7}$$

with the creation rates related through $\tilde{\Gamma} = -\Gamma$ (just as $\tilde{H} = -H$) in such a way that there is no actual creation or annihilation of particles but merely a transfer from one metric to the conjugate. Now replacing these terms in the time derivative of the second DG-Friedman equation and then adding and subtracting the two DG-Friedman equations we get :

$$a\ddot{a} = K(a^4(\rho - 3p) + \frac{1}{2}(C_r + \tilde{C}_r)) \tag{8}$$

$$\tilde{a}\ddot{\tilde{a}} = K(\tilde{a}^4(\tilde{\rho} - 3\tilde{p}) + \frac{1}{2}(C_r + \tilde{C}_r)) \tag{9}$$

including the creation/annihilation terms $C_r = a^4\frac{\Gamma}{H}(\rho + p)$, $\tilde{C}_r = \tilde{a}^4\frac{\Gamma}{H}(\tilde{\rho} + \tilde{p})$, which can be solved numerically for physically acceptable solutions: the resulting $a(t)$ and $\rho(t)$ of Figure 1 show that the density increases very sharply near t=0 because of the incoming matter from the dark side while the scale factor is almost constant. The density reaches a maximum for $\Gamma/H = 3$ then decreases as expected according the actual equation of state of matter as soon as exchanges become negligible. This occurs when our side scale factor becomes dominant over $\tilde{a} = 1/a$. Eventually our cosmological equations were reconciled by the introduction of an additional degree of freedom, our scalar offshell (should not extremize the action) Γ. Notice that the conjugate densities are equal at the origin of time but also at the crossing time in Figure 1. Alternatively to genuine matter-radiation exchange, the rates $\tilde{\Gamma}$, Γ could be interpreted as being the result of conjugate variations of (still offshell) fundamental constants such as G or h, for instance $\Gamma = \frac{\dot{h}}{h} = -\frac{\dot{\tilde{h}}}{\tilde{h}} = -\tilde{\Gamma}$ as this would produce similar differential equations and solutions (see [1]).

3 Cosmology

3.1 Reproducing GR cosmology

The expansion of our side implies that the dark side of the universe is in contraction. Provided dark side terms and the exchange terms can be neglected which is certainly an excellent approximation

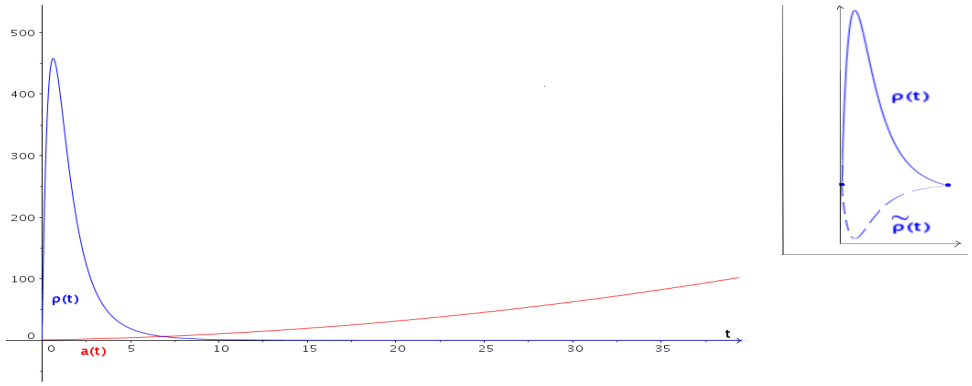

Figure 1: a(t) and $\rho(t)$ when including the effect of the transfer rate Γ to restore the consistency of Friedmann and conservation equations.

far from t=0 (this origin of time is defined to be the time of scale factors equality), our cosmological equations reduce to equations known to be also valid within GR. For this reason it is straightforward for DG to reproduce the same scale factor expansion evolution as obtained within the standard LCDM Model at least up to the redshift of the LCDM Lambda dominated era. The evolution of our side scale factor before the transition to the accelerated regime is depicted in red on the top left of Figure 2 as a function of the conformal time t and the corresponding evolution laws as a function of standard time t′ are also given in the radiative and cold era.

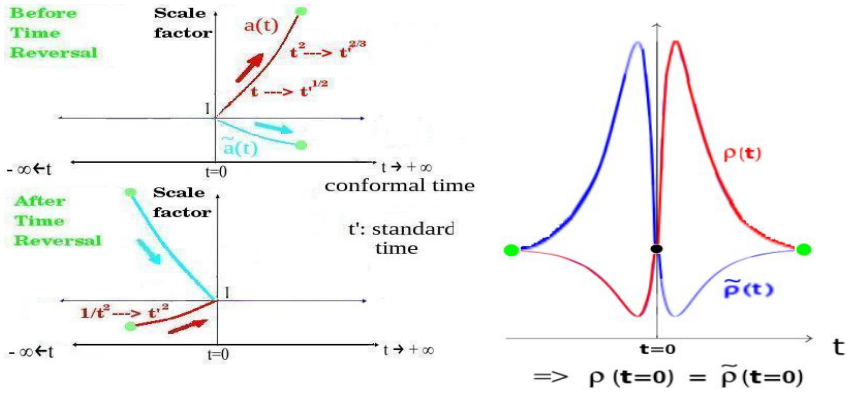

Figure 2: Evolution laws and time reversal of the conjugate universes, our side in red

3.2 A discontinuous transition triggered the acceleration of the universe

The permutation symmetry of our equations (the two sides of the Janus field play the same role in them) allows a discrete transition to take place at the time the densities of the two sides cross each other : a permutation of the scale factor values keeping the densities and Hubble rates unchanged. This permutation (at the green point depicted on figure 2) could produce the subsequent recent acceleration of the universe. Specifically, just before the transition we have for instance: $a^4(\rho - 3p) >> \tilde{a}^4(\tilde{\rho} - 3\tilde{p})$ just because $a(t) >> \tilde{a}(t)$ and $\rho - 3p \approx \tilde{\rho} - 3\tilde{p}$ resulting in the usual (as in GR) expansion laws whereas just after the transition, $a^4(\rho - 3p) << \tilde{a}^4(\tilde{\rho} - 3\tilde{p})$ because now $a(t) << \tilde{a}(t)$ and $\rho - 3p \approx \tilde{\rho} - 3\tilde{p}$ resulting in the dark side source term now driving the evolution, producing a constant

acceleration of our side scale factor in standard time coordinate t' following the transition redshift : $a(t') \propto t'^2$.

Because our solutions turn out to satisfy the fundamental relation:

$$\tilde{a}(t) = \frac{1}{a(t)} = a(-t) \tag{10}$$

we can also interpret our permutation symmetry as a global time reversal symmetry about privileged origin of conformal time t=0. Then the evolution of both densities and scale factors are cyclic as illustrated in fig 2. This also insures the stability of our homogeneous solutions in the sense that these remain bounded and confirms that we completely avoid any singularity issue. By the way having equal initial densities is also ideal to have equal amounts of matter and anti-matter at the origin of time, but then, following the separation of the two sides, a small excess of matter on our side corresponding to the same exact small excess of anti-matter on the conjugate side. This would presumably be the origin of the baryonic asymmetry of our universe after almost complete matter anti-matter annihilation.

Gravity from sources on our side is expected to be almost switched off at the transition. This problem can be solved by considering spatial domains and discontinuities (see [1]) having far reaching consequences.

3.2.1 Confrontation with the SN, Cepheids, BAO, CMB and oldest stars data

In this section t and H now denote the standard time and Hubble rate. First noticeable is the remarkable (and not expected within LCDM) agreement between the supernovae Hubble diagram up to z=0.6 and a constantly accelerated universe [8] .ie. with $a(t) \propto t^2$ meaning a deceleration parameter q=-0.5. With the JLA sample of SN we fit α of a power law t^α evolution of the scale factor for redshifts restrained to the [0,z_{max}] interval to confirm this: $\alpha = 1.85 \pm 0.15$ for z_{max}=0.6 (one standard deviation from 2.)

The parameter which replaces the cosmological constant in our framework is merely the redshift of densities equality i.e. the transition redshift z_{tr}. So our goal is to check if there is a value of z_{tr} that can fit the main current cosmological data: CMB, the Hubble diagram of Cepheid calibrated SN, BAO and the oldest stars ages. The next step is therefore to fit the transition redshift between a fixed $t^{2/3}$ and subsequent t^2 evolution laws for the JLA SN sample, and we get: $z_{tr} = 0.67 + 0.24 - 0.12$ with a $\chi^2 = 740.8$ only slightly larger than that of the LCDM fit (739.4).

The next step is to use our Geogebra graphical tool to play with cursors and hopefully determine a z_{tr} value lying in the allowed interval according our previous SN fits, a H_0 close to the directly obtained value by Riess et all [6] (local distance ladder method through Cepheids and SN) and simultaneously allowing a good agreement to both the CMB data (angular position of first acoustic peak θ* at decoupling and comoving sound horizon r_{drag}) [7] and BAO data (H(z), $D_M(z)$) [3]. We first of course need to correct the BAO data, obtained assuming the r_{drag} of a fiducial LCDM cosmology, to adapt them to our r_{drag}. Ω_{rad} is fixed as usual from the present day photon and neutrino densities. What's new is that Ω_M is then not anymore a free parameter. Indeed, we may define $\Omega_M(z_{tr}) = \frac{8\pi G\rho_M(z_{tr})}{3H_{tr}^2} = 1 - \Omega_r(z_{tr}) \approx 1$ since, beyond the transition redshift, we are indistinguishable from a mere CDM flat cosmology without any dark energy nor cosmological constant. We can then extrapolate this to the usual present $\Omega_M = \frac{8\pi G\rho_M(0)}{3H_0^2}$ given that $\rho_M(z_{tr}) = \rho_M(0)(1+z_{tr})^3$ and $H_{tr} = H_0(1+z_{tr})^{1/2}$ for a constantly accelerated regime between z=0 and z=z_{tr}. Then, $\Omega_M = (1+z_{tr})^{-2}$.

Our attempts resulted in one of the best fits for $z_{tr} = 0.83$ (see Figure 4) for which we nevertheless cannot avoid a potential tension at the two sigma level for the lowest z D_M point (our prediction in the $D_M(z)$ plot is the red band) but we notice that this kind of tension appears almost unavoidable for any model that would fit the high H_0 value from Riess. The most likely origin of this tension is that linear regime perturbations from the contracting dark side start to grow differently than within LCDM after the transition redshift and as their gravity dominates over our side dark matter gravity,

those may deform the BAO peak in an unexpected way for those who analyze the data with LCDM as fiducial model to estimate various systematics.

The small tension in H(z=0.7) corresponding to the full shape analysis of the BAO data remains acceptable but would become more serious with the value obtained through reconstruction techniques [3] [4] [5], not only correcting various non-linear effects and reducing the errors but also assuming a growth rate of linear perturbations and correcting for redshift space distorsions (RSD) in a way which is valid for LCDM but certainly not for Dark Gravity.

The confrontation with Big Bang nucleosynthesis data is also granted to be successful given how close to the LCDM one is our H(z) at high redshift (Figure 3). Our r_d is only less than three percent lower than the LCDM one and the age of the Universe is still reasonable given the oldest stars ages (13.6 billion years) : this is because the much higher than LCDM H(z) that we have at low redshifts is compensated by a much lower H(z) than LCDM between 0.6 and 1.6 (Figure 3) : needless to say that this good property is not shared by most models trying to solve the H_0 tension with new physics at low redshifts.

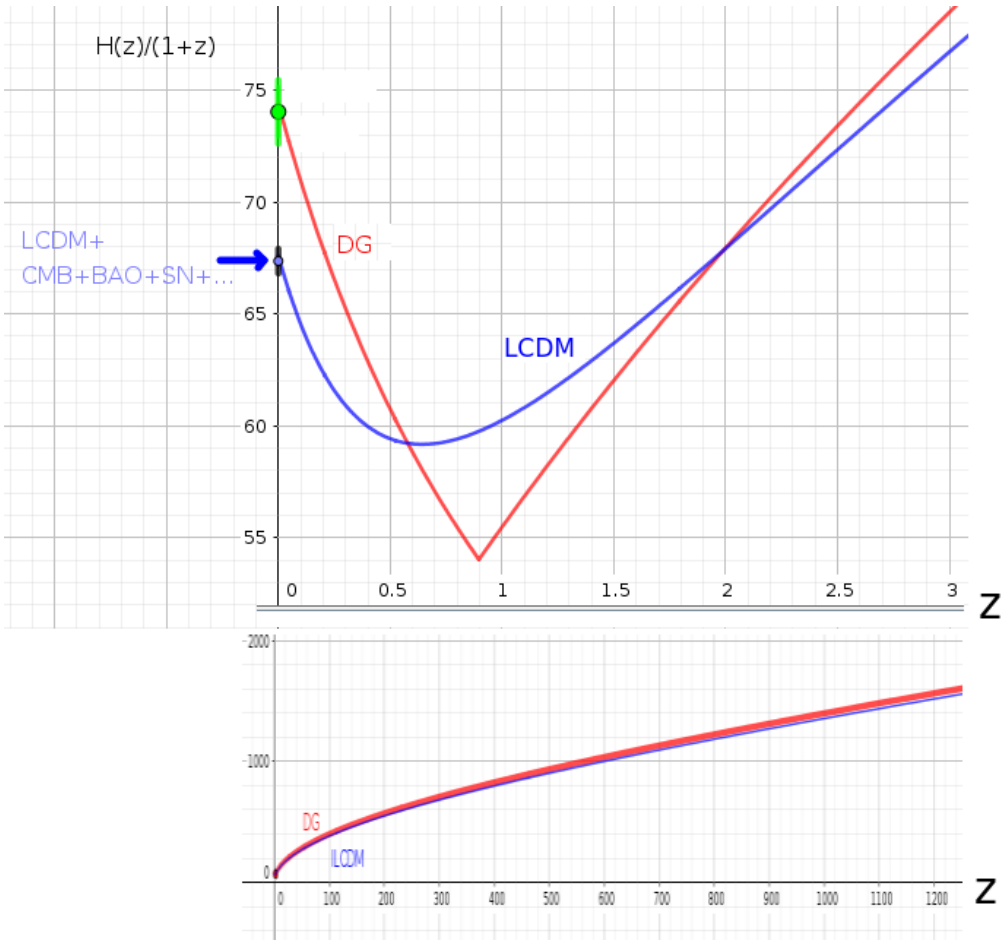

Figure 3: A transition scenario vs the LCDM best fit

Figure 4: A transition scenario confronted to CMB and BAO data, the red band is our prediction for $D_M(z)$ (bottom). The red data points in the H(z)/(1+z) plot are corrected for r_d DG cosmology and not expected to fit LCDM anymore. The green band is the allowed interval for the transition redshift (within 1 standard deviation) according our SN Hubble diagram fit

4 Conclusions

In contrast to a cosmological constant which just corresponds to one theoretical possibility out of a myriad of other terms that one could arbitrarily add either on the left or the right of the Einstein equation, everything in our framework follows from a different conceptual choice from the beginning: the existence of a non dynamical background. Our ability to solve the H_0 tension at the price of a couple of two sigma tensions with the BAO data at low z is therefore remarkable given that new systematical effects could solve such residual tensions in our case. DG also avoids singularity issues (both BH and primordial ones), explains the flatness of our universe, and is the ideal framework to understand the origin of the baryonic asymmetry and solve the old cosmological constant problem (see details in [1]).

References

[1] www.darksideofgravity.com/DG.pdf

[2] S. Pan, J. de Haro, A. Paliathanasis, R. J. Slagter (2016) arXiv:1601.03955

[3] S.Alam et all, The Completed SDSS-IV extended Baryon Oscillation Spectroscopic Survey: Cosmological Implications... arXiv:2007.08991

[4] Improving Cosmological Distance Measurements by Reconstruction of the Baryon Acoustic Peak D. J. Eisenstein , H-j Seo, E. Sirko , D. Spergel arXiv: astro-ph / 0604362

[5] N. Padmanabhan, M. White, J.D. Cohn Reconstructing Baryon Oscillations: A Lagrangian Theory Perspective arXiv:0812.2905

[6] A.G.Riess, A 2.4 percent Determination of the Local Value of the Hubble Constant,arXiv:1604.01424

[7] Planck collaboration, Planck 2018 results. VI. Cosmological parameters arXiv:1807.06209

[8] F. Henry-couannier, C. Tao, A. Tilquin, Negative Energies and a Constantly Accelerating Flat Universe arXiv:gr-qc/0507065

Constraints on neutrino masses from cosmological observations

Bruce Hoeneisen

e-mail: bhoeneisen@usfq.edu.ec

Universidad San Francisco de Quito

Presented at the 3rd World Summit on Exploring the Dark Side of the Universe
Guadeloupe Islands, March 9-13 2020

Abstract

I present an overview of studies that lead to a measurement of the sum of masses of the three neutrino flavors using cosmological observations. The result is $\sum m_\nu = 0.27 \pm 0.08$ eV for $h = 0.6990 \pm 0.0030$. The correlation between these two parameters is $h + 0.020 \sum m_\nu = 0.7038 \pm 0.0060$.

1 Introduction

At the 2020 Guadeloupe conference I presented an overview of several studies of neutrino masses published in references [1], [2], and [3]. We measure the sum of the masses of the three neutrino flavors $\sum m_\nu$. The measurement is illustrated in Figure 2. Shown is the power spectrum of linear density perturbations $P(k)$ for $\sum m_\nu = 0$ and $\sum m_\nu = 0.6$ eV, multiplied by a bias factor, compared to the galaxy power spectrum $P_{\text{gal}}(k)$ [4]. k is the comoving wavenumber. The power spectrum depends on 5 independent cosmological parameters [2] [5] [6]: Ω_m, h, n_s, $\sum m_\nu$, and the amplitude $N^2 \equiv A_s/(4\pi) \equiv \Delta^2_R/(4\pi)$. (We use the standard notation in cosmology as defined in [7].) We treat Ω_r as a dependent parameter: it depends on h, and has contributions from photons and neutrinos. So we need at least 5 measurements to obtain $\sum m_\nu$.

The measurements, used in various combinations, are: (1) The Sachs-Wolfe effect, that constrains $P(k)$ in the range $-3.1 \lesssim \log_{10}(k/h\,\text{Mpc}^{-1}) \lesssim -2.7$, from the COBE mission, and the Planck experiment. (2) σ_8, that constrains $P(k)$ in the range $-1.3 \lesssim \log_{10}(k/h\,\text{Mpc}^{-1}) \lesssim -0.6$, measured with gravitational lensing, and with galaxy clusters. (3) A measurement of Ω_m with Baryon Acoustic Oscillations (BAO) (used as an uncalibrated standard ruler), and the sound horizon angle θ_* obtained by the Planck collaboration. (4) A constraint between h, Ω_m, and $\sum m_\nu$ obtained with BAO (used as a calibrated standard ruler), and θ_*. (5) A combination of Ω_m from BAO, with the Planck global fit, to be described in Section 2. (6) The galaxy power spectrum measured by the BOSS colaboration. (7) Measurements of $P_{\text{gal}}(k)$ at four values of k. To use the measurements of $P_{\text{gal}}(k)$ we need to introduce two new parameters: a bias factor, and its slope.

2 Combination of Baryon Acoustic Oscillation and Planck data

We measure Ω_m with BAO used as an uncalibrated standard ruler (with Sloan Digital Sky Survey SDSS DR14 data [8, 9]), and the sound horizon angle θ_* from the Planck analysis [3]. Assuming $\Omega_k = 0$, and Ω_Λ independent of the expansion parameter a (assumptions that are consistent with

Figure 1: Guadeloupe Islands.

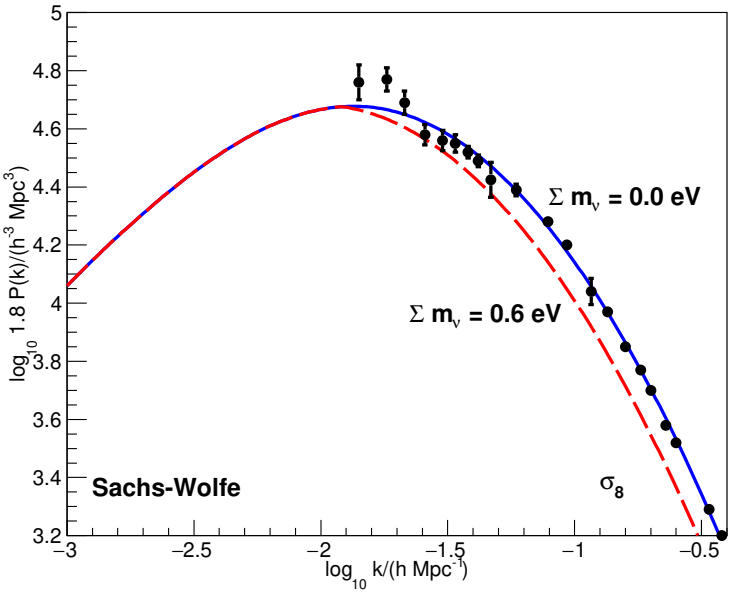

Figure 2: Comparison of $P_{\rm gal}(k)$ obtained from the SDSS-III BOSS survey [4] ("reconstructed") with $b^2P(k)$ for $\sum m_\nu = 0$ eV. Also shown for comparison is the curve with the same parameters, except $\sum m_\nu = 0.6$ eV.

data [10]), we obtain $\Omega_m = 0.2724 \pm 0.0047$ [3]. This result is independent of any other cosmological parameter. This measurement of Ω_m has a 4.9 σ tension with the Planck analysis.

We embark on a study of the Cosmic Microwave Background fluctuation spectra, and find that a 10% shift in Ω_m results in a 0.11% root-mean-square deviation of the CMB spectra relative to the first acoustic peak, see Figure 3. So the Planck analysis can benefit with a combination with Ω_m from BAO. The combination, obtained with the "base_mnu_plikHM_TTTEEE_lowTEB_lensing_*.txt MC chains", made public by the Planck Collaboration [11], is presented in Table 1. This combination is preliminary due to the sparseness of the MC chains at low values of Ω_m.

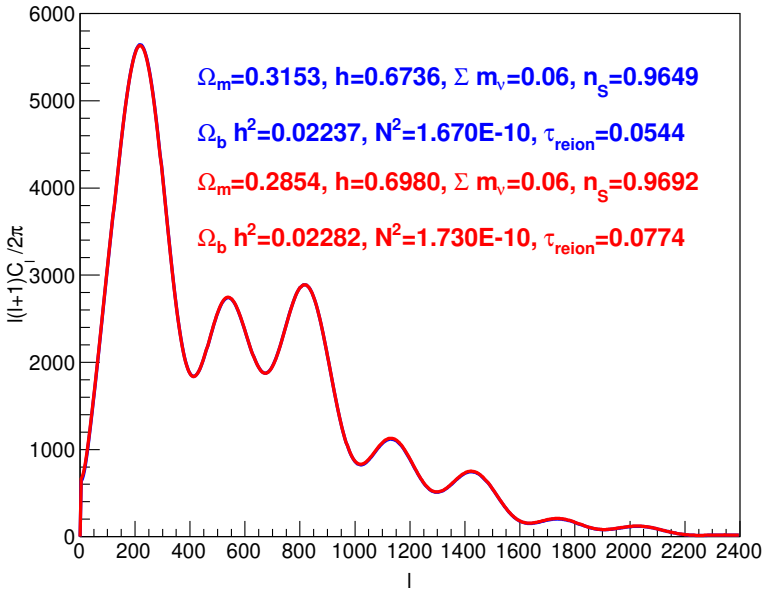

Figure 3: Comparison of the power spectra $l(l+1)C^S_{TT,l}/(2\pi)$ $[\mu\text{K}^2]$ for the Planck 2018 "TT,TE,EE+lowE+lensing" parameters, with the best fit spectra with $\Omega_m = 0.2854$ and $\sum m_\nu = 0.06$ eV fixed, calculated with the approximate Equation (7.2.41) of [5] (modified to include $\sum m_\nu$). The r.m.s. difference is $6.07\mu\text{K}^2$, corresponding to 0.11% of the first acoustic peak, so the two spectra can not be distinguished by eye.

Note that this combination raises the Planck χ^2 from 12956.78 to 12968.64, while it lowers the Planck+Ω_m combination χ^2 from 13040.09 to 12976.17. Note that the combination obtains $\Omega_m = 0.2853 \pm 0.0040$, and $h = 0.6990 \pm 0.0030$.

We quote from Reference [3]: "We consider four direct measurements: (i) $h = 0.7348 \pm 0.0166$ by the Sh$_0$es Team [12], (ii) $\sigma_8 \approx [0.746 \pm 0.012\text{ (stat)} \pm 0.022\text{ (syst)}]\,(0.3/\Omega_m)^{0.47}$ from the abundance of rich galaxy clusters [7, 13], (iii) $\sigma_8 \approx [0.745 \pm 0.039]\,(0.3/\Omega_m)^{0.5}$ from weak gravitational lensing [7, 14], and (iv) $\Omega_m = 0.2724 \pm 0.0047$ from galaxy BAO and θ_* from Planck, this analysis. Comparing these measurements with Planck (left hand column of Table 1) we obtain differences of 3.5σ, 2.5σ, 1.8σ, and 4.9σ, respectively. Comparing these measurements with the Planck+Ω_m combination (right hand column of Table 1) we obtain differences of 2.1σ, 2.3σ, 1.5σ, and 2.1σ, respectively. In conclusion, the Planck+Ω_m combination reduces the tensions with the direct measurements, including h, leaving no significant anomalies. Note that the Planck+Ω_m combination has σ_8 greater than the direct measurements. This 2.7σ tension may be due to neutrino masses."

3 Results

The final measurement of $\sum m_\nu$ is obtained by fitting 6 parameters to minimize a χ^2 with 8 terms. The 6 fitted parameters are $\sum m_\nu$, N^2, h, n_s, and the $P_{\text{gal}}(k)$ bias and slope. The 8 terms of the χ^2 are $N^2 = (2.08 \pm 0.33) \times 10^{-10}$, $h = 0.6990 \pm 0.0030$, and $n_s = 0.9726 \pm 0.0017$ from the Ω_m+Planck combination, σ_8 from a combination of gravitational lensing [7, 14] and galaxy cluster [7, 13] measurements, and 4 measurements of $P_{\text{gal}}(k)$. This fit has no significant pulls. The calibrated BAO measurement

	Planck	Planck+Ω_m
$\Omega_b h^2$	0.02237 ± 0.00015	0.02265 ± 0.00012
$\Omega_c h^2$	0.1200 ± 0.0012	0.1155 ± 0.0005
$100\theta_*$	1.04092 ± 0.00031	1.04125 ± 0.00022
τ	0.0544 ± 0.0073	0.078 ± 0.006
$\ln 10^{10} A_s$	3.044 ± 0.014	3.102 ± 0.020
n_s	0.9649 ± 0.0042	0.9726 ± 0.0017
Ω_Λ	0.6847 ± 0.0073	0.7147 ± 0.0040
Ω_m	0.3153 ± 0.0073	0.2853 ± 0.0040
h	0.6736 ± 0.0054	0.6990 ± 0.0030
σ_8	0.8111 ± 0.0060	0.8346 ± 0.0054
$\chi^2_{\rm P}$	12956.78	12968.64
$\chi^2_{\rm G}$	83.31	7.53
$\chi^2_{\rm tot}$	13040.09	12976.17

Table 1: Combination of the Planck 2018 "TT,TE,EE+lowE+lensing" analysis [11] with the directly measured $\Omega_m = 0.2724 \pm 0.0047$ [3]. Uncertainties are at 68% confidence. The Planck $\chi^2_{\rm P} \equiv -2 \cdot \ln \mathcal{L}$ increases from 12956.78 to 12968.64 with this combination. The galaxy $\chi^2_{\rm G} \equiv (\Omega_m - 0.2724)^2/0.0047^2$. Preliminary.

combined with the acoustic angular scale θ_* obtains the following constraint [3] [7]:

$$\begin{aligned} \theta_* &\equiv \frac{d_*}{\chi(z_*)} = 0.0104092 \pm 0.0000031 \\ &= 0.010427 \left(\frac{h + 0.020 \sum m_\nu}{0.70}\right)^{0.503} \times \left(\frac{\Omega_m}{0.28}\right)^{0.156} \left(\frac{0.0225}{\Omega_b h^2}\right)^{0.097}, \end{aligned} \tag{1}$$

with $\Omega_b h^2 = 0.02265 \pm 0.00012$ [7]. σ_8 is obtained from the combination of $\sigma_8 \approx [0.746 \pm 0.012\ (\text{stat}) \pm 0.022\ (\text{syst})]\,(0.3/\Omega_m)^{0.47}$ from the abundance of rich galaxy clusters [7, 13], and $\sigma_8 \approx [0.745 \pm 0.039]\,(0.3/\Omega_m)^{0.5}$ from weak gravitational lensing [7, 14], with Ω_m obtained from the constraint (1).

The final fit obtains

$$\sum m_\nu = 0.27 \pm 0.08\ \text{eV}, \tag{2}$$

with $\chi^2 = 1.6$ for two degrees of freedom. The correlation between h and $\sum m_\nu$ is [3]

$$h + 0.020 \sum m_\nu = 0.7038 \pm 0.0060. \tag{3}$$

Acknowledgements

I thank Pierre Petroff and the sponsors for a most interesting and dramatic meeting: not easy getting back home with the world falling apart!

References

[1] Hoeneisen, B. (2018) Constraints on Neutrino Masses from Baryon Acoustic Oscillation Measurements. *International Journal of Astronomy and Astrophysics*, 8, 1-5. https://doi.org/10.4236/ijaa.2018.81001

[2] B. Hoeneisen (2018) Study of Galaxy Distributions with SDSS DR14 Data and Measurement of Neutrino Masses. *International Journal of Astronomy and Astrophysics*, 8, 230-257, 2018. https://doi.org/10.4236/ijaa.2018.83017

[3] Hoeneisen, B.(2018) Measurements of the Cosmological Parameters Ω_m and H_0. *International Journal of Astronomy and Astrophysics*, 8, 386-405. https://doi.org/10.4236/ijaa.2018.84027

[4] Anderson, L. *et al.* (2012) The clustering of galaxies in the SDSS-III Baryon Oscillation Spectroscopic Survey: baryon acoustic oscillations in the Data Release 9 spectroscopic galaxy sample. MNRAS **427**, 3435.

[5] Steven Weinberg, Cosmology, Oxford University Press, 2008.

[6] Lesgourgues, J., and Pastor, S. (2006) Massive neutrinos and cosmology. *Phys. Rep.* 429, 307.

[7] Tanabashi, M. *et al.* (Particle Data Group) (2018), The Review of Particle Physics, *Phys. Rev. D 98*, 030001.

[8] Blanton, M.R. *et al.*, Sloan Digital Sky Survey IV: Mapping the Milky Way, Nearby Galaxies, and the Distant Universe, The Astronomical Journal, Volume 154, Issue 1, article id. 28, 35 pp. (2017)

[9] Dawson, K.S., *et al.*, The Baryon Oscillation Spectroscopic Survey of SDSS-III, The Astronomical Journal, Volume 145, Issue 1, article id. 10, 41 pp. (2013)

[10] Hoeneisen, B. (2017) Study of Baryon Acoustic Oscillations with SDSS DR13 Data and Measurements of Ω_k and $\Omega_{\text{de}}(a)$. *International Journal of Astronomy and Astrophysics*, 7, 11-27. https://doi.org/10.4236/ijaa.2017.71002

[11] Planck Collaboration: Aghanim, N. *et al.* (2018) Planck 2018 results. VI. Cosmological parameters, arXiv:1807.06209.

[12] Riess, A. G., Casertano, S., Yuan W., *et al.* (2018) New Parallaxes of Galactic Cepheids from Spatially Scanning the Hubble Space Telescope: Implications for the Hubble Constant, *ApJ*, 861, 126. arXiv:1801.01120.

[13] Vikhlinin, A. *et al.* (2009) Chandra Cluster Cosmology Project III: Cosmological Parameter Constraints, *Astrophys. J.* 692, 1060.

[14] Hildebrandt, H. *et al.* (2017) KiDS-450: cosmological parameter constraints from tomographic weak gravitational lensing, *Mon. Not. R. Astron.* Soc 465, 1454.

Neutrinoless Double Beta Decay Status and Prospects

Kota Ueshima

e-mail: ueshima@awa.tohoku.ac.jp

RCNS Tohoku University

Presented at the 3rd World Summit on Exploring the Dark Side of the Universe
Guadeloupe Islands, March 9-13 2020

Abstract

It is very important problem in physics whether neutrino is Dirac or Majorana particles. If neutrinos are Majorana particle, the neutrinoless double beta decay ($0\nu2\beta$) may occur. It is very big impact on particle physics such as effective neutrino mass and mass hierarchy determination. In addition $0\nu2\beta$ mode is lepton number violation process. The current status of $0\nu2\beta$ search experiment was presented.

1 Introduction

By the discovery of the atmospheric neutrino oscillation [1], it was found that the neutrino had finite mass. However, the neutrino mass scale is still not understood. If $0\nu2\beta$ signal is observed, there are very important impacts for particle physics, such as the effective neutrino mass, mass hierarchy determination and evidence of Majorana particle. In addition, the $0\nu2\beta$ is a lepton number violating process. There are many $0\nu2\beta$ search experiments in the world using various detectors and BG reduction techniques. $0\nu2\beta$ signal is very rare events. The current limit of $0\nu2\beta$ half life is more than 10^{26} year [2]. In addition, the tail events of normal two neutrino emitted double beta decay ($2\nu2\beta$) events became BG of $0\nu2\beta$ signal. So $0\nu2\beta$ search experiment is required ultra low BG detector with high energy resolution.

2 Current status

The current status of the $0\nu2\beta$ search experiments is listed Table1. There are many current running or proposed experiments for $0\nu2\beta$ search to reduce BG and achieve high energy resolution at signal region. I categorized 5 types of $0\nu2\beta$ search experiment based on BG reduction technique, such as LS based detector, Xe TPC, Bolometer, Tracking and Germanium detector.

KamLAND-Zen and SNO+ experiment reuse large neutrino detector. Xenon or Tellurium loaded Liquid Scintillator (LS) is feed into the detector. KamLAND-Zen experiment was used 1 kton liquid scintillator detector to achieve ultra low BG environment. The current main BGs of $0\nu2\beta$ search in the KamLAND-Zen experiment [2] are ^{214}Bi, ^{10}C and $2\nu2\beta$ tail events. Usually ^{214}Bi events are tagged using Bi-Po continuum decay. However, in case that the α-particle emitted by the ^{214}Po decay stops in the mini-balloon film which is a dead region for the energy deposition by radiation, the ^{214}Bi events become BG for the $0\nu2\beta$ search. They plan to make new mini-balloon using thin scintillation film. There is no dead region for the energy deposition by radiation. Therefore, the ^{214}Bi events are reduced by the tagging of Bi-Po continuum decay.

Experiment	Isotope	Exposure (kg yr)	$T_{1/2}$limit (x10^{25}yr) 90% C.L.	mass limit (meV)	Ref
KamLAND-Zen	^{136}Xe	504	10.7	61 - 165	[2]
EXO-200	^{136}Xe	234.1	3.5	93 - 286	[3]
GERDA	^{76}Ge	53.9	9.0	104 - 228	[4]
Majorana demo.	^{76}Ge	26	2.7	200 - 433	[5]
CUORE	^{130}Te	372.5	3.2	75 - 350	[6]
CUPID-0	^{82}Se	5.29	0.35	311 - 638	[7]

Table 1: Current running or concluded $0\nu2\beta$ search experiment

SNO+ experiment use Tellurium loaded liquid scintillator. The concentration of Tellurium in LS is 0.5% for 1st phase. The LS filling was started in last year. The Tellurium plants commissioning is started. They estimates the main BG is 8B solar neutrino. Target sensitivity is 1.9×10^{26} yr for 5 yr data taking.

EXO-200 experiment used liquid xenon time projection chamber (TPC) detector. Using event multiplicity to recognize the dominant gamma ray BG, the gamma ray BG was rejected. The data taking started in 2011 as a phase I. After electronics upgrade and Rn reduction, the phase 2 started in 2016. In Dec.2018 the EXO-200 data taking was finished. The main BGs are ^{214}Bi and ^{208}Tl. Total exposure is 234 kg yr. $0\nu2\beta$ half life limit is more than 3.5×10^{25} yr. EXO collaboration plan to upgrade liquid xenon TPC detector toward ton scale detector. The nEXO detector will be constructed in SNOLAB. The mass of enriched Xenon is 5 ton and the sensitivity reached to 9.2×10^{27} yr [8].

NEXT experiment is high pressure xenon gas TPC detector. Current NEXT-white phase is running to demonstrate the energy resolution at Q value and the topological BG reduction. $0\nu2\beta$ signal has two blobs at endpoints. On the other hand BGs like gamma ray and single beta is only one blob. They achieved 1% (FWHM) energy resolution at 2.6MeV [9]. Ton scale detector sensitivity reach more than 1×10^{27} yr for 3 years data taking.

CUORE experiment use 988 Tellurium oxide crystals. The CUORE detector is bolometer detector. The operation temperature is 10mK. The thermal signal is detected. There were many BGs near signal region. The dominant BG is alpha particles from the surface of crystal.

CUPID experiment is upgrade program of CUORE with particle identification. In addition the thermal signal, they detect light signal. Using pulse shape of the light signal, the alpha BG could be reduced drastically. Zinc Selenium crystal was used to demonstrate Scintillating bolometer technique.

GERDA and Majorana experiments used high purity Germanium detector GERDA experiment achieved BG free $0\nu2\beta$ search. The energy resolution of Germanium detector is 3 keV at Q value. Majorana demo used 44.1kg Germanium detector. The Germanium detector is point contact detector. Many gamma ray BGs was reduced using pulse shape information. LEGEND is upgrade program of GERDA and MAJORANA experiment. LEGEND plant to construct ton scale Germanium detector array. The 3 sigma discovery potential reach 1×10^{28} yr.

3 Conclusions

The current status of the effective neutrino mass limit is near the Inverted Hierarchy region. There are many proposed experiments to fully covered the Inverted Hierarchy region. If the effective neutrino mass sensitivity reach 15 meV, the half of Normal Hierarchy region is covered.

References

[1] Y. Fukuda, T. Hayakawa, E. Ichihara, K. Inoue, K. Ishihara, H. Ishino, Y. Itow, T. Kajita, J. Kameda, S. Kasuga, et al., *Evidence for oscillation of atmospheric neutrinos*, *Physical Review Letters* **81** (1998), no. 8 1562.

[2] A. Gando, Y. Gando, T. Hachiya, A. Hayashi, S. Hayashida, H. Ikeda, K. Inoue, K. Ishidoshiro, Y. Karino, M. Koga, et al., *Search for majorana neutrinos near the inverted mass hierarchy region with kamland-zen*, *Physical review letters* **117** (2016), no. 8 082503.

[3] G. Anton, I. Badhrees, P. Barbeau, D. Beck, V. Belov, T. Bhatta, M. Breidenbach, T. Brunner, G. Cao, W. Cen, et al., *Search for neutrinoless double-β decay with the complete exo-200 dataset*, *Physical review letters* **123** (2019), no. 16 161802.

[4] M. Agostini, A. Bakalyarov, M. Balata, I. Barabanov, L. Baudis, C. Bauer, E. Bellotti, S. Belogurov, A. Bettini, L. Bezrukov, et al., *Probing majorana neutrinos with double-β decay*, *Science* **365** (2019), no. 6460 1445–1448.

[5] S. Alvis, I. Arnquist, F. Avignone III, A. Barabash, C. Barton, V. Basu, F. Bertrand, B. Bos, M. Busch, M. Buuck, et al., *Search for neutrinoless double-β decay in ge 76 with 26 kg yr of exposure from the m ajorana d emonstrator*, *Physical Review C* **100** (2019), no. 2 025501.

[6] D. Adams, C. Alduino, K. Alfonso, F. Avignone III, O. Azzolini, G. Bari, F. Bellini, G. Benato, M. Biassoni, A. Branca, et al., *Improved limit on neutrinoless double-beta decay in te 130 with cuore*, *Physical Review Letters* **124** (2020), no. 12 122501.

[7] O. Azzolini, J. Beeman, F. Bellini, M. Beretta, M. Biassoni, C. Brofferio, C. Bucci, S. Capelli, L. Cardani, P. Carniti, et al., *Final result of cupid-0 phase-i in the search for the se 82 neutrinoless double-β decay*, *Physical Review Letters* **123** (2019), no. 3 032501.

[8] J. Albert, G. Anton, I. Arnquist, I. Badhrees, P. Barbeau, D. Beck, V. Belov, F. Bourque, J. Brodsky, E. Brown, et al., *Sensitivity and discovery potential of the proposed nexo experiment to neutrinoless double-β decay*, *Physical Review C* **97** (2018), no. 6 065503.

[9] J. Renner, G. D. López, P. Ferrario, J. H. Morata, M. Kekic, G. Martínez-Lema, F. Monrabal, J. J. Gómez-Cadenas, C. Adams, V. Álvarez, et al., *Energy calibration of the next-white detector with 1% resolution near $Q_{\beta\beta}$ of ^{136}Xe*, *Journal of High Energy Physics* **2019** (2019), no. 10 230.

Experimental Status of Coherent Neutrino Scattering and the NUCLEUS Experiment

Thierry Lasserre

e-mail: thierry.lasserre@cea.fr

IRFU (DPhP & APC), CEA, Université Paris-Saclay, 91191 Gif-sur-Yvette, France

Presented at the 3rd World Summit on Exploring the Dark Side of the Universe
Guadeloupe Islands, March 9-13 2020

Abstract

Neutrino nucleus coherent elastic scattering is a process involving the neutral current scattering of a neutrino with an entire nucleus. We introduce the experimental discovery of this process next to a neutron spallation facility and describe the prospect for detecting low-energy neutrinos with the NUCLEUS cyogenic experiment that will be deployed at the Chooz nuclear power station in France.

1 Introduction

Low energy neutrino detection (of less than 50 MeV) usually requires large detectors if the source is not in very close proximity. However, the Standard Model of Particle Physics predicts that a particular interaction of neutrinos with atomic nuclei, called coherent elastic scattering (CENS), occurs with a relatively high probability, and could be used to significantly reduce the size of neutrino detectors. This reduction in detector size is possible because the probability of neutrinos interacting via this process is increased by a factor that varies as the number of neutrons in the target nuclei squared, which is considerable in the case of a high atomic number target such as tungsten, for instance. The probability of interaction can thus exceed by more than two orders of magnitude that of standard neutrino detection methods, such as inverse beta decay (IBD), which is by far the most widely used method for measuring reactor neutrinos to date. However, despite the increased probability of interaction, the experimental signature, i.e. nuclear recoil, is at the same time attenuated in proportion to the mass of the target nucleus. This ambivalence imposes strict optimizations of the detection systems, and call for the usage of cryogenic detectors for detecting reactor neutrinos.

In 2017, the COHERENT collaboration [1] made the first observation of coherent neutrino scattering using a sodium-doped cesium-iodine scintillator exposed to neutrinos from a spallation neutron facility at the U.S. National Laboratory in Oak Ridge. This is a significant breakthrough in fundamental physics since the coherent elastic scattering of neutrinos has been undetected for four decades! This delay was due to the difficulty of detecting the low energy (below keV) nuclear recoil produced as a unique result of the interaction while reducing background noise.

Since the first experimental detection of coherent scattering in 2017, fundamental research in this field has become more popular internationally. Indeed, this new detection channel may allow major advances in the understanding of neutrinos, and has the potential to discover new physics beyond the standard model. The scientific community involved is therefore growing and a wide range of experimental projects using various techniques is being developed.

2 Coherent Neutrino Scattering on Nuclei (CEvNS)

CEvNS is a neutral current interaction, so all neutrino flavors will participate with the same cross section. Since its original proposal in 1974 [2], the Coherent Neutrino Scattering on Nuclei (CEvNS) has attracted increasing attention in the field of particle physics.

The coherence condition is generally met for neutrinos with an energy below 100 MeV. In this energy range, coherent neutrino scattering on neutrino nuclei has a large effective cross-section on neutron-rich targets compared to other common detection channels such as inverse beta decay (IBD) and electron scattering of neutrinos. After the interaction, it is not possible to see the neutrino, but it is possible to detect the small nucleus recoil. Considering neutrinos from spallation neutron facility the relevant recoils are in the sub-keV range. But for reactor neutrinos these recoils drop to the few tens of electron-volt.

The physical implications are vast. This technique could allow to study non-standard neutrino interactions, to search for sterile neutrinos, to constrain the nucleon structure, and to better understand the ultimate backgrounds of direct dark matter experiments (called the <eutrino floor).

3 Experimental Discovery in 2017

In 2017, using 15 months of data collection time, the COHERENT experiment [1] observed for the first time the process of coherent elastic scattering of neutrinos at a confidence level of 6.7σ using a 14.6 kg CsI scintillator doped with sodium and exposed to neutrinos from a spallation neutron facility located at the U.S. National Laboratory in Oak Ridge.

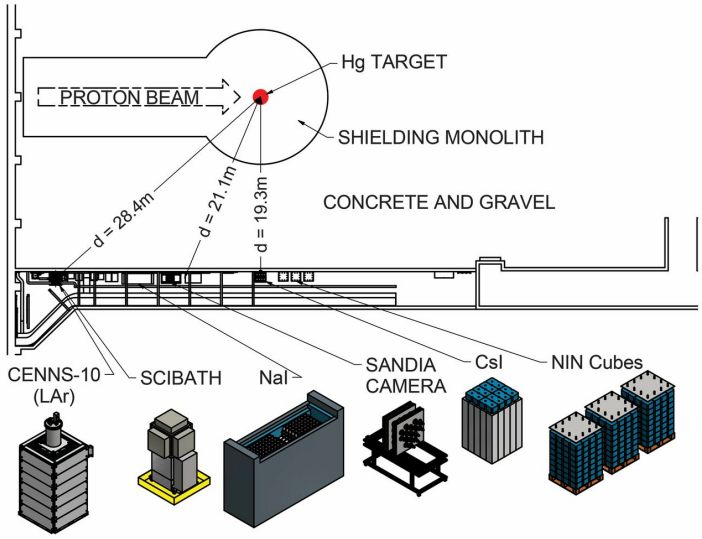

Figure 1: Detectors from the COHERENT experiment located at the Oak Ridge spallation source (US). The experimental sites, located in a basement corridor, benefit from a shielding of more than 19 m against neutrons associated to the beam, and a modest overburden of 8 m thick concrete to reduce cosmic ray induced backgrounds (adapted from [1]).

The COHERENT experiment is set up in a basement corridor benefiting from more than 19 m of shielding against neutrons associated to the proton beam and a modest vertical overburden of 8 meter water equivalent, capable of reducing the background noise induced by cosmic radiation (see figure 1).

Moreover, this spallation source is pulsed, which has been a valuable asset for this first detection.

By comparing the CsI [Na] signals occurring before the neutrino emission and those occurring immediately after, an excess is visible both in the energy spectrum and in the distribution of signal arrival times (see figure 2). The agreement with the predictions of the standard model is excellent even if the measurement uncertainties are still relatively high: 134 ± 22 observed events for 173 ± 48 expected [1].

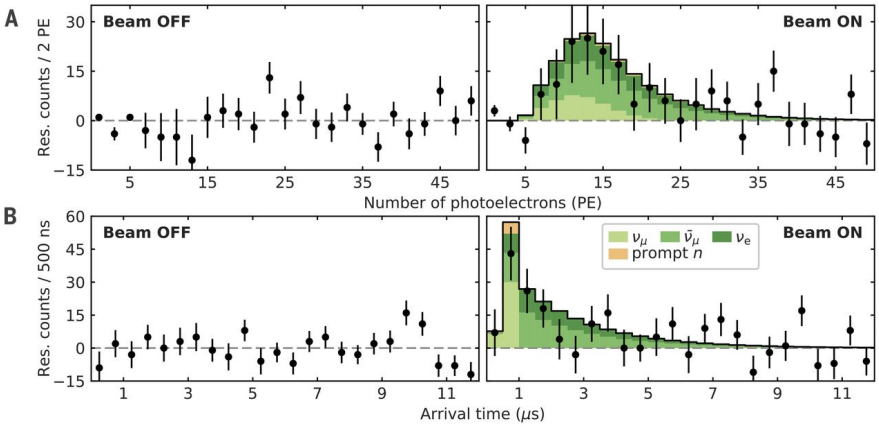

Figure 2: First observation of the coherent elastic neutrino scattering of neutrinos on nuclei. Residual differences (datapoints) between the CsI [Na] signals and the next/previous 12 µs-POT trigger events are indicated according to their energy (A) and the arrival time of the event (B). Error bars are statistical. They are shown for 153.5 actual days of SNS inactivity ("Beam OFF") and 308.1 actual days of neutrino production ("Beam ON"), during which 7.48 GWh of energy was supplied to the mercury target. About 1.17 photoelectrons per keV of nuclear energy from CsI [Na] recoil are expected. Characteristic excesses closely following the prediction of the standard model (histograms) are observed for periods of neutrino production only, with a rate correlated to the instantaneous beam power (adapted from [1]).

4 Search for Coherent Neutrino Scattering at Nuclear Reactors

The coherent neutrino scattering process was observed for the first time in 2017 at a spallation source emitting neutrinos of a few tens of million electron volts (MeV). At these energies, the recoils of the detected atomic nuclei are of the order of kilo-electron-volt (keV). Contrary to reactor neutrinos, the neutrinos produced at the spallation lead to a partial coherence of the interaction . An enhanced coherence is expected in the case of reactor neutrinos.

Nuclear reactors deliver large flux of neutrinos with typical energies of a few MeV, about ten times lower than a neutrino spallation source, leading therefore to nuclear recoil at least ten times lower and then much more difficult to detect with certainty. Thus, the first crucial step lies in the detection of reactor neutrinos by the process of coherent diffusion on atomic nuclei.

This is already a well identified short-term objective in fundamental research prospects, with for example the NUCLEUS, Ricochet Billard:2016giu, or CONUS [3] experiments that are currently being designed, built, or collecting data. It is reasonable to think that this crucial step could be achieved within the next 5 years.

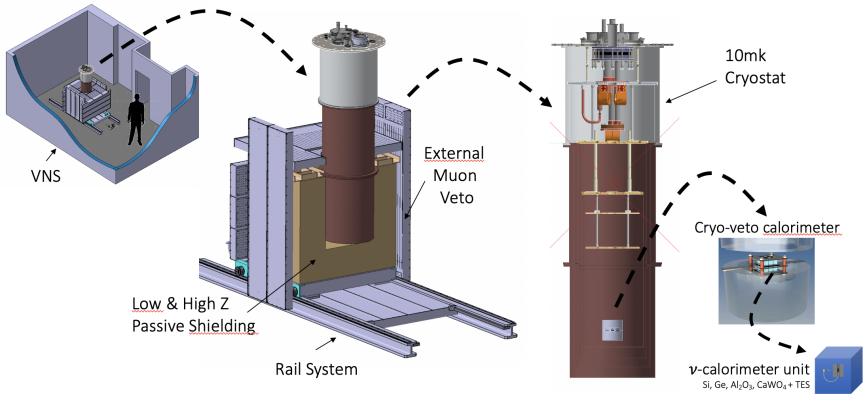

Figure 3: Sketch of the NUCLEUS cryogenic detector that will be located at the Very Near Site inside the Chooz nuclear power station (France).

5 The NUCLEUS experiment

NUCLEUS [4] is a new-generation experiment dedicated to the detection and study of the process of coherent elastic scattering of neutrinos emitted by nuclear reactors.

The Chooz nuclear power plant in France offers an ideal setting for the first detection of the CEvNS process with low energy neutrinos. The complex comprises two commercial nuclear reactors with a combined thermal power of 8.54 GW. The NUCLEUS experiment will be installed at a new experimental site, called Very-Near-Site (VNS),located right between the two 4.25 GWth reactor cores, separated by 160 meters.

This project brings together a European consortium of physicists, engineers and technicians from Austria, France, Germany, and Italy. It should be recalled here that the detection of reactor neutrinos using this process has never yet been established. With the primary objective of demonstrating the coherent scattering of reactor neutrinos, the NUCLEUS experiment will use an array of tiny cryogenic detectors that are characterized by a particularly low threshold (20 eV) for detecting nuclear recoils and a fast response time (ms), requested for operating the detector close to the surface (i.e. with an overburden of less than ten meter water equivalent).

NUCLEUS will use cryogenic calorimeter technology that measures the temperature rise following the deposition of energy in a target. The technological breakthrough envisaged is to reduce the detection threshold to less than 20 electron volts in order to further miniaturize the fiduciary volume of the experiment. The main target material will be $CaWO_4$, a scintillating bolometric crystal developed in the framework of the CRESST dark matter research experiment. The effective cross section on heavy nuclei such as tungsten, as well as the envisaged detection threshold of 20 eV, increase the signal proportion compared to the background noise that must remain sufficiently low in the target detector. The NUCLEUS target detectors are installed in a cryostat. The experimental volume is surrounded by shielding for active and passive background noise reduction. The physics reach of NUCLEUS will depend strongly on the background level reached at sub-keV energies. By using active and passive background reduction techniques, the NUCLEUS experiment aims to achieve a background count rate of ≤ 100 counts/(keV-kg-day). One coherent neutrino scattering interaction is expected every two days. Figure 3 shows a sketch of the NUCLEUS experiment at Chooz Very Near Site.

In the first phase of the experiment, NUCLEUS-10g, the objective is the first observation of the coherent diffusion of neutrinos on a nuclear reactor with a total target mass of only 10 g! Because of its low threshold NUCLEUS could probe, for the first time, the antineutrino spectrum of the reactor below 1.8 MeV - below the generally used inverse beta decay threshold. NUCLEUS-10g will explore

this background for the first time at energies below 100 eV and at a shallow site. NUCLEUS-10g is expected to take data from 2022 onwards. A second phase, NUCLEUS-1kg will follow.

6 Conclusion and Outlook

Coherent neutrino scattering on nuclei is a new experimental process at reach. It has been detected for the first time in 2017 with neutrinos of 50 MeV by the COHERENT experiment. The NUCLEUS experiment aims to detect this process with low energy reactor neutrinos (5 MeV on average). This process will now be used by physics community to further explore non-standard interactions, to study independently the form factors of nuclear neutrons and to establish complementary limits on the Weinberg angle and sterile neutrinos. In addition, with a sufficiently low threshold, the magnetic moment of neutrinos can also be addressed. All in all, CEvNS presents interesting possibilities from a theoretical and phenomenological point of view.

Acknowledgments

I thank the organizers of the 3rd World Summit on Exploring the Dark Side of the Universe (9 to 13 March 2020) for the invitation and an excellent semi-virtual conference held in Pointe-à-Pitre, Guadeloupe.

References

[1] **COHERENT** Collaboration, D. Akimov et al., *Observation of Coherent Elastic Neutrino-Nucleus Scattering*, *Science* **357** (2017), no. 6356 1123–1126, [arXiv:1708.01294].

[2] D. Z. Freedman, *Coherent effects of a weak neutral current*, *Phys. Rev. D* **9** (Mar, 1974) 1389–1392.

[3] J. Hakenmüller et al., *Neutron-induced background in the CONUS experiment*, *Eur. Phys. J. C* **79** (2019), no. 8 699, [arXiv:1903.09269].

[4] **NUCLEUS** Collaboration, J. Rothe et al., *NUCLEUS: Exploring Coherent Neutrino-Nucleus Scattering with Cryogenic Detectors*, *J. Low Temp. Phys.* **199** (2019), no. 1-2 433–440.

Status and Prospects of eV Sterile Neutrino Searches

Ivan Martinez-Soler

e-mail: ivan.martinezsoler@northwestern.edu

Fermi National Accelerator Laboratory, Batavia, IL 60510, USA
Department of Physics & Astronomy, Northwestern University, Evanston, IL 60208, USA
Colegio de Física Fundamental e Interdisciplinaria de las Américas (COFI), 254 Norzagaray street, San Juan, Puerto Rico 00901.

Presented at the 3rd World Summit on Exploring the Dark Side of the Universe
Guadeloupe Islands, March 9-13 2020

Abstract

In this talk, we present the results of the global analysis [1] on the $3+1$ neutrino scenario. After a brief discussion of the neutrino oscillation probabilities in the presence of a sterile neutrino, we describe the main experimental results. We pay particular attention to the anomalies in the reactor neutrino experiments and the ν_e excess in the appearance channel oscillation channel. The combined analysis of the data shows some tensions between the disappearance and the appearance oscillation results.

1 Introduction

The excess of electron neutrinos observed by LSND and MiniBooNE can be explained by the oscillation of a muon neutrino into an electron neutrino driven by mass parameter $\Delta m^2_{41} \sim 1\text{eV}^2$. The combined results of both experiments show an excess significance of 6σ.

In addition to those experiments, there are some anomalies that can also be explained by the existence of a sterile neutrino with mass in the same range. This is the case of the Gallium anomaly or the Reactor anomaly. All these anomalies, that have been measured in the electron disappearance channel, consist on a deficit in the number of expected events. The survival probability of ν_e or $\overline{\nu}_e$ in the presence of a ν_s with a mass of the order of $\Delta m^2 \geq 1\text{eV}^2$ can reduce the significance of those anomalies.

Looking into the muon-disappearance channel measurements, there no evidence for such new particle. In this channel, we have contributions from MiniBooNE looking for the number of ν_μ events. Similar results were found using Long-Baseline experiments like MINOS/MINOS+ or NOνA, and atmospheric neutrinos like DeepCore or IceCube.

In this talk, we are going to describe the status of the oscillation experiments able to observe a sterile neutrino with a mass around 1 eV. In section 2, we will describe the neutrino evolution in the presence of a sterile neutrino. Using the framework, several experiments has analyzed their data, finding different results, we will describe the most relevant in section 3. Those results will be combined into a global analysis. In section 4, we will present the results of the global analysis. Finally, the conclusions of the work will be presented in section 5.

2 Scenario 3+1

In the standard neutrino picture (3 active neutrinos), the evolution is described by the Schrodinger equation that depends on two mass parameters, the difference between the mass squared of the three massive states (Δm^2_{21} and Δm^2_{31}), and the lepton mixing matrix, that correlates massive and the flavor states. The mixing matrix (U) is described by 3 rotation angles and a complex phase (θ_{12}, θ_{13}, θ_{23} and δ_{13}). If we consider the existence of a sterile neutrino, the Schrodinger equation can be written as

$$i\frac{d\vec{\nu}}{dt} = \frac{1}{2E}\left[U^{\dagger} diag(0, \Delta m^2_{21}, \Delta m^2_{31}, \Delta m^2_{41}) U \pm V_{mat}\right]\vec{\nu} \tag{1}$$

where we have included the mass difference of the new state (Δm^2_{41}). In the case of four neutrinos, U is a 4×4 complex. To parameterize the mixing matrix, we need to add three additional rotation angles and two complex, $U \equiv R(\theta_{34})\, R(\theta_{24}, \delta_{24})\, R(\theta_{14})\, R(\theta_{23})\, R(\theta_{13}, \delta_{13})\, R(\theta_{12}, \delta_{12})$. If neutrinos propagate though the matter, the coherent interaction of the neutrino with the medium will modify the neutrino evolution. That interaction is described by the potential $V_{mat} = \sqrt{2} G_F \text{diag}\,(N_e - N_n, -N_n, -N_n, 0)$ for an electrically neutral medium. N_e and N_n represent the electron and neutron densities along the neutrino path.

Solving Eq. 1 we obtain the probability that ν_α oscillate into ν_β ($P_{\alpha\beta}$) as a function of the neutrino energy and the baseline. Working in the short-baseline limit ($\Delta m^2_{21} L/4E << 1$ and $\Delta m^2_{31} L/4E << 1$), we can derive some approximated expressions for the oscillation probability, that will be very useful to analyze the results in the next section. Since all the neutrino sources that we are going to consider consist on beams of electron or muon neutrinos, we will focus mainly in the following oscillation channels

$$\begin{aligned}
P^{SBL}_{ee} &= 1 - 4|U_{e4}|^2\left(1 - |U_{e4}|^2\right)\sin^2\left(\frac{\Delta m^2_{41} L}{4E}\right) \\
P^{SBL}_{\mu e} &= 4|U_{e4}|^2|U_{\mu 4}|^2 \sin^2\left(\frac{\Delta m^2_{41} L}{4E}\right) \\
P^{SBL}_{\mu\mu} &= 1 - 4|U_{\mu 4}|^2\left(1 - |U_{\mu 4}|^2\right)\sin^2\left(\frac{\Delta m^2_{41} L}{4E}\right)
\end{aligned} \tag{2}$$

As shown by the previous equations, the different oscillation channels are not independent, they are correlated by the lepton mixing matrix. If there is an oscillation of ν_e to ν_μ that requires $|U_{e4}|^2 \neq 0$ and $|U_{\mu 4}|^2 \neq 0$, and therefore we also must observe an oscillation in the electron and muon disappearance channels.

3 Oscillation experiment results

In this section we will make a brief summary of the most relevant oscillation results for the detection of a sterile neutrino with masses around 1 eV.

In nuclear reactors, anti-electron neutrinos are created via the fission of four isotopes ^{235}U, ^{238}U, ^{239}Pu and ^{241}Pu. Theoretical evaluations of the flux [2, 3] indicate a deficit of 5% in the number of events observed, this called Reactor anomaly. For baselines larger than $L \geq 50$ m, the oscillation driven by a sterile neutrino with mass around the eV scale would be averaged out, as can be obtained from Eq. 2. That would be observed as a deficit on the flux, so it can explain the anomaly. The hypothesis of the sterile neutrino also predict that the flux created by all the isotopes should be equally affected. The yield to the neutrino flux depends on each isotope. The measurement of the fuel correlation with the $\overline{\nu}_e$ flux done by Daya-Bay [4] rejects the hypothesis of a constant neutrino flux, finding a discrepancy of 7.8% between the predicted yield for the ^{235}U. That suggests that the anomaly primarily comes from that isotope. Another present in the reactor neutrino flux is found

around $\sim$ 5 MeV, where has been observed an excess of the flux predicted over the measurements. The origin of that spectral distortion can also be the ^{235}U isotope [5].

For baselines shorter than $L \leq 20m$, the energy distortion introduced by a sterile neutrino of 1 eV on the reactor anti-neutrino flux can be detected. That is the goal of the experiment DANSS [6], a movable detector that measures the reactor neutrino flux between $\sim$ 10 m and $\sim$ 12.7 m from the reactor core. Another experiment that could also measure that oscillation is NEOS [7], placed $\sim$ 23 m from the core. Both experiments have observed an oscillation that is compatible with an eV sterile neutrino. The latest results from DANSS [6] shows some disagreement in the allowed regions.

In the Sun, ν_e are created via nuclear fusion reactions in an energy range that extend up to $\sim$ 20 MeV. That flux was measured by experiments that used Gallium as a target, like GALLEX and SAGE. In those experiments, electron neutrinos are absorbed by the Gallium creating Germanium and an electron. In both experiments, the detector response was tested using a radioactive source (^{51}Cr, ^{37}Ar). The results showed a 15% deficit in the expected signal, that corresponds to a 3σ [8] of significance the measurement uncertainties. This Gallium anomaly can be explained with a sterile neutrino [9] with mass larger or equal to 0.1 eV. New evaluations of the cross-section [10] has reduced the anomaly significance to $\sim 2.3\sigma$.

LSND is a beam dump experiment that searched for $\overline{\nu}_\mu \rightarrow \overline{\nu}_e$ from the μ^+ decay at rest [11] (DAR). Using the ν_μ flux originated by π^+ decay in flight (DIF), the searched for the same oscillation using neutrinos. The detection of $\overline{\nu}_e$ via Inverse Beta Decay (IBD) shows an excess compatible with $\Delta m^2 0.2 - 10\text{eV}^2$ range. The DIF measurement, which is populated with a lot of background, shows an excess compatible with the signal of anti-neutrinos. MiniBooNE search for the neutrino and anti-neutrinos in a $\overset{(-)}{\nu}_\mu$ [12]. The experimental configuration shows the same L/E as LSND. The results of the $\overset{(-)}{\nu}_\mu \rightarrow \overset{(-)}{\nu}_e$ shows an excess of both ν_e and $\overline{\nu}_e$ that is compatible with $0.1 < \Delta m^2_{41} < 1$. MiniBooNE can also look for sterile neutrinos in the muon-disappearance channel. Although the detector sensitivity is small for $\Delta m^2_{41} \leq 1\text{eV}^2$, the results don't show any evidence of oscillation.

Similar to the muon-disappearance analysis done by MiniBooNE, there are several other experiments where there is no evidence of a sterile neutrino. In particular, that is the result found in the analysis carry on by Long-Baseline experiments like MINOS/MINOS+ [13] or NOνA [14]. Those experiments uses a near to far detector ratio to cancel most of the flux uncertainties. NOνA uses a ν_μ beam that peaks at 2 GeV and a baseline of $\sim$ 800 km, and search for a deficit in the number of Neutral Currents in the far detector. To avoid an oscillation in the near detector, the analysis is limited to $\Delta m^2_{41} \in [0.05, 0.5]\text{eV}^2$. In the case of MINOS/MINOS+, the far detector (735 km) is located on the neutrino beam direction. Each detector used a different energy beam that peaks at 3 GeV/7 GeV. Using a near to far detector comparison, those experiments have been able to search for sterile neutrino via the ν_μ disappearance channel in two different mass regimes. For $\Delta m^2_{41} \in [0.05, 0.5]$ eV^2, the oscillation is developed in the far detector whereas for masses in the range $\Delta m^2_{41} \in [1, 100]$ eV^2 the oscillation would be observed in the near detector. For masses above 100 eV, both detectors would observe a deficit.

The study of the atmospheric neutrinos has not found any robust evidence of a sterile neutrino has been observed. The baseline for the neutrinos created in the atmosphere is of the order of $\sim$ 1000 km, and the flux extends from $\sim$ 100 MeV to $\sim$ 10 TeV. For the experiments that are able to measure the flux up to $\sim$ 10 GeV, like DeepCore [15] or Super-Kamiokande [16], the energy distortion introduced by the oscillation of a 1 eV cannot be observed. So, the oscillation shows up as a deficit in the flux. At the TeV scale, the anti-neutrino flux will under-go through a flavor resonance (total flavor conversion) for trajectories crossing the Earth's mantle. That resonance can be measured by neutrino telescope experiments, like IceCube [17], that are able to measure the high energy part of the atmospheric flux. Although the latest results of IceCube, that are based on 8 years of data, exclude the no-sterile hypothesis at 90% CL, in the global analysis, we used the result that contains just 1 year of data, where the no-oscillation hypothesis was allowed at 1σ CL.

4 Global analysis

In the analysis of all the reactor data, we deal with the flux uncertainties following the theoretical prediction [2, 3] (fixed fluxes) or we assume a free normalization (free fluxes) for the contribution of each isotope. Combining all the reactor data, there is preference of $\sim 3\sigma$ for the sterile neutrino hypothesis. If we include in the analysis all the electron-disappearance data the exclusion of the no-oscillation hypothesis increases driven by the gallium anomaly.

The combined result of all the data in the muon-disappearance channel leads a strong suppression on $|U_{\mu 4}|$. For masses around ≤ 1 eV, the constraint comes from the high energy atmospheric neutrinos measured by IceCube. For larger masses, the results of MiniBooNE and MINOS/MINOS+ constraint the mixing angle.

In the appearance channel, the results are dominated by LSND and MiniBooNE. The combined analysis excludes the no-oscillation hypothesis to $\sim 6\sigma$, although the global analysis has a poor goodness of fit due to the MiniBooNE which doesn't fit well in the $3+1$ oscillation scenario.

In order to show whether there is any inconsistency between the different data sets, we can divide the all the data into several pieces to compare the results between them. We have divided the data between disappearance and appearance measurements, in such a way we cam compare the prediction for the mixing elements $|U_{e4}|^2$ and $|U_{\mu 4}|^2$ from independent data. The results of the analysis are presented in terms of the effective mixing angle $\sin^2 2\theta_{\mu e} \equiv 4\,|U_{e4}|^2\,|U_{\mu 4}|^2$, Fig. 1, and it shows that there are some inconsistencies between the appearance and the disappearance results.

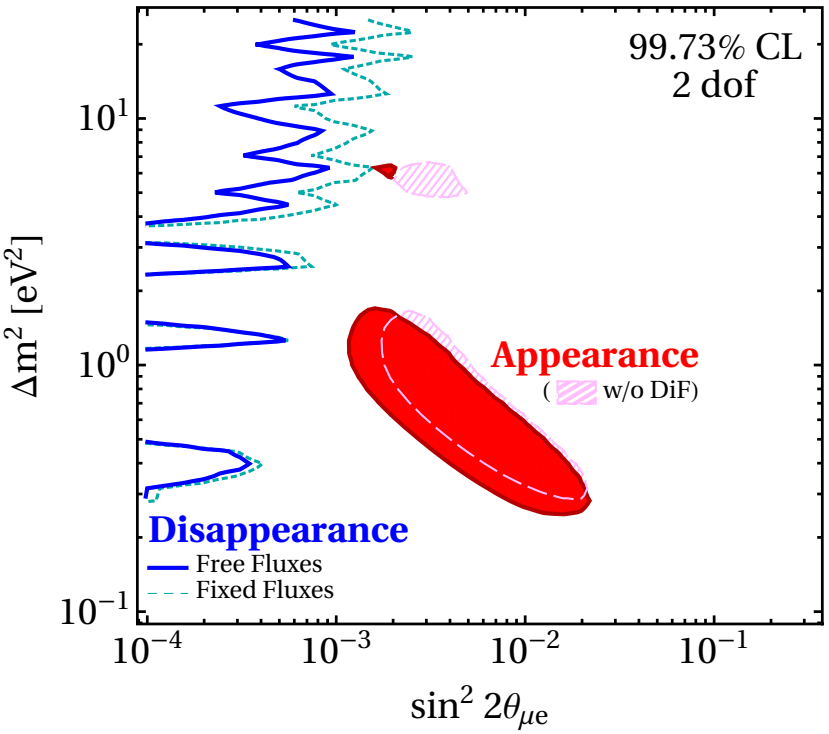

Figure 1: Results of the appearance and the disappearance global analysis. All the contours correspond to the 99.73% CL. For the reactor data, we consider two different possibilities, free fluxes or fixed fluxes. About the LSND results, we consider two options with or without DIF data. We refer to the text for more information.

5 Conclusions

In this talk, we present the results of the global analysis [1] of the $3+1$ neutrino oscillation scenario. The anomalies found in the ν_e disappearance channel and the event excess in the electron-appearance points towards the existence of a sterile neutrino with mass a around 1 eV. On the other side, the muon-disappearance channel place a strong constraint on $U_{\mu 4}$. The combined analysis shows a strong tension between the appearance and the disappearance channels.

Acknowledgements

Fermilab is operated by the Fermi Research Alliance, LLC under contract No. DE-AC02-07CH11359 with the United States Department of Energy. IMS acknowledge travel support from the Colegio de Fisica Fundamental e Interdisciplinaria de las Americas (COFI).

References

[1] M. Dentler, A. Hernandez-Cabezudo, J. Kopp, P. A. Machado, M. Maltoni, I. Martinez-Soler, and T. Schwetz, *Updated Global Analysis of Neutrino Oscillations in the Presence of eV-Scale Sterile Neutrinos*, *JHEP* **08** (2018) 010, [arXiv:1803.10661].

[2] T. Mueller et al., *Improved Predictions of Reactor Antineutrino Spectra*, *Phys. Rev. C* **83** (2011) 054615, [arXiv:1101.2663].

[3] P. Huber, *On the determination of anti-neutrino spectra from nuclear reactors*, *Phys. Rev. C* **84** (2011) 024617, [arXiv:1106.0687]. [Erratum: Phys.Rev.C 85, 029901 (2012)].

[4] **Daya Bay** Collaboration, F. An et al., *Evolution of the Reactor Antineutrino Flux and Spectrum at Daya Bay*, *Phys. Rev. Lett.* **118** (2017), no. 25 251801, [arXiv:1704.01082].

[5] J. M. Berryman and P. Huber, *Sterile Neutrinos and the Global Reactor Antineutrino Dataset*, arXiv:2005.01756.

[6] **DANSS** Collaboration, M. Danilov, *Recent results of the DANSS experiment*, in *2019 European Physical Society Conference on High Energy Physics*, 11, 2019. arXiv:1911.10140.

[7] **NEOS** Collaboration, Y. Ko et al., *Sterile Neutrino Search at the NEOS Experiment*, *Phys. Rev. Lett.* **118** (2017), no. 12 121802, [arXiv:1610.05134].

[8] C. Giunti and M. Laveder, *Statistical Significance of the Gallium Anomaly*, *Phys. Rev. C* **83** (2011) 065504, [arXiv:1006.3244].

[9] J. Kopp, P. A. N. Machado, M. Maltoni, and T. Schwetz, *Sterile Neutrino Oscillations: The Global Picture*, *JHEP* **05** (2013) 050, [arXiv:1303.3011].

[10] J. Kostensalo, J. Suhonen, C. Giunti, and P. C. Srivastava, *The gallium anomaly revisited*, *Phys. Lett. B* **795** (2019) 542–547, [arXiv:1906.10980].

[11] **LSND** Collaboration, A. Aguilar-Arevalo et al., *Evidence for neutrino oscillations from the observation of $\bar{\nu}_e$ appearance in a $\bar{\nu}_\mu$ beam*, *Phys. Rev. D* **64** (2001) 112007, [hep-ex/0104049].

[12] **MiniBooNE** Collaboration, A. Aguilar-Arevalo et al., *Significant Excess of ElectronLike Events in the MiniBooNE Short-Baseline Neutrino Experiment*, *Phys. Rev. Lett.* **121** (2018), no. 22 221801, [arXiv:1805.12028].

[13] **MINOS+** Collaboration, P. Adamson et al., *Search for sterile neutrinos in MINOS and MINOS+ using a two-detector fit*, *Phys. Rev. Lett.* **122** (2019), no. 9 091803, [arXiv:1710.06488].

[14] **NOvA** Collaboration, P. Adamson et al., *Search for active-sterile neutrino mixing using neutral-current interactions in NOvA*, *Phys. Rev. D* **96** (2017), no. 7 072006, [arXiv:1706.04592].

[15] **IceCube** Collaboration, M. G. Aartsen et al., *Determining neutrino oscillation parameters from atmospheric muon neutrino disappearance with three years of IceCube DeepCore data*, *Phys. Rev. D* **91** (2015), no. 7 072004, [arXiv:1410.7227].

[16] **Super-Kamiokande** Collaboration, R. Wendell, *Atmospheric Results from Super-Kamiokande*, *AIP Conf. Proc.* **1666** (2015), no. 1 100001, [arXiv:1412.5234].

[17] **IceCube** Collaboration, M. Aartsen et al., *Searches for Sterile Neutrinos with the IceCube Detector*, *Phys. Rev. Lett.* **117** (2016), no. 7 071801, [arXiv:1605.01990].

Directional direct Dark Matter searches with gaseous TPCs

Elisabetta Baracchini

e-mail: elisabetta.baracchini@gssi.it

Gran Sasso Science Institute

Presented at the 3rd World Summit on Exploring the Dark Side of the Universe
Guadeloupe Islands, March 9-13 2020

Abstract

The presence of DM in the Universe is nowadays established, but still unexplained mystery. The determination of the incoming DM direction can provide an astrophysical correlation that offers an unique key for unambiguous identification of DM. Time Projection Chambers can supply the best observables for a directional DM searches and are today a mature technology aiming at the ton-scale. We will review current directional R&Ds effort and the CYGNUS proto-collaboration concept towards a large scale multi-site directional galactic observatory.

1 Introduction

The existence of an unknown gravitational source in the Universe, commonly referred to as Dark Matter (DM), has been extensively demonstrated through a plethora of astrophysical measurements (from cosmic microwave background to cluster and galaxy rotations, lensing and Big Bang nucleosynthesis and so on [1]). Among the different explanation, the existence of unidentified Weakly Interactive Massive Particles (WIMPs) is still a well motivated interpretation of these experimental observations. WIMPs can potentially be observed by three complementary approaches: they can be produced at particle colliders, their annihilation can give an indirect signal in astrophysics experiments or they can be directly detected on Earth through their elastic scattering with the common matter, due to our motion around the centre of the Galaxy.

The main experimental challenge of direct DM searches is to detect the very low energy (1-100 keV) expected DM-nuclear recoils and discriminate them from interactions induced by other particles, which have typically 10^6-10^9 higher rates. Classical background minimisation techniques are operation in deep underground laboratories (to suppress cosmic rays), use of radio-pure components (to avoid natural radioactivity) and active or passive shielding of the detector. Additionally, experiments exploit the different materials response to energy deposit of different particles to discriminate nuclear from electron recoils. Neutral particles, unfortunately, produce a detector response nearly identical to WIMPs, unless some additional topology or directional handle is employed for further discrimination. In large detectors with heavy dense targets, fast neutron with O(cm) mean free path can be suppressed by rejecting multiple scattering events and defining an internal fiducial volume, but at the price of reducing the active material sometimes even of 50%. Neutrinos, on the other hand, can not be shielded, nor are expected to multiple scatter. Current Xe-based experiment [2] (and several next generation detectors [3, 4]) will be sensitive to a new background coming from

solar, atmospheric and diffuse supernovae neutrinos, that they will not be able to discriminate from WIMPs.

In this context, the incoming direction of the DM particle could provide an unique tool for DM identification, together with rejection of such annoying backgrounds [5]. The ordinary, luminous galactic matter in fact, including planets and stars and our Solar system as well, is concentric to the DM halo and rotating with an average orbital velocity of ~ 220 km/s: this implies an apparent WIMP wind for an observer on the Earth, that creates two effects.

In its rotation around the Sun, the Earth orbital velocity is antiparallel to the DM wind in summer and parallel in winter, creating a seasonal modulation of the observed DM rates inside the detector. Unfortunately, since the Earth's orbital speed is small compared to the Sun speed with respect to the Galaxy rest frame, this modulation is expected to be only a few $\%$ and therefore very difficult to disentangle from systematic effects, such as possible seasonal dependence of the background rates. Consequently, its detection requires a large mass detector, able to stay very stable over a long period of time and to strongly suppress any background. The DAMA/LIBRA claim of DM observation [6] is based on the measurement of such annual asymmetry of the rate inside the detector.

A much more robust signature comes from the diurnal directional modulation of the DM signal. This originates from the orientation of solar system motion around the centre of our Galaxy, which happens to point towards the constellation Cygnus. Due to the Earth rotation around its axis, an observer on our planet would see the average direction of the WIMPs changing of $\sim 90^o$ for every 12 sidereal hours. This is a directional correlation with an astrophysical source that no background whatsoever can mimic. A detector sensitive to direction and sense of the arrival of particles can therefore hold the key to an unambiguous, positive observation of a DM signal. This holds true even in presence of an unknown amount of isotropic background, such as neutrons from environmental or detector materials radioactivity [7]. Directionality allows also to positively identify the Solar neutrinos thanks to the correlation with the Sun position in the sky, transforming this background (usually referredto as a "Floor") into an opportunity rather than a nuisance [8, 9]. Directionality information can furthermore discriminate between various DM halo models and provide constraints on WIMP properties, like no other non-directional detector [5, 10].

2 The case for directional DM searches with gaseous TPC

The main experimental challenges of DM detectors aiming at directional sensitivity are to instrument a large volume with high enough granularity to infer recoiling tracks direction down to low energy, while staying background-free. The spatial resolution required is ultimately set by the density of the target material, since it determines the characteristic length of a WIMP induced recoil, which in turn fixes the minimum energy threshold for which the track direction and orientation can be inferred and the electrons discriminated from nuclear recoils using topology information.

Although inherently challenging, gaseous TPCs constitute therefore the natural approach to directional DM searches and can potentially provide the best architecture and the best observables for the following reasons:

- A measurement of the total ionisation indicates the energy of the recoil. α particles and electrons can be easily identified comparing their track topology to the energy released along the path (i.e. dE/dx), providing excellent background rejection;
- The track itself indicates the axis of the recoil and the charge measured along its path encodes the track orientation, providing an additional powerful observable (usually referred to "head-tail" asymmetry, given that most charge is released at the start of the track at these energies). It has been in fact demonstrated how this information improves by a factor 10 the directional sensitivity of a detector, while a pure axial signal (the track orientation via 2D or 3D reconstruction) can in practice be washed-out by the WIMP velocity distribution [11];

- The active target volume can be made free of background-producing material: it contains only the gases, which can be purified of Radon (Rn) and recirculated. Large choice of gases can be employed in a TPC, from light to heavy nuclei, with both odd and even spins, therefore sensitive to both SI and SD interactions also in the low WIMP mass region;

- Only one wall of the detector needs to be instrumented with an amplification and readout systems, and the other with a cathode, leading to favourable cost-volume scaling and to reduced radioactive contamination due to the detector materials. Radon Progeny Recoils (RPRs) from such sources constitute, indeed, one of the most dangerous backgrounds for direct DM searches [12]. This happens when ^{222}Rn from internal detector radioactivity decays into ^{218}Po and the unstable positively charged ion $^{218}Po^{+}$ (80% of times), drifts and plates out on the cathode with the emission of a 6.11 MeV α particle. The geometry of this process implies an high probability for the α to be completely embedded in the cathode, leaving only the ^{218}Po recoiling in the fiducial volume and mimicking a WIMP interaction. In order to reject these events, the full 3D position of the track, including along the drift direction, needs to be reconstructed (a technique usually referred to as "fiducialization");

- TPCs up to 100 m^3 of active volume have already been sucessfully operated at the ALICE LHC experiment [13] and up nearly 20000 m^3 approved for construction in the neutrino field [14], showing the feasibility of very large detectors with large active masses;

In the following, we will review the current status of experimental R&D efforts for the development of TPCs for directional DM searches at large scale, and how these are working together as proto-collaboration towards the development of CYGNUS, a multi-site, multi-target Directional Galactic Recoil Observatory of DM and neutrinos at the ton scale.

3 Current R&D efforts

3.1 DRIFT: multi-wire proportional chambers with negative ion drift

The DRIFT collaboration [15] at the Boulby Underground Laboratory has pioneered since 2001 the construction and operation of the only existing directional DM TPC at 1 m^3 scale. The DRIFT II detector is composed of 2 back-to-back TPCs, each with 50 cm drift length, separated by 0.9 μm thick texturised mylar cathode, conveniently shaped to minimise recoils induced by materials radioactivity [16]. Gas amplification and readout is obtained with Multi Wire Proportional Chambers technique. DRIFT employs a 30:10:1 Torr CS_2:CF_4:O_2 gas mixture to obtain negative ion drift (NID).

NID is a peculiar modification of the TPC principle, suggested in 2000 by J. Martoff [17], in order to overcome the restrictions due to electron diffusion (since all DM TPCs lack of the magnetic field typically present in experiments at colliders). When an highly electronegative dopant is added to the gas mixture, primary electrons liberated by the track while ionising the gas are captured at very short distances $\leqslant$ 10-100 μm by the electronegative molecules, creating negative ions. These anions drift to the anode, where their additional electron is stripped and gives rise to a standard electron avalanche. Thanks to the anions mass being much larger than electrons, their diffusion is reduced to the thermal limit without the need of magnetic fields, achieving a dispersion of $\sim$1 mm/m (to be compared to $\sim$ 20 mm/m expected for conventional electron drift). This characteristic allows for the use of longer drift distances, combined with improved tracking performances. Recently, a new remarkable feature has been observed in negative ion gas mixtures: the presence of multiple charge carriers in the time signal, with different masses [18]. Since anions mobility depends on the mass, the difference in time of arrival of different anions effectively provides a measurement of the absolute position of the event along the drift direction. This feature allows to reject backgrounds coming from detector surfaces (an action typically referred to as *fiducialization*), a procedure not possible in self-triggering TPCs. The combination of the complete electron rejection (2×10^{-5} at 20 keV) with the fiducialization offered by

the minority charge carriers in a negative ion TPC, allowed DRIFT to put the most stringent constraint from a directional detector on SD WIMP-nucleon proton coupling [19].

SF_6 has been recently demonstrated to work very well as negative ion gas between 20 and 100 Torr, including the possibility of high gains and fiducialization via minority SF_5^- charge carriers [20]. Recently, the feasibility of NID operation at nearly atmospheric pressure with He:CF_4:SF_6 at 360:240:10 Torr with triple thin GEMs amplification has also been demonstrated [21]. Compared to the high vapour pressure, low flash point and low explosive mixture in air of the CS_2 employed by DRIFT, SF_6 has the substantial advantages of much more safer handling, combined with easier Radon purification and recirculation [22], while at the same time increasing the target Fluorine mass.

Given the stronger avalanche fields required at the anode plane to achieve field ionisation with SF_6 with respect to CS_2 due to its higher electron affinity, DRIFT recently moved to development of an hybrid readout through the combination of 1 mm Thick GEMs (ThGEM, where the field ionization of the anions occur) with low capacitance 100 μm multi-wires at 1 mm pitch (through which the induced charge signals are readout) [23].

The detector used in this work has a 2 cm $\times$ 2 cm readout for 5 cm drift distance. The signal multiplication was induced by setting the opposite (induction) side of the ThGEM to a positive potential and biasing the wire at 0 V, in order for the avalanche electrons to induce equivalent current on the wires [24, 25]. These induced charge signals were used as avalanche electrons can reattach to SF_6 to form anions while drifting from the induction side of the ThGEM to the charge collection wires.

With X-rays produced by a ^{55}Fe source, gas gain was measured in the range of 1120 $\pm$ 90 to 2470 $\pm$ 160 at a reduced drift field E/N range of 56 Td (10$-$17 V cm^2) to 93 Td (10$-$17 V cm^2) in 20 Torr of pure SF_6 gas. αs from an ^{241}Am source allowed to determine drift velocity and reduced mobility of SF_6 anions in this same E/N range and found compatible with previous results.

Hence, the ThGEM-Multiwire technology has the potentials to serve as a robust, economic, low noise charge readout for future development of large scale directional TPCs.

3.2 NEWAGE: micro-pixelated chambers with single GEM amplification

The NEWAGE experiment main peculiarity is the use of micro-pixels chambers (μ-PIC) coupled to GEM to amplify and detect the track ionisation cloud [26]. μ-PIC can be built on monolithic, 100 μm thick printed circuit boards allowing easy scalability. μ-PIC gas amplification structures (70 μm-diameter anode electrodes with a 400 μm pitch) act also as a 2D pixel readout, thanks to the circular cathode strips with 260 μm diameter around them. The GEM is built onto a 100 μm-thick liquid crystal polymer, and the hole size and pitch are 70 μm and 140 μm, respectively. NEWAGE developed a custom DAQ system based on FPGA to record two data types: "charge" and "track". An amplifier-shaper-discriminator chip collects the analog signals from the cathodes, grouping them into four channels. A flash ADC (FADC) records the waveforms from the four channels with 100 MHz sampling and from the summed waveforms (FADC-sum) the energy deposition of a charged particle is extracted ("charge"). The "track" data are extracted as the addresses and time-over-threshold (TOT) of all strips hit by an event.

The current version of the detector NEWAGE-0.3b" at the Kamioka Observatory has a readout area of 30.7 $\times$ 30.7 cm^2 coupled to a 31.0 $\times$ 32.0 cm^2 GEM, with 41 cm drift length. The target gas is pure CF_4 at 76 Torr and the gas gain with this setup is about 2500. NEWAGE-0.3b" demonstrated directional capability down to $\sim$ 50 keV (with head-tail sensitivity in the range 70-400 keV on a statistical basis) and $\sim$ 2.5 $\times$ 10^{-5} gamma rejection at the same energy [27]. NEWAGE-0.3b" has been more recently equipped with an improved, low radioactivity version of μ-PIC, LAμ-PIC, developed to reduce the αs emission from the surface [28]. This was achieved substituting the surface exposed to the detection volume (originally made of polyimide reinforced with a glass cloth-sheet) with a new material combining polyimide and epoxy, which is a factor of hundred times less contaminated by ^{238}U and ^{232}Th. This allowed to reduce the background in the region [50, 100] keV of a factor 30 [29].

While LAμ-PIC contributed to a significant background reduction, ^{210}Po decay on the detector surface were still observed with an emission rate of (2.1 $\pm$ 0.5) $\times$ 10^{-4} α/cm^2/hr, contributing to

backgrounds mainly located around the GEM, LAμ-PIC and cathode. These could be removed if the absolute Z coordinate of the track was measured, a feature not available with pure CF_4 in self-triggering TPCs. For this reason, NEWAGE collaboration recently developed a negative ion micro time projection chamber (NIμTPC) with detection volume of 12.8 $\times$ 25.6 $\times$ 144 mm^3 to study full 3D tracking, including fiducialization, with NID and SF_6 (see Sec.3.1). With αs from a ^{241}Am source and exploiting SF_5^- minority carriers, the NIμTPC showed capability of reconstructing the absolute Z coordinate between 39 mm and 139 mm distance from the anode with 16 mm uncertainty [30]. With the same setup, 3D tracking with absolute Z determination was demonstrated for the first time, with a spatial resolution of 130 μm for single hits. The NIμTPC results are therefore extremely promising in expanding the reach of directional DM searches.

Another very interesting recent advancement from the NEWAGE collaboration is the development of an innovative approach to field cage manufacturing, using a commercial resistive sheet [31]. Typical field cage are composed of field-shaping electrodes connected through a resistor chain. This design, however, causes some non-uniformity of the electric field near the borders, at a distance of about the width of the electrode. Moreover, the electrodes material (typically Cu) and the ceramic in the resistors exhibit an amount of radioactivity that can be dangerous for rare event searches. The material used for this study, Achilles-Vynilas, was selected among several candidates because of the better uniformity along 1 m, with a resistivity of 3.3 $\pm$ 0.3 $\times$ $10^{10}\Omega/\square$. Achilles-Vynilas foils are thin (200 μm), transparent, of easier assemble and with 2-3 order of magnitude less radioactivity than typical resistors. The measurement with cosmic muons showed a good tracking-performance even in the volume close to (20 mm) the field cage. This innovation can significantly benefit any TPC development, not only for DM searches.

3.3 D^3: pixel and Micromegas readout with thin GEMs amplification

The D^3 project is based on the use of a double (or more recently triple) thin GEM charge amplification coupled to ATLAS FE-I4B ASIC pixels readout (50 x 250 um^2 pixel size with 40 MHz sampling) [32]. Preliminary results with very small prototypes and Ar/He:CO_2 gas mixtures at 1 bar show the possibility of 150-200 um single point resolution for cosmic muons, few degrees angular resolution for α tracks and gain resolution of $\sim 9\%$ at 5.9 keV$_{ee}$ [33]. With a 2.0 $\times$ 1.68 cm^2 pixel readout area for 15 cm drift length in a 70:30 mixture of He:CO_2, they demonstrated also the capability of extracting absolute Z measurement in electron drift gases with αs [32]. This is possible using charge cloud topology information and fitting it to extract the track diffusion during drift (from which the distance between the original track and the GEMs, i.e. absolute Z, is recovered). The precision achieved over mm-length α track segments is of $\sim$ 1 cm uncertainty over 15 cm drift distance.

Eight devices similar to this named BEAST TPCs, with 2.0 $\times$ 1.68 cm^2 readout area for 10 cm drift, are currently operating as fast neutron detectors at the Belle II experiment at SuperKEKB [34]. In this context, BEAST TPCs were optimized for the directional detection of fast neutrons, and operated at low gain in order to maximize operational stability in the high-background and high magnetic fields environment at SuperKEKB. As fast neutron detectors, BEAST TPCs demonstrated excellent angular resolution, energy resolution, and long term stability, exceeding all design goals [34]. Two recent PhD theses [35, 36] demonstrated that even at such low gain, the detectors have a nuclear recoil energy threshold of $\sim$ 10 keV and good particle identification capabilities above $\sim$ 10-20 keV.

Very recently the D^3 project started developing a scale up of the BEAST TPC to be operated as directional DM detector, with two back-to-back TPCs with 50 cm drift and 20 $\times$ 20 cm^2 readout area for a 40 L fiducial volume filled with He:CF_4:C_4H_{10}/CHF_3 mixtures at 1 bar and equipped with resistive strip Micromegas readout by SRS CERN system [37].

3.4 CYGNO and INITIUM: optical 3D readout with CMOS cameras and PMTs

The distinctive traits of the CYGNO and INITIUM approaches to directional DM detection is the optical readout of the secondary scintillation light produced together with electron avalanches by a

triple thin GEMs amplification stage and the use of He:CF_4(:SF_6) mixtures at 1 bar for simultaneous sensitivity to both SI and SD interaction at O(GeV) WIMP masses. Tracks are reconstructed in 3D combining an high granularity 2D projection on the X-Y plane imaged by CMOS cameras with relative Z measurement offered by signal waveforms from PMTs [38]. The advantages of the using CMOS cameras resides in the lower noise with respect to CCDs (about 1/3), the single photon sensitivity and the possibility to decouple it from the target and image large areas with a single device by proper optics. The ERC Consolidator Grant INITIUM goal is to explore the feasibility of NID within such optical approach with a very modest doping of SF_6, and its development is therefore highly synergic with CYGNO's (which is on the contrary based on electron drift).

The larger prototype developed with this approach (LEMON) has 7 L active volume, with 20 $\times$ 24 cm^2 triple thin GEMs amplification and 20 cm drift length. In this configuration, the CMOS camera Orca Flash (2048 $\times$ 2048 pixels with an area of 6.5 $\times$ 6.5 μm^2 each) equipped with a Schneider lens (25 mm Focal Length, 0.95 aperture), is placed at a distance of 52.5 cm, so that each pixel images an effective area of 130 $\times$ 130 μm^2. LEMON results in the following have been all obtained with He:CF_4 60:40 gas mixture at 1 bar. Studies are on-going to develop NID within this context.

In order to estimate the energy threshold and resolution, the sensor electronic noise and the response to ^{55}Fe was studied with LEMON [39]. For the first, the distribution of the number of pixels counting fake clusters (i.e. ghosts) reconstructed in data collected with the camera shutter closed was studied. From this, a threshold of a total of 400 photons collected was established, in order to ensure a fake events rate $\leqslant$ 10 per year. From the study of ^{55}Fe events, LEMON response is measured to be 1200 photon/cluster, i.e 1 photon each 5 released eV, with 15% energy resolution at 5.9 keV_{ee}. Therefore, the 400 photons threshold extracted from the noise study, with such 0.2 photon/eV sensitivity determined with ^{55}Fe, represent an energy threshold of 2 keV. By visual inspection of the fake clusters, is moreover easy to see how pattern recognition algorithms could easily reject a significant portion of ghosts, effectively lowering the energy threshold estimated in this way.

With LEMON, the possibility to determine the absolute Z position of the event in electron drift was studied with 450 MeV electrons from the Frascati BTF facility, extracting from the recorded CMOS images and PMT waveforms the track diffusion during drift (a technique similar to the one discussed in Sec.3.3). The transverse recorded light profile, in fact, possess a Gaussian shape with the total light being proportional to $\sigma_{light} \times A_{light}$ (where σ_{light} is the sigma and A_{light} the amplitude of the Gaussian). The ratio $\eta_{light} = \sigma_{light}/A_{light}$ is found to increases linearly with the drift distance and can be therefore used to evaluate the absolute Z with about 15% uncertainty over 20 cm drift distance [40].

In order to study within the CYGNO/INITIUM approach the nuclear recoils reconstruction efficiency at low energies and the capability to distinguish them from electron recoils, Ambe and ^{55}Fe sources were employed in LEMON. The iDBSCAN algorithm with multiple iteration (based the well-known Density-Based Spatial Clustering of Applications with Noise) was developed to select track with different ionization patterns. With iDBSCAN and exploiting very simple topological information, a natural radioactivity background rejection in the energy region around 5.9 keV_{ee} of 10^{-3} was obtained, with 40% nuclear recoil efficiency [41]. While these results are already encouraging, the collaboration is working on a more sophisticated multivariate approach, with which rejection can significantly be improved.

The CYGNO/INITIUM collaboration recently manufactured a larger, 50 L prototype (LIME), imaged by a single sCMOS and a 4 small PMT and with same dimensions (33 $\times$ 33 cm^2 readout area for 50 cm drift) of a single module of the 18 foreseen for the CYGNO/INITIUM 1 m^3 detector (already funded). LIME goals are in fact to verify in an underground environment and on realistic dimensions the performances expected for 1 m^3 detector, while at the same time test part of the materials and construction techniques and also provide a precise, spectral and directional measurement of the underground environmental neutron flux. Overground commissioning of LIME is ongoing, and already established detector stability at nominal operational values similar to LEMON and an energy resolution of 15% along the whole drift volume at 5.9 keV_{ee} from ^{55}Fe events.

4 CYGNUS: a multi-site, multi-target Directional Galactic Recoil observatory of DM and Neutrinos at the ton scale

The CYGNUS project is a new international collaboration formed by nearly all the members of the experimental efforts described in Sec. 3. CYGNUS aim is to develop a large modular Galactic Recoil Observatory that could test the DM hypothesis beyond the Neutrino Floor and measure galactic Neutrinos. The key features of the proposed experiment is a modular design of recoil sensitive TPCs filled with He:SF_6(:CF_4) (low and high pressure operations envisaged, as well as electron or negative ion drift) with full fiducialization and energy and directional threshold at O(keV) and installation in multiple underground sites (including the Southern Hemisphere) to minimise location systematics and improve sensitivity. A coordinated R&D effort to optimise technologies and gas mixture choices is currently undergoing in several laboratories in the participating countries, as can be seen by the studies discussed in each subsection of Sec. 3.

The proto-collaboration recently developed an comprehensive feasibility study for a 1000 m^3 detector, based on MC simulation backed up by experimental measurements [42]. In this, in addition to the DM and Neutrinos physics cases, a detailed simulation of six different charge readout options with NID and the study of their electron recoil discrimination and directional capabilities are discussed. Furthermore, foreseen external and internal backgrounds and engineering requirements are examined. From a cost/benefit study, taking into account costs, directional performance at low recoil energies and intrinsic radioactivity content, the strip readout technologies emerges as the best choice in a NID context with SF_6 as dopant.

The simulations presented in [42] indicate moreover the possibility of electron rejection down to 1 keV_{ee} in an atmospheric pressure He:SF_6 mixture. By simply exploiting the measured track length versus energy released, background discrimination can exceed 10^6 at 5 keV_{ee} for fluorine, and 10 keV_{ee} for helium. A preliminary investigations with deep learning neutral networks suggest that this can be improved upon by several orders of magnitude. A ton-scale 'Cygnus-1000' detector, with the characteristics discussed in [42], would have a non-directional sensitivity to WIMP-nucleon cross sections significantly extending to sub-10 GeV WIMP masses for SI coupling, whereas for SD interactions even a 10 m^3 scale would compete with generation-two (G2) detectors currently under construction, and would breach the Xe Neutrino Floor. Final recommendations suggest to experimentally demonstrate on prototypes with full drift length and high readout resolution all energy-dependent performances and to continue pursuing alternative approaches, based on electron drift with optical or high granularity charge readout.

5 Conclusions

The determination of the incoming direction of WIMP particles can offer a very powerful handle for a positive, unambiguous identification of a DM signal, together with an excellent capability of rejection of the annoying backgrounds, including neutrons and neutrinos. Gaseous Time Projection Chambers, constituting the most natural, although inherently challenging, approach to directional DM searches, have nowadays reached the technological maturity to aim at 1 ton scale experiment. In this context, several R&Ds are on-going to found the best technologies and gas mixtures choices to this goal. A coordinate endeavour among such experimental efforts is in progress, as a new international proto-collaboration called CYGNUS, that recently presented a detailed feasibility study for a modular, multi-target ton scale experiment. From these studies, a 'Cygnus-1000' detector would be able to put significant constraints to both SD and SI interactions extending the expected reach of G2 detectors, while at the same time measure Solar Neutrinos.

Acknowledgements

The INITIUM project is funded by the European Research Council (ERC) under the European Union Horizon 2020 programme (grant agreement No. 818744).

References

[1] J. Silk et al., *Particle Dark Matter: Observations, Models and Searches*. Cambridge Univ. Press, Cambridge, 2010.

[2] **XENON** Collaboration, E. Aprile et al., *Dark Matter Search Results from a One Ton-Year Exposure of XENON1T*, *Phys. Rev. Lett.* **121** (2018), no. 11 111302, [arXiv:1805.12562].

[3] **XENON** Collaboration, E. Aprile et al., *Projected WIMP Sensitivity of the XENONnT Dark Matter Experiment*, arXiv:2007.08796.

[4] **LZ** Collaboration, D. Akerib et al., *The LUX-ZEPLIN (LZ) Experiment*, *Nucl. Instrum. Meth. A* **953** (2020) 163047, [arXiv:1910.09124].

[5] F. Mayet et al., *A review of the discovery reach of directional Dark Matter detection*, *Phys. Rept.* **627** (2016) 1–49, [arXiv:1602.03781].

[6] R. Bernabei et al., *First results from DAMA/LIBRA2*, *Nucl. Part. Phys. Proc.* **303-305** (2018) 74–79.

[7] A. M. Green and B. Morgan, *Optimizing WIMP directional detectors*, *Astropart. Phys.* **27** (2007) 142–149, [astro-ph/0609115].

[8] M. Abdullah, D. Aristizabal Sierra, B. Dutta, and L. E. Strigari, *Coherent Elastic Neutrino-Nucleus Scattering with directional detectors*, *Phys. Rev. D* **102** (2020), no. 1 015009, [arXiv:2003.11510].

[9] J. Seguinot, T. Ypsilantis, and A. Zichichi, *A High rate solar neutrino detector with energy determination*, *Conf. Proc. C* **920310** (1992) 289–313.

[10] C. A. O'Hare, C. McCabe, N. W. Evans, G. Myeong, and V. Belokurov, *Dark matter hurricane: Measuring the S1 stream with dark matter detectors*, *Phys. Rev. D* **98** (2018), no. 10 103006, [arXiv:1807.09004].

[11] F. Mayet and J. Billard, *A review on the discovery reach of Dark Matter directional detection*, *J. Phys. Conf. Ser.* **469** (2013) 012013, [arXiv:1310.0214].

[12] **DRIFT** Collaboration, M. Pipe, *Background reduction and spin-dependent limits using DRIFT: A directionally sensitive dark matter detector*, *J. Phys. Conf. Ser.* **315** (2011) 012017.

[13] J. Alme et al., *The ALICE TPC, a large 3-dimensional tracking device with fast readout for ultra-high multiplicity events*, *Nucl. Instrum. Meth. A* **622** (2010) 316–367, [arXiv:1001.1950].

[14] **DUNE** Collaboration, R. Acciarri et al., *Long-Baseline Neutrino Facility (LBNF) and Deep Underground Neutrino Experiment (DUNE): Conceptual Design Report, Volume 4 The DUNE Detectors at LBNF*, arXiv:1601.02984.

[15] G. Alner et al., *The DRIFT-II dark matter detector: Design and commissioning*, *Nucl. Instrum. Meth. A* **555** (2005) 173–183.

[16] J. Battat et al., *Reducing DRIFT Backgrounds with a Submicron Aluminized-Mylar Cathode*, *Nucl. Instrum. Meth. A* **794** (2015) 33–46, [arXiv:1502.03535].

[17] C. Martoff, D. Snowden-Ifft, T. Ohnuki, N. Spooner, and M. Lehner, *Suppressing drift chamber diffusion without magnetic field*, *Nucl. Instrum. Meth. A* **440** (2000) 355–359.

[18] D. P. Snowden-Ifft, *Discovery of multiple, ionization-created CS2 anions and a new mode of operation for drift chambers*, *Rev. Sci. Instrum.* **85** (2014) 013303.

[19] **DRIFT** Collaboration, J. Battat et al., *First background-free limit from a directional dark matter experiment: results from a fully fiducialised DRIFT detector*, *Phys. Dark Univ.* **9-10** (2015) 1–7, [arXiv:1410.7821].

[20] N. Phan, R. Lafler, R. Lauer, E. Lee, D. Loomba, J. Matthews, and E. Miller, *The novel properties of SF_6 for directional dark matter experiments*, *JINST* **12** (2017), no. 02 P02012, [arXiv:1609.05249].

[21] E. Baracchini, G. Cavoto, G. Mazzitelli, F. Murtas, F. Renga, and S. Tomassini, *Negative Ion Time Projection Chamber operation with SF_6 at nearly atmospheric pressure*, *JINST* **13** (2018), no. 04 P04022, [arXiv:1710.01994].

[22] A. Ezeribe, W. Lynch, R. Gregorio, J. Mckeand, A. Scarff, and N. Spooner, *Demonstration of radon removal from SF_6 using molecular sieves*, *JINST* **12** (2017), no. 09 P09025, [arXiv:1707.07772].

[23] A. Ezeribe, C. Eldridge, W. Lynch, R. M. Gregorio, A. Scarff, and N. C. Spooner, *Demonstration of ThGEM-Multiwire Hybrid Charge Readout for Directional Dark Matter Searches*, arXiv:1909.13881.

[24] W. Shockley, *Currents to conductors induced by a moving point charge*, *J. Appl. Phys.* **9** (1938), no. 10 635–636.

[25] S. Ramo, *Currents induced by electron motion*, *Proc. Ire.* **27** (1939) 584–585.

[26] K. Miuchi et al., *First underground results with NEWAGE-0.3a direction-sensitive dark matter detector*, *Phys. Lett. B* **686** (2010) 11–17, [arXiv:1002.1794].

[27] K. Nakamura et al., *Direction-sensitive dark matter search with gaseous tracking detector NEWAGE-0.3b'*, *PTEP* **2015** (2015), no. 4 043F01.

[28] T. Hashimoto et al., *Development of a low-α-emitting μ-PIC as a readout device for direction-sensitive dark matter detectors*, *Nucl. Instrum. Meth. A* **977** (2020) 164285, [arXiv:2002.12633].

[29] T. Ikeda, K. Miuchi, T. Hashimoto, H. Ishiura, T. Nakamura, T. Shimada, and K. Nakamura, *Results of a directional dark matter search from the NEWAGE experiment*, *J. Phys. Conf. Ser.* **1468** (2020), no. 1 012042.

[30] T. Ikeda, T. Shimada, H. Ishiura, K. Nakamura, T. Nakamura, and K. Miuchi, *Development of a Negative Ion Micro TPC Detector with SF_6 Gas for the Directional Dark Matter Search*, *JINST* **15** (2020), no. 07 P07015, [arXiv:2004.09706].

[31] K. Miuchi et al., *Development of a time projection chamber with a sheet-resistor field cage*, *PTEP* **2019** (2019), no. 6 063H01, [arXiv:1903.01663].

[32] P. Lewis, S. Vahsen, I. Seong, M. Hedges, I. Jaegle, and T. Thorpe, *Absolute Position Measurement in a Gas Time Projection Chamber via Transverse Diffusion of Drift Charge*, *Nucl. Instrum. Meth. A* **789** (2015) 81–85, [arXiv:1410.1131].

[33] S. Vahsen, M. Hedges, I. Jaegle, S. Ross, I. Seong, T. Thorpe, J. Yamaoka, J. Kadyk, and M. Garcia-Sciveres, *3-D tracking in a miniature time projection chamber*, *Nucl. Instrum. Meth. A* **788** (2015) 95–105, [arXiv:1407.7013].

[34] I. Jaegle et al., *Compact, directional neutron detectors capable of high-resolution nuclear recoil imaging*, *Nucl. Instrum. Meth. A* **945** (2019) 162296, [arXiv:1901.06657].

[35] M. D. Hedges, *Performance and first deployment of novel 3d nuclear recoil detectors*. PhD thesis, University of Hawaii at Manoa, 2018.

[36] T. N. Thorpe, *Gain resolution studies and first dark matter search with novel 3d nuclear recoil detectors*. PhD thesis, University of Hawaii at Manoa, 2018.

[37] S. E. Vahsen. Private communication, July, 2020.

[38] V. Antochi, E. Baracchini, G. Cavoto, E. Marco, M. Marafini, G. Mazzitelli, D. Pinci, F. Renga, S. Tomassini, and C. Voena, *Combined readout of a triple-GEM detector*, *JINST* **13** (2018), no. 05 P05001, [arXiv:1803.06860].

[39] I. A. Costa et al., *Performance of Optically Readout GEM-based TPC with a 55Fe source*, arXiv:1905.04066.

[40] D. Pinci, E. Baracchini, G. Cavoto, E. Di Marco, M. Marafini, G. Mazzitelli, F. Renga, S. Tomassini, and C. Voena, *High resolution TPC based on optically readout GEM*, *Nucl. Instrum. Meth. A* **936** (2019) 453–455.

[41] E. Baracchini et al., *Identification of low energy nuclear recoils in a gas TPC with optical readout*, arXiv:2007.12508.

[42] S. Vahsen et al., *CYGNUS: Feasibility of a nuclear recoil observatory with directional sensitivity to dark matter and neutrinos*, arXiv:2008.12587.

Dark Matter in Stars

Aaron C. Vincent

e-mail: aaron.vincent@queensu.ca

Department of Physics, Engineering Physics and Astronomy,
Queen's University, Kingston ON K7L 3N6, Canada
Arthur B. McDonald Canadian Astroparticle Physics Research Institute,
Kingston ON K7L 3N6, Canada
Perimeter Institute for Theoretical Physics, Waterloo ON N2L 2Y5, Canada

Presented at the 3rd World Summit on Exploring the Dark Side of the Universe
Guadeloupe Islands, March 9-13 2020

Abstract

I review some key aspects of capture and possible observable effects of particle dark matter in stars. Focusing on the transport of heat from captured asymmetric dark matter, I outline existing computational methods, and the challenges that must be overcome to continue pushing the field forward.

1 Introduction

Significant efforts are underway at underground laboratories around the world to detect the minute but telltale signatures of direct interactions between galactic dark matter (DM) and ordinary baryonic nuclei. Because — by definition — DM must be very weakly interacting, such searches must take place in well-shielded environments, where interference from cosmic rays, thermal noise and radiogenic backgrounds are as low as possible. Such direct detection (DD) experiments rely on elastic scattering between DM and target nuclei to provide a detectable signature in heat, ionization, scintillation, or a combination thereof. Weak couplings necessarily mean that DD experiments are limited by exposure, and with each subsequent generation, experiments have gotten larger. Currently, the strongest limits on spin-independent are set by XENON1T [1], a 3500 kg liquid xenon detector, and planning has begun for hundred-ton scale argon and xenon experiments with the potential to pummel their way through the dreaded neutrino floor.

If present in the lab, elastic scattering between DM and nuclei must also occur in natural systems. The largest nearby target for such an effect is the Sun: at 2×10^{30} kg and exposure $t_\odot = 4.57$ Gyr, it constitutes a truly titanic (if noisy) detector. Indeed, if DM scattering off solar nuclei brings it below the local escape velocity, the DM will become gravitationally bound and settle into an equilibrium configuration near the core. Depending on the nature of the DM itself, it may then suffer one of three possible fates: 1) if it is too light, it will "evaporate" from momentum exchanges large enough to bring it above the local escape velocity[1] 2) if it is self-conjugate, or if sufficient quantities of "anti-DM" are present in the star, it will annihilate, or 3) if it is sufficiently heavy and asymmetric [5], it can act as a heat conductor [6], thanks to its long mean free path inside the solar plasma.

[1] as long as it does not interact again on the way out [2–4].

The latter two fates have observable consequences. DM annihilation into SM products and their subsequent decays into neutrinos can produce observable signals at underground (or under-ice) neutrino telescopes. Indeed, the strongest bounds on DM-nucleon scattering for certain DM candidates come from this channel. Heat transport can have more subtle consequences: by flattening the temperature gradient in the inner Sun, neutrino fluxes can be reduced, and the pressure and density profile of the Sun can be modified, changing helioseismology observables such as the convective zone radius r_{CZ}, the surface helium composition, and the inferred sound speed profile [7]. In other main sequence stars, convective cores can be erased, and with large enough concentrations, evolutionary trajectories on the Hertzsprung-Russel (HR) diagram can be severely modified.

In the following, I will focus on the latter effects, with special emphasis on some of the details of the calculations. However, I would be remiss not to mention that DM of various shapes and sizes can have even more spectacular consequences when combined with the exotic environments of white dwarfs or neutron stars, see e.g. [8–13] and references therein.

We shall start by recalling the capture rate of DM in stars, and briefly look at annihilation before turning our full attention to the perplexing problem of particle propagation and heat transport.

2 Capture and annihilation

If the Milky Way's DM halo is near hydrostatic equilibrium, its velocity distribution in our vicinity should be roughly Maxwellian, with a dispersion velocity around 220 km/s, which can be obtained from the mass enclosed within the Sun's orbit. Though prior simulations cast doubt on this simple model, newer numerical simulations including the hydrodynamics of gas, star formation and feedback indicate that it is a fairly reasonable assumption [14]. The capture rate $C_\star$ of DM in a star of radius $R_\star$ is:

$$C_\star(t) = 4\pi \int_0^{R_\star} r^2 \int_0^\infty \frac{f_\star(u)}{u} w\Omega(w) \mathrm{d}u\mathrm{d}r. \tag{1}$$

where u is the DM speed in the star's frame, and $w(r) = \sqrt{u^2 + v_{esc}(r)^2}$, where $v_{esc}(r)$ is the escape velocity from a distance r from the centre of the star. $f_\star(u)$ is the local DM speed distribution, and $\Omega(w)$ is a function that encodes the scattering kinematics: $w\Omega(w)$ it is proportional to the probability per unit time of a collision occurring that brings a DM particle with speed w below v_{esc}. Note that this expression should be modified if the DM must scatter multiple times before capture [15, 16]

For the Sun, the only free parameters in (1) are the DM mass m_χ and the DM-nucleon[2] cross section $\sigma \equiv d\sigma_{\chi-n}/dE_R$. The latter can result in non-trivial DM-*nucleus* interactions. Depending on the Lorentz structure of the DM-quark vertex, the cross section depends generically on combinations of the non-relativistic quantum operators $\mathbb{1}$ (the identity), $\vec{q}$ (the exchanged momentum), $\vec{v}^\perp$ (the relative velocity component orthogonal to $\vec{q}$), $\vec{S}_\chi$ and $\vec{S}_n$ (the DM and nucleon spins) [18]. Each bilinear combination of these operators leads to both different kinematics and a different multipole projection onto the nuclear state, leading in turn to an isotope-dependent *nuclear response*. These have been computed and tabulated in a number of references, including [19] in the context of the Sun. Operators that depend on S_n are particularly interesting, as they do not benefit from the coherent enhancement $\sigma \propto A^2$ that spin-independent models do, and thus are much more difficult to probe with puny Earth-based detectors. Different scattering kinematic also mean that DD experiments probe very different areas of q and v-space, leading to strong complementarity between approaches (see e.g. [20, 21]).

Finally it is worth noting that $C_\star$ cannot be larger than the geometric limit set by the size of the stellar disk itself. This turns out to be larger than $\pi R_\star^2$ thanks to gravitational focusing. I point the interested reader to *Capt'n General*[3] [22, 23], a set of numerical functions for calculating the capture of DM in stars including the above effects. I also note [24] who explored the effects of general uncertainties in the DM velocity distribution.

[2] Interactions with electrons can also lead to capture, for a lower mass range [17].

[3] https://github.com/aaronvincent/captngen

If the DM then self-annihilates, annihilation products can produce high-energy neutrinos, detectable at Earth [25–30]. If the DM population attains an equilibrium between decay and annihilation, the neutrino production rate depends only on σ. For spin-independent interactions DD experiments are far more sensitive; however, for spin-dependent interactions, leading limits at high masses are set by SuperKamiokande [31] and IceCube [32]. Before moving on to the main topic of heat transport, I point out the recent code χaroν [33] which self-consistently computes production and propagation of neutrinos from DM in the Sun.

3 Heat transport: the Knudsen problem

If the DM can accumulate in sufficient quantities, its small interaction cross section $\sigma \ll \sigma_T$ leads to measurable heat transport even for comparatively low DM populations (in the Sun, the local DM density means that $m_\chi N_\chi \lesssim 10^{-10} M_\odot$). Computing the observable effects of such heat transport requires implementation of the capture and transport calculations into a full Standard Stellar (Solar) Model (SSM) simulation such as GARSTEC [34] or MESA [35], and evolving the star within the DM halo up to its current age $t_\odot$. SSM's typically have two free parameters: the initial helium density, and a mixing length parameter used to model convection in a 1d simulation. This means that the presence of an additional transport mechanism can still lead to solar models that satisfy the observed luminosity, age and radius.

As mentioned earlier, ADM can lead to a reduction (or spectral change [36]) of the ^{8}B and ^{7}Be neutrino fluxes from the Sun by an $O(1)$ fraction due to the lower central temperature without affecting the overall luminosity. Changes in structure also introduce effects on heliosesimological measures [7, 37, 38] including the radius of the convective zone boundary r_{CZ}, the sound speed profile $c_s(r)$ and dimensionless frequency separation ratios which can be constructed to probe the core composition without systematic effects from higher radii . In slightly more massive stars than the Sun, the convective core can be erased by flattening the temperature profile so as to smoothly maintain local hydrostatic equilibrium across r. This has already been probed via aseteroseismological measurements [39–41].

The computation of heat transport effects in stars is conceptually straightforward, but devilish in implementation. The phase space distribution $F(\mathbf{u}, \mathbf{r}, t)$ of captured DM follows a Boltzmann Collision Equation (BCE):

$$DF(\mathbf{u}, \mathbf{r}, t) = (\partial_t + \mathbf{u} \cdot \nabla_\mathbf{r} - \mathbf{g}(\mathbf{r}) \cdot \nabla_\mathbf{u}) F(\mathbf{u}, \mathbf{r}, t) = \frac{1}{l} C F(\mathbf{u}, \mathbf{r}, t), \tag{2}$$

where $\mathbf{g} = \nabla\phi$ is the local gravitational acceleration, l is the typical interscattering distance and C is the collision operator. $CF(\mathbf{u}, \mathbf{r}, t)$ represents the scattering rate of DM with nuclei from any velocity to $\mathbf{u}$ minus the scattering rate from $\mathbf{u}$ to any other velocity. The microphysics of the DM-nucleus interactions are encoded in the collision operator — see [42] for a general treatment. Spherical symmetry and the fact that the equilibration time scale is much faster than the stellar evolution time scale (i.e. $\partial_t F \simeq 0$) simplify things a little bit. Alas, not nearly enough for comfort.

Projecting the kinetic energy times the solution, $(mu^2/2)F(\mathbf{u}, rr)$, onto the radial direction, one arrives at the luminosity $L(r)$ carried through a shell at radius r by DM. The energy deposited per unit stellar density ρ per unit time is:

$$\epsilon(r) = \frac{1}{4\pi r^2 \rho(r)} \frac{dL(r)}{dr}. \tag{3}$$

Three approaches are generally available to us in tackling the BCE depending on the *Knudsen number* $K = l/r_\chi$, i.e. the ratio of the mean interscattering distance $l \sim 1/(\sigma n_{nuc})$ to the DM scale height in the star.

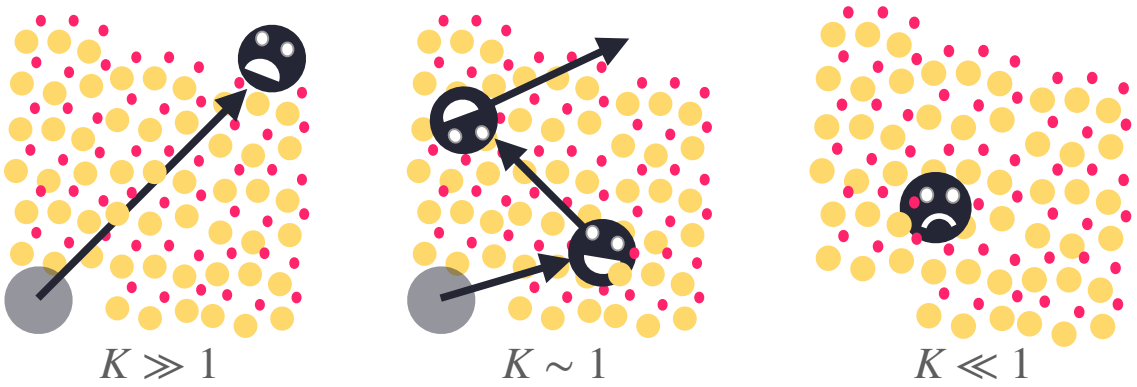

Figure 1: Three heat conduction regimes by dark matter in the solar plasma. Left (Knudsen regime): large mean free paths (small σ) computable with the Spergel and Press (SP) approach lead to low overall energy deposition. Right (LTE regime): small mean free paths, computable with the Gould and Raffelt (GR) approach, mean the DM is "stuck" as σ grows. Centre: at the Knudsen transition, heat transport is optimized. This regime does not have an analytical solution and must be calculated with a Monte Carlo-calibrated interpolation. The SP solution is based on incorrect assumptions, and GR can be numerically unstable and breaks down at small radii.

1. In the weakly-interacting regime, CF is very small, giving a simple solution to the BC(ollisionless)E $DF = 0$:

$$n_{\chi,\mathrm{iso}} \propto e^{-\phi(r)/T_\chi}, \tag{4}$$

where the DM temperature T_χ is a weighted average of the temperatures of the heat bath the DM interacts with. After "some algebra" , the transported energy (3) was obtained by **Spergel and Press** (SP [43]):[4]

$$\epsilon_{\mathrm{SP}}\left(r,t,T_\chi\right) = \frac{8\sqrt{\frac{2}{\pi}}\mathrm{k}^{3/2}}{\rho_\star(r,t)} n_{\chi,\mathrm{iso}}(r,t)\left[T_\star(r,t) - T_\chi(t)\right]\sigma n_{nuc}(r,t)\frac{m_\chi m_{\mathrm{nuc},i}}{(m_\chi+m_{\mathrm{nuc}})^2}\left(\frac{T_\star(r,t)}{m_{\mathrm{nuc}}} + \frac{T_\chi(t)}{m_\chi}\right)^{1/2}. \tag{5}$$

Note that ϵ gets weaker with smaller σ, as the interaction rate becomes smaller. This looks very thermodynamicsy, but the inconsistent assumption that $CF = 0$ will turn out to be [3] one of the reasons that this treatment will yield inaccurate results.

2. In the *Local Thermal Equilibrium* (LTE) $K \ll 1$ regime, the DM is locally at the same temperature at the nuclei. This allowed **Gould and Raffelt** (GR, [44])[5] to expand the BCE to first order in the small quantity $\varepsilon = l(r)|\nabla \log T(r)|$:

$$F(v,r) = F_0 + \varepsilon \cdot dipole, \tag{6}$$

where F_0 is again the Maxwell-Boltzmann solution to $DF = 0$ but with $T(r)$ equal to the local stellar temperature, and the *dipole* contribution is responsible for the local flux of heat due to DM. This allows for the computation of two quantities that depend only on $\mu = m_\chi/m_{nuc}$, the ratio of the DM to nucleon masses. These are a molecular diffusion coefficient $\alpha(\mu)$ (or "fluffiness parameter") that governs the DM radial distribution, and $\kappa(\mu)$[6], a thermal conductivity

[4] I have omitted the requisite sum over nuclear species to keep this equation on a single line. Pretend that it is there.

[5] This builds on earlier work Faulkner & Gilliland [45] and Gilliland et al. [46].

[6] κ is a function of r in Eq. (7). This is because the isotopic abundances, which govern the average value of μ, are radially-dependent.

coefficient. The luminosity is

$$L_{LTE} = 4\pi r^2 n_\chi(\alpha, r) l(r) \kappa(r) \sqrt{\frac{T}{m_\chi}} \frac{dT}{dr}, \tag{7}$$

And ϵ is obtained via Eq. (3).

In contrast with the SP solution, the LTE solution becomes weaker with increasing cross section.

3. A direct Monte Carlo simulation can yield an equilibrium solution of the BCE, as the set of phase space coordinates sampled in the long time limit in a static background plasma is ergotically equivalent to a large collection of particles in equilibrium. While this allows for an exact solution of the BCE in principle, it is practically infeasible as it requires a separate simulation for every set of DM parameters, and for every evolutionary time step in the star's lifetime. Still, it may be used to validate the above approaches: this was done by Gould & Raffelt [44, 47], who notably concluded that the isothermality assumption in the SP approach indeed leads to an incorrect luminosity curve, and while the GR calculation yields accurate results over most of the star in the LTE regime, the luminosity at low radii is overestimated in both cases, because the isotropy assumption in $\mathbf{v}$ breaks down near $r = 0$.

The "correct" technique that is accepted and widely used today is the GR (LTE) technique, rescaled with a "Knudsen correction" based on the GR MC simulations that recovers the correct behaviour in the large K regime, and a "radial correction" that accounts for the isotropy effects [48] by suppressing luminosity at low r.

The effect of ADM heat transport is largest for DM masses that are best kinematically-matched with H and He, while heavy enough to avoid evaporation: $m \sim 3 - 5$ GeV. The most interesting effects unsurprisingly occur near the Knudsen transition. For a constant DM-nucleon cross section this is around 10^{-35} cm^2 for spin-dependent interactions, and 10^{-37} cm^2 in the spin-independent case. While these fall above upper limits set by earth-based DD experiments, non-constant interactions $\sigma \propto v^n, q^n$ $(n = -2, 2, 4)$ [20, 42, 49, 50] as well as some theoretically-motivated models [51, 52] can give Knudsen transitions for values of the cross section that are compatible with DD limits. Such models can also improve on the SSM by up to 6σ, providing a possible path [53–55] to resolving the *Solar Composition Problem*, a strong disagreement between helioseismological observables and SSMs [56–58]. The left panel of Fig 2 shows the improvement in the sound speed profile for a variety of dark matter models with $\sigma = \sigma_0(v/v_0)^n$ or $\sigma = \sigma_0(q/q_0)^n$. These can be related with the NREO models described earlier.

Thanks to DD experiments, the parameter space is rapidly closing, and we may well be forced deep into the Knudsen regime. Here, solar effects may be more difficult to observe, but stars near the galactic centre (GC) that can capture far more DM over their lifetimes can still serve as competitive probes of new physics for small values of σ. Indeed, large amounts of DM can affect the relation between a star's mass, luminosity and temperature by changing the conditions of local thermal and hydrostatic equilibrium. This ultimately means that a star's trajectory on the main sequence can be very different from the standard prediction [59–63]. This is where trouble arises. There are three issues at play:

1. The GR formalism relies on two numerical derivatives, $L \propto dT/dr$ and $\epsilon \propto dL/dr$. Modern stellar evolution codes typically contain small discontinuities in their temperature profiles which are ordinarily not a problem. However, when DM heat transport is large, these discontinuities are amplified and can yield wild, unphysical self-amplifying oscillations for interstellar DM densities larger than:

$$\log\left(\frac{\rho}{\mathrm{GeV}}\right) \gtrsim 0.5 - 2\log\left(\frac{\sigma}{10^{-37}\mathrm{cm}^2}\right). \tag{8}$$

We refer to this region as the *Danger Zone* [64, 65].

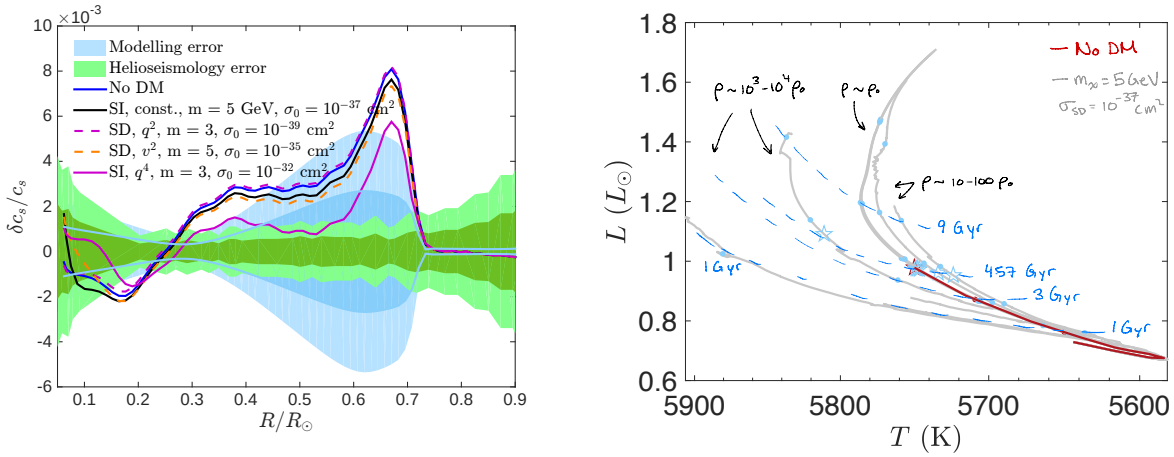

Figure 2: Left: Figure from [50]. Improvement of the difference in the radial sound speed profile $c_s(r)$ between standard solar models without (blue) and with the capture and heat transport of asymmetric dark matter (other colored lines). Bands represent 1 and 2 σ modelling (blue) and helioseismology (green) errors. Right: Luminosity-Temperature plot showing the evolution of a 1 $M_\odot$ star capturing ADM with different local densities (grey bands). Approximate lines of constant age are shown in dashed blue.

2. As we are deep in the Knudsen regime, it becomes increasingly unsettling to use an extrapolation of the GR formalism which *was developed using the explicit assumption of small mean free paths*.

3. The alternative approach, SP, is not self-consistent and does not agree with Monte Carlo simulations.

In order to progress beyond point 1., many references have nonetheless gone ahead and obtained interesting results using the SP approach. These lead to interesting and suggestive results: increased heat transport leads to changes in the HR evolution of MS stars, notably erasing convective cores and significantly extending their main sequence lifetime [60–63]. On a color-magnitude diagram, this means a modification of the MS turnoff that depends on the local density of DM. I show this in the right panel of Fig. 2, which shows a number of trajectories for a 1 $M_\odot$ star interacting with DM with densities varying from 1-10^4 times the local DM density $\rho_0 = 0.4$ GeV cm^{-3}, produced using the MESA [35] stellar evolution software and the SP approach.

These conclusions are likely to be fairly robust, even if they are built on shaky theoretical foundations. But the above objections should emphasize the fact that more work is needed if we are to use stars and stellar populations not only as a probe for the effects of dark matter, but as a way to measure the DM properties themselves. The way forward is twofold: 1) revisiting the BCE from the non-local point of view; and 2) careful comparison with state-of-the-art Monte Carlo simulations.

4 Conclusions

The night sky is strewn with thousands upon thousands of free, ultra-massive dark matter direct detection experiments. As more precise observations make it possible to perform asteroseismology on individual stars and quality population analyses, better computational techniques will be needed to accurately predict the impact of DM on these stars in the hopes of advancing in our quest for knowledge of the dark side.

Acknowledgements

I thank Air Canada and the Canadian Government for waiting until the day after I returned home before halting all travel in March of 2020. Special thanks to Pierre Petroff, Betty Calpas and the other members of the local organizing committee for EDSU2020. I acknowledge support from the Arthur B. McDonald Institute, CFI (Canada) and MEDJCT (Ontario).

References

[1] XENON: E. Aprile *et. al.*, *Dark Matter Search Results from a One Ton-Year Exposure of XENON1T*, *Phys. Rev. Lett.* **121** (2018) 111302, [arXiv:1805.12562].

[2] A. Gould, *Weakly interacting massive particle distribution in and evaporation from the sun*, *ApJ* **321** (1987) 560–570.

[3] M. Nauenberg, *Energy transport and evaporation of weakly interacting particles in the Sun*, *Phys. Rev. D* **36** (1987) 1080–1087.

[4] G. Busoni, A. De Simone, P. Scott, and A. C. Vincent, *Evaporation and scattering of momentum- and velocity-dependent dark matter in the Sun*, *JCAP* **10** (2017) 037, [arXiv:1703.07784].

[5] K. M. Zurek, *Asymmetric Dark Matter: Theories, signatures, and constraints*, *Phys. Rep.* **537** (2014) 91–121, [arXiv:1308.0338].

[6] G. Steigman, H. Quintana, C. L. Sarazin, and J. Faulkner, *Dynamical interactions and astrophysical effects of stable heavy neutrinos*, *AJ* **83** (1978) 1050–1061.

[7] I. P. Lopes, J. Silk, and S. H. Hansen, *Helioseismology as a new constraint on supersymmetric dark matter*, *MNRAS* **331** (2002) 361–368, [astro-ph/0111530].

[8] I. Goldman and S. Nussinov, *Weakly interacting massive particles and neutron stars*, *Phys. Rev. D* **40** (1989) 3221–3230.

[9] G. Bertone and M. Fairbairn, *Compact Stars as Dark Matter Probes*, *Phys. Rev. D* **77** (2008) 043515, [arXiv:0709.1485].

[10] J. Bramante, *Dark matter ignition of type Ia supernovae*, *Phys. Rev. Lett.* **115** (2015) 141301, [arXiv:1505.07464].

[11] J. Bramante, T. Linden, and Y.-D. Tsai, *Searching for dark matter with neutron star mergers and quiet kilonovae*, *Phys. Rev. D* **97** (2018) 055016, [arXiv:1706.00001].

[12] J. F. Acevedo and J. Bramante, *Supernovae Sparked By Dark Matter in White Dwarfs*, *Phys. Rev. D* **100** (2019) 043020, [arXiv:1904.11993].

[13] J. F. Acevedo, J. Bramante, R. K. Leane, and N. Raj, *Warming Nuclear Pasta with Dark Matter: Kinetic and Annihilation Heating of Neutron Star Crusts*, *JCAP* **03** (2020) 038, [arXiv:1911.06334].

[14] N. Bozorgnia and G. Bertone, *Implications of hydrodynamical simulations for the interpretation of direct dark matter searches*, *Int. J. Mod. Phys. A* **32** (2017) 1730016, [arXiv:1705.05853].

[15] J. Bramante, A. Delgado, and A. Martin, *Multiscatter stellar capture of dark matter*, *Phys. Rev. D* **96** (2017) 063002, [arXiv:1703.04043].

[16] B. Dasgupta, A. Gupta, and A. Ray, *Dark matter capture in celestial objects: Improved treatment of multiple scattering and updated constraints from white dwarfs*, *JCAP* **08** (2019) 018, [arXiv:1906.04204].

[17] R. Garani and S. Palomares-Ruiz, *Dark matter in the Sun: scattering off electrons vs nucleons*, *JCAP* **05** (2017) 007, [arXiv:1702.02768].

[18] A. L. Fitzpatrick, W. Haxton, E. Katz, N. Lubbers, and Y. Xu, *The effective field theory of dark matter direct detection*, *JCAP* **2** (2013) 4, [arXiv:1203.3542].

[19] R. Catena and B. Schwabe, *Form factors for dark matter capture by the Sun in effective theories*, *JCAP* **1504** (2015) 042, [arXiv:1501.03729].

[20] A. C. Vincent, A. Serenelli, and P. Scott, *Generalised form factor dark matter in the Sun*, *JCAP* **1508** (2015) 040, [arXiv:1504.04378].

[21] B. Dasgupta, A. Gupta, and A. Ray, *Dark matter capture in celestial objects: light mediators, self-interactions, and complementarity with direct detection*, arXiv:2006.10773.

[22] GAMBIT: P. Athron *et. al.*, *Global analyses of Higgs portal singlet dark matter models using GAMBIT*, *Eur. Phys. J. C* **79** (2019) 38, [arXiv:1808.10465].

[23] N. Avis Kozar *in prep.* (2020).

[24] J. Lopes, T. Lacroix, and I. Lopes, *Towards a more rigorous treatment of uncertainties on the velocity distribution of dark matter particles for capture in stars*, arXiv:2007.15927.

[25] J. Silk, K. A. Olive, and M. Srednicki, *The Photino, the Sun and High-Energy Neutrinos*, *Phys. Rev. Lett.* **55** (1985) 257–259.

[26] J. S. Hagelin, K. W. Ng, and K. A. Olive, *A high-energy neutrino signature from supersymmetric relics*, *Physics Letters B* **180** (1986) 375–380.

[27] M. Srednicki, K. A. Olive, and J. Silk, *High-Energy Neutrinos from the Sun and Cold Dark Matter*, *Nucl. Phys. B* **279** (1987) 804–823.

[28] T. Gaisser, G. Steigman, and S. Tilav, *Limits on Cold Dark Matter Candidates from Deep Underground Detectors*, *Phys. Rev. D* **34** (1986) 2206.

[29] K. A. Olive and M. Srednicki, *Solar Neutrino Searches and Cold Dark Matter*, *Phys. Lett. B* **205** (1988) 553.

[30] A. E. Faraggi, K. A. Olive, and M. Pospelov, *Probing the desert with ultraenergetic neutrinos from the sun*, *Astropart. Phys.* **13** (2000) 31–43, [hep-ph/9906345].

[31] Super-Kamiokande: K. Choi *et. al.*, *Search for neutrinos from annihilation of captured low-mass dark matter particles in the Sun by Super-Kamiokande*, *Phys. Rev. Lett.* **114** (2015) 141301, [arXiv:1503.04858].

[32] IceCube: M. Aartsen *et. al.*, *Search for annihilating dark matter in the Sun with 3 years of IceCube data*, *Eur. Phys. J. C* **77** (2017) 146, [arXiv:1612.05949]. [Erratum: Eur.Phys.J.C 79, 214 (2019)].

[33] Q. Liu, J. Lazar, C. A. Argüelles, and A. Kheirandish, *χarov: a tool for neutrino flux generation from WIMPs*, arXiv:2007.15010.

[34] A. Weiss and H. Schlattl, *GARSTEC: the Garching Stellar Evolution Code. The direct descendant of the legendary Kippenhahn code*, *Ap&SS* **316** (2008) 99–106.

[35] B. Paxton, L. Bildsten, *et. al.*, *Modules for Experiments in Stellar Astrophysics (MESA)*, *ApJS* **192** (2011) 3, [arXiv:1009.1622].

[36] I. Lopes and J. Silk, *Dark matter imprint on ^8B neutrino spectrum*, *Phys. Rev. D* **99** (2019) 023008, [arXiv:1812.07426].

[37] I. Lopes and J. Silk, *Solar Constraints on Asymmetric Dark Matter*, *ApJ* **757** (2012) 130, [arXiv:1209.3631].

[38] I. Lopes, K. Kadota, and J. Silk, *Constraint on Light Dipole Dark Matter from Helioseismology*, *ApJ* **780** (2014) L15, [arXiv:1310.0673].

[39] J. Casanellas and I. Lopes, *First Asteroseismic Limits on the Nature of Dark Matter*, *ApJ* **765** (2013) L21, [arXiv:1212.2985].

[40] J. Casanellas, I. M. Brandão, and Y. Lebreton, *Stellar convective cores as dark matter probes*, *Phys. Rev. D* **91** (2015) 103535, [arXiv:1505.01362].

[41] A. Martins, I. Lopes, and J. Casanellas, *Asteroseismic constraints on asymmetric dark matter: Light particles with an effective spin-dependent coupling*, *Phys. Rev. D* **95** (2017) 023507, [arXiv:1701.03928].

[42] A. C. Vincent and P. Scott, *Thermal conduction by dark matter with velocity and momentum-dependent cross-sections*, *JCAP* **4** (2014) 19, [arXiv:1311.2074].

[43] D. N. Spergel and W. H. Press, *Effect of hypothetical, weakly interacting, massive particles on energy transport in the solar interior*, *ApJ* **294** (1985) 663–673.

[44] A. Gould and G. Raffelt, *Thermal conduction by massive particles*, *ApJ* **352** (1990) 654–668.

[45] J. Faulkner and R. L. Gilliland, *Weakly interacting, massive particles and the solar neutrino flux*, *ApJ* **299** (1985) 994–1000.

[46] R. L. Gilliland, J. Faulkner, W. H. Press, and D. N. Spergel, *Solar models with energy transport by weakly interacting particles*, *ApJ* **306** (1986) 703–709.

[47] A. Gould and G. Raffelt, *Cosmion energy transfer in stars - The Knudsen limit*, *ApJ* **352** (1990) 669–680.

[48] A. Bottino, G. Fiorentini, *et. al.*, *Does solar physics provide constraints to weakly interacting massive particles?*, *Phys. Rev. D* **66** (2002) 053005, [hep-ph/0206211].

[49] A. C. Vincent, P. Scott, and A. Serenelli, *Possible Indication of Momentum-Dependent Asymmetric Dark Matter in the Sun*, *Phys. Rev. Lett.* **114** (2015) 081302, [arXiv:1411.6626].

[50] A. C. Vincent, P. Scott, and A. Serenelli, *Updated constraints on velocity and momentum-dependent asymmetric dark matter*, *JCAP* **11** (2016) 007, [arXiv:1605.06502].

[51] I. Lopes, P. Panci, and J. Silk, *Helioseismology with Long-range Dark Matter-Baryon Interactions*, *ApJ* **795** (2014) 162, [arXiv:1402.0682].

[52] B. Geytenbeek, S. Rao, *et. al.*, *Effect of electromagnetic dipole dark matter on energy transport in the solar interior*, *JCAP* **03** (2017) 029, [arXiv:1610.06737].

[53] M. T. Frandsen and S. Sarkar, *Asymmetric dark matter and the Sun*, *Phys. Rev. Lett.* **105** (2010) 011301, [arXiv:1003.4505].

[54] M. Taoso, F. Iocco, G. Meynet, G. Bertone, and P. Eggenberger, *Effect of low mass dark matter particles on the Sun*, *Phys. Rev. D* **82** (2010) 083509, [arXiv:1005.5711].

[55] D. T. Cumberbatch, J. A. Guzik, J. Silk, L. S. Watson, and S. M. West, *Light WIMPs in the Sun: Constraints from helioseismology*, *Phys. Rev. D* **82** (2010) 103503, [arXiv:1005.5102].

[56] M. Asplund, N. Grevesse, and A. J. Sauval, *The Solar Chemical Composition*, in *Cosmic Abundances as Records of Stellar Evolution and Nucleosynthesis* (I. Barnes, Thomas G. and F. N. Bash, eds.) **336** (2005) 25.

[57] M. Asplund, N. Grevesse, A. Sauval, and P. Scott, *The chemical composition of the Sun*, *Ann. Rev. Astron. Astrophys.* **47** (2009) 481–522, [arXiv:0909.0948].

[58] A. Serenelli, S. Basu, J. W. Ferguson, and M. Asplund, *New Solar Composition: The Problem With Solar Models Revisited*, *ApJ* **705** (2009) L123–L127, [arXiv:0909.2668].

[59] P. Scott, M. Fairbairn, and J. Edsjö, *Dark stars at the Galactic Centre - the main sequence*, *MNRAS* **394** (2009) 82–104, [0809.1871].

[60] A. R. Zentner and A. P. Hearin, *Asymmetric Dark Matter May Alter the Evolution of Low-mass Stars and Brown Dwarfs*, *Phys. Rev. D* **84** (2011) 101302, [arXiv:1110.5919].

[61] F. Iocco, M. Taoso, F. Leclercq, and G. Meynet, *Main Sequence Stars with Asymmetric Dark Matter*, *Phys. Rev. Lett.* **108** (2012) 061301, [arXiv:1201.5387].

[62] T. Hurst, *Astrophysical probes of dark matter*. PhD thesis, Pittsburgh U., 2016.

[63] J. Lopes and I. Lopes, *Asymmetric Dark Matter Imprint on Low-mass Main-sequence Stars in the Milky Way Nuclear Star Cluster*, *ApJ* **879** (2019) 50, [arXiv:1907.05785].

[64] J. L. Fraser-Leach and A. C. Vincent *In Preparation* (2020).

[65] K. Loggins, *Danger Zone*, *Columbia Records* (1986).

What is dark matter made of?

Bruce Hoeneisen

e-mail: bhoeneisen@usfq.edu.ec

Universidad San Francisco de Quito

Presented at the 3rd World Summit on Exploring the Dark Side of the Universe
Guadeloupe Islands, March 9-13 2020

Abstract

I present an overview of detailed and redundant measurements of dark matter properties, and discuss discrepancies with current limits.

1 Introduction

At the 2020 Guadeloupe meeting I presented measurements of dark matter properties published in References [1], [2], [3], [4], and [5]. These detailed, precise and redundant measurements, summarized in Table 1 below, are in disagreement with some limits on thermal relic masses [6] [7] [8] [9]. In these Proceedings I present a short overview of the measurements, and a few comments on the disagreements.

Figure 1: Guadeloupe Islands.

2 Motivation

We assume that dark matter is a gas of particles, either fermions or bosons. As the universe expands, this gas becomes non-relativistic. We assume that these non-relativistic particles have negligible interactions with the standard model sector, and negligible inelastic self interactions, except for gravitation. Let a be the expansion parameter of the universe normalized to $a = 1$ at the present time. As the universe expands and cools, the root-mean-square (rms) velocity of the dark matter particles scales as $\propto 1/a$, and the dark matter density scales as $\propto 1/a^3$:

$$v_{h\text{rms}}(a) = \frac{v_{h\text{rms}}(1)}{a}, \qquad \rho_h(a) = \frac{\Omega_c \rho_{\text{crit}}}{a^3}. \tag{1}$$

Note that the adiabatic invariant $v_{h\text{rms}}(a)/\rho_h(a)^{1/3}$ is independent of a. (Throughout, the sub-index h stands for "dark matter halo". We use the standard notation of [10].) The adiabatic invariant remains constant if the mean number of particles per orbital remains constant.

Now consider a free observer in a density peak in the expanding universe. This observer feels no gravity. The matter in this peak expands, reaches maximum expansion, and then, due to gravitational attraction, collapses adiabatically forming the core of a galaxy. Let $\sqrt{3}\left\langle v_{rh}^2 \right\rangle^{1/2}$ be the rms velocity of dark matter particles in the galaxy (v_{rh} is the radial component), and $\rho(r \to 0)$ be the dark matter density in the core of the galaxy. Adiabatic expansion implies

$$\frac{v_{h\text{rms}}(a)}{\rho_h(a)^{1/3}} = \frac{v_{h\text{rms}}(1)}{(\Omega_c \rho_{\text{crit}})^{1/3}} = \frac{\sqrt{3}\left\langle v_{rh}^2 \right\rangle^{1/2}}{\rho(r \to 0)^{1/3}}. \tag{2}$$

The interest in Equation (2) is that we can measure both $\left\langle v_{\text{rh}}^2 \right\rangle^{1/2}$ and $\rho_h(r \to 0)$, and hence $v_{h\text{rms}}(1)$, in spiral galaxies. Furthermore, the core of spiral galaxies can have 10^8 times the mean dark matter density of the universe [3], and therefore, is a promising place to study dark matter.

In conclusion, we *predict* that the adiabatic invariant $v_{h\text{rms}}(1)$ is of cosmological origin, and therefore is the same for all relaxed, steady-state, spiral galaxies.

Fermions Observable	$v_{h\text{rms}}(1)$ [km/s]	$a'_{h\text{NR}} \times 10^6$	m_h [eV]	k_{fs} [Mpc^{-1}]	$\log_{10}(M_{\text{fs}}/M_\odot)$
Spiral galaxies	0.76 ± 0.29	2.54 ± 0.97	79^{+35}_{-17}	$0.80^{+0.42}_{-0.24}$	12.08 ± 0.50
No freeze-in/-out	$0.81^{+0.47}_{-0.25}$	$2.69^{+1.57}_{-0.84}$	75 ± 23	0.76 ± 0.31	12.14 ± 0.52
M_s distribution				$0.90^{+0.44}_{-0.34}$	11.93 ± 0.56
Bosons Observable	$v_{h\text{rms}}(1)$ [km/s]	$a'_{h\text{NR}} \times 10^6$	m_h [eV]	k_{fs} [Mpc^{-1}]	$\log_{10}(M_{\text{fs}}/M_\odot)$
Spiral galaxies	0.76 ± 0.29	2.54 ± 0.97	51^{+22}_{-11}	$0.51^{+0.28}_{-0.15}$	12.66 ± 0.50
No freeze-in/-out	$0.26^{+0.16}_{-0.08}$	$0.88^{+0.52}_{-0.28}$	113 ± 35	1.26 ± 0.50	11.49 ± 0.52
M_s distribution				$0.90^{+0.44}_{-0.34}$	11.93 ± 0.56

Table 1: Summary of three independent measurements of the adiabatic invariant $v_{h\text{rms}}(1)$ [4], the expansion parameter at which dark matter particles become non-relativistic $a'_{h\text{NR}} \equiv v_{h\text{rms}}(1)/c$, the cut-off wavenumber of warm dark matter k_{fs}, the transition galaxy mass M_{fs}, and the mass m_h of dark matter particles (for the case of zero chemical potential). The top (bottom) table is for fermions with $N_f = 2$ (bosons with $N_b = 1$). Update of Table 2 of Reference [4].

3 Validation

To test this prediction we study spiral galaxies in the "Spitzer Photometry and Accurate Rotation Curves" (SPARC) sample [11]. The SPARC galaxy sample includes a very broad range of lumi-

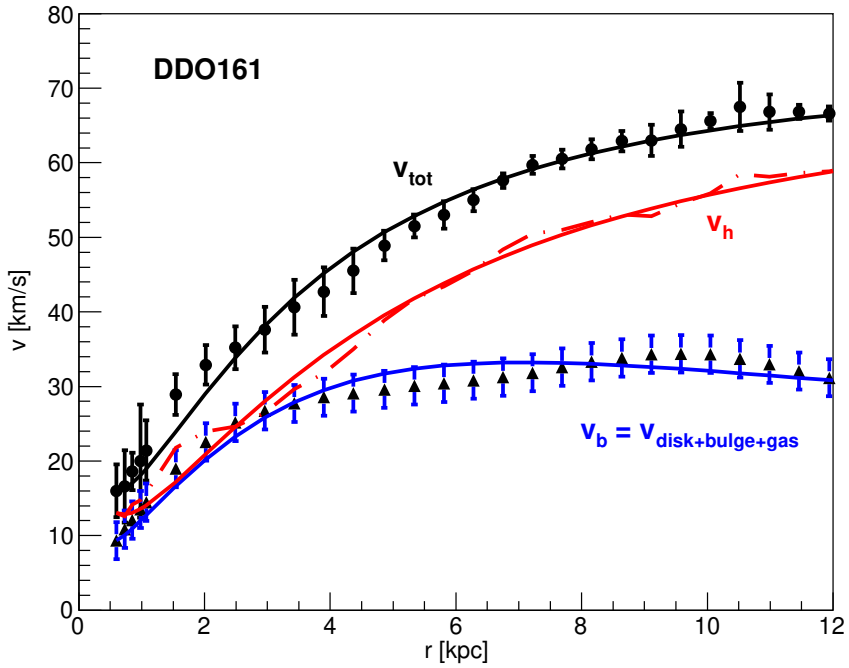

Figure 2: Observed rotation curve $v_{\rm tot}(r) \equiv v(r)$ (dots) and the baryon contribution $v_b(r)$ (triangles) of galaxy DDO161 [11]. The dot-dash line is from $v_h(r)^2 = v(r)^2 - v_b(r)^2$. The solid lines are obtained by numerical integration [1].

nosities, surface brightnesses, rotation velocities, and Hubble types. As an example, the rotation curves of galaxy DDO161 are presented in Figure 2. $v_{\rm tot}(r) \equiv v(r)$ is the velocity of rotation of a test particle in a circular orbit of radius r in the plane of the galaxy. This rotation velocity $v(r)$ has contributions from baryons (stars in the disk and bulge, and gas), and from the halo of dark matter: $v(r)^2 = v_b(r)^2 + v_h(r)^2$. The flat rotation velocity $v(r)$ at large r determines the root-mean-square (rms) of the radial component of the velocities of the dark matter particles $\langle v_{rh}^2 \rangle^{1/2} = v_{\rm flat}/\sqrt{2}$. The slopes of $v(r)$ and $v_b(r)$ at small r determine the dark matter density in the core of the galaxy: $\rho_h(r \to 0) = 3\left[v(r)^2 - v_b(r)^2\right]/(4\pi G r^2)$. So we are able to measure the adiabatic invariant (2) for each SPARC galaxy.

To take full advantage of all measured rotation velocities $v(r)$ and $v_b(r)$, we fit four boundary conditions needed to integrate differential equations describing two self-gravitating non-relativistic gases: dark matter and baryons. These numerical integrations are shown with continuous lines in Figure 2. Note that we do not fit templates. Good fits are obtained assuming that the dark matter rms velocity $\sqrt{3}\,\langle v_{rh}^2 \rangle^{1/2}$ is independent of r. This important observation implies that the velocities of dark matter particles satisfy approximately the Boltzmann distribution. How did dark matter acquire the Boltzmann distribution of velocities? Was dark matter ever in thermal equilibrium with "something"? From the rotation curves of 40 well measured, relaxed, steady-state galaxies we obtain the distribution of $v_{h\rm rms}(1)$ presented in Figure 3 [3]. This distribution has a mean 0.87 km/s, and a standard deviation of 0.27 km/s. This small relative standard deviation is noteworthy given that the galaxies in this sample have luminosities, central densities, and central surface brightnesses that span three orders of magnitude. We do not find any statistically significant dependence of $v_{h\rm rms}(1)$ on the

galaxy properties, see Table 2.

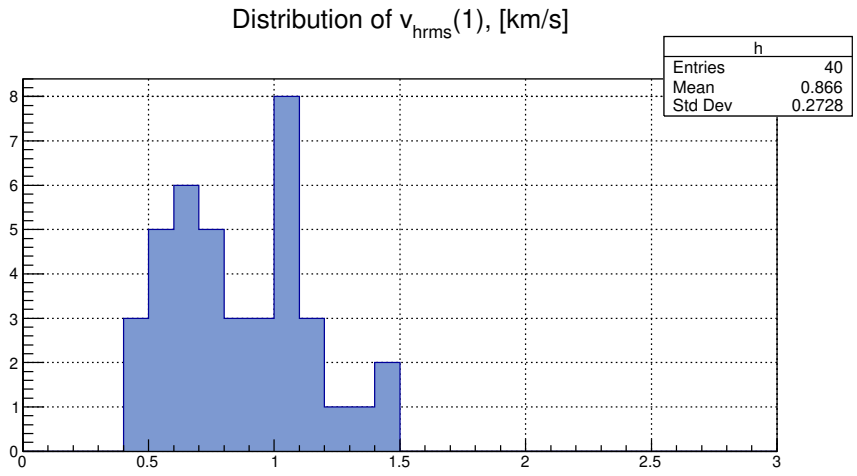

Figure 3: Distribution of the adiabatic invariant $v_{h\mathrm{rms}}(1)$ obtained from fits to rotation curves of 40 spiral galaxies in the SPARC sample [11]. Case for chemical potential $\mu \ll 0$.

From Figure 3, and a similar figure for fermions with chemical potential $\mu = 0$ [3], we take

$$v_{h\mathrm{rms}}(1) = (0.82 \pm 0.31)\sqrt{1-\kappa_h}\ \mathrm{km/s} = 0.76 \pm 0.29\ \mathrm{km/s}. \tag{3}$$

The factor $\sqrt{1-\kappa_h}$ is a correction for possible dark matter rotation. We take $\kappa = 0.15 \pm 0.15$ [1] [2] [3]. This range is also consistent with $v_{h\mathrm{rms}}(1)$ obtained from 10 different galaxies in the THINGS sample [2] [12].

Galaxy selection	N	Mean $v_{h\mathrm{rms}}(1)$ [km/s]	Std. dev. [km/s]
All	40	0.866	0.273
$L_{3.6} < 1 \times 10^9 L_\odot$	11	0.838	0.297
$L_{3.6} > 4 \times 10^9 L_\odot$	11	1.036	0.192
$M_{HI} < 1 \times 10^9 M_\odot$	17	0.714	0.239
$\langle v_{rh}^2 \rangle^{1/2} < 50$ km/s	17	0.786	0.259
$\langle v_{rh}^2 \rangle^{1/2} > 60$ km/s	16	0.969	0.227
de Vaucouleurs class 5, 6 or 7	15	0.820	0.277
de Vaucouleurs class 9 or 10	18	0.869	0.258
SBdisk $< 100 \times 10^9 L_\odot/\mathrm{pc}^2$	10	0.843	0.174
$\rho_h(0) > \rho_b(0)$	37	0.842	0.255

Table 2: Mean and standard deviation of $v_{h\mathrm{rms}}(1)$ for several galaxy selections [3]. N is the number of galaxies in the selection. $L_{3.6}$ is the absolute luminosity at 3.6 μm. M_{HI} is the mass of atomic hydrogen gas (HI). "SBdisk" is the Disk Central Surface Brightness at 3.6 μm. The galaxy classes are 5 = Sc, 6 = Scd, 7 = Sd, 9 = Sm, 10 = Im. The data is from the SPARC sample of spiral galaxies [11].

In conclusion, we observe that, within experimental uncertainties, the "adiabatic invariant" $v_{h\mathrm{rms}}(1)$ is approximately the same for all relaxed, steady-state, galaxies in our sample. This observation suggests that $v_{h\mathrm{rms}}(1)$ is indeed of cosmological origin.

We define $a'_{h\text{NR}} \equiv v_{h\text{rms}}(1)/c$. Dark matter is ultra-relativistic for $a \ll a'_{h\text{NR}}$, and non-relativistic for $a \gg a'_{h\text{NR}}$. Note that the mass of matter inside the horizon at $a = a'_{h\text{NR}}$ is $\approx 3 \times 10^{11} M_\odot$, not much smaller than the Milky Way mass. Is this a coincidence?

4 Lower bounds to the dark matter particle mass m_h

As we lower the dark matter particle mass m_h in the fits to the observed spiral galaxy rotation curves, we obtain disagreement due to the onset of Fermi-Dirac or Bose-Einstein degeneracy in the galaxy core. This disagreement sets lower bounds to m_h of 16 eV for fermions, and 45 eV for bosons, at 99 % confidence [1]. These limits exclude Einstein condensation, and exclude full fermion degeneracy. Chemical potential $\mu \leq 0$ is allowed for both fermions and bosons.

5 Why a core and not a cusp?

Consider galaxy UGC11914. The measured dark matter density in the core $\rho_h(r \to 0)$ is $(2.1 \pm 0.5) \times 10^8$ times the mean dark matter density of the universe $\Omega_c \rho_{\text{crit}}$ [3]! What prevented dark matter from collapsing to infinite density as suggested by simulations in the cold dark matter ΛCDM scenario? Why a core and not a cusp? The answer: a galaxy with a given $v_{\text{flat}} = \sqrt{2} \left\langle v_{rh}^2 \right\rangle^{1/2}$ has a well defined dark matter density in the core $\rho_h(r \to 0)$ given by Equation (2).

6 Free-streaming

Let $P(k)$ be the power spectrum of linear density perturbations in the cold dark matter ΛCDM model. k is the comoving wavenumber. If dark matter is warm, the power spectrum becomes $P(k)\tau^2(k/k_{\text{fs}})$, where $\tau^2(k/k_{\text{fs}})$ is a cut-off factor due to dark matter free-streaming. We use the approximation $\tau^2(k/k_{\text{fs}}) = \exp\left(-k^2/k_{\text{fs}}^2\right)$ [5]. The cut-off wavenumber k_{fs} can be calculated from $a'_{h\text{NR}}$, see Reference [4]. We obtain $k_{\text{fs}} = 0.80^{+0.42}_{-0.24}$ Mpc^{-1}. The halo "transition" mass, corresponding to a gaussian cut-off factor, is defined to be $M_{\text{fs}} \equiv 4\pi(1.555/k_{\text{fs}})^3 \Omega_m \rho_{\text{crit}}/3$. Results derived from Equation (3) are presented in Table 1. Note that the measured M_{fs} is similar to the Milky Way mass, and hence addresses the "small scale crisis" problems.

7 Measurement of the cut-off wavenumber with galaxy stellar mass distributions

Figure 4 compares galaxy stellar mass distribution predictions with observations at $z \approx 4.5$. The cold and warm dark matter models coincide for halo masses $M_h > M_{\text{fs}}$, and differ for $M_h < M_{\text{fs}}$. Therefore, to measure the cut-off wavenumber k_{fs}, we first adjust the relation between the halo mass M_h and the stellar mass M_s to obtain agreement for $M_h > M_{\text{fs}}$, and obtain $\log_{10}(M_s/M_h) = -1.5$, consistent with Figure 9 of Reference [13]. From Figure 4, and similar figures at $z = 6$, 7, and 8, we obtain $k_{\text{fs}} = 0.90^{+0.44}_{-0.34}$ Mpc^{-1} [5]. The agreement with the value of k_{fs} obtained in Section 6 is evidence that k_{fs} is indeed due to free-streaming, and confirms, once again, that $v_{h\text{rms}}(1)$ is of cosmological origin.

8 Warm dark matter with no freeze-in and no freeze-out

The measurements of $v_{h\text{rms}}(1)$, or equivalently k_{fs}, described above do not determine the dark matter particle mass m_h, only the dark matter temperature-to-mass ratio $T_h(a)/m_h$. To obtain m_h and $T_h(a)$

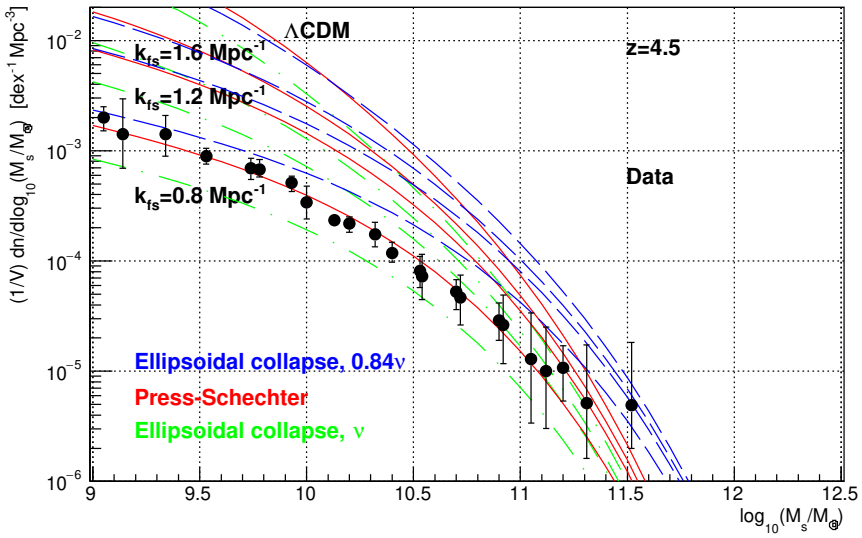

Figure 4: Calculated stellar mass functions with the Press-Schechter [14], Ellipsoidal Collapse with $\tilde{\nu} = \nu$, and Ellipsoidal Collapse with $\tilde{\nu} = 0.84\nu$ [15] [16] approximations, for ΛCDM, and ΛWDM with $k_{\rm fs} = 1.6, 1.2$, and 0.8 Mpc^{-1}, at redshift $z = 4.5$, compared with observations at $z \approx 4.5$ [13] [17] [18] [19]. $\log_{10}(M_h) = \log_{10}(M_s) + 1.5$.

separately, we need one more constraint. It turns out that if we assume that dark matter decoupled while ultra-relativistic and has zero chemical potential, then dark matter was in thermal equilibrium with the standard model sector in the early universe, *with the measured adiabatic invariant* $v_{hrms}(1)$ *and the measured cosmic microwave background radiation temperature* T_0 [1] [2] [4]. This miracle is either a coincidence, or strong evidence that dark matter was once in diffusive and thermal equilibrium with the standard model sector in the early universe, and decoupled from the standard model sector and from self annihilations while still ultra-relativistic. In other words, strong evidence that dark matter has no freeze-in and no freeze-out. The assumption of no freeze-in and no freeze-out leads to parameters presented in Table 1.

9 Comments on discrepancies with thermal relic limits

Fermion phase space density limits: Limits on fermion dark matter mass, from phase space density considerations, are obtained from a study of dwarf spheroidals (dSph) of the Milky Way [6]. From the Pauli exclusion principle the limit obtained is $m_{\rm DEG} = 0.41$ keV. Stronger limits are obtained with additional assumptions, e.g. the Tremaine-Gunn limit. These limits assume that dwarf spheroids are dominated by dark matter. However, at this 2020 Guadeloupe meeting, Francois Hammer presented evidence that dwarf spheroids have negligible amounts of dark matter [20], [21], [22], [23], so these limits need to be revised. In Section 4 above we present the corresponding limits from spiral galaxy rotation curves.

The UV luminosity function limit: We comment on Reference [8]. The analysis in [8] is very similar to our analysis in [5]. The conclusions, however, are quite different. In [5] we obtain excellent agreement with observations, see Figure 4, while [8] obtains a limit on the thermal relic mass $m_h \geq 2.4$ keV at 2σ.

There are three differences between these analysis: 1) The cut-off function in [8] has the form

$\tau^2 = \left[1 + (\alpha k)^{2\mu}\right]^{-10/\mu}$, originally derived in [24]. This functional form is numerically the same as our gaussian cut-off function for all practical purposes. The values of α, and the equivalent $k_{\rm fs}$'s, for several early thermal relic masses, are presented in Table 3. The values of $k_{\rm fs}$ used in [5], calculated with the method outlined in [4], is also presented in the Table. 2) To calculate the variance $\sigma^2(M, z)$, needed by the Press-Schechter calculation of the galaxy mass distribution, Reference [8] uses the top-hat window function in k-space, while in [5] we use the gaussian window function. The "knee" between the asymptotes for $k \ll k_{\rm fs}$ and $k \gg k_{\rm fs}$ is more pronounced in the former, and more rounded in the latter analysis. However, neither 1) nor 2) can account for the very different conclusions. 3) The main source of difference between the two analysis appears to be the different approximations for $P(k)$. The analysis in [5] uses Eq. (8.1.42) of Reference [25] with the astrophysical parameters in [10]. This approximation to $P(k)$ is valid for all k, so normalizing $P(k)$ to the measured σ_8 is accurate, and coincides with the Planck normalization in [10]. Reference [8] does not specify the approximation used for $P(k)$, and obtains a steeper slope in Figure 1 of [8] at large M than we do.

m_h	$1/\alpha$ [8]	$k_{\rm fs}$ [8]	$k_{\rm fs}$ [5][4]	k_J
3000 eV	48.5 Mpc^{-1}	18.9 Mpc^{-1}	20.9 Mpc^{-1}	39.6 Mpc^{-1}
1000 eV	14.3 Mpc^{-1}	5.59 Mpc^{-1}	7.8 Mpc^{-1}	13.2 Mpc^{-1}
79 eV	0.86 Mpc^{-1} *	0.33 Mpc^{-1} *	0.86 Mpc^{-1}	1.04 Mpc^{-1}

Table 3: Relation between the early thermal relic mass m_h, and the corresponding free-streaming cut-off wavenumber $k_{\rm fs}$, obtained by the methods described in References [8], and [5][4]. Also shown is the Jeans wavenumber k_J: modes with $k < k_J$ grow due to gravity, modes with $k > k_J$ are damped due to free-streaming. * Out of range?

Lyman-α forest limits: The Lyman-α forest allows measurements of the neutral hydrogen density profile along the line of sight to far away quasars (at redshifts $z \approx 5.5$). From the analysis of these density profiles, with model dependent simulations of the inter-galactic medium (including the highly ionized hydrogen), the cut-off wavenumber $k_{\rm fs}$ is excluded in the range from ≈ 0.4 Mpc^{-1} to ≈ 27 Mpc^{-1} [7]. In comparison, the measured galaxy stellar mass distributions presented in [5] obtain $k_{\rm fs} = 0.90^{+0.44}_{-0.34}$ Mpc^{-1} [5]. So, these two analysis, based on very different *data* sets, are incompatible. This discrepancy needs to be resolved.

Limits from quasar gravitational lensing: We consider Reference [9]. Strong lensing with multiple images often have anomalous flux ratios between the images. The anomaly may be due to halos with mass in the range $10^6 M_\odot$ to $10^8 M_\odot$ along the line of sight [9]. To constrain $k_{\rm fs}$ it is necessary to predict the halo mass function in the mass range $10^6 M_\odot$ to $10^8 M_\odot$ at redshifts $z < 3$. Do we really know how to predict the halo mass function at these low masses and redshifts where the Press-Schechter formalisms is already saturated [5]? Note that the Press-Schechter method, and its Sheth-Tormen modification, can only be used so long as the fraction of mass locked up in halos with mass greater than M, $F(M, z)$, is less than approximately 0.01. If $F(M, z) > 0.01$, a "would be galaxy of mass M" may "not fit", will loose mass to neighboring galaxies, and will collapse as a halo with mass $< M$ [4]. At $z < 3$, the Press-Schechter method for halos of mass $M < 10^{12} M_\odot$ is already saturated, and does not predict correctly the galaxy mass function [5].

10 Extension of the Standard Model

An integration of the Boltzmann equation for the production of sterile Majorana neutrinos after Electroweak Symmetry Breaking (when sterile and active neutrinos acquire mass and couple together) is presented in Figure 5. This example is consistent with the measurements presented in Table 1. Such sterile Majorana neutrinos evade all current (and future?) dark matter searches, and are consistent with Big Bang Nucleosynthesis.

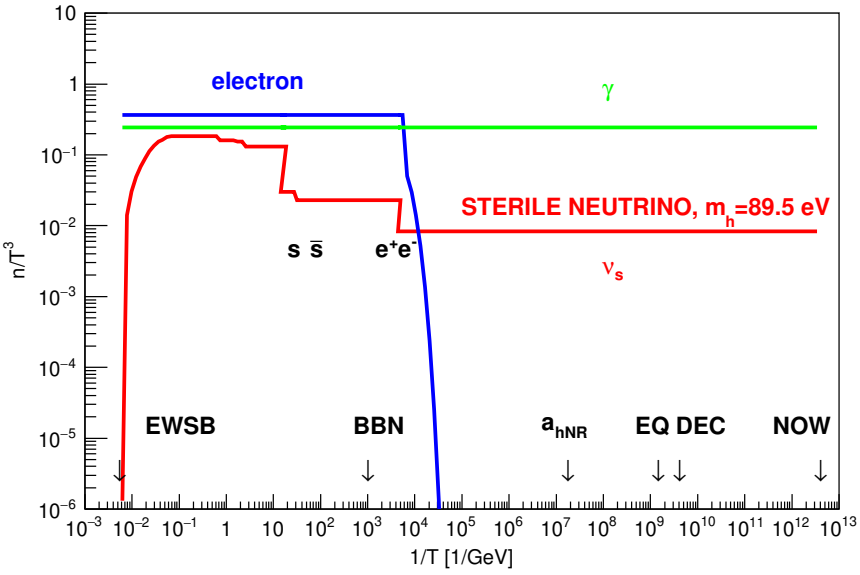

Figure 5: Example. Number density n of photons, electrons, and Majorana sterile neutrino dark matter particles with $m_h = 89.5$ eV, divided by T^3, as a function of $1/T$. T is the photon temperature. The lifetime of this sterile Majorana neutrino is 7×10^{27} yr. Big Bang Nucleosynthesis (BBN) is satisfied. From Reference [1].

11 Conclusions

We have presented detailed, precise, and redundant *measurements* of dark matter properties, that do not depend on any particular extension of the standard model, see Table 1. These measurements result in several "miracles": 1) the adiabatic invariant $v_{h\mathrm{rms}}(1)$ is the same, within experimental uncertainties, for 50 measured spiral galaxies, indicating that $v_{h\mathrm{rms}}(1)$ is of cosmological origin; 2) the measured $v_{h\mathrm{rms}}(1)$ obtains k_{fs} in agreement with k_{fs} obtained from the galaxy stellar mass functions, demonstrating that k_{fs} is due to free-streaming and $v_{h\mathrm{rms}}(1)$ is of cosmological origin; 3) the measured $v_{h\mathrm{rms}}(1)$ is consistent with no freeze-in and no freeze-out; 4) the measured transition mass M_{fs} is similar to the Milky Way mass, and so addresses the "small scale crisis"; 5) the mass of matter inside the horizon at $a'_{h\mathrm{NR}}$ is $\approx 3 \times 10^{11} M_\odot$, not much less than the Milky Way mass. Are these "miracles" coincidences, or are they suggesting that these measurements are indeed correct? In conclusion, these measurements should be taken seriously, and the disagreements with limits need to be resolved. Nature will have the last word.

Acknowledgements

I thank Pierre Petroff and the sponsors for a most interesting and dramatic meeting: not easy getting back home with the world falling apart!

References

[1] Hoeneisen, B. (2019) A Study of Dark Matter with Spiral Galaxy Rotation Curves. *International Journal of Astronomy and Astrophysics*, **9**, 71-96.

[2] Hoeneisen, B. (2019) A Study of Dark Matter with Spiral Galaxy Rotation Curves. Part II. *International Journal of Astronomy and Astrophysics*, **9**, 133-141.

[3] Hoeneisen, B. (2019) The adiabatic invariant of dark matter in spiral galaxies. *International Journal of Astronomy and Astrophysics*, **9**, 355-367.

[4] Hoeneisen, B. (2019) Simulations and Measurements of Warm Dark Matter Free-Streaming and Mass. *International Journal of Astronomy and Astrophysics*, **9**, 368-392. https://doi.org/10.4236/ijaa.2019.94026

[5] Hoeneisen, B. (2020) Cold or Warm Dark Matter?: A Study of Galaxy Stellar Mass Distributions *International Journal of Astronomy and Astrophysics*, **10**, 57-70. https://doi.org/10.4236/ijaa.2020.102005

[6] Boyarsky, A., Ruchayskiyc, O., and Iakubovskyi, D. (2009) A lower bound on the mass of Dark Matter particles, https://arxiv.org/abs/0808.3902

[7] Baur, J., *et al.* (2016) Lyman-alpha Forests cool WarmDark Matter https://arxiv.org/pdf/1512.01981.pdf

[8] Menci N., Grazian A., Castellano M., Sanchez N.G. (2016) A Stringent Limit on the Warm Dark Matter Particle Masses from the Abundance of z=6 Galaxies in the Hubble Frontier Fields

[9] M. Miranda, A.V. Macciò (2007) Constraining Warm Dark Matter using QSO gravitational lensing, Mon. Not. R. Astron. Soc.000, 000–000 (2007), https://arxiv.org/pdf/0706.0896.pdf

[10] Tanabashi, M., *et al.*, (Particle Data Group) (2018) The Review of Particle Physics. *Physical Review* D, **98**, Article ID: 030001.

[11] Lelli F., McGaugh S. S., Schombert (2016), SPARC: Mass models for 175 disk galaxies with Spitzer Photometry and Accurate Rotation Curves *The Astronomical Journal*, 152:157. doi:10.3847/0004-6256/152/6/157 The data in digital form is publicly available in files SPARC_Lelli2016c.mrt and LTG_data.txt.

[12] de Blok, W.J.G., *et al.* (2008), High-Resolution Rotation Curves and Galaxy Mass Models from THINGS. *The Astronomical Journal*, **136**, 2648-2719.

[13] Lapi, A. *et al.* (2017) Stellar mass function of active and quiescent galaxies via the continuity equation, https://arxiv.org/pdf/1708.07643.pdf

[14] Press, W.H., and Schechter, P. (1974) Formation of galaxies and clusters of galaxies by self-similar gravitational condensation. *The Astrophysical Journal*, **187**, 425-438.

[15] Sheth R.K., Tormen G., (1999) Large-scale bias and the peak background split, Mon. Not. R. Astron. Soc., **308**, 119-126

[16] Sheth, R.K., Mo, H.J., Tormen, G. (2001), Ellipsoidal collapse and an improved model for the number and spatial distribution of dark matter haloes, Mon. Not. R. Astron. Soc. **323**, 1-12

[17] Song, M., Finkelstein, S. L., Ashby, M. L. N., *et al.* (2016) The Evolution of the Galaxy Stellar Mass Function at $z = 4$ - 8: A Steepening Low-mass-end Slope with Increasing Redshift, ApJ, **825**, 5

[18] Grazian, A., Fontana, A., Santini, P., *et al.* (2015) The galaxy stellar mass function at $3.5 \leq z \leq 7.5$ in the CANDELS/UDS, GOODS-South, and HUDF fields, A & A, **575**, A96

[19] Davidzon, I., Ilbert, O., Laigle, C., *et al.* (2017) The COSMOS2015 galaxy stellar mass function: 13 billion years of stellar mass assembly in 10 snapshots, ApJ, in press, arXiv:1701.02734

[20] Hammer, F., Yang, Y. B., Arenou, F., Puech, M., Flores, H., Babusiaux, C., (2019) On the absence of dark matter in dwarf galaxies surrounding the Milky Way. ApJ, 883, 171

[21] Hammer, F., Yang Y., Arenou F., Wang J., Li H., Bonifacio P., and Babusiaux, C. (2020) Orbital Evidences for Dark-matter-free Milky Way Dwarf Spheroidal Galaxies.

[22] Yang Y., Hammer F., Fouquet S., Flores H., Puech M., Pawlowski M.S., and Kroupa P. (2014) Reproducing properties of MW dSphs as descendants of DM-free TDGs. MNRAS442,2419–2433

[23] Hammer F., Yang Y. B., Arenou, F., Babusiaux, C., PuechM., Flores H., (2018), Galactic Forces Rule the Dynamics of Milky Way Dwarf Galaxies. ApJ, 860, 76

[24] Bode, P., Ostriker, J.P., Turok, N. (2001) Halo Formation in Warm Dark Matter Models. *The Astrophysical Journal*, 556, 93

[25] Steven Weinberg, Cosmology, Oxford University Press (2008)

The Muon Puzzle in Cosmic Ray Induced Air Showers and possible solutions

Hans Dembinski

e-mail: hans.dembinski@tu-dortmund.de

TU Dortmund, Otto-Hahn-Str. 4a, 44227 Dortmund, Germany

Presented at the 3rd World Summit on Exploring the Dark Side of the Universe
Guadeloupe Islands, March 9-13 2020

Abstract

High-energy cosmic rays are messengers of extreme astrophysical events and therefore offer an unique view into the universe. High-energy cosmic rays induce particle cascades, called air showers, in Earth's atmosphere, which are also the main sources of diffuse background for neutrino and gamma ray observatories. Air showers are the only feasible way to observe high-energy cosmic rays. Inference of cosmic ray properties requires a quantitatively correct physical model of the hadronic interactions in an air shower. Current models are challenged by the Muon Puzzle: a growing discrepancy in the description of muons produced in air showers over shower energies from a few PeV to tens of EeV, which was confirmed in 2018 at 8σ by a collaboration of eight air shower experiments. The Muon Puzzle points to a common mismodeling of hadron production in soft hadron-ion collisions and thus presents a unique opportunity to learn more about non-perturbative QCD in hadron–nucleus collisions. To address it, several experiments at the LHC study forward hadron-production in proton-ion collisions. Very important in the next years will be the planned measurements with oxygen beams in the LHC to study proton-oxygen collisions at the highest energies.

1 Introduction

Cosmic rays are highly energetic nuclei from astrophysical sources. They are charged and bent onto chaotic paths by extrasolar magnetic fields and appear isotropic in the sky. The arrival directions cannot be used to learn about their origins, but the energy spectrum and the elemental composition carry an imprint of the sources.

Cosmic rays with energies larger than 10^{15} eV can only be indirectly observed via extensive air showers. By measuring the energy deposit of the air shower, the longitudinal depth $X_{\max}$ of its maximum in the atmosphere and the muon abundance N_μ, one can infer the energy and mass (which is identifying the element) of the cosmic ray. A detailed understanding of the hadronic physics in an air shower is needed to accurately infer energy and mass from air shower observables. The actual observables can be well measured with an accuracy of 10 % of the proton–iron difference by leading experiments [1], but the inferred mass is ambiguous, because air showers are not consistently described by simulations.

The problem is illustrated by Fig. 1, in which the elemental composition is summarized by the mean-logarithmic mass $\langle \ln A \rangle$ and shown as a function of the cosmic-ray energy E. The predictions for $\langle \ln A \rangle$ (lines) for different origin theories vary strongly. It is technically feasible to measure $\langle \ln A \rangle$ accurately enough in leading experiments to severely constrain origin theories. However, actual measurements form wide envelopes due to variations in the hadronic interaction models used to simulate

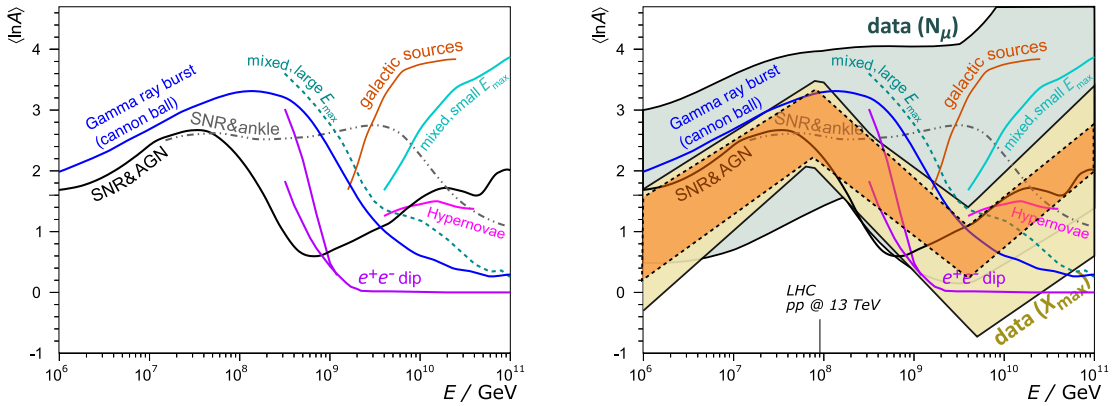

Figure 1: Mass composition of cosmic rays quantified by $\langle \ln A \rangle$ as a function of cosmic-ray energy E. Model predictions (markers and lines) are compared to data bands, all taken from the review by Kampert and Unger [2]. The left plot shows predictions from astrophysical models that assume different dominant sources. The right plot shows an overlay of the spread of experimental data, grouped by the type of air shower variable used ($X_{\rm max}$ or N_μ, see text for details). The dotted band is a projection of the purely experimental uncertainties in current leading experiments. The arrow at the bottom shows a collisions at the LHC equivalent in center-of-mass energy to the first interaction.

the air shower development (different experiments use different interaction models to convert their measurements to $\langle \ln A \rangle$).

The disagreement between the mass composition inferred from N_μ and $X_{\rm max}$ is the main obstacle. Muon measurements above about 10^{17} eV suggest a heavier mass composition than measurements based on the shower depth [2]. When combined, the measurements cover the whole parameter space and no theory can be excluded. The average composition is not expected to be heavier than iron, but that is suggested by several muon measurements [3–5]. This discrepancy between air shower simulations and measurements is called the Muon Puzzle.

Muons are produced after several generations of hadronic interactions in air when light mesons decay rather than interact again with air nuclei. The number of muons produced in this way is a function of several characteristics of microscopic hadronic interactions in air showers [6,7]. Influential are the number of light hadrons produced and the fraction of energy diverted into neutral pions for particles produced in the forward region. More data on the production of light hadrons in the forward direction is needed from collider experiments [8] and studies are ongoing, in particular in LHCb. The common disagreement of all hadronic interaction models – which are tuned to collider data on centrally produced hadrons – with air shower data suggests that something fundamental is off in our understanding of light hadron production in the forward direction, which is governed by soft-QCD.

2 Experimental data on the Muon Puzzle in air showers

In 2018, a working group was formed by members of eight leading air shower experiments for the UHECR 2018 workshop in Paris, France, with the goal to review and combine the existing muon measurements [3, 5, 9–17]. The joint report [4] was signed by the EAS-MSU, IceCube, KASCADE-Grande, NEVOD-DECOR, Pierre Auger, SUGAR, Telescope Array, Yakutsk EAS Array collaborations, which is a great achievement and unprecedented in this field.

The report establishes the Muon Puzzle as an experimental fact: the muon abundance increases faster with the shower energy than all current predictions. The abstract z scale was introduced to

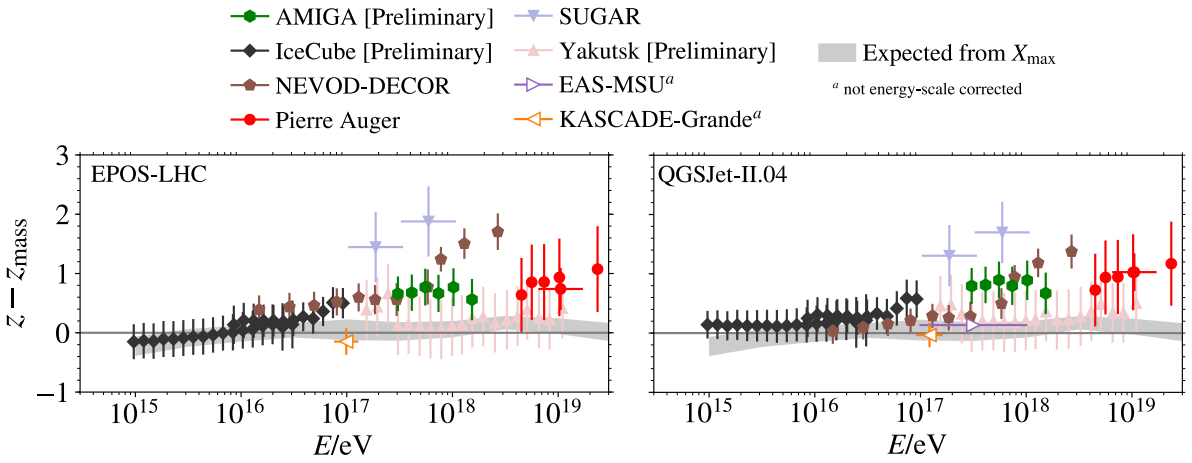

Figure 2: Difference between observed z and the expectation from $X_{\max}$ measurements from Ref. [4]. The positive slope of the combined data is highly significant to 8σ, since the error bars mostly show positively correlated systematic uncertainties.

demonstrate this,

$$z = \frac{\ln N_\mu - \ln N_{\mu_p}^{\mathrm{sim}}}{\ln N_{\mu_{\mathrm{Fe}}}^{\mathrm{sim}} - \ln N_{\mu_p}^{\mathrm{sim}}}, \tag{1}$$

where $\ln N_\mu$ is the logarithm of the measured muon abundance estimate and $\ln N_{\mu_p}^{\mathrm{sim}}$ and $\ln N_{\mu_{\mathrm{Fe}}}^{\mathrm{sim}}$ are simulations of the estimate for proton and iron showers. The measured shower energy enters implicitly in $\ln N_{\mu_p}^{\mathrm{sim}}$ and $\ln N_{\mu_{\mathrm{Fe}}}^{\mathrm{sim}}$. These numbers are usually obtained by simulating air showers at the measured energy E that corresponds to the measured N_μ.

The z scale has several advantages. The strong energy dependence of N_μ is absorbed and very diverse muon number estimators are converted into a comparable number. The z-values are sensitive to the energy-scale, so a cross-calibration of the experimental energy scales was performed, which significantly reduced the systematic scatter between experiments. Since the z scale depends on the simulation, values for six hadronic interaction models were studied; three leading post-LHC models [18–20], and three older pre-LHC models [21–23]. No model predicted the increase that is observed in data. The discrepancy is shown for the two most common models in Fig. 2. Only by combining all datasets, a faster-than-predicted increase of the muon abundance with energy could be established at 8σ. Using measurements over five orders of magnitude in energy provides the necessary lever-arm, and the cross-calibration reduced the overall uncertainty of the combined data.

Establishing the Muon Puzzle at a high significance was very important to raise awareness in the collider community about this issue. The report was pivotal in a proposal to accelerate oxygen ions at the LHC [8] and to collide them with protons at a center-of-mass energy of 10 TeV, which would mimic the first interaction of a 10^{17} eV cosmic-ray proton with air. Accelerating oxygen beams at the LHC is currently planned for 2023.

3 Hadron production in hadron-ion collisions at the LHC

The formation of the air shower cascade is a complex process. This makes connecting the observed muon discrepancy with observables in collider experiments a challenge. Muons are produced at the end of a hadronic cascade and yet the issue must be in the first interactions, since showers at lower energies (which are effectively later stages of showers at higher energy) seem to be adequately described.

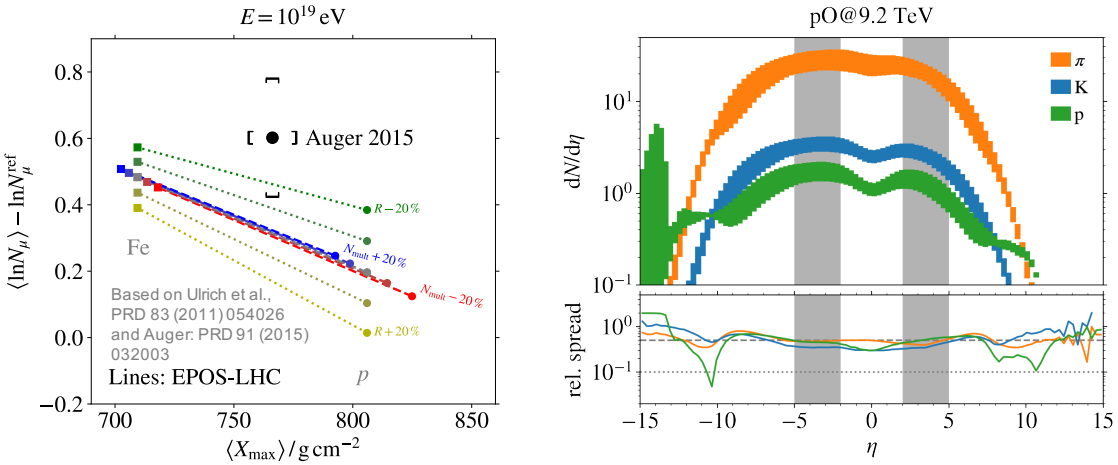

Figure 3: Left: Lines show predictions from the hadronic interaction model EPOS-LHC for the averages of $X_{\rm max}$ and $\ln N_\mu$ for 10^{19} eV air showers, from Ref. [8]. In this log-log plot, any possible elemental composition (from pure proton to pure iron) produces a point on a line. The data point with brackets indicates a representative measurement by the Pierre Auger Observatory with systematic uncertainties. Changing hadron multiplicity $N_{\rm mult}$ moves the model line parallel to itself. Only by reducing R can the line be moved upwards to meet the data point. Right: Model spread of EPOS-LHC, QGSJet-II.04, and SIBYLL-2.3 for charged pion, kaon, and proton production in a proton-oxygen collision at 9.2 TeV. Grey bars show the LHCb acceptance. The model spread is about 50 % in the forward region, even though it is only 5 % at mid-rapitity in proton-proton collisions at 13 TeV.

The simplified Heitler-Matthews model [6] has proven itself as a viable tool to study these connections. It points to the hadronic energy flow as the most important factor for the muon abundance. At each step of the cascade, some energy is diverted into an electromagnetic subshower by decays of neutral pions, which are copiously produced in hadronic interactions. Feedback from the electromagnetic subshower into muons is negligible, therefore the diverted energy is lost for muon production. This places prime importance on measuring the energy ratio

$$R = \frac{\text{energy carried by neutral pions}}{\text{energy carried by other hadrons}}, \tag{2}$$

an experimental proxy for the energy fraction carried away by neutral pions in hadron-ion collisions. These insights were quantitively confirmed by full air shower simulations with ad hoc modified hadronic interactions [7, 8]. The impact of R on muon production in air showers and current uncertainties in forward hadron production are illustrated in Fig. 3.

Since energy flow in hadron-ion collisions is important, the experimental focus is put on forward hadron production. While most particles are produced at mid-rapidity, the largest energy per particle is carried by the most forward produced particles. Between these two extremes is the important rapidity region, illustrated in Fig. 4 for proton-proton and proton-lead collisions at the LHC. The excellent data available at mid-rapidity on hadron production from ALICE in proton-proton and proton-lead collisions [24] alone is not able to resolve the Muon Puzzle for two reasons. Firstly, particles produced at mid-rapidity only produce a negligible amount of muons in a full air shower cascade. The data is very important for model tuning, but does not cast direct light on the Muon Puzzle. Secondly, the nuclear modification of production cross-sections in proton-ion collisions is very strong for forward-produced particles and not accurately predicted by theory. The modification factor R_{pPb} = cross-section in p-Pb collions/(cross-section in p-p $\times$ 208) is far away from 1 for J/ψ production measured with LHCb [25] and in neutral pion production measured with LHCf [26]. The

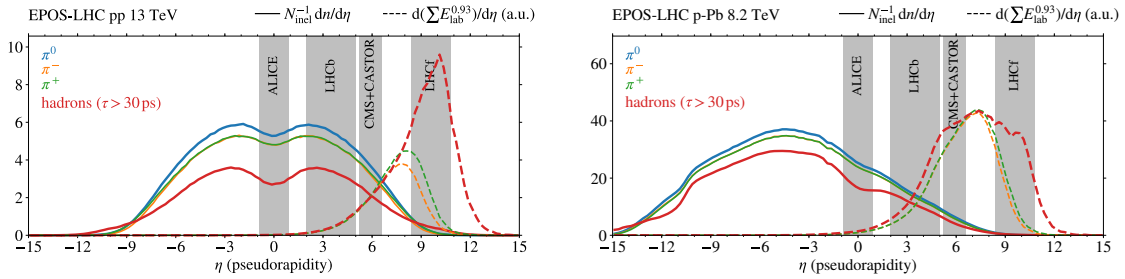

Figure 4: Shown are the spectra of pions and long-lived hadrons produced in proton-proton collisions at 13 TeV (left-hand side) and proton-lead collisions at 8.2 TeV (right-hand side) in solid lines. These spectra were converted into estimates of the number of muons that would be produced by these hadrons in air showers (dashed lines, not to scale). The most relevant phase-space to resolve the Muon Puzzle is the one where the produced number of muons is large. Grey bands show the acceptance of several LHC experiments for comparison.

importance of nuclear effects has been further emphasized by a recent measurement [27] of R in proton-proton collisions at 13 TeV by the CASTOR experiment, which showed that current hadronic interaction models predict a value that is already too low, while it must be even lower than the current values in hadron-nitrogen and hadron-oxygen collisions to solve the Muon Puzzle.

For solving the Muon Puzzle, specialized forward detectors like CASTOR [28] and LHCf [29] are very important, since these cover the most relevant phase-space. Equally important are complementary measurements with LHCb [30]. LHCb is a general purpose forward spectrometer with particle identification capabilities in the region $2 < \eta < 5$, which is unique among the four large LHC experiments. It can study charged pions, kaons, and protons in the forward direction in great detail at the onset of the relevant phase-space for air showers, while the specialized forward detectors are limited to energy flow in case of CASTOR and neutral particles in case of LHCf. Several measurements in LHCb to that end in proton-proton and proton-lead collisions at the highest LHC energies are currently underway.

Very important will be follow up measurements of these interactions in proton-oxygen beam collisions, which were proposed in Ref. [8] and are planned for 2023, near the end of Run 3 of the LHC. Together with proton-proton and proton-lead measurements, these measurements will allow us to study the evolution of forward production with the size of the nucleus purely in data. These measurements will severly constrain R in proton-oxygen collisions, achieving an accuracy of 5 % seems realistic. According to our quantitative projections, these measurements should resolve the Muon Puzzle in air showers and thus to shed light on the missing physics in the soft sector of QCD.

4 Conclusions

The Muon Puzzle in air showers points towards missing physics in the soft-QCD sector of hadron-ion collisions, since none of the current hadronic interaction models is able to consistently describe air shower and LHC data. Projections show that the origin of the discrepancy must be observable in measurements of forward hadron production at the highest LHC energies. The relevant forward region is covered by specialized forward experiments at the LHC, CASTOR and LHCf, and by the general purpose spectrometer LHCb. Studies of hadron production in proton-proton and proton-lead collisions with LHCb are currently ongoing. Together with future data from high-energy proton-oxygen beam collisions at the LHC, these measurements have the potential to solve the Muon Puzzle.

References

[1] PIERRE AUGER collaboration, *Depth of maximum of air-shower profiles at the Pierre Auger Observatory: Measurements above* $10^{17.2}$ *eV and Composition Implications*, *PoS* **ICRC2017** (2018) 506.

[2] K.-H. Kampert and M. Unger, *Measurements of the Cosmic Ray Composition with Air Shower Experiments*, *Astropart. Phys.* **35** (2012) 660 [1201.0018].

[3] J.A. Bellido, R.W. Clay, N.N. Kalmykov, I.S. Karpikov, G.I. Rubtsov, S.V. Troitsky et al., *Muon content of extensive air showers: comparison of the energy spectra obtained by the Sydney University Giant Air-shower Recorder and by the Pierre Auger Observatory*, *Phys. Rev.* **D98** (2018) 023014 [1803.08662].

[4] EAS-MSU, ICECUBE, KASCADE-GRANDE, NEVOD-DECOR, PIERRE AUGER, SUGAR, TELESCOPE ARRAY, YAKUTSK EAS ARRAY collaboration, *Report on Tests and Measurements of Hadronic Interaction Properties with Air Showers*, *EPJ Web Conf.* **210** (2019) 02004 [1902.08124].

[5] A.G. Bogdanov, R.P. Kokoulin, G. Mannocchi, A.A. Petrukhin, O. Saavedra, V.V. Shutenko et al., *Investigation of very high energy cosmic rays by means of inclined muon bundles*, *Astropart. Phys.* **98** (2018) 13.

[6] J. Matthews, *A Heitler model of extensive air showers*, *Astropart. Phys.* **22** (2005) 387.

[7] R. Ulrich, R. Engel and M. Unger, *Hadronic Multiparticle Production at Ultra-High Energies and Extensive Air Showers*, *Phys. Rev.* **D83** (2011) 054026 [1010.4310].

[8] Z. Citron, A. Dainese, J. Grosse-Oetringhaus, J. Jowett, Y.-J. Lee, U. Wiedemann et al., *Future physics opportunities for high-density QCD at the LHC with heavy-ion and proton beams*, Tech. Rep. CERN-LPCC-2018-07, CERN, Geneva (2018).

[9] A.G. Bogdanov, D.M. Gromushkin, R.P. Kokoulin, G. Mannocchi, A.A. Petrukhin, O. Saavedra et al., *Investigation of the properties of the flux and interaction of ultrahigh-energy cosmic rays by the method of local-muon-density spectra*, *Phys. Atom. Nucl.* **73** (2010) 1852.

[10] PIERRE AUGER collaboration, *Muons in air showers at the Pierre Auger Observatory: Mean number in highly inclined events*, *Phys. Rev.* **D91** (2015) 032003 [1408.1421].

[11] Y.A. Fomin, N.N. Kalmykov, I.S. Karpikov, G.V. Kulikov, M.Y. Kuznetsov, G.I. Rubtsov et al., *No muon excess in extensive air showers at 100–500 PeV primary energy: EAS–MSU results*, *Astropart. Phys.* **92** (2017) 1 [1609.05764].

[12] PIERRE AUGER collaboration, *Testing Hadronic Interactions at Ultrahigh Energies with Air Showers Measured by the Pierre Auger Observatory*, *Phys. Rev. Lett.* **117** (2016) 192001 [1610.08509].

[13] ICECUBE collaboration, *Muon measurements with icetop*, *EPJ Web Conf.* **208** (2019) 03003.

[14] KASCADE-GRANDE collaboration, *Probing the evolution of the EAS muon content in the atmosphere with KASCADE-Grande*, *Astropart. Phys.* **95** (2017) 25 [1801.05513].

[15] TELESCOPE ARRAY collaboration, *Study of muons from ultrahigh energy cosmic ray air showers measured with the Telescope Array experiment*, *Phys. Rev.* **D98** (2018) 022002 [1804.03877].

[16] PIERRE AUGER collaboration, *Direct Measurement of the Muon Density in Air Showers with the Pierre Auger Observatory*, in *Ultra High Energy Cosmic Rays (UHECR 2018): Paris, France, October 8-12, 2018*, vol. 210, p. 02013, 2019, DOI.

[17] A. V. Glushkov, M. I. Pravdin, and A. Sabourov for the Yakutsk collaboration. private communication, 2018.

[18] T. Pierog, I. Karpenko, J.M. Katzy, E. Yatsenko and K. Werner, *EPOS LHC: Test of collective hadronization with data measured at the CERN Large Hadron Collider*, *Phys. Rev.* **C92** (2015) 034906 [1306.0121].

[19] S. Ostapchenko, *QGSJET-II: physics, recent improvements, and results for air showers*, *EPJ Web Conf.* **52** (2013) 02001.

[20] F. Riehn, H.P. Dembinski, R. Engel, A. Fedynitch, T.K. Gaisser and T. Stanev, *The hadronic interaction model SIBYLL 2.3c and Feynman scaling*, *PoS* **ICRC2017** (2017) 301 [1709.07227].

[21] E.-J. Ahn, R. Engel, T.K. Gaisser, P. Lipari and T. Stanev, *Cosmic ray interaction event generator SIBYLL 2.1*, *Phys. Rev.* **D80** (2009) 094003 [0906.4113].

[22] S. Ostapchenko, *Nonlinear screening effects in high energy hadronic interactions*, *Phys. Rev.* **D74** (2006) 014026 [hep-ph/0505259].

[23] N.N. Kalmykov and S.S. Ostapchenko, *The Nucleus-nucleus interaction, nuclear fragmentation, and fluctuations of extensive air showers*, *Phys. Atom. Nucl.* **56** (1993) 346.

[24] ALICE collaboration, *Production of light-flavor hadrons in pp collisions at $\sqrt{s}$ = 7 and $\sqrt{s}$ = 13 TeV*, 2005.11120.

[25] LHCb collaboration, *Prompt and nonprompt J/ψ production and nuclear modification in pPb collisions at $\sqrt{s_{NN}} = 8.16$ TeV*, *Phys. Lett. B* **774** (2017) 159 [1706.07122].

[26] LHCf collaboration, *Measurements of longitudinal and transverse momentum distributions for neutral pions in the forward-rapidity region with the LHCf detector*, *Phys. Rev. D* **94** (2016) 032007 [1507.08764].

[27] CMS collaboration, *Measurement of the average very forward energy as a function of the track multiplicity at central pseudorapidities in proton-proton collisions at $\sqrt{s} = 13$ TeV*, *Eur. Phys. J. C* **79** (2019) 893 [1908.01750].

[28] V. Andreev et al., *Performance studies of a full-length prototype for the CASTOR forward calorimeter at the CMS experiment*, *Eur. Phys. J. C* **67** (2010) 601.

[29] LHCf collaboration, *Technical design report of the LHCf experiment: Measurement of photons and neutral pions in the very forward region of LHC*, .

[30] LHCb collaboration, *The LHCb Detector at the LHC*, *JINST* **3** (2008) S08005.

AGILE Experiment

Alexander Novikov
on behalf of AGILE collaboration

e-mail: alexander.novikov@ku.edu

University of Kansas, Lawrence, KS, USA

Presented at the 3rd World Summit on Exploring the Dark Side of the Universe
Guadeloupe Islands, March 9-13 2020

Abstract

AGILE (Advanced enerGetic Ion eLectron tElescope) is a NASA-funded instrument currently being developed aimed to characterize solar, magnetospheric, and cosmic ray particles. The main of goal of this project is to build a compact, low-mass, low-power, and low-cost device capable of registration and discrimination of a large variety of particles (ions from H to Fe and electrons) in a wide energy range: 1-100 MeV/nucleon for ions and 1-10 MeV for electrons. In order to accomplish this, the AGILE collaboration proposed a technique (pulse shape discrimination or PSD) for the identification of particles' species and energies using very fast silicon detectors and electronics with consequent analysis of the signals in real-time. AGILE will be the first space-based instrument to use the techniques of fast on-board PSD.

1 Introduction: Science Motivation

Robust detection and identification of charged particle species and energy is a very important problem for a variety of space experiments. AGILE (Advanced enerGetic Ion eLectron tElescope) is an instrument which is being developed to register and discriminate ions (H-Fe) in the 1-100 MeV/nucleon energy range and electrons in the 1-10 MeV/nucleon range that can be used for better understanding of the charged particle energization, loss, and transport throughout the heliosphere and the radiation belts, in particular in the following studies.

1.1 Anomalous Cosmic Rays and Solar Energetic Particles

AGILE instrument is sensitive to the charged particle types and energies corresponding to the Anomalous Cosmic Rays (ACRs) and the Solar Energetic Particles (SEP), thus it should help gain better understanding of these phenomena. The origin of ACRs is the interstellar neutral gas which is ionized and then accelerated at the solar wind termination shock. There have been predictions and later evidence [1] that ACRs can penetrate the Earth's magnetosphere and get trapped in the radiation belts. Accurate measurements of the ACRs composition and fluxes in the outer belts by the AGILE instrument can results in deeper comprehension of the ACRs dynamics within the solar system, general properties of the heliosphere, and the nature of interstellar material.

With regard to SEPs, AGILE should be able to precisely measure their dynamics in particular to elucidate two types of events: impulsive (^{3}He-rich) and gradual (proton-rich). As can be seen in Fig. 1, the fluxes of various ions are different for these two types of events, and robust measurements of the particle species and energies will help to broaden the knowledge of those mechanisms on the Sun.

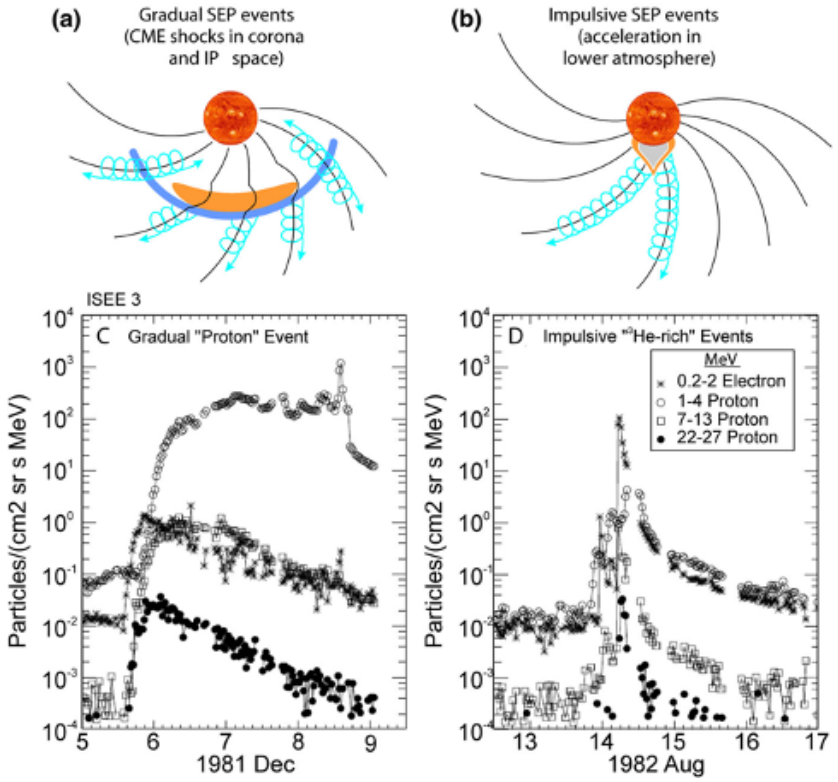

Figure 1: Gradual and impulsive SEP events, adapted from [2] and [3]. a - gradual events produced by the acceleration driven by coronal mass injection (CME) shock wave, b - impulsive events produced by a solar flare. c and d - flux profiles of different particles (protons and electrons) for the two types of SEP events discussed.

1.2 Relativistic Electrons in the Radiation Belts

The question about the presence or absence of the relativistic electrons (E >1 MeV) in the inner radiation belt still remains open since it is extremely difficult to measure these particles due to the high "contamination" of this region of space by protons [4]. Therefore using a robust technique for discrimination of particles and their energies will not only help answer this question but also will result in a deeper understanding of the electrons dynamics due to geomagnetic activity in the inner radiation belt.

Precise measurements of the relativistic electrons' energies and fluxes in the outer radiation belt will help to examine the nature of various competing acceleration, transport, and loss processes.

1.3 Space Weather and Space Travel

Another important goal of the AGILE instrument is the studies of space weather and its effects on human activities in space. For example, during geomagnetic disturbances SEP particles can reach the International Space Station orbits, which can cause significant harm to both people and on-board equipment. Since particles with different charge and mass (various ions) have different effect on both humans and hardware, e.g. the equivalent dose received by a human depends not only on the absorbed dose (energy absorbed per unit of mass), but also on the type of particle depositing this energy, it is very important to not only know the total flux of all of particles, but to differentiate it by

particle types and energies. Understanding these fluxes is crucial for preparing future space travels, in particular in terms of shielding design and optimizing exposure time.

2 Instrument Description

The AGILE instrument combines the heritage of the preceeding particle telescopes, in particular MERIT (Miniaturized Electron pRoton Telescope) onboard CeREs (Compact Radiation belt Explorer) [5], and the expertise in development of the ultra fast silicon detectors and electronics for ground-based experiments [6].

The main sensitive part of the AGILE instrument is a stack of silicon (Si) detectors MSD040 [7] manufactured by Micron Semiconductor Ltd with the active area diameter of 40 mm and the thickness of 300 μm. The same detectors but with a different thickness were used in the MERIT instrument [5]. In the initial studies the number of layers is chosen to be 16. This number is sufficient to completely stop the heavy ions (e.g. Fe) with energies up to 100 MeV/nucleon and the light ones (e.g. p or α) with energies up to 30 MeV/nucleon. In order to extend the energy range for lighter ions, the number of layers can be increased and/or additional absorbing layers (e.g. Al) can be added. Some key characteristics of MSD040 detectors used in these studies are shown in Table 1: The main operational characteristics like thickness and bias voltage were chosen in order to get a large effective area and to cover a wide energy range while providing stable and efficient performance of the read-out electronics (both analog and digital) with regard to the detector capacitance and the signal's amplitude and length. Since the AGILE instrument covers a very wide variety of charged particles and energies, the range of signals produced by incoming particles in the Si detector is about 10^{-7} A - 10^{-2} A ($\sim$ 5 orders of magnitude) according to the simulations (see section 3). It is very challenging to use a single read-out circuit while maintaining a reasonable signal-to-noise ratio for such a wide range of input signal amplitudes; in order to address this, an amplifier with two (low and high) gains was designed, the key principles and components were adapted from the multipurpose read-out board described in work [6]. The duration of the "useful" signal in the chosen configuration is $\sim$ 20 ns.

Active area diameter	$40mm$
Thickness	$300\mu m$
Typical Full Depletion (FD)	$< 60V$
Total Leakage Current (at FD +10V)	$< 10nA$
Capacitance (FD)	40 pF/cm^2
Resistivity	(3 – 10) $k\Omega\times cm$
Bias Voltage	$110V$

Table 1: MSD040 detectors: main characteristics

To get the best results from the digital PSD method, the signals from the detector should be digitized with high time resolution. For this purpose a SAMPIC (SAMpler for PICosecond time pick-off) chip will be used. Originally developed for very fast timing detectors in particle physics [8] and having showed reliable performance [6], SAMPIC is a very good candidate for the AGILE signal read-out due to the following characteristics:

- The entire signal from the detector ($\sim$ 20 ns long) can be digitized and processed;
- High sampling rate: up to 15 GSa/s;
- Very high time resolution: $\sim$ 10 ps;
- Relatively low power consumption: $\sim$ 10 mW/channel;

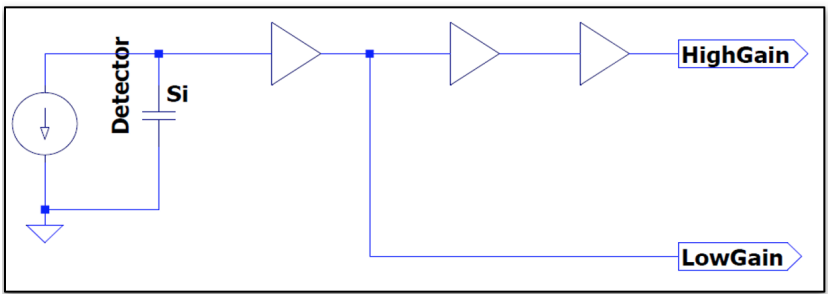

Figure 2: Two Gain Amplifier (principle schematic): the amplifier used in this work has 3 stages of amplification and two outputs. The signals with high amplitude are read-out after the first stage of amplification (low gain) and the low amplitude signals are read out at the end of the amplification circuit (high gain).

3 Pulse Shape Discrimination

The key feature of the AGILE instrument is its ability to identify charged particle species and its energy on-board a satellite (e.g. CubeSat) in real-time because the raw signals cannot be sent to the ground stations due to very limited bandwidth. In order to accomplish this, a Pulse Shape Discrimination (PSD) method [9] is proposed for implementation. The main idea of PSD is to use the fact that different particles deposit different energies along their tracks through the detector medium, leading to varying detector responses (output signals). Careful analysis of these signals and their main characteristics (both amplitude and timing) leads to a set of so-called "markers" - unique characteristics of the signals corresponding to specific particle/energy pairs. One such set of "markers" which can be used for particle species and energy discrimination is pulse rise time and pulse amplitude (proportional to the deposited energy) [10]. However to fully exploit this method, very fast detectors, front-end electronics, and read-out systems are required, which is the main reason for choosing the hardware described in section 2. It should be mentioned that AGILE will apply the on-board techniques of real-time PSD for the first time for space based instrumentation.

In order to obtain the markers mentioned above, detailed simulations of the AGILE instrument were performed. The main steps of the simulations are the following:

1. Simulation of the energy deposition profiles in every layer of the Si detector using GEANT4 toolkit;

2. Simulation of the detector response: the energy deposition profile obtained by GEANT4 is passed to Weightfield2 software [11], a simulator for silicon and diamond detectors which has been adapted for AGILE hardware and produces the current signals ($i(t)$);

3. Simulation of the amplifier output signal: the current signal is passed to the two gain amplifier model in LTspice circuit simulator [12] that produces two voltage signals (low and high gain) which then will be digitized by SAMPIC.

Fig. 3 shows an example of the simulated signals for an α-particle with the energy of 5 MeV/nucleon.

Preliminary analysis of the simulated data shows that a pair of markers which can be used to identify particle species and energy is the maximum amplitude and the rise time of the signal (similar to the approach described in [10]), for an event from 3 these values are $\sim$ 0.68V and $\sim$ 15 ns respectively. However to fully use these markers a particle should completely stop in the detector layer being considered, in this case the energy deposition has a distinct profile (Bragg-curve), causing the corresponding output pulse to have a distinct shape as well.

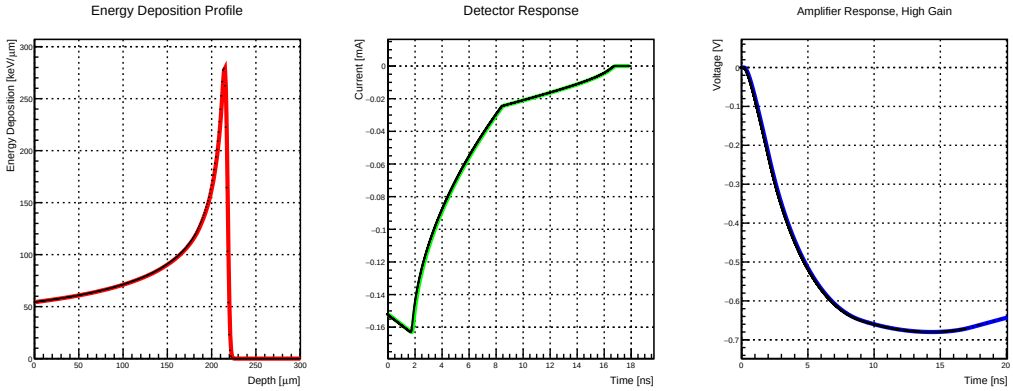

Figure 3: Output signal simulation example, from left to right: energy deposition profile simulated in GEANT4 ($\frac{dE}{dx}(x)$); detector response (current pulse ($i(t)$); amplifier (high gain) output (voltage pulse $V(t)$). The output voltage signal also has a long exponential decay part determined by RC-constant of the amplifier (not shown), which can be ignored and not digitized and stored by SAMPIC. Thus the length of the "useful" pulse is $\sim$ 20 ns.

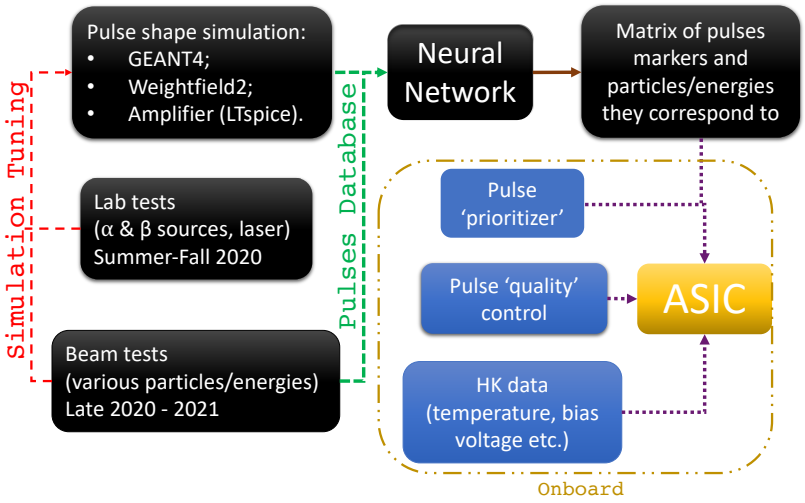

Figure 4: AGILE Pulse Shape Discrimination Method Implementation

Fig. 4 shows a simplified algorithm of PSD method implementation for the AGILE project. As mentioned above the key idea of the method is to use a set (matrix) of unique markers of the signals corresponding to specific particle species and energies. These markers are obtained via detailed simulation of the instrument response for a large variety of charged particles in a wide energy range and will be compared (tuned) with the experimental data: currently the first laboratory test are being performed, then in the late 2020 - 2021 it is planned to conduct a beam test with a variety of different ions in a wide energy range, followed by a test with an electron beam. To get better accuracy for

the values of these markers, a neural network will be trained with both simulated and experimental data. In order to implement the algorithm for real-time on-board processing in a simple integrated circuit (e.g. FPGA or ASIC), the markers' matrix should be simple enough and should not use a lot of memory. Once the characteristics of a real signal (amplitude and rise time) from an incident particle are calculated they are compared with the values from the matrix, and if there is a match within a predefined confidence level the values of a particle type and energy corresponding to these markers are stored. Since the operational characteristics (e.g. ambient temperature, bias voltage etc.) of the instrument may vary during the operation time, the shape of the output signals and thus the values of the markers may change as well, however it is possible to control these characteristics (housekeeping or HK data) and adjust the markers' values accordingly. Since AGILE covers a large variety of charged particles in a wide energy range and the expected fluxes vary a lot from one particle to another (for instance the predicted probability to detect a proton is much higher than the probability to detect a heavy ion (e.g. Fe)), it is important to implement a "pulse prioritizer" which in the case of simultaneous detection of more than one particle will "sacrifice" the information about the particles with low priority and will process and store the information only about the high priority ones. The detailed simulations with their subsequent tuning should also result in a set of markers for "bad pulses" - the signals which cannot be used to identify particle type and energy with a predefined confidence level.

4 Conclusions

The AGILE instrument is currently being developed, the key goal of it is to study and differentiate a large variety of solar, magnetospheric, and cosmic ray particles in a wide energy range by means of implementing the method for on-board digital real-time pulse shape discrimination for the first time in a space-based instrument. This becomes possible due to the utilization of a very fast detection system along with very fast front-end electronics (both analog and digital). The results of the first simulations show that a charged particle type and energy can be identified using the unique characteristics ("markers") of the signals produced by this particle depositing its energy in the detector medium. Detailed analysis of the simulated data is currently in progress along with the first laboratory tests and preparations for a beam test. A similar technique can also be used to detect high energy primary cosmic rays, however in this case a larger stack of detectors and/or additional layers of high density absorbers will be needed to stop these particles.

The same ideas of using fast silicon detectors and electronics with similar pulse processing can be used for medical applications, e.g. the instantaneous dose a patient receives during radiotherapy for cancer treatment can be calculated and a beam profile can be monitored by counting every single particle passing through the detector with very high time resolution, the initial simulations and tests of such applications are currently undergoing.

Acknowledgements

These studies are supported by Heliophysics Technology and Instrument Development for Science (HTIDS) ITD and LNAPP program part of NASA Research Announcement (NRA) NNH18ZDA001N-HTIDS for Research Opportunities in Space and Earth Science – 2018 (ROSES-2018). The author would like to thank Association Physique-Outremer for the opportunity to present this work at the Summit.

References

[1] J. Cummings et al., *New evidence for anomalous cosmic rays trapped in the magnetosphere*, *Geophys. Res. Lett.* **20** (1993) 2003–2006.

[2] D. Reames, *Particle acceleration at the Sun and in the heliosphere*, *Space Science Reviews* **90** (1999) 413–491.

[3] M. Desai and J. Giacalone, *Large gradual solar energetic particle events*, *Living Reviews in Solar Physics* **13** (2016), no. 1.

[4] X. Li et al., *Upper limit on the inner radiation belt MeV electron intensity*, *J. Geophys. Res. Space Physics* **120** (2015), no. 2 1215–1228.

[5] S. G. Kanekal et al., *The MERiT Onboard the CeREs: A Novel Instrument to Study Energetic Particles in the Earth's Radiation Belts*, *Journal of Geophysical Research: Space Physics* **124** (2019), no. 7 5734–5760.

[6] N. Minafra et al., *Test of Ultra Fast Silicon Detectors for picosecond time measurements with a new multipurpose read-out board*, *Nuclear Instruments and Methods in Physics Research A* **867** (2017) 88–92.

[7] "Msd040, http://www.micronsemiconductor.co.uk/product/msd040/."

[8] C. Royon, *SAMPIC: a readout chip for fast timing detectors in particle physics and medical imaging*, in *Proceedings of the Workshop on Applications of Novel Scintillators for Research and Industry (ANSRI), 12-14 January 2015, University College, Dublin, Ireland*, 2015.

[9] C. Ammerlaan et al., *Particle identification by pulse shape discrimination in the pin type semiconductor detector*, *Nuclear Instruments and Methods* **22** (1963) 189–200.

[10] S. Carboni et al., *Particle identification using the ΔE–E technique and pulse shape discrimination with the silicon detectors of the FAZIA project*, *Nuclear Instruments and Methods in Physics Research A* **664** (2012), no. 1 251–263.

[11] "Weightfield2, http://personalpages.to.infn.it/ cartigli/weightfield2/main.html."

[12] "Ltspice, https://www.analog.com/en/design-center/design-tools-and-calculators/ltspice-simulator.html."

The Hubble Constant Tension Problem: An Overview

Dillon Brout

e-mail: dbrout@physics.upenn.edu

University of Pennsylvania & NASA Einstein Fellow

Presented at the 3rd World Summit on Exploring the Dark Side of the Universe
Guadeloupe Islands, March 9-13 2020

Abstract

The last two decades of progress has pushed us into an era of precision tests of the standard cosmological model. Measurements of the Hubble constant in both the early and late universe, which are now below 1% and 2% precision respectively, provide a critical test of 14 billion years of cosmic expansion history, the nature of dark matter and dark energy, the scale of departures from flat geometry, and pre-recombination physics. The value of the Hubble constant extrapolated from the cosmic microwave background measurements is in $>4\sigma$ tension with the value measured directly from the local universe cosmic distance ladder. I will review the current state of the tension, lay out possible sources of systematic uncertainty, discuss numerous additional cosmological probes that have contributed to the discussion, and present the compelling story that such tension is evidence for significant deviations from the standard cosmological model.

1 Introduction

In the last decade, there has been significant progress in accuracy of measurements of the expansion rate of the universe at present day. This expansion rate, the Hubble Constant (H_0), can be determined through direct measurements of the absolute distance scale and nearby bulk flow velocities (e.g. SH0ES: Riess et al. 2016; Freedman et al. 2019), but can also be inferred from the cosmic microwave background (Planck Collaboration et al. 2018) in combination with the assumption of a cosmological model. With the former reporting 2% (stat+syst) uncertainties and the latter reporting 0.7% (stat+syst) uncertainties, a precise comparison can be made that tests the viability of the standard model of cosmology. Estimates of H_0 using the local distance ladder approach (e.g. SH0ES; Reid et al. 2019) are in 4σ tension with the value inferred from the early universe. Furthermore, there are two independent methods that corroborate both the early and late universe measurements. For the early universe, measurements of cosmic structure (BAO) in combination with big bang nucleosynthesis (BBN) data and constraints on dark matter (Ω_M) are in agreement with Planck (DES: Abbott et al 2018). However, corroborating late time H_0 measurements are the results from time-delay distances to strongly lensed quasars, which also suggest a high value in agreement with SH0ES. When analyzed in combination, these probes bring the early and late universe measurements of H_0 to greater than 5σ tension (Wong et al. 2019; Shajib et al. 2019).

The talk presented at the 3rd World Summit on Exploring the Dark Side of the Universe on March 12th was largely an overview talk. Here I briefly focus on two main aspects of the Hubble constant tension discussion: tests of exotic models and the impact of systematic uncertainties.

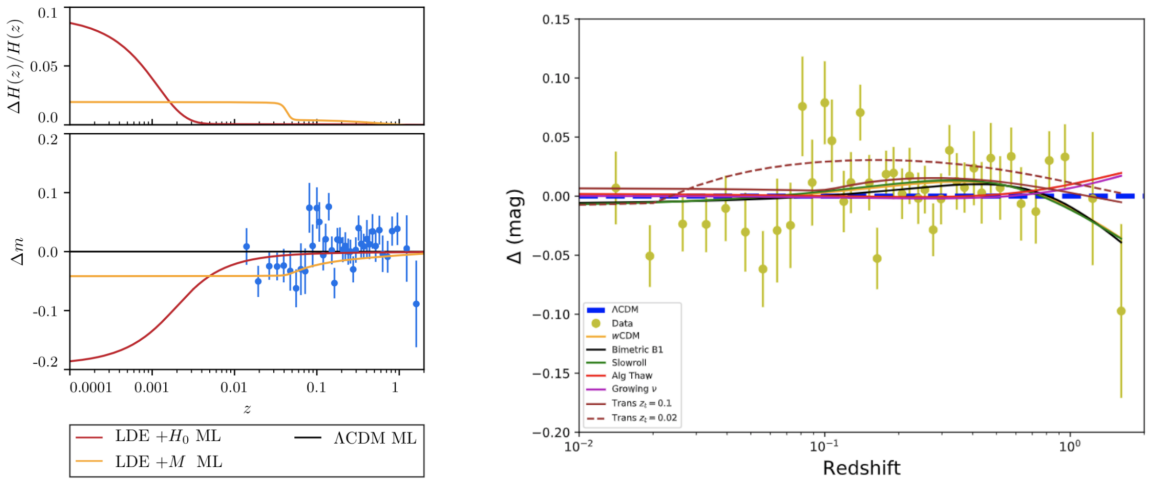

Figure 1: Constraints on exotic cosmological models and late time evolution. **Left**: Benevento, Hu, Raveri 2020 **Right**: Dahwan, et al. 2020.

2 Theoretical Resolutions are Restricted by Observations

The observed tension could be indicative of the presence of exotic physics beyond the standard model (for e.g., see Mortsell and Dhawan 2018; D'Eramo et al. 2018; Kreisch et al. 2019; Aylor et al. 2019). Many of these exotic models result in predictions that can be measured from the SN Ia rung of the distance ladder. Dahwan et al. 2020 analyze the change in the inferred value of local H_0 by altering the assumption of the cosmological model describing the expansion history of the universe. They also introduce a new formalism to account for the systematic uncertainties that affect the calibrator and Hubble flow supernovae simulataneously, motivated for calibrator and z < 0.15 Hubble flow SNe in previous studies (e.g. Zhang et al. 2017; Feeney et al. 2018).

While in Riess et al. (2016), the SN systematics are treated as variants in the analysis and are not combined in the same way as analyses of the latest high-z SN Ia samples (Betoule et al. 2014; Scolnic et al. 2018), Dahwan et al. 2020 adopt the formalism used for measuring dark energy properties (Brout et al. 2019b) from high-z samples and extend it to the other rungs of the cosmic distance ladder, so that covariance between the calibrator and Hubble flow SNe distances can be captured for a comprehensive list of systematics and accounted for in the H_0 inference

Dahwan et al. 2020 (shown on the right side of Figure 1) find that the assumption on the dark energy model does not significantly change the local distance ladder value of H_0, with a maximum difference between the inferred value for different models of 0.47 km/s/Mpc , i.e. a 0.6% shift in H_0, significantly smaller than the observed tension. Dahwan et al. 2020 also find that additional freedom in the dark energy models does not increase the error in the inferred value of H_0. They do find however, that including systematics covariance between the calibrators, low redshift SNe, and high redshift SNe can induce small shifts in the inferred value for H_0 and that improved systematics treatment of the SN Ia calibrators contributes 0.8% to the total uncertainty on H_0.

These findings were also backed up by the work of Benevento, Hu, Raveri 2020 (shown in left side of Figure 1), who test late time transitions in scalar field models that exhibit a sharp dip or bump in the potential within a fraction of an e-fold of the present, i.e. at redshifts between the calibrator set of SNe and the first Hubble flow SNe. They find that such potentials, including the model proposed by Mortonson, Hu, Huterer 2009, are not viable solutions to the resolution of the H_0 controversy.

3 Systematic Uncertainties

The benefit of the distance ladder approach that SH0ES takes is that potential systematic uncertainties will cancel out due to the calibration based approach. That is, if a systematic is present in more than one rung of the ladder, systematics that are demographic independent or redshift independent will nullify. The search for single rung systematics and demographic differences are at the heart of any theorized explanations for the tension.

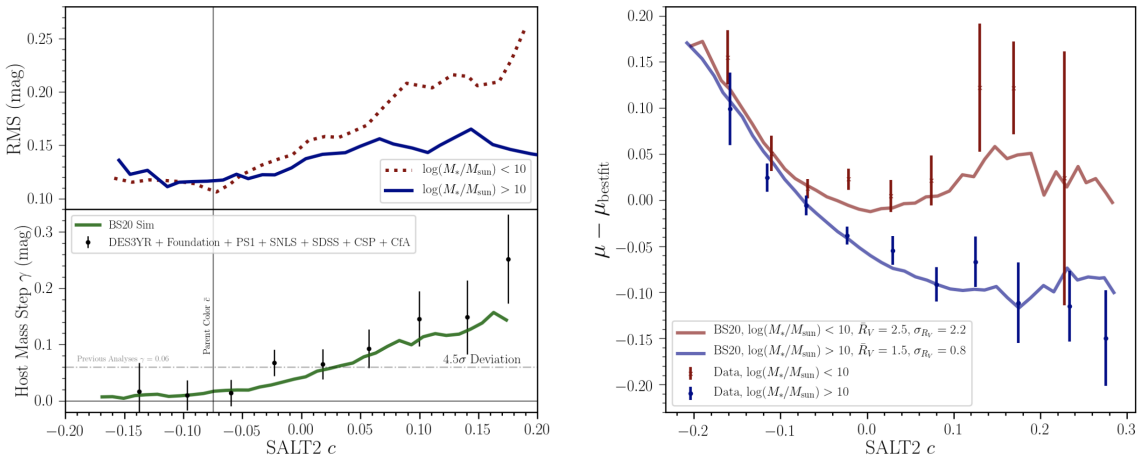

Figure 2: **Left**: (Upper) Hubble Diagram scatter binned by SALT2 observed color and compared for SNe in host galaxies with low and high mass. (Lower) Recovered values of the host stellar mass step (γ) for SNe Ia in high ($\log(M_*/M_{\rm sun}) > 10$) versus low ($\log(M_*/M_{\rm sun}) < 10$) mass hosts, binned by SALT2 observed color. Predictions from the BS20 Mass-split model is shown in green. Significance of the deviation from a constant γ of 0.06 is shown (4.5σ). b) Binned Hubble Diagram residuals versus color split on host-mass. Biases are shown for the observed data (points) and predicted using the scatter models (solid lines). The difference between the red and blue points has typically been found by marginalizing over color and finding a single step γ. The BS20 model parameters for the rolling surveys are given in the legend.

Because the absolute distance calibration only takes place in the first rung of the distance ladder, it does not retain the benefit of systematic uncertainty "cancellation". For this reason, the SH0ES measurement utilizes five independently determined, geometric distance estimators to calibrate the luminosity of Cepheids in Type Ia supernova (SN Ia) host galaxies. Independent estimates of H0 from the local, Cepheid distance ladder find no obvious source of systematic error accounting for this discrepancy (Cardona et al. 2017; Wu and Huterer 2017; Feeney et al. 2018; Follin and Knox 2017; Zhang et al. 2017; Dhawan et al. 2018).

One such systematic that could potentially plague the SNIa in the second and third rungs of the distance ladder is due to host galaxy SN Ia luminosity correlations. Global and local properties of SN Ia host galaxies such as stellar mass, star formation rate (SFR), stellar population age, and metallicity have all been shown to correlate with the distance modulus residuals after standardization (Hicken et al. 2009a; Sullivan et al. 2010; Lampeitl et al. 2010; Childress et al. 2013; Rose et al. 2019). This correlation is often parameterized as a step function in host-galaxy stellar mass and is now commonplace in SN Ia cosmology analyses despite the lack of understanding of its physical underpinning or convincing evidence for exactly which host-galaxy property is most influential on SN Ia luminosity (e.g. Jones et al. 2018a; Scolnic et al. 2020). To explain this correlation, recent studies have suggested a potential relation between the luminosity of the SN and the progenitor, which can be related to the age of the galaxy, or the local environment of the galaxy (Childress et al. 2013; Rigault et al. 2013;

Roman et al. 2018).

However, a new dust based explanation for this effect has been shown viable by Brout & Scolnic (BS20). BS20 introduce a physical model of color where intrinsic SN Ia colors with a relatively weak correlation with luminosity are combined with extrinsic dust-like colors ($E(B-V)$) with a wide range of extinction parameter values (R_V). This model captures the observed trends of Hubble residual scatter and indicates that the dominant component of SN Ia intrinsic scatter is from variation in R_V . They also find that the recovered $E(B-V)$ and R_V distributions differ based on global host-galaxy stellar mass and this explains the observed correlation γ between mass and Hubble residuals seen in past analyses as well as an observed 4.5σ dependence of γ on SN Ia color. This finding removes any need to prescribe different intrinsic luminosities to different progenitor systems.

As the H_0 measurement has different systematic sensitivity than w due to the comparison of SNe in calibrator galaxies versus Hubble flow galaxies, BS20 recommend these two samples to have similar demographics of blue and red SNe.

4 Conclusions

Several studies in the literature have found the local value of H_0 to be robust to different sources of systematic uncertainty, e.g. the statistical inference model, sample variance, Cepheid systematics and using near infrared data for SNe Ia. In addition, we have now witnessed multiple combinations of independent probes arrive at a similar conclusions for both the early and late time estimates of H_0. No longer is a single probe needed to drive the observed tension in H_0. For this reason, ever increased efforts to understand systematic uncertainties are necessary. In addition, because cosmological model independent parameterizations with additional degrees of freedom fit to the SH0ES SN Ia data result in fit parameters that are in agreement with ΛCDM, more and more precise measurements of cosmological distances will be required in order to begin the process of selecting growing field of possible explanations for the observed tension.

Acknowledgements

Thank you very much to the EDSU organizing committee for inviting me to give the overview lecture on this lively subject. Support for this work was provided by NASA through the NASA Hubble Fellowship grant HST-HF2-51430.001 awarded by the Space Telescope Science Institute, which is operated by Association of Universities for Research in Astronomy, Inc., for NASA, under contract NAS5-26555.

MiniBooNE Neutrino Oscillation Search Results and Predicted Background Events

Teppei Katori for the MiniBooNE collaboration

e-mail: teppei.katori@kcl.ac.uk

King's College London, Strand, WC2R 2LS London, UK

Presented at the 3rd World Summit on Exploring the Dark Side of the Universe
Guadeloupe Islands, March 9-13 2020

Abstract

In this short review, we discuss the 2020 MiniBooNE electron neutrino appearance oscillation results with a special attention on background predictions relevant to the MiniBooNE oscillation results and other (anti)electron neutrino appearance search experiments.

1 MiniBooNE 2020 Oscillation results

MiniBooNE was a short-baseline neutrino oscillation experiment at Fermilab. A ν_μ ($\bar{\nu}_\mu$) dominant beam was created by the Booster neutrino beamline (BNB) [1]. A mineral-oil-based spherical Cherenkov detector [2], located 541 m away from the target, was used to search for single-isolated electron-like signals produced by charged-current (CC) interactions of ν_e ($\bar{\nu}_e$) neutrinos. Data excesses of signals over backgrounds have been reported [3]. Data taking was stopped in 2019, and in 2020 we presented the results from the 17-year full data set [4]. Fig. 1 shows the final result of ν_e candidate spectrum as a function of E_ν^{QE}, the reconstructed neutrino energy under the quasi-elastic (QE) assumption [5] which assumes two-body kinematics and a target nucleon at rest. The data excess can be interpreted as a signal of neutrino oscillations at a $\sim$ 1 eV mass scale, or as the presence of sterile neutrinos around the 1 eV mass scale. MiniBooNE signals are statistically the strongest signals of the so-called short-baseline anomalies [6] which all suggest a $\sim$ 1 eV sterile neutrinos, and there are world-wide programs to search for such a neutrino candidate.

The data exhibit an excess of events over simulated backgrounds in the lower energy region. Here, 6 main backgrounds are explicitly shown. In brief, beam-origin backgrounds (ν_e from $\mu^\pm$, ν_e from $K^\pm$, and ν_e from K^0) are intrinsic ν_e backgrounds, and they tend to spread over wide energy region. This feature makes it difficult to explain the excess by a mis-modelling of the beam without exotic effects [7]. On the other hand, other backgrounds (π° misid, $\Delta \to N\gamma$, dirt) are mis-identification (misID) backgrounds, mainly photons that are misidentified as electrons from ν_eCCQE interactions. These backgrounds have similar shapes as the excess, and we discuss these backgrounds further in this short note.

2 π° misid

Every experiments searching for $\nu_e(\bar{\nu}_e)$ appearance signals, neutral current single π° (NC1π°) production is a serious background channel. Although π° normally decays to two gamma rays, boosted

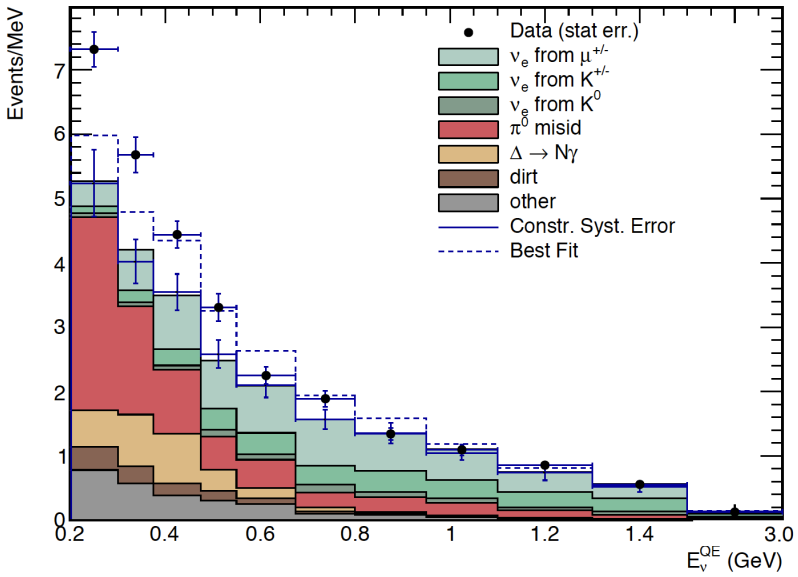

Figure 1: MiniBooNE data-MC comparison for the ν_e oscillation candidate event distribution [4]. This is a function of reconstructed electron neutrino energy under the QE assumption (E_ν^{QE}).

π° can decay to one gamma ray, or one gamma ray is undetected, then the final state is a single gamma which is resemble to a single-isolated electron-like event by Cherenkov detectors. The prediction of such background is difficult, because the prediction of neutrino produced single pion is very difficult. This problem comes from two parts. First, we need to predict production rates of pions from the primary process correctly. Such calculation relies on advanced nuclear models of baryonic resonances and non-resonant meson productions from neutrino interactions. Models are tuned and tested with electron scattering data [8], however, axial form factors need to be tuned from low statistics neutrino scattering experiments [9]. Confusions increase if the energy goes higher and higher resonances [10] (beyond the Δ resonance) and transition region to DIS (so-called shallow inelastic scattering, SIS [11, 12, 13]) are non-negligible. Second part is the final state interactions (FSIs). Hadrons experience effects from the nuclear environment, and these modify both kinematics and types of hadrons leaving the target nuclei. Simulations of FSIs for hadrons are also difficult, and thus correct simulation of photon background is very challenging. To overcome these problems, MiniBooNE utilizes an internal constraint by measuring π° events in MiniBooNE [14]. These data are used to tune the simulation of π° spectrum. Then, the photon background from π°s is simulated by performing decays of data-tuned π°s.

Fig. 2 shows a coordinate distribution of data and simulated background events with function of cube of normalized radial distance R from the center of the detector. Note, fiducial volume of the MiniBooNE detector is a 500 cm spherical region of the mineral oil volume. Because of the geometric effect, the photon background from π°s makes a characteristic shape and the peak is not around the centre. Absence of this feature in the data suggest NC1π° cannot explain the data excess.

3 $\Delta \rightarrow N\gamma$

A high-energy single photon can be made by a radiative decay of a baryonic resonance. In MiniBooNE, such NC single gamma (NC1γ) channel is not simulated by Monte Carlo, instead, the prediction is made from measured π° rate. In brief, measured π° rate is used to extrapolate the Δ-resonance rate after correcting the FSIs, then branching ratio is applied to predict the single gamma ray back-

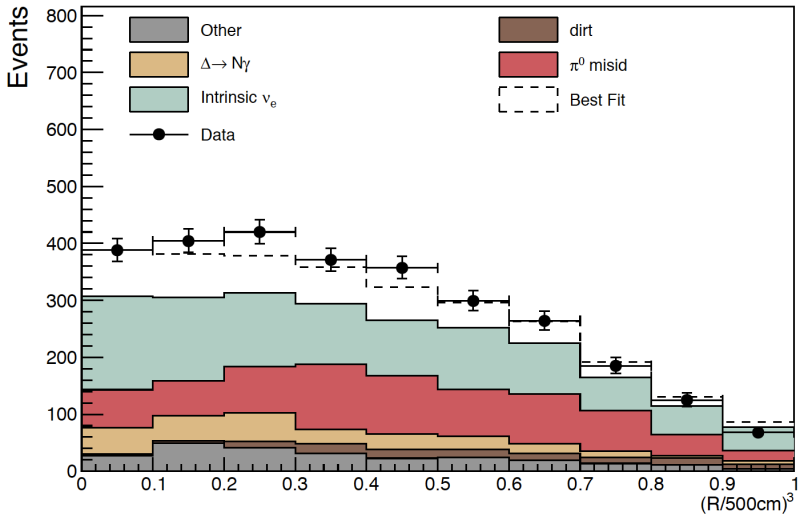

Figure 2: Oscillation candidate data-MC comparison with function of $(R/500cm)^3$ [4], note 500 cm is the fiducial volume of the MiniBooNE detector. π° background makes a peak slightly off-centre, which do not agree with the shape of the data excess.

ground via the radiative Δ-decay. As Fig. 3 shows, the MiniBooNE prediction agreed with the predictions from the latest nuclear calculations [15]. Similar results are obtained from other advanced NC1γ models [16, 17]. These theoretical calculations give us a confidence that we predict this background correctly. However, the radiative Δ-decay has not been experimentally confirmed, and only limits are available [18, 19]. Therefore, it might be possible to explain all excesses by the radiative Δ-decay if the theoretical prediction is wrong around 300%. Furthermore, it is also possible that exotic processes (mainly Z'-decay) contribute similar signals [20, 21, 22, 23]. These possibilities are testable soon by high-resolution detectors such as the MicroBooNE experiment (liquid argon time projection chamber) [24] and the NINJA experiment (emulsion cloud chamber) [25].

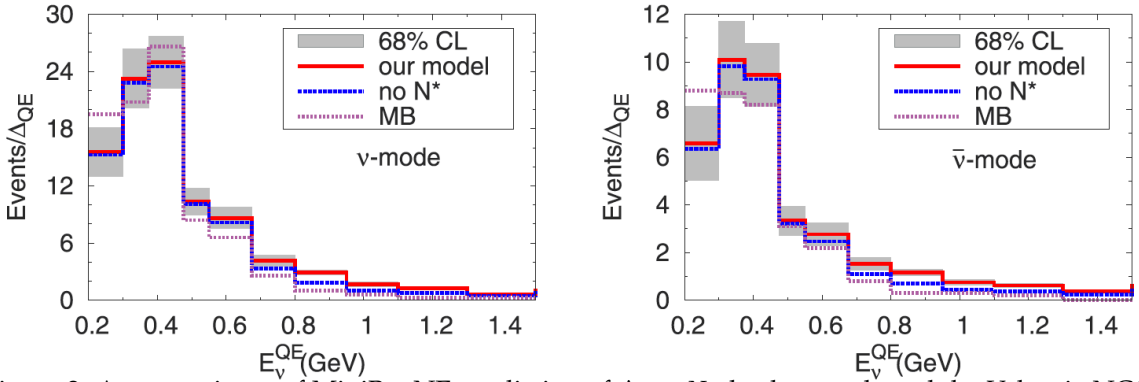

Figure 3: A comparisons of MiniBooNE prediction of $\Delta \to N\gamma$ backgrounds and the Valencia NC1γ model [15]. Agreements are within the theoretical errors except the lowest bins. Similar agreement is obtained from other modern NC1γ models [16, 17].

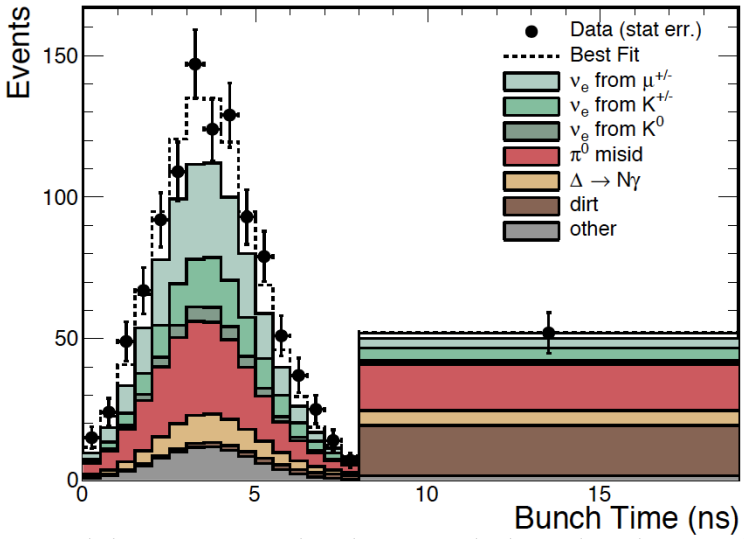

Figure 4: Oscillation candidate event time distribution in the beam bunch timing [4]. The bunch time is ∼2 ns with ∼19 ns separation to repeat 82 times. The dirt event is out of the phase of bunch time and it makes a peak outside of the bunch timing. Both intrinsic backgrounds and misID backgrounds show slight delays compared with oscillation signal events from ν_eCCQE interactions.

4 dirt

High-energy photons generated outside of the detector can come inside of the detector without showering in the veto region. This type of background, called dirt events in MiniBooNE, is challenging to simulate since materials and geometry outside of the detector are not completely modeled, and prediction is not reliable. To estimate dirt background, we use a data-driven correction. Events outside of the fiducial volume are measured to find a distribution of dirt events with a function of R, the distance from the detector center. This gives a better estimation of the dirt background inside of the fiducial volume.

We also imply the timing information to further check this background. Among the 84 BNB buckets, ∼83 buckets are usually filled, where 2 ns bunches are separated with 19 ns. Fig. 4 shows the bunch timing of ν_e candidate events with background simulations. This precise timing structure is used for the search of the beam produced boosted dark matter [26, 27]. Here, the timing data is used to look for sterile neutrinos. First, dirt background is out of phase and we can confirm our prediction of this background is correct from the data-MC agreement outside of the bunch timing. Second, beam-origin intrinsic backgrounds show a slight delay (∼1 ns) due to heavier parents (kaon decay background) or additional processes (muon decay background). Third, misID photon backgrounds also show a slight delay (∼1 ns) due to additional showering process compared with electron oscillation candidate signals from ν_eCCQE interaction. Note, timing information is not currently used to select $\nu_e(\bar{\nu}_e)$ oscillation candidates.

5 Nucleon correlations

Neutrino interaction physics around 1-10 GeV has extremely rich structures [28], and future long-baseline oscillation experiments, such as DUNE [29] and Hyper-Kamiokande (HyperK) [30], are likely to be systematically limited including neutrino interaction errors. Among them, the discovery of the role of nucleon correlations [31, 32] in neutrino interactions attract many interests and actively studied by many experiments. Neutrinos often interact with more than one nucleon, or correlated nucleon pair. This changes outgoing particle kinematics, and also this enhances the cross-section more than incoherence sum of all nucleon contributions. This additional channel, often called MEC (meson

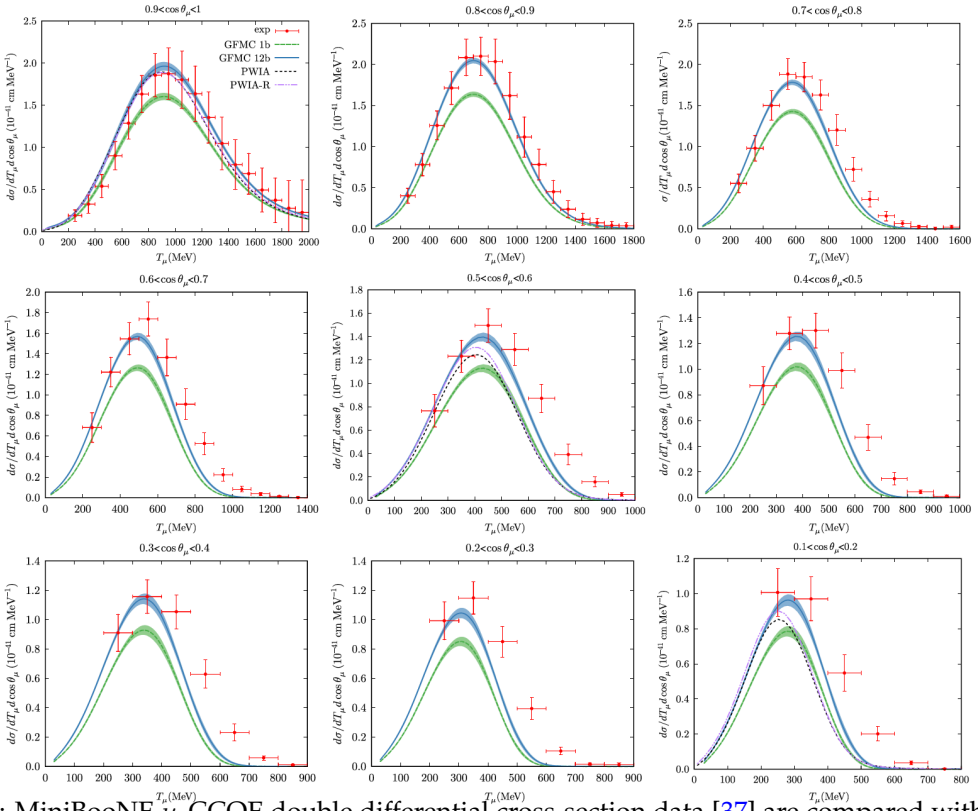

Figure 5: MiniBooNE ν_μCCQE double differential cross-section data [37] are compared with *ab initio* quantum Monte Carlo prediction [38]. In the theory, all nuclear potentials are included, and five response functions are calculated in wide range of momentum transfer, from 100 to 700 MeV.

exchange current) or 2p2h (two-particle 2-hole), are introduced in modern neutrino interaction generators [33, 34, 35, 36]. Fig. 5 shows the data-theory comparison of MiniBooNE flux-integrated ν_μCCQE double differential cross-section data [37] and *ab initio* quantum Monte Carlo (QMC) calculation [38]. This precise nuclear theory includes both two-nucleon and three-nucleon potentials, and cross-section predictions capture the detailed features of MiniBooNE high-statistics ν_μ cross-section data. Since MiniBooNE does not include this channel in the simulation and effect of cross-section enhancement is tuned through CCQE channel, it was argued that data excess could be related to the neutrino energy mis-reconstruction [39, 40]. This idea is interesting, because energy mis-reconstruction would shift the energy spectrum to the lower energy, namely the data excess would be higher energy region more consistent with sterile neutrino oscillation hypothesis. So far, detailed study does not support this [41], but the jury is still out. Current knowledge of nucleon correlations in neutrino physics is very limited, and experiments require to tune this channel a lot to improve data-MC agreements within their simulations [36, 42, 43]. This may have some implications on a mild tension of oscillation results between T2K [44] and NOvA [45].

6 $\nu_e(\bar{\nu}_e)$ cross-sections

Although neutrino pion production and 2p2h models are tested many times with $\nu_\mu(\bar{\nu}_\mu)$CC data, $\nu_e(\bar{\nu}_e)$ appearance oscillation experiments need these models to provide correct predictions for $\nu_e(\bar{\nu}_e)$CC interactions. This is difficult to test, mainly because neutrino beams including the BNB [1], J-PARC neutrino beamline [46], and NuMI [47] do not produce large $\nu_e(\bar{\nu}_e)$ flux in the region where experiments expect $\nu_\mu \to \nu_e$ ($\bar{\nu}_\mu \to \bar{\nu}_e$) oscillations. To take account this error, we introduced a neutrino-

energy dependent ν_e/ν_μ ratio error which blows up exponentially at low energy. It is only few % at 400 MeV but over 30% error at 200 MeV. There are only 5 low statistics data available for ν_e cross-section [48, 49, 50, 51, 52] in entire particle physics history. Thus, we have unavoidable systematic errors on $\nu_e(\bar{\nu}_e)$ interactions, and this is an issue for all $\nu_e(\bar{\nu}_e)$ appearance experiments including MiniBooNE, T2K, NOvA, and future experiments such as DUNE and HyperK.

7 Conclusions

In this brief review, we go through some of key developments of our background study. The statistical significance of the excess is very high, but currently there is no convincing explanation of this through any existing background channels.

Acknowledgements

I thank Bill Louis and Rex Tayloe for their careful checks of this article. I thank the hospitality of the organizers for hosting the participants during this conference even though the pandemic made the organization extremely difficult.

References

[1] **MiniBooNE** Collaboration, A. Aguilar-Arevalo et al., *The Neutrino Flux prediction at MiniBooNE*, *Phys. Rev. D* **79** (2009) 072002, [arXiv:0806.1449].

[2] **MiniBooNE** Collaboration, A. Aguilar-Arevalo et al., *The MiniBooNE Detector*, *Nucl. Instrum. Meth. A* **599** (2009) 28–46, [arXiv:0806.4201].

[3] **MiniBooNE** Collaboration, A. Aguilar-Arevalo et al., *Significant Excess of ElectronLike Events in the MiniBooNE Short-Baseline Neutrino Experiment*, *Phys. Rev. Lett.* **121** (2018), no. 22 221801, [arXiv:1805.12028].

[4] **MiniBooNE** Collaboration, A. Aguilar-Arevalo et al., *Updated MiniBooNE Neutrino Oscillation Results with Increased Data and New Background Studies*, arXiv:2006.16883.

[5] **MiniBooNE** Collaboration, A. Aguilar-Arevalo et al., *Measurement of muon neutrino quasi-elastic scattering on carbon*, *Phys. Rev. Lett.* **100** (2008) 032301, [arXiv:0706.0926].

[6] A. Diaz, C. Argüelles, G. Collin, J. Conrad, and M. Shaevitz, *Where Are We With Light Sterile Neutrinos?*, arXiv:1906.00045.

[7] C. Giunti and M. Laveder, *electron-neutrino Disappearance in MiniBooNE*, *Phys. Rev. D* **77** (2008) 093002, [arXiv:0707.4593].

[8] E. Hernández, J. Nieves, and M. J. Vicente Vacas, *Single π production in neutrino-nucleus scattering*, *Phys. Rev. D* **87** (2013), no. 11 113009, [arXiv:1304.1320].

[9] C. Wilkinson, P. Rodrigues, S. Cartwright, L. Thompson, and K. McFarland, *Reanalysis of bubble chamber measurements of muon-neutrino induced single pion production*, *Phys. Rev. D* **90** (2014), no. 11 112017, [arXiv:1411.4482].

[10] S. Nakamura, H. Kamano, and T. Sato, *Dynamical coupled-channels model for neutrino-induced meson productions in resonance region*, *Phys. Rev. D* **92** (2015), no. 7 074024, [arXiv:1506.03403].

[11] **NuSTEC** Collaboration, C. Andreopoulos et al., *Summary of the NuSTEC Workshop on Shallow- and Deep-Inelastic Scattering*, in *NuSTEC Workshop on Shallow- and Deep-Inelastic Scattering*, 7, 2019. arXiv:1907.13252.

[12] M. Sajjad Athar and J. G. Morfin, "Neutrino(Antineutrino)-Nucleus Interactions in the Shallow- and Deep-Inelastic Scattering Regions." arXiv:2006.08603, April, 2020.

[13] L. Alvarez-Ruso et al., *Snowmass 2021 LoI: Neutrino-induced Shallow- and Deep-Inelastic Scattering*, in *2021 Snowmass Summer Study*, 9, 2020. arXiv:2009.04285.

[14] **MiniBooNE** Collaboration, A. Aguilar-Arevalo et al., *First Observation of Coherent π^0 Production in Neutrino Nucleus Interactions with $E_\nu < 2$ GeV*, *Phys. Lett. B* **664** (2008) 41–46, [arXiv:0803.3423].

[15] E. Wang, L. Alvarez-Ruso, and J. Nieves, *Single photon events from neutral current interactions at MiniBooNE*, *Phys. Lett. B* **740** (2015) 16–22, [arXiv:1407.6060].

[16] R. J. Hill, *On the single photon background to nu_e appearance at MiniBooNE*, *Phys. Rev. D* **84** (2011) 017501, [arXiv:1002.4215].

[17] X. Zhang and B. D. Serot, *Can neutrino-induced photon production explain the low energy excess in MiniBooNE?*, *Phys. Lett. B* **719** (2013) 409–414, [arXiv:1210.3610].

[18] **NOMAD** Collaboration, C. Kullenberg et al., *A search for single photon events in neutrino interactions*, *Phys. Lett. B* **706** (2012) 268–275, [arXiv:1111.3713].

[19] **T2K** Collaboration, K. Abe et al., *Search for neutral-current induced single photon production at the ND280 near detector in T2K*, *J. Phys. G* **46** (2019), no. 8 08LT01, [arXiv:1902.03848].

[20] P. Ballett, S. Pascoli, and M. Ross-Lonergan, *MeV-scale sterile neutrino decays at the Fermilab Short-Baseline Neutrino program*, *JHEP* **04** (2017) 102, [arXiv:1610.08512].

[21] E. Bertuzzo, S. Jana, P. A. N. Machado, and R. Zukanovich Funchal, *Dark Neutrino Portal to Explain MiniBooNE excess*, *Phys. Rev. Lett.* **121** (2018), no. 24 241801, [arXiv:1807.09877].

[22] Argüelles, Carlos A. and Hostert, Matheus and Tsai, Yu-Dai, *Testing New Physics Explanations of MiniBooNE Anomaly at Neutrino Scattering Experiments*, arXiv:1812.08768.

[23] J. R. Jordan, Y. Kahn, G. Krnjaic, M. Moschella, and J. Spitz, *Severe Constraints on New Physics Explanations of the MiniBooNE Excess*, *Phys. Rev. Lett.* **122** (2019), no. 8 081801, [arXiv:1810.07185].

[24] **MicroBooNE** Collaboration, R. Acciarri et al., *Design and Construction of the MicroBooNE Detector*, *JINST* **12** (2017), no. 02 P02017, [arXiv:1612.05824].

[25] A. Hiramoto et al., *First measurement of $\overline{\nu}_\mu$ and ν_μ charged-current inclusive interactions on water using a nuclear emulsion detector*, arXiv:2008.03895.

[26] **MiniBooNE** Collaboration, A. Aguilar-Arevalo et al., *Dark Matter Search in a Proton Beam Dump with MiniBooNE*, *Phys. Rev. Lett.* **118** (2017), no. 22 221803, [arXiv:1702.02688].

[27] **MiniBooNE DM** Collaboration, A. Aguilar-Arevalo et al., *Dark Matter Search in Nucleon, Pion, and Electron Channels from a Proton Beam Dump with MiniBooNE*, *Phys. Rev. D* **98** (2018), no. 11 112004, [arXiv:1807.06137].

[28] **NuSTEC** Collaboration, L. Alvarez-Ruso et al., *NuSTEC White Paper: Status and challenges of neutrino–nucleus scattering*, *Prog. Part. Nucl. Phys.* **100** (2018) 1–68, [arXiv:1706.03621].

[29] **DUNE** Collaboration, B. Abi et al., *Deep Underground Neutrino Experiment (DUNE), Far Detector Technical Design Report, Volume I Introduction to DUNE*, *JINST* **15** (2020), no. 08 T08008, [arXiv:2002.02967].

[30] **Hyper-Kamiokande** Collaboration, K. Abe et al., *Hyper-Kamiokande Design Report*, arXiv:1805.04163.

[31] M. Martini, M. Ericson, G. Chanfray, and J. Marteau, *A Unified approach for nucleon knock-out, coherent and incoherent pion production in neutrino interactions with nuclei*, *Phys. Rev. C* **80** (2009) 065501, [arXiv:0910.2622].

[32] J. Nieves, I. Ruiz Simo, and M. Vicente Vacas, *Inclusive Charged–Current Neutrino–Nucleus Reactions*, *Phys. Rev. C* **83** (2011) 045501, [arXiv:1102.2777].

[33] J. T. Sobczyk, *Multinucleon ejection model for Meson Exchange Current neutrino interactions*, *Phys. Rev. C* **86** (2012) 015504, [arXiv:1201.3673].

[34] O. Lalakulich, K. Gallmeister, and U. Mosel, *Many-Body Interactions of Neutrinos with Nuclei - Observables*, *Phys. Rev. C* **86** (2012), no. 1 014614, [arXiv:1203.2935]. [Erratum: Phys.Rev.C 90, 029902 (2014)].

[35] J. Schwehr, D. Cherdack, and R. Gran, *GENIE implementation of IFIC Valencia model for QE-like 2p2h neutrino-nucleus cross section*, arXiv:1601.02038.

[36] **T2K** Collaboration, K. Abe et al., *Measurement of neutrino and antineutrino oscillations by the T2K experiment including a new additional sample of ν_e interactions at the far detector*, *Phys. Rev. D* **96** (2017), no. 9 092006, [arXiv:1707.01048]. [Erratum: Phys.Rev.D 98, 019902 (2018)].

[37] **MiniBooNE** Collaboration, A. Aguilar-Arevalo et al., *First Measurement of the Muon Neutrino Charged Current Quasielastic Double Differential Cross Section*, *Phys. Rev. D* **81** (2010) 092005, [arXiv:1002.2680].

[38] A. Lovato, J. Carlson, S. Gandolfi, N. Rocco, and R. Schiavilla, *Ab initio study of $(\boldsymbol{\nu_\ell}, \ell^-)$ and $(\boldsymbol{\bar{\nu}_\ell}, \ell^+)$ inclusive scattering in ^{12}C: confronting the MiniBooNE and T2K CCQE data*, *Phys. Rev. X* **10** (2020), no. 3 031068, [arXiv:2003.07710].

[39] M. Martini, M. Ericson, and G. Chanfray, *Neutrino energy reconstruction problems and neutrino oscillations*, *Phys. Rev. D* **85** (2012) 093012, [arXiv:1202.4745].

[40] J. Nieves, F. Sanchez, I. Ruiz Simo, and M. Vicente Vacas, *Neutrino Energy Reconstruction and the Shape of the CCQE-like Total Cross Section*, *Phys. Rev. D* **85** (2012) 113008, [arXiv:1204.5404].

[41] M. Ericson, M. Garzelli, C. Giunti, and M. Martini, *Assessing the role of nuclear effects in the interpretation of the MiniBooNE low-energy anomaly*, *Phys. Rev. D* **93** (2016), no. 7 073008, [arXiv:1602.01390].

[42] **MINERvA** Collaboration, D. Ruterbories et al., *Measurement of Quasielastic-Like Neutrino Scattering at $\langle E_\nu \rangle \sim 3.5$ GeV on a Hydrocarbon Target*, *Phys. Rev. D* **99** (2019), no. 1 012004, [arXiv:1811.02774].

[43] **NOvA** Collaboration, M. Acero et al., *Adjusting Neutrino Interaction Models and Evaluating Uncertainties using NOvA Near Detector Data*, arXiv:2006.08727.

[44] **T2K** Collaboration, K. Abe et al., *Constraint on the matter–antimatter symmetry-violating phase in neutrino oscillations*, *Nature* **580** (2020), no. 7803 339–344, [arXiv:1910.03887]. [Erratum: Nature 583, E16 (2020)].

[45] K. J. Kelly, P. A. Machado, S. J. Parke, Y. F. Perez Gonzalez, and R. Zukanovich-Funchal, *Back to (Mass-)Square(d) One: The Neutrino Mass Ordering in Light of Recent Data*, arXiv:2007.08526.

[46] **T2K** Collaboration, K. Abe et al., *T2K neutrino flux prediction*, *Phys. Rev. D* **87** (2013), no. 1 012001, [arXiv:1211.0469]. [Addendum: Phys.Rev.D 87, 019902 (2013)].

[47] P. Adamson et al., *The NuMI Neutrino Beam*, *Nucl. Instrum. Meth. A* **806** (2016) 279–306, [arXiv:1507.06690].

[48] **Gargamelle** Collaboration, J. Blietschau et al., *Total Cross-Sections for electron-neutrino and anti-electron-neutrino Interactions and Search for Neutrino Oscillations and Decay*, *Nucl. Phys. B* **133** (1978) 205–219.

[49] **T2K** Collaboration, K. Abe et al., *Measurement of the Inclusive Electron Neutrino Charged Current Cross Section on Carbon with the T2K Near Detector*, *Phys. Rev. Lett.* **113** (2014), no. 24 241803, [arXiv:1407.7389].

[50] **MINERvA** Collaboration, J. Wolcott et al., *Measurement of electron neutrino quasielastic and quasielasticlike scattering on hydrocarbon at $\langle E_\nu \rangle = 3.6$ GeV*, *Phys. Rev. Lett.* **116** (2016), no. 8 081802, [arXiv:1509.05729].

[51] **ArgoNeuT** Collaboration, R. Acciarri et al., *First measurement of electron neutrino scattering cross section on argon*, *Phys. Rev. D* **102** (2020), no. 1 011101, [arXiv:2004.01956].

[52] **T2K** Collaboration, K. Abe et al., *Measurement of the charged-current electron (anti-)neutrino inclusive cross-sections at the T2K off-axis near detector ND280*, arXiv:2002.11986.

Toward the Frontiers of Particle Physics With the Muon g-2 Experiment[1]

Eremey Valetov[2]
On Behalf of the Muon g-2 (E989) Collaboration at Fermilab

e-mail: evaletov@fnal.gov

Lancaster University, the Cockcroft Institute, and Michigan State University

Presented at the 3rd World Summit on Exploring the Dark Side of the Universe
Guadeloupe Islands, March 9-13 2020

Abstract

The Muon g-2 Experiment (E989) at Fermilab has a goal of measuring the muon anomaly (a_μ) with unprecedented precision using positive muons. This measurement is motivated by the difference between the previous Brookhaven a_μ measurement and Standard Model prediction exceeding three standard deviations, which hints at the possibility of physics beyond the Standard Model. Muons are circulated in a storage ring, and the measurement requires a precise determination of the muon anomalous precession frequency (spin precession relative to momentum) from the resulting decay positron time and energy measurements collected with calorimeters. The average magnetic field seen by the muons needs to be known with high precision, and so the storage ring magnetic field is shimmed to be very uniform and is continually monitored with nuclear magnetic resonance (NMR) probes. Detailed Muon Campus beamline and muon storage ring simulations are also required for quantifying beam dynamics and spin-related systematic effects in the determination of the muon anomalous precession frequency, e.g. muon losses during the measurement window. At the time of the conference, the experiment has recently commenced Run-3[3], and the release of Run-1 physics results is planned for 2020.

1 Introduction

The Muon g-2 Experiment (E989), located at the Muon Campus of Fermilab, measures the muon magnetic anomaly a_μ using antimuons μ^+ ("muons" for brevity) circulating around a storage ring with a highly uniform magnetic field within $\pm 0.5\%$ of the momentum $p_0 = 3.094\ \mathrm{GeV}/c$. This momentum p_0, called the "magic" momentum, is defined by $p_0 = m/\sqrt{a_\mu}$, where m is the muon mass, and which makes the spin precession relative to the muon momentum independent of any external transverse electric fields (see also Eq. 3).

The current Standard Model prediction of a_μ is [1]

$$a_\mu^{\mathrm{SM}} = (116\,591\,810 \pm 43) \times 10^{-11}, \tag{1}$$

[1] Fermilab report FERMILAB-CONF-20-463-E.

[2] ORCID: 0000-0003-4341-0379. Presently affiliated with Tsung-Dao Lee Institute of Shanghai Jiao Tong University, with Michigan State University, and with Lepton Dynamics, LLC.

[3] Data-taking in long-running experiments is often divided into campaigns called "runs". One run in the Muon g-2 Experiment roughly corresponds to one year.

while the current experimental world average is [2]

$$a_\mu^{\text{Exp}} = (116\,592\,089 \pm 63) \times 10^{-11}. \tag{2}$$

The contributions to a_μ in the Standard Model (SM) are quantum electrodynamical (QED), electroweak, leading order (LO) hadronic (Had), hadronic light-by-light (LbL), and higher order (HO) hadronic. Ref. [3] shows recent values of these SM contributions to a_μ.

Recent progress on the computation of a_μ^{SM} includes improvements in the dispersive evaluations of the hadronic vacuum polarization (VP) contributions, which rely on experimental measurements of the hadronic cross section. The recent estimate of the leading order hadronic VP contribution from the Muon g-2 Theory Initiative, $a_\mu^{\text{Had, LO VP}} = (693.1 \pm 4.0) \times 10^{-10}$ [1], represents a combination of direct energy scan results from CMD-3, SND, and KEDR experiments and radiative return results from BABAR, KLOE, and BESIII experiments.

A recent achievement in the theory regarding a_μ is the calculation [4] of hadronic vacuum polarization $a_\mu^{\text{Had, VP}}$ and hadronic light-by-light $a_\mu^{\text{Had, LbL}}$ contributions from first principles using lattice QCD. Several collaborations are working on this, including RBC/UKQCD and Mainz. The precision of this calculation is subject to improvement, and the calculation is a work-in-progress.

In case the Muon g-2 Experiment yields a beyond–Standard Model value of a_μ, some of the possible contributions to the discrepancy could be dark photons, inelastic dark matter (iDM), supersymmetry (SUSY), extra dimensions, axion-like particles [5], and additional Higgs bosons [6].

The Muon g-2 Experiment (E989) at Fermilab improves upon its predecessor, the Muon g-2 Experiment (E821) at Brookhaven National Laboratory (BNL), by using a higher intensity muon beam, having an improved muon storage function, employing better beam dynamics modeling, having higher field uniformity and better field monitoring, and achieving reduced spin precession frequency systematics. The technical design projection [7] of E989 is to obtain $\sim$20 times more data and a $\sim$3-fold reduction of systematic errors compared to E821.

2 Systems and Methods of the Muon g-2 Experiment

The Muon g-2 storage ring uses a toroidal C-magnet of $7\,\text{m}$ radius with $1.45\,\text{T}$ magnetic field. Electrostatic quadrupoles provide vertical beam focusing. Muons are injected into the storage ring through an inflector, which cancels the $1.45\,\text{T}$ field at injection, and are deflected onto the design orbit by three kickers located 90° downstream of the inflector.

By tuning the momentum of muons in the Muon g-2 storage ring to the "magic" momentum $p_0 = 3.094\,\text{GeV}/c$, the anomalous precession frequency is proportional to both the parameter of interest a_μ and the traversed magnetic field:

$$\vec{\omega}_a = -a_\mu \frac{q_\mu \vec{B}}{m_\mu}, \tag{3}$$

where ω_a is the muon anomalous spin precession frequency, q_μ is the muon charge, m_μ is the muon mass, and B is the magnetic field, which must be highly uniform for the measurement. Thus, in principle, to measure a_μ it is necessary to measure ω_a and B with high precision.

In E989, we determine the magnetic field in the storage region by measuring at-rest proton spin precession with nuclear magnetic resonance (NMR) probes. The formula to calculate a_μ by the experiment is as follows:

$$a_\mu = \frac{g_e}{2} \frac{m_\mu}{m_e} \frac{\omega_a}{\tilde{\omega}_p'(T)} \frac{\mu_p'(T)}{\mu_e}, \tag{4}$$

where g_e is the g-factor of the electron, m_e is the electron mass, ω_p is the angular precession frequency of the proton, μ_e and μ_p are the spin magnetic moments of the electron and the proton respectively, the prime symbol ('$\prime$') denotes shielding of the proton, the tilde on ω_p' denotes the muon-weighted average over space and time, and T is the temperature. The frequencies ω_a and ω_p are obtained from decay positron time spectra and NMR, respectively.

The values of g_e, m_μ/m_e, and μ_e/μ_p are known from CODATA [8] with uncertainties that are low enough to not be a concern. The proposed systematic and statistical errors on ω_a, according to the technical design report (TDR) [7] of the experiment, are 70 ppb and 100 ppb, respectively. The proposed systematic error of ω_p as per the TDR is 70 ppb.

The detector systems of the Muon g-2 storage ring for measuring ω_a are straw trackers and calorimeters. The straw trackers reconstruct decay positron trajectories, while the calorimeters detect decay positron energies and arrival times.

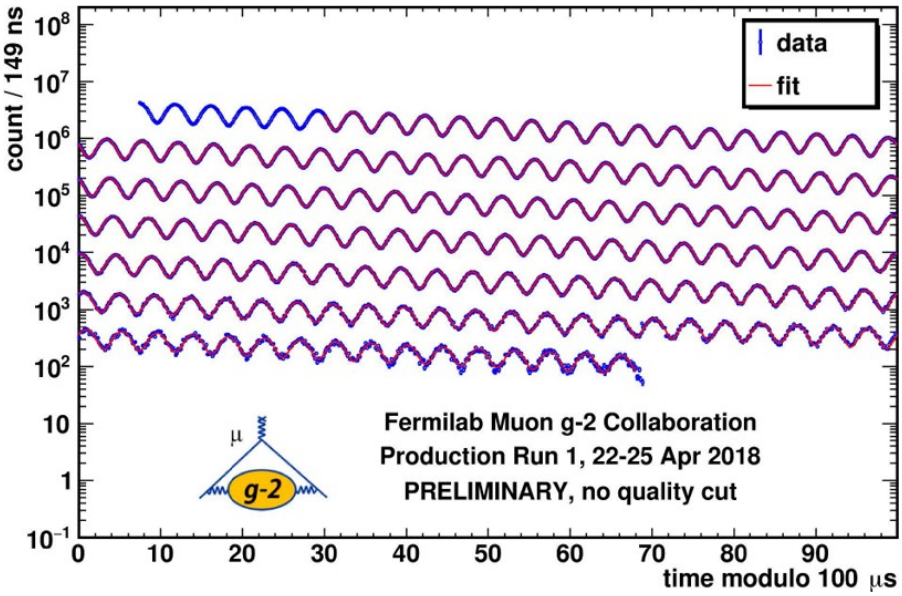

Figure 1: A decay positron time distribution ("wiggle plot", preliminary data).

The decay positron time distribution, or the "wiggle plot" (see Fig. 1 for an example), has the same count oscillation frequency as ω_a. This oscillation occurs because the decay positron energy spectrum has maxima and minima when the muon spin and momentum are aligned and anti-aligned, respectively.

The basic fitting function for the wiggle plot is

$$f(t) = N_0 \exp(-\lambda t) [1 + A \cos(\omega_a t + \phi)], \tag{5}$$

where N_0 is an initial positron count and λ is the exponential decay constant. Fitting functions with a higher number of parameters are usually used, such as a 22-parameter fitting function.

From Eq. 5, we can see that any time-dependence of ϕ due to additional time-varying phenomena in the ring affects the measured value of ω_a. For example, if $\phi = \phi(t) = \phi_0 + \phi_1 t$, then

$$\begin{aligned} \cos(\omega_a t + \phi) &= \cos(\omega_a t + \phi_0 + \phi_1 t) = \\ &= \cos((\omega_a + \phi_1) t + \phi_0). \end{aligned} \tag{6}$$

Such effects are referred to as 'early-to-late' phase change systematics and need to be carefully studied and quantified. One such study is briefly discussed in Sec. 3.

Passive shimming is performed by inserting tiny metal pieces to increase the magnetic field. Using passive shimming, the magnetic field was made three times more uniform than in E821 at BNL. Active shimming is also used.

For measuring ω_p, a mobile device called the trolley is used to sweep the storage ring with 17 NMR probes. There are also 378 NMR probes installed outside the vacuum chamber at fixed locations.

Scanning of ω_p using the trolley is performed regularly, where the trolley moves around the storage ring inside the vacuum chamber while the beam is off. The fixed NMR probes monitor ω_p between the trolley runs.

Tables with expected uncertainties on ω_a and ω_p are available in the TDR [7] of the experiment. We will discuss some details regarding the lost muons systematic error of ω_a in the next section.

3 End-to-End Beamline Simulations and Systematic Analyses

In this section, we will focus on the recent contributions to the Muon g-2 experiment by the author of this proceedings paper.

There are *G4Beamline* [9] and *MARS* [10, 11] beam dynamics models [12] of the target station that include the generation of the secondary beam of π^+ particles by impinging the proton primary beam on the Inconel target, the lithium lens that is used to focus the secondary beam, the copper collimator that provides radiation shielding to the pulsed magnet (PMAG) that is located directly downstream of it, and the PMAG.

We carefully checked the *G4Beamline* and *MARS* models of the target station against its documentation and drawings, and we consulted a number of specialists regarding the layout of the target station and the geometry of its particle optical elements. We revised the *G4Beamline* and *MARS* models based on this verification.

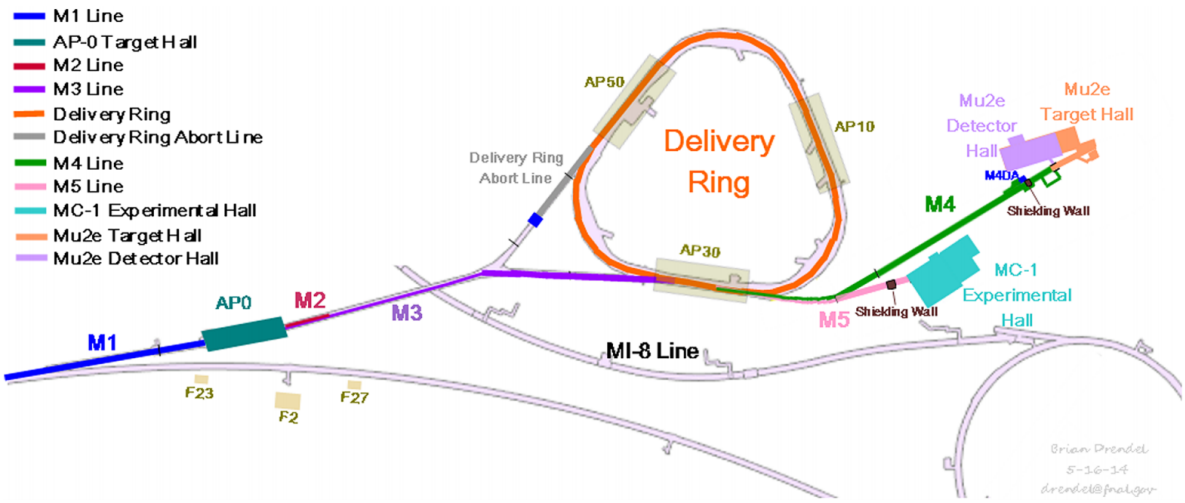

Figure 2: Layout of the beamlines of the Muon Campus at Fermilab. (Image used with permission from Brian Drendel.)

To accurately model and quantify the early-to-late phase change systematics, we must understand the potential sources of these systematics. To that end, we have performed [13] high-statistics simulations of the beamlines of the Muon Campus of Fermilab, starting from the Muon g-2 target station (AP0), through the M2 and M3 beamlines, for four turns around the Delivery Ring, and through the M4 and M5 beamlines (see Fig. 2). The simulations further continued through the injection channel, including the inflector, and up to 2000 turns around the Muon g-2 storage ring.

In the experiment, $\sim 1 \times 10^{12}$ protons-on-target (PoT) yield several thousand muons after the first turn around the storage ring, considering factors including the tertiary beam nature of the muon beam, the losses of $\sim 50\%$ on the aperture of the inflector, and further losses of $\sim 99.5\%$ in the first turn around the storage ring. For end-to-end beamline simulations to yield sufficiently high statistics in the storage ring, it is thus necessary to run simulations of at least $\sim 1 \times 10^{12}$ PoT in aggregate.

The high-statistics simulations of the Muon g-2 beamlines were performed with 3×10^{12} PoT using *G4beamline*-3.04 from the upstream end of the target station to the end of the M3 beamline, and using *BMAD* [14, 15] from the end of the M3 beamline to up to 2000 turns in the Muon g-2 storage ring. High-performance computing (HPC) resources of the National Energy Research Scientific Computing Center (NERSC) were used for the simulations.

The simulations kept track of the initial phase space coordinates of the muons, enabling the analysis of their correlations with the characteristics of the muons as they circulate around the storage ring.

Our studies based on the simulation results include a g-2 phase-versus-momentum-deviation study, which is useful for the determination of the systematic shift of ω_a due to momentum-dependent muon losses; a muon losses study; and a principal component analysis (PCA) with k-means clustering. The purpose of the PCA was to find correlations between orbital and spin coordinates in the storage ring and the position within the beamlines where the muon was originally produced [13].

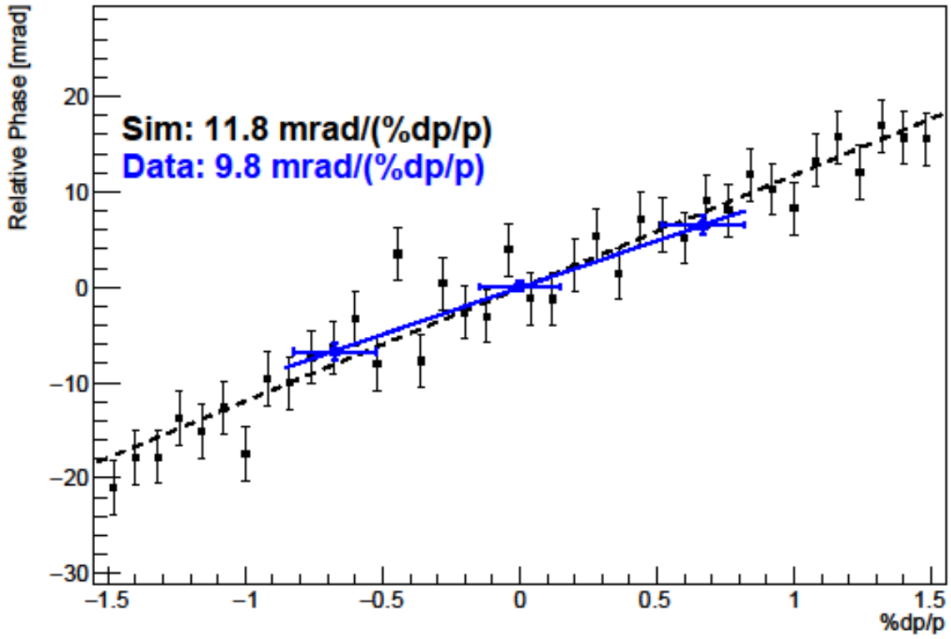

Figure 3: Momentum dependence of the initial phase ϕ in Eq. 5 due to the magnetic dipoles in the Delivery Ring. The simulations (black plot markers) are in good agreement with experimental data (blue, preliminary). The experimental data were obtained by studying the behavior of muons with momenta above and below the magic momentum in the storage ring.

The g-2 phase-versus-momentum-deviation slope at injection from our simulations is in good agreement with experimental data, as Fig. 3 shows. The equilibrium radius x_e of a muon in the storage ring depends on its momentum deviation $\Delta p/p_0$ with a linear approximation $\Delta p/p_0 = \eta x_e$, where η is the periodic dispersion. Because of the amplitude-dependent tune shifts and the scattering on the collimators, the momentum-dependent x_e causes a momentum dependence of the muon losses in the storage ring. Thus, there is an early-to-late spin phase change in the storage ring due to muon losses.

The muon distribution at the end of the M5 beamline from the 3×10^{12} PoT simulations is being used as a new initial muon distribution for simulations of the Muon g-2 storage ring using *gm2ringsim* [16], which is a custom simulation code based on *Geant4* and Fermilab's *art* event-processing framework [17].

While work on the early-to-late phase change due to muon losses is still in progress, we expect a

$10-20\,\mathrm{ppb}$ error of ω_a due to muon losses, which is far below the overall $70\,\mathrm{ppb}$ TDR systematic error on the spin precession, and meets the TDR goal of $20\,\mathrm{ppb}$ for the systematic error due to muon losses.

4 Conclusion

As of the time of the conference, the Muon g-2 experiment is running well and has entered Run-3. We are making progress on the analysis, and we are expecting to release the first results in 2020.

We have developed sophisticated modeling tools and data-driven approaches to quantify systematics, such as the muon loss phase.

The author of this paper performed high-statistics simulations of the Muon Campus beamlines using *G4beamline* and *BMAD*, and a number of systematic analyses based on the 3×10^{12} PoT simulations. The momentum dependence of the initial g-2 phase from the 3×10^{12} PoT simulations is in good agreement with preliminary experimental data. The muon distribution from the 3×10^{12} PoT simulations is used for *Geant4*-based *gm2ringsim* simulations of the Muon g-2 storage ring.

Acknowledgements

We are thankful to Ian Bailey, Jim Morgan, Diktys Stratakis, Sergei Striganov, Chris Polly, Alex Herrod, Maxim Korostelev, Yun He, Anthony Leveling, Alex Keshavarzi, Ronald Lebeau, Dean Still, Nikolai Mokhov, and Vladimir Tishchenko for productive and interesting discussions. This work was supported by the Cockcroft Institute of Accelerator Science and Technology, a Science and Technology Facilities Council facility, under STFC grant no. ST/P002056/1. This manuscript has been authored by Fermi Research Alliance, LLC under Contract No. DE-AC02-07CH11359 with the U.S. Department of Energy, Office of Science, Office of High Energy Physics. This research used the resources of the National Energy Research Scientific Computing Center (NERSC), a U.S. Department of Energy Office of Science User Facility operated under Contract No. DE-AC02-05CH11231. This material is based upon work supported by the U.S. Department of Energy, Office of Science, under Contract No. DE-FG02-08ER41546 and Contract No. DE-SC0018636.

References

[1] T. Aoyama et al., *The anomalous magnetic moment of the muon in the Standard Model*, *arXiv e-prints* (2020) arXiv:2006.04822.

[2] C. Patrignani et al. (Particle Data Group), *Review of Particle Physics*, *Chinese Physics C* **40** (2016), no. 10 100001. See also its 2017 update.

[3] F. Jegerlehner, *The Muon g-2 in Progress*, *Acta Physica Polonica B* **49** (2018), no. 6 1157.

[4] V. Guelpers, *Recent Developments of Muon g-2 from Lattice QCD*, in *Proceedings of 37th International Symposium on Lattice Field Theory — PoS(LATTICE2019)*, vol. 363, p. 224, 2020.

[5] W. J. Marciano, A. Masiero, P. Paradisi, and M. Passera, *Contributions of axionlike particles to lepton dipole moments*, *Phys. Rev. D* **94** (2016) 115033.

[6] S. Iguro, Y. Omura, and M. Takeuchi, *Testing the 2HDM explanation of the muon g-2 anomaly at the LHC*, *Journal of High Energy Physics* **2019** (2019), no. 11.

[7] J. Grange et al., *Muon (g-2) Technical Design Report*, Design Report FERMILAB-FN-0992-E, Muon g-2 Collaboration, Fermi National Accelerator Laboratory, Batavia, IL, 2015.

[8] P. J. Mohr, D. B. Newell, and B. N. Taylor, *CODATA recommended values of the fundamental physical constants: 2014*, *Rev. Mod. Phys.* **88** (2016) 035009.

[9] Muons, Inc., *G4beamline (version 3.04)*, 2017. Available from http://www.muonsinternal.com/muons3/G4beamline [accessed 14-Sep-2020].

[10] N. V. Mokhov and C. C. James, *The MARS Code System User's Guide Version 15(2016)*, Technical Report FERMILAB-FN-1058-APC, Fermi National Accelerator Laboratory, Batavia, IL, 2017.

[11] N. Mokhov, P. Aarnio, Y. Eidelman, K. Gudima, A. Konobeev, V. Pronskikh, I. Rakhno, S. Striganov, and I. Tropin, *MARS15 Code Developments Driven by the Intensity Frontier Needs*, *Prog. Nucl. Sci. Tech.* **4** (2014) 496–501.

[12] D. Stratakis, M. E. Convery, C. Johnstone, J. Johnstone, J. P. Morgan, D. Still, J. D. Crnkovic, V. Tishchenko, W. M. Morse, and M. J. Syphers, *Accelerator performance analysis of the Fermilab Muon Campus*, *Phys. Rev. Accel. Beams* **20** (2017) 111003.

[13] E. Valetov, *Muon g-2 End-to-End Beamline Simulations, and Systematic Analyses of Muon Losses and Origin Effects*, G-2 Experiment Document GM2-doc-19979, Muon g-2 Collaboration, Fermi National Accelerator Laboratory, Batavia, IL, 2020.

[14] D. Sagan, *Bmad: A relativistic charged particle simulation library*, *Nucl. Instrum. Meth.* **A558** (2006), no. 1 356–359. Proceedings of the 8th International Computational Accelerator Physics Conference.

[15] M. Korostelev, I. Bailey, A. Herrod, J. Morgan, W. Morse, D. Stratakis, V. Tishchenko, and A. Wolski, *End-to-End Beam Simulations for the New Muon G-2 Experiment at Fermilab*, in *7th International Particle Accelerator Conference*, 2016. Paper WEPMW001.

[16] Muon g-2 Collaboration, *gm2ringsim (version 9.52.00)*, 2020. Available from https://cdcvs.fnal.gov/redmine/projects/gm2ringsim [accessed 12-Sep-2020].

[17] C. Green, J. Kowalkowski, M. Paterno, M. Fischler, L. Garren, and Q. Lu, *The Art Framework*, *J. Phys. Conf. Ser.* **396** (2012) 022020.


Moutarde
Cumin
POIVRE NOIR
EPICE CREOLE
SAUCE CHIEN
Jaeger
EPICE DU ROTISSEUR N.4
ROTISSEUR 4
3kg

B physics anomalies

Marco Santimaria
on behalf of the LHCb collaboration

e-mail: marco.santimaria@cern.ch

INFN - Laboratori Nazionali di Frascati

Presented at the 3rd World Summit on Exploring the Dark Side of the Universe
Guadeloupe Islands, March 9-13 2020

Abstract

Multiple hints of a lepton flavour universality violation have been reported by Belle, BaBar and LHC experiments in B meson decays. More convincing evidences arise if the measurements are considered together, and several New Physics models have been proposed to provide a coherent explanation. The LHCb experiment plays a leading role in this regard, and after the end of Run 2 it has collected an unprecedented amount of b hadron decays. In this note, an overview of the anomalies is presented in the light of the latest measurements.

1 Introduction

In the Standard Model (SM), the couplings of gauge bosons to leptons have equal magnitude. This property of Lepton Flavour Universality (LFU) is not protected by an underlying symmetry but precisely verified in $Z \to l^+l^-$, $J/\psi \to l^+l^-$ as well as $\pi, K \to l\nu$ decays among others [1]. However, measurements of theoretically clean observables from both B-factories and LHC experiments show deviations from this universality in B decays, to a degree that requires further investigation. Such measurements concern both neutral-current $b \to sll$ and charged-current $b \to cl\nu$ processes, as reported in Sec. 2 and Sec. 3, respectively, while a possible New Physics (NP) explanation is discussed in Sec. 4. Finally, recent LHCb searches for B decays that explicitly violate lepton flavour conservation are presented in Sec. 5.

2 Lepton Flavour Universality tests with $b \to sll$ decays

Being flavour-changing neutral current transitions, $b \to sll$ decays can only occur at the loop level in the SM, and are predicted to be rare due to the GIM mechanism [2]. For this reason, precise measurements of their branching fraction or angular observables allow to access indirectly new possible degrees of freedom, probing NP scales which are out of reach of direct searches.

Since QCD interactions at the b quark mass scale are non-perturbative, an Effective Field Theory (EFT) can be employed to factorise high- and low-energy contributions. The full theory can therefore be simplified with an effective Hamiltonian:

$$\mathcal{H}_{eff} = \frac{G_F}{\sqrt{2}} \sum_i V^i_{\text{CKM}} C_i(\lambda) \mathcal{O}_i(\lambda), \tag{1}$$

where G_F is the Fermi constant and V_{CKM} is the CKM matrix. The long-distance (i.e. low-energy) contributions are described by local operators $\mathcal{O}_i$, which are factorised from the short-distance contributions, encoded in the Wilson coefficients C_i at a given scale λ. The SM local operators describing $b \to sll$ processes are $\mathcal{O}_9^{(\prime)} = (\bar{s}P_{L(R)}b)(\bar{l}\gamma^\mu l)$ and $\mathcal{O}_{10}^{(\prime)} = (\bar{s}P_{L(R)}b)(\bar{l}\gamma^\mu\gamma^5 l)$, where the primed operators are chirality flipped, as projected by $P_{L(R)} = (1\pm\gamma^5)/2$. In the amplitude evaluation, the hadronic matrix element, parametrised as a form factor, is computed with non-perturbative techniques such as lattice QCD, and usually represents the largest source of uncertainty. A generic NP contribution at the scale Λ takes the form $\Delta\mathcal{H}_{eff} = (c_i/\Lambda^2_{\rm NP})\mathcal{O}_i$, and can therefore alter the SM Wilson coefficients or introduce new operators.

2.1 Branching fractions of $b \to s\mu^+\mu^-$ processes

The simplest observable for $b \to sll$ processes is the branching fraction, which can be measured as a function of the dilepton invariant mass squared, q^2.

Several measurements of $b \to s\mu^+\mu^-$ differential branching fractions, performed with Run 1 data at LHCb, indicated a downward deviation with respect to the SM prediction in the low q^2 regime. Three examples, which involve $B^+ \to K^+\mu^+\mu^-$, $B^0 \to K^0\mu^+\mu^-$ and $B^+ \to K^{*+}\mu^+\mu^-$ transitions are given in Fig. 1. Whether these deviations are due to a weaker muon coupling or to an issue in the treatment of hadronic interactions cannot be assessed. At low q^2, the theoretical prediction is in fact limited by the knowledge of the form factors, so it is crucial to define observables in which this source of uncertainty is reduced.

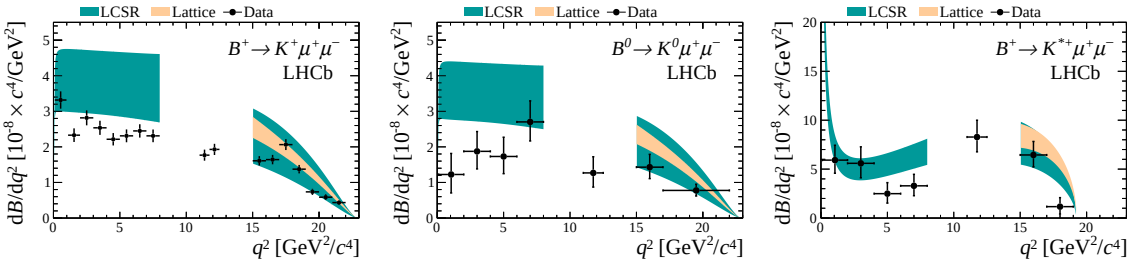

Figure 1: Differential branching fractions for three $b \to s\mu^+\mu^-$ processes measured at LHCb, together with two predictions using different form factor computations [3].

2.2 Angular distributions of $b \to s\mu^+\mu^-$ processes

The $B^0 \to K^{*0}\mu^+\mu^-$ differential decay rate can be described by the q^2 and three angles $\vec{\Omega} = (\phi, \theta_K, \theta_L)$ (defined in Fig. 2 (left)) as

$$\frac{d^4\overline{\Gamma}[B^0 \to K^{*0}\mu^+\mu^-]}{dq^2 d\vec{\Omega}} = \frac{9}{32\pi}\sum_i \overline{I}_i(q^2) f_i(\vec{\Omega}), \tag{2}$$

i.e. as a superposition of angular moments f_i with coefficients I_i. By using ratios of angular coefficients, optimised observables can be defined, in which the leading hadronic uncertainty cancels. Among those is

$$P_5' = \frac{S_5}{\sqrt{F_L(1-F_L)}}, \tag{3}$$

where S_5 is a CP-averaged angular coefficient and F_L is the fraction of longitudinal polarisation of the K^{*0}, as defined in Ref. [5].

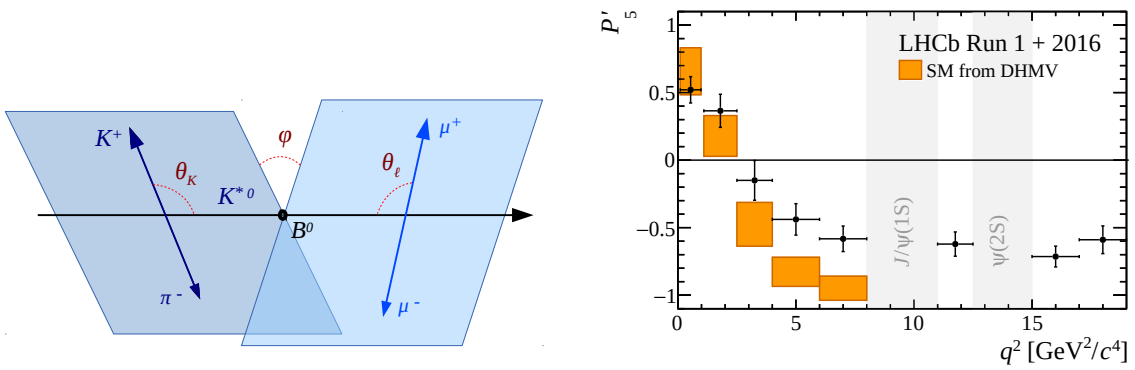

Figure 2: Left: angular basis for the $B^0 \to K^{*0}\mu^+\mu^-$ analysis. Right: P_5' measurement from LHCb compared with the SM prediction [4].

P_5' measurements performed at Belle [6] and with Run 1 data at LHCb [7] and ATLAS [8], coherently indicate a deviation from the SM prediction. LHCb recently updated this measurement by adding a portion of Run 2 data, as shown in Fig. 2 (right). The local deviations in the fourth and fifth q^2 bins are $2.5\ \sigma$ and $2.9\ \sigma$, respectively. The global fit to the full set of CP-averaged angular observables measured at LHCb yields a discrepancy with respect to the C_9 SM value of $3.3\ \sigma$, though this significance depends on the choice of the SM nuisance parameters [4].

It is worth noticing that even though the J/ψ and $\psi(2S)$ resonant regions are excluded in this analysis, the theoretical estimate of the charm-loop contribution to the adjacent q^2 regions is far from trivial [9].

2.3 Ratios of branching fractions

A way to probe the relative magnitude of muon and electron couplings, such that the QCD uncertainties cancel, is to measure the ratio of branching fractions

$$R_H = \frac{\int_{q^2_{min}}^{q^2_{max}} \frac{d\Gamma[B\to H\mu^+\mu^-]}{dq^2} dq^2}{\int_{q^2_{min}}^{q^2_{max}} \frac{d\Gamma[B\to He^+e^-]}{dq^2} dq^2}, \tag{4}$$

where H is a hadron. For example, the SM prediction of R_K is 1 with an uncertainty of $\mathcal{O}(1\%)$, due to tiny QED and lepton mass effects [10].

R_K [11] and R_{K^*} [12] measurements performed at the LHCb experiment on Run 1 data showed tensions at the $2.5\ \sigma$ level. In 2019, the LHCb collaboration improved the Run 1 R_K measurement by adding a portion of Run 2 data to double the previous sample size [13]. To allow for the cancellation of detection differences between electrons and muons, R_K is measured at LHCb as a double ratio with respect to the J/ψ resonant modes:

$$R_K = \frac{\mathcal{B}(B^+ \to K^+\mu^+\mu^-)}{\mathcal{B}(B^+ \to K^+e^+e^-)} \Big/ \frac{\mathcal{B}(B^+ \to K^+J/\psi(\mu^+\mu^-))}{\mathcal{B}(B^+ \to K^+J/\psi(e^+e^-))}, \tag{5}$$

which exploits the fact that $J/\psi \to l^+l^-$ branching fractions are lepton-universal within 0.4% [1].

The experimental measurement of Eq. 5 translates into correcting the observed yield of each mode, estimated from invariant mass fits, by the corresponding trigger and selection efficiencies. To ensure that these efficiencies are well determined, the ratio of the $\mu^+\mu^-$ and e^+e^- resonant modes, which does not benefit from the cancellation of systematic effects of Eq. 5, is preventively measured and

found to be compatible with unity:

$$r_{J/\psi} = \frac{\mathcal{B}(B^+ \to K^+ J/\psi(\mu^+\mu^-))}{\mathcal{B}(B^+ \to K^+ J/\psi(e^+e^-))} = 1.014 \pm 0.035. \tag{6}$$

R_K is then measured in the range $1.1 < q^2 < 6.0\,\text{GeV}^2/\text{c}^4$ and found to be

$$R_K = 0.846^{+0.060+0.016}_{-0.054-0.014}, \tag{7}$$

where the first error is statistical, and dominated by the size of the $B^+ \to K^+e^+e^-$ sample, while the second error is systematic. This is the most precise measurement of R_K to date and falls 2.5 σ below the SM prediction.

Recently, the first LFU test on Λ_b^0 baryons has been performed at LHCb: $R_{pK} = 0.86^{+0.14}_{-0.11} \pm 0.05$ [14], which is about one standard deviation below the SM, though with larger statistical uncertainty with respect to B meson measurements.

Contrary to differential branching fractions and optimised angular observables, these anomalies are difficult to be explained with theoretical unknowns in the SM predictions.

2.4 Global fit to Wilson coefficients

The $b \to sll$ and correlated observables can be considered together in a global fit to the Wilson coefficients C_9 and C_{10} [15]. The fit result, showed in Fig. 3 (left), indicates a preference for NP of the form $C_9 = -C_{10}$, disfavouring right-handed currents. The experimental precision on C_{10} is actually driven by the $B_s^0 \to \mu^+\mu^-$ branching fraction measurement, currently sitting at $\sim 2\sigma$ below the precise SM prediction, as shown in Fig. 3 (right). The statistical significance of these tensions calls for more precise measurements, in particular those exploiting the full Run 2 data at LHCb.

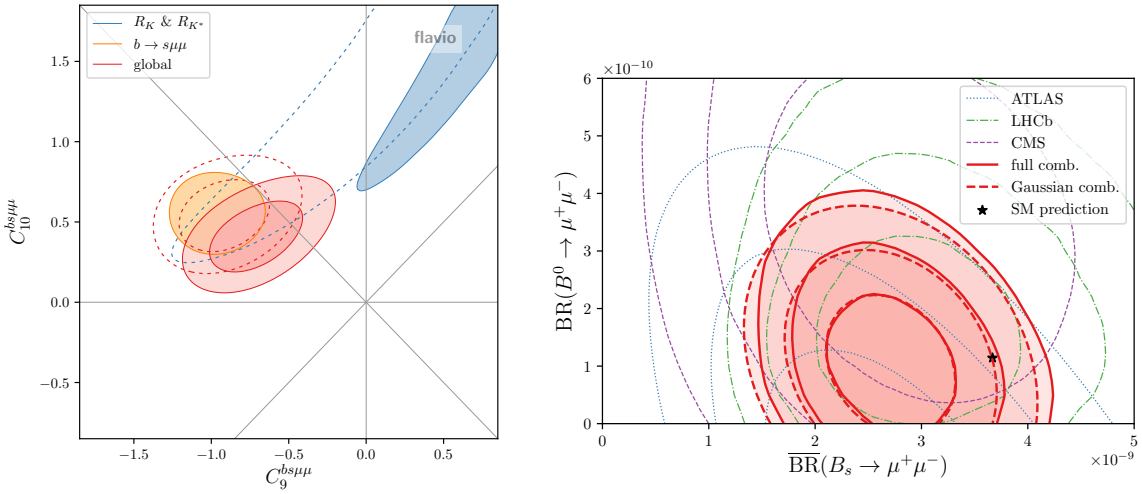

Figure 3: Left: Global fit to the NP contributions on C_9 and C_{10} [15]. The dashed contours exclude the R_K and R_{K^*} results presented at Moriond-2019. Right: experimental combination of the $B^0_{(s)} \to \mu^+\mu^-$ branching fraction measurements [15].

3 Lepton Flavour Universality tests with $b \to cl\nu$ decays

Contrary to $b \to sll$, $b \to cl\nu$ processes are charged-current tree-level decays in the SM with typical branching fractions of $\mathcal{O}(1\%)$. Their differential decay rate receives contributions from V_{cb} and from

QCD interactions, parametrised as a form factor f: $d\Gamma/dq^2(H_b \to H_c l^- \overline{\nu}_l) \propto G_F^2 |V_{cb}|^2 f(q^2)^2$. In the ratio of branching fractions

$$R(H_c) = \frac{\mathcal{B}(H_b \to H_c \tau^- \overline{\nu}_\tau)}{\mathcal{B}(H_b \to H_c \mu^- \overline{\nu}_\mu)}, \tag{8}$$

V_{cb} is absent and form factors partially cancel, therefore allowing for a precise SM prediction.

This observable, which tests the ratio of τ/μ couplings, has been measured by the Belle, BaBar and LHCb collaborations in $B \to D$ and $B \to D^*$ decays, as shown in Fig. 4. The present experimental

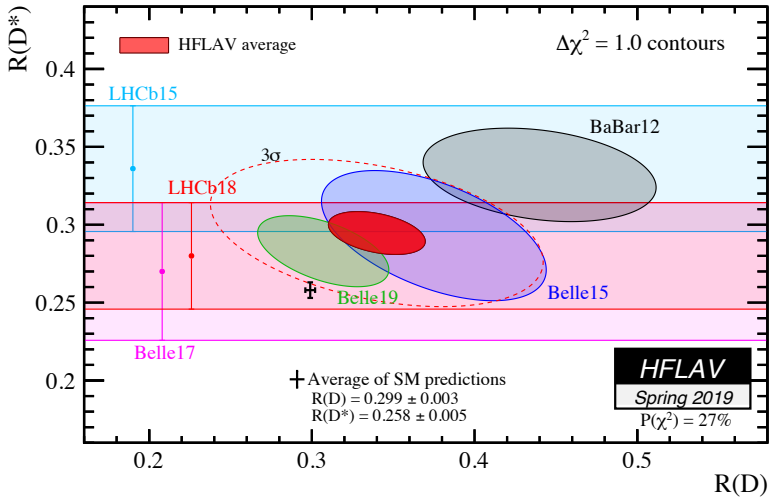

Figure 4: LHCb, Belle and BaBar measurements in the $R(D) - R(D^*)$ plane together with their combination (red ellipse) and an average of SM predictions [16].

average is 3.1 σ above the SM prediction, the latter being limited by the knowledge of the form factors [17] but also characterised by non-trivial QED corrections [18]. On the experimental side, the modelling of $B \to D^{**}$ and $B \to D^* X$ backgrounds as well as QED corrections [19] performed with PHOTOS [20] represent common sources of systematic error.

An additional LFU test on $B_c \to J/\psi l \nu_l$ decays, $R(J/\psi) = B_c \to J/\psi \tau^- \overline{\nu}_\tau / B_c \to J/\psi \mu^- \overline{\nu}_\mu$, has been performed at LHCb [21] and found to be about 2 σ above the SM value [22].

4 A New Physics explanation

Within the SM EFT, two quark-lepton operators can produce a LFU violation in quark decays assuming NP coupling to the third generation:

$$\mathcal{O}_{\rm NP}^{(S)} = Q'_{L,3}\gamma_\mu Q'_{L,3} L'_{L,3}\gamma^\mu L'_{L,3} \qquad \text{and} \qquad \mathcal{O}_{\rm NP}^{(T)} = Q'_{L,3}\gamma_\mu \sigma^i Q'_{L,3} L'_{L,3}\gamma^\mu \sigma^i L'_{L,3}, \tag{9}$$

where σ^i are the Pauli matrices. $\mathcal{O}_{\rm NP}^{(T)}$ can generate large tree-level charged current effects to explain the $b \to c\tau\nu_\tau$ anomalies, while smaller couplings, comparable to SM loop level, can be achieved with suitable mixing angles to fit the $b \to s\mu\mu$ tensions [23]. Models with a single tree-level mediator which can generate the effective operators in Eq. 9 either feature new gauge bosons with non-universal couplings (e.g Z') or bosons carrying both baryon and lepton numbers, i.e. Leptoquarks (LQ). Since Z' bosons mediate the $B_s - \overline{B}_s$ mixing at tree-level, and are restricted by di-muon direct searches, the LQ option seems favoured [24]. The work reported in Fig. 5 (left) shows how data bounds indicate a preference for a vector singlet leptoquark model (U_1), which can arise from the breaking of a $SU(4)$ Pati-Salam symmetry [25, 26].

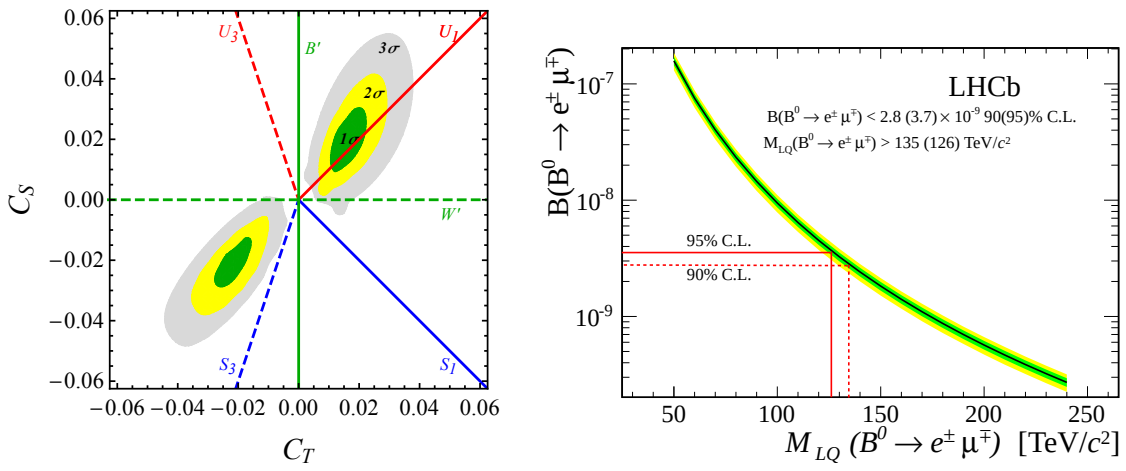

Figure 5: Left: $1, 2, 3\ \sigma$ contours from data fit in the space of $C_S - C_T$ coefficients of the operators defined in Eq. 9. The lines indicate the correlation in single-mediator models with singlet (solid lines) and triplet (dashed lines) colour-less vectors (green), coloured scalar (blue) and coloured vectors (red) [24]. Right: LQ mass exclusion range determined by a $B^0 \to e^\pm\mu^\mp$ branching fraction limit [27].

5 Search for Lepton Flavour Violating decays at LHCb

NP models proposed to accommodate the observed LFU deviations typically imply a violation of the lepton flavour (LFV) [28]. Its conservation is an accidental symmetry of the SM, and known to be violated in neutrino oscillations. Charged LFV, which is induced in the SM at the loop level with a neutrino oscillation, is therefore predicted to occur but at unmeasurable small rates of $\mathcal{O}(10^{-54})$ [29]. However, NP contributions can enhance these rates to experimentally accessible levels. For this reason, searches for LFV in B decays have been performed at LHCb on $e\mu$ and $\tau\mu$ modes, as summarised in Tab. 1, but no signal has been yet observed. As an example, Fig. 5 (right) shows how a precise measurement of the $B^0 \to e^\pm\mu^\mp$ branching fraction is able to probe LQ masses in the 100 TeV range.

Decay mode	Branching fraction	Reference
$B^0 \to e^\pm\mu^\mp$	$< 1.3(1.0) \times 10^{-9}$	[30]
$B_s^0 \to e^\pm\mu^\mp$	$< 6.3(5.4) \times 10^{-9}$	[30]
$B^0 \to \tau^\pm\mu^\mp$	$< 1.4 \times 10^{-5}$	[31]
$B_s^0 \to \tau^\pm\mu^\mp$	$< 4.2 \times 10^{-5}$	[31]
$B^+ \to K^+\mu^-e^+$	$< 9.5(7.0) \times 10^{-9}$	[32]
$B^+ \to K^+\mu^+e^-$	$< 8.8(6.4) \times 10^{-9}$	[32]
$B^+ \to K^+\mu^-\tau^+$	$< 8.8(6.4) \times 10^{-9}$	[33]

Table 1: Upper limits at $95\%(90\%)$ confidence level on the branching fractions of LFV B decays set by the LHCb experiment.

6 Conclusions

Several intriguing anomalies in B decays have triggered theoretical interest in possible New Physics mediators coupling differently to the lepton flavours. For this reason, a strong effort to provide more precise predictions and more sensitive measurements is ongoing. With Belle II starting its activity, and LHCb to start taking data for the Run 3 in 2021, the next few years will be fundamental to clarify the picture. Noticeably, the precision on the crucial observables $R_{K^{(*)}}$ and $R(D^{(*)})$ is foreseen to be competitive between the two experiments [34].

References

[1] **Particle Data Group** Collaboration, M. Tanabashi et al., *Review of Particle Physics*, *Phys. Rev. D* **98** (2018), no. 3 030001.

[2] S. Glashow, J. Iliopoulos, and L. Maiani, *Weak Interactions with Lepton-Hadron Symmetry*, *Phys. Rev. D* **2** (1970) 1285–1292.

[3] **LHCb** Collaboration, R. Aaij et al., *Differential branching fractions and isospin asymmetries of $B \to K^{(*)}\mu^+\mu^-$ decays*, *JHEP* **06** (2014) 133, [arXiv:1403.8044].

[4] **LHCb** Collaboration, R. Aaij et al., *Measurement of CP-averaged observables in the $B^0 \to K^{*0}\mu^+\mu^-$ decay*, *Phys. Rev. Lett.* **125** (2020), no. 1 011802, [arXiv:2003.04831].

[5] J. Matias, F. Mescia, M. Ramon, and J. Virto, *Complete Anatomy of $\bar{B}_d \to \bar{K}^{*0}(\to K\pi)l^+l^-$ and its angular distribution*, *JHEP* **04** (2012) 104, [arXiv:1202.4266].

[6] **Belle** Collaboration, S. Wehle et al., *Lepton-Flavor-Dependent Angular Analysis of $B \to K^*\ell^+\ell^-$*, *Phys. Rev. Lett.* **118** (2017), no. 11 111801, [arXiv:1612.05014].

[7] **LHCb** Collaboration, R. Aaij et al., *Angular analysis of the $B^0 \to K^{*0}\mu^+\mu^-$ decay using 3 fb^{-1} of integrated luminosity*, *JHEP* **02** (2016) 104, [arXiv:1512.04442].

[8] **ATLAS** Collaboration, M. Aaboud et al., *Angular analysis of $B_d^0 \to K^*\mu^+\mu^-$ decays in pp collisions at $\sqrt{s} = 8$ TeV with the ATLAS detector*, *JHEP* **10** (2018) 047, [arXiv:1805.04000].

[9] A. Khodjamirian, T. Mannel, A. Pivovarov, and Y.-M. Wang, *Charm-loop effect in $B \to K^{(*)}\ell^+\ell^-$ and $B \to K^*\gamma$*, *JHEP* **09** (2010) 089, [arXiv:1006.4945].

[10] M. Bordone, G. Isidori, and A. Pattori, *On the Standard Model predictions for R_K and R_{K^*}*, *Eur. Phys. J. C* **76** (2016), no. 8 440, [arXiv:1605.07633].

[11] **LHCb** Collaboration, R. Aaij et al., *Test of lepton universality using $B^+ \to K^+\ell^+\ell^-$ decays*, *Phys. Rev. Lett.* **113** (2014) 151601, [arXiv:1406.6482].

[12] **LHCb** Collaboration, R. Aaij et al., *Test of lepton universality with $B^0 \to K^{*0}\ell^+\ell^-$ decays*, *JHEP* **08** (2017) 055, [arXiv:1705.05802].

[13] **LHCb** Collaboration, R. Aaij et al., *Search for lepton-universality violation in $B^+ \to K^+\ell^+\ell^-$ decays*, *Phys. Rev. Lett.* **122** (2019), no. 19 191801, [arXiv:1903.09252].

[14] **LHCb** Collaboration, R. Aaij et al., *Test of lepton universality with $\Lambda_b^0 \to pK^-\ell^+\ell^-$ decays*, *JHEP* **05** (2020) 040, [arXiv:1912.08139].

[15] J. Aebischer, W. Altmannshofer, D. Guadagnoli, M. Reboud, P. Stangl, and D. M. Straub, *B-decay discrepancies after Moriond 2019*, *Eur. Phys. J. C* **80** (2020), no. 3 252, [arXiv:1903.10434].

[16] **HFLAV** Collaboration, Y. S. Amhis et al., *Averages of b-hadron, c-hadron, and τ-lepton properties as of 2018*, arXiv:1909.12524. updated results and plots available at https://hflav.web.cern.ch/.

[17] M. Bordone, M. Jung, and D. van Dyk, *Theory determination of $\bar{B} \to D^{(*)}\ell^-\bar{\nu}$ form factors at $\mathcal{O}(1/m_c^2)$*, *Eur. Phys. J. C* **80** (2020), no. 2 74, [arXiv:1908.09398].

[18] S. de Boer, T. Kitahara, and I. Nisandzic, *Soft-Photon Corrections to $\bar{B} \to D\tau^-\bar{\nu}_\tau$ Relative to $\bar{B} \to D\mu^-\bar{\nu}_\mu$*, *Phys. Rev. Lett.* **120** (2018), no. 26 261804, [arXiv:1803.05881].

[19] S. Calí, S. Klaver, M. Rotondo, and B. Sciascia, *Impacts of radiative corrections on measurements of lepton flavour universality in $B \to D\ell\nu_\ell$ decays*, *Eur. Phys. J. C* **79** (2019), no. 9 744, [arXiv:1905.02702].

[20] P. Golonka and Z. Was, *PHOTOS Monte Carlo: A Precision tool for QED corrections in Z and W decays*, *Eur. Phys. J. C* **45** (2006) 97–107, [hep-ph/0506026].

[21] **LHCb** Collaboration, R. Aaij et al., *Measurement of the ratio of branching fractions $\mathcal{B}(B_c^+ \to J/\psi\tau^+\nu_\tau)/\mathcal{B}(B_c^+ \to J/\psi\mu^+\nu_\mu)$*, *Phys. Rev. Lett.* **120** (2018), no. 12 121801, [arXiv:1711.05623].

[22] J. Harrison, C. T. Davies, and A. Lytle, *$R(J/\psi)$ and $B_c^- \to J/\psi\ell^-\overline{\nu}_\ell$ Lepton Flavor Universality Violating Observables from Lattice QCD*, arXiv:2007.06956.

[23] B. Bhattacharya, A. Datta, D. London, and S. Shivashankara, *Simultaneous Explanation of the R_K and $R(D^{(*)})$ Puzzles*, *Phys. Lett. B* **742** (2015) 370–374, [arXiv:1412.7164].

[24] D. Buttazzo, A. Greljo, G. Isidori, and D. Marzocca, *B-physics anomalies: a guide to combined explanations*, *JHEP* **11** (2017) 044, [arXiv:1706.07808].

[25] J. C. Pati and A. Salam, *Lepton Number as the Fourth Color*, *Phys. Rev. D* **10** (1974) 275–289. [Erratum: Phys.Rev.D 11, 703–703 (1975)].

[26] M. Bordone, C. Cornella, J. Fuentes-Martin, and G. Isidori, *A three-site gauge model for flavor hierarchies and flavor anomalies*, *Phys. Lett. B* **779** (2018) 317–323, [arXiv:1712.01368].

[27] **LHCb** Collaboration, R. Aaij et al., *Search for the lepton-flavor violating decays $B_s^0 \to e^\pm\mu^\mp$ and $B^0 \to e^\pm\mu^\mp$*, *Phys. Rev. Lett.* **111** (2013) 141801, [arXiv:1307.4889].

[28] S. L. Glashow, D. Guadagnoli, and K. Lane, *Lepton Flavor Violation in B Decays?*, *Phys. Rev. Lett.* **114** (2015) 091801, [arXiv:1411.0565].

[29] L. Calibbi and G. Signorelli, *Charged Lepton Flavour Violation: An Experimental and Theoretical Introduction*, *Riv. Nuovo Cim.* **41** (2018), no. 2 71–174, [arXiv:1709.00294].

[30] **LHCb** Collaboration, R. Aaij et al., *Search for the lepton-flavour violating decays $B^0_{(s)} \to e^\pm\mu^\mp$*, *JHEP* **03** (2018) 078, [arXiv:1710.04111].

[31] **LHCb** Collaboration, R. Aaij et al., *Search for the lepton-flavour-violating decays $B_s^0 \to \tau^\pm\mu^\mp$ and $B^0 \to \tau^\pm\mu^\mp$*, *Phys. Rev. Lett.* **123** (2019), no. 21 211801, [arXiv:1905.06614].

[32] **LHCb** Collaboration, R. Aaij et al., *Search for Lepton-Flavor Violating Decays $B^+ \to K^+\mu^\pm e^\mp$*, *Phys. Rev. Lett.* **123** (2019), no. 24 241802, [arXiv:1909.01010].

[33] **LHCb** Collaboration, R. Aaij et al., *Search for the lepton flavour violating decay $B^+ \to K^+\mu^-\tau^+$ using B_{s2}^{*0} decays*, *JHEP* **06** (2020) 129, [arXiv:2003.04352].

[34] S. Bifani, S. Descotes-Genon, A. Romero Vidal, and M.-H. Schune, *Review of Lepton Universality tests in B decays*, *J. Phys. G* **46** (2019), no. 2 023001, [arXiv:1809.06229].

Axion Like Particles and Dark Matter using intact protons at the LHC

Christophe Royon

e-mail: christophe.royon@ku.edu

Department of Physics and Astronomy, The University of Kansas, Lawrence KS 66047, USA

Presented at the 3rd World Summit on Exploring the Dark Side of the Universe
Guadeloupe Islands, March 9-13 2020

Abstract

We present a new method to look for extra-dimensions and the production of axion-like particles at the Large Hadron Collider at CERN, produced via photon exchanges, by measuring intact protons after interactions. We also discuss possible applications of fast timing detectors including the measurement of cosmic ray particles in collaboration with NASA.

1 Search for quartic anomalous couplings at the LHC using intact proton in the final state

We discuss a new method to look for extra-dimensions and the production of axion-like particles at the Large Hadron Collider (LHC) located at CERN, Switzerland. We consider the exclusive production of di-photon, WW boson pairs and $Z\gamma$, as shown in Fig. 1, produced by photon exchanges. In these processes, the photons, Z and W bosons can be measured in the main ATLAS and CMS detectors while the intact protons in the final state can be tagged in special detectors called roman pots located at about 220 m from the interaction point. After describing briefly the proton detectors, we will discuss the motivation to look for these events and the reach at the LHC.

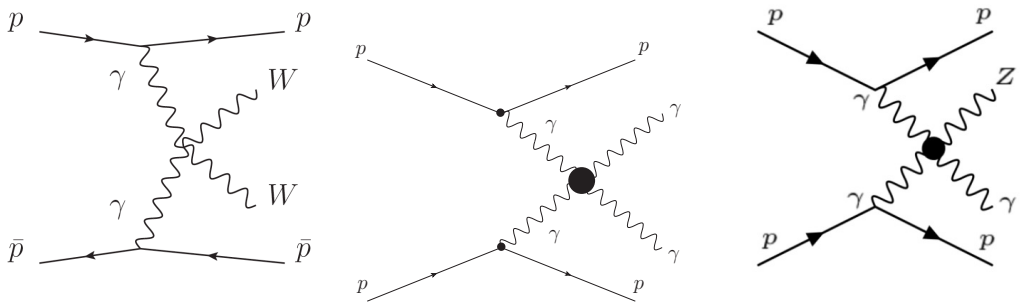

Figure 1: Diagram of exclusive production of WW, $\gamma\gamma$ and $Z\gamma$ events at high mass.

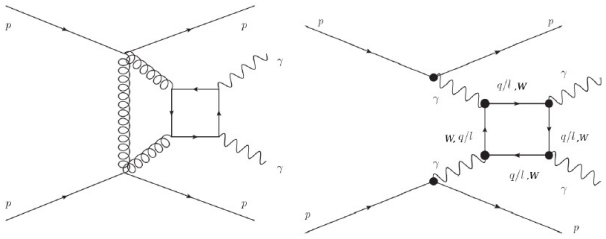

Figure 2: Exclusive di-photon production. Left: QCD process, Right: QED process.

1.1 Detecting intact protons at the LHC

The CMS-TOTEM and ATLAS collaborations installed some roman pot detectors at about 220 m from the interaction point in order to detect and measure intact protons in the final state. The CMS-TOTEM Precision Proton Spectrometer (PPS) [1, 2] and the ATLAS Forward Proton (AFP) [3] detectors have an acceptance in diffractive mass at high luminosity, for standard LHC beam lattice, above 350 GeV and below 2000 GeV allowing to be sensitive to high mass $\gamma\gamma$, WW and γZ production as illustrated in Fig 1. The protons lose parts of their energy after interaction and the LHC magnets bend the scattered protons outside the beam envelope. Protons scattered a few millimeters away from the beam are detected in the roman pots. The PPS detector has been accumulating about 115 fb^{-1} of data together with CMS since 2015. The goal for the next runs at the LHC is to record intact protons at high LHC luminosities and to collect similar luminosity as the CMS or ATLAS main detectors.

1.2 Search for $\gamma\gamma\gamma\gamma$ anomalous couplings

1.2.1 Standard Model production of exclusive di-photons

In the section, we will describe the search for $\gamma\gamma$ exclusive production using PPS or AFP in a very clean way. The QCD [4] and QED [5] diagrams leading to exclusive di-photon production are respectively shown in Fig. 2, left and right. We also distinguish between the QED exclusive production of di-photons via loops of quarks, leptons and W bosons. The di-photon exclusive cross sections are given in Fig. 3 for different contributions [5]: QCD contribution in full purple line, QED contributions from quark and lepton loops in dashed green line, W loop contribution in dotted red line, and the total QED contribution in black dashed dotted line. We note that the QCD contribution can be neglected above a di-photon mass of 200 GeV. It means that measuring two photons in CMS or ATLAS and two protons in PPS or AFP corresponding to the same interaction is a photon-induced process. We also note that the cross section of exclusive di-photon SM production at high mass is very small and will lead to a small background if we request the di-photon mass to be above 350 GeV (in order to be in the acceptance of the forward proton detectors).

1.2.2 $\gamma\gamma\gamma\gamma$ anomalous couplings

Four-photon couplings can be modified by loops of new particles or produced resonances that decay into two photons. In case of loops $\zeta_1 = \alpha_{em}^2 Q^4 m^{-4} N c_{1,s}$ where the coupling depends only on the fourth power of the charge Q and mass m of the charged particle, and on spin, $c_{1,s}$. This leads to ζ_1 of the order of 10^{-14}-10^{-13}. In case of resonances, $\zeta_1 = (f_s m)^{-2} d_{1,s}$ where f_s is the $\gamma\gamma X$ coupling of the new particle to the photon, m the mass of the new particle, and $d_{1,s}$ depends on the spin of the particle. For instance, 2 TeV dilatons lead to $\zeta_1 \sim 10^{-13}$.

The number of events for 300 fb^{-1} as a function of di-photon mass is displayed in Fig. 4 for signal and background [5] using the FPMC generator [6]. The exclusive di-photon and double Pomeron

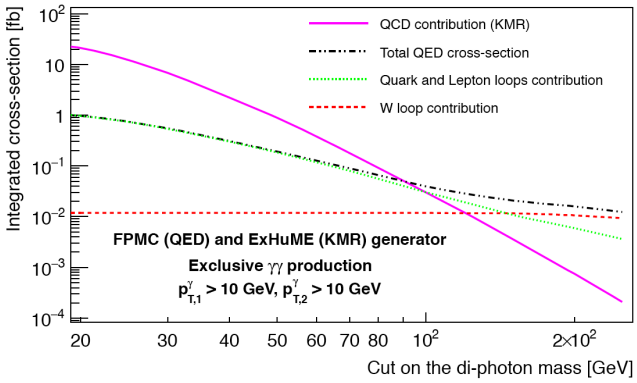

Figure 3: Exclusive di-photon cross section above a given diphoton mass (in abscissa) for different processes.

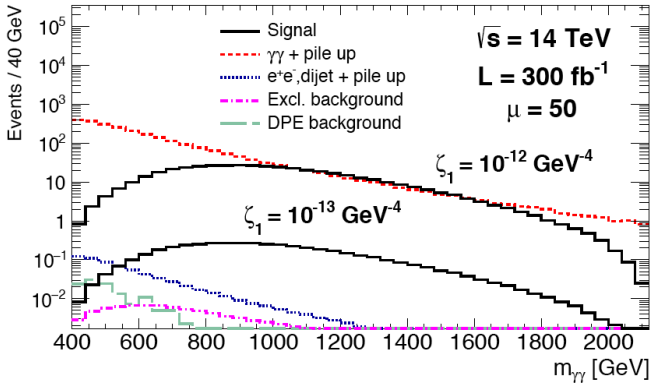

Figure 4: Number of events as a function of the di-photon mass for signal ($\zeta_1 = 10^{-12}$ and 10^{-13} GeV^{-4}) and background.

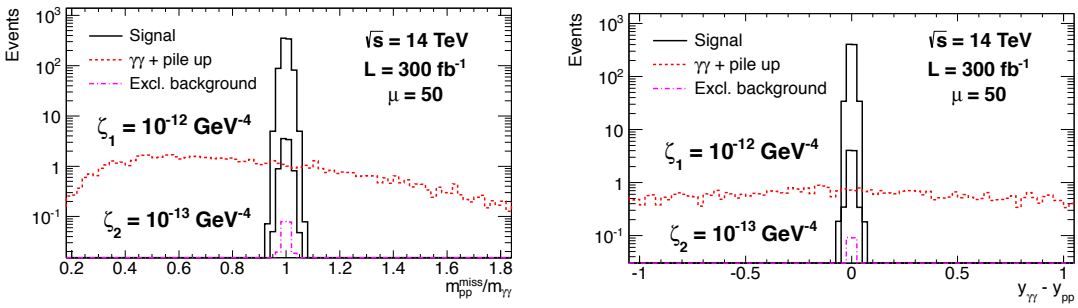

Figure 5: Left: Ratio between the proton missing mass and di-photon mass for exclusive di-photon signal events and background. Right: Difference between the di-photon and di-proton rapidity for exclusive di-photon signal and background.

exchange (DPE) backgrounds are found to be negligible at high mass. The only background that contributes at high mass is the inclusive non-diffractive di-photon and di-lepton production with pile up where leptons are misidentified as photons. The LHC collides packets of protons together and this means that there are multiple proton collisions occurring within the same bunch crossing, up to 50 with present conditions. The issue is that the two photons or the two W/Z bosons can originate from a different interaction than the two protons originating from soft additional interactions, called pile up. Pile up events can be as large as 50 at the LHC at high luminosity per bunch crossing and a typical pile up event contaminating our sample will be made of one di-photon non-diffractive event and two intact protons originating from soft diffractive events.

Since the signal only shows two photons and two intact protons in the final state, we measure all final state particles. That allows us to obtain a negligible background for 300 fb^{-1} at the LHC. The basic idea is to compare the proton missing mass and the di-photon mass as shown in Fig. 5, left [5, 7]. The signal peaks around 1.0 and the gaussian width is due to the detector resolution whereas the pile-up background leads to a much flatter distribution since the two protons are not related with the two photons. The same requirement can be performed using the difference in rapidity between the di-photon and di-proton systems, as shown in Fig. 5, right. This leads to a background of less than 0.1 event for 300 fb^{-1} [5]. The gain on sensitivity compared to other methods at the LHC without detecting intact protons is more than two orders of magnitude on the $\gamma\gamma\gamma\gamma$ anomalous coupling, reaching values down to a few 10^{-15}. It is worth noticing that, without exclusivity cuts described in Fig. 5, the background would be much larger for 300 fb^{-1}, namely about 80.3 events. We also extrapolated our results to high luminosity LHC for a luminosity of about 3000 fb^{-1}, and the sensitivity can be even further improved by a factor 10 as shown in Fig. 6 in a conservative way.

The search for anomalous couplings with tagged protons is now being pursued by the PPS collaboration and the first limit on $\gamma\gamma\gamma\gamma$ anomalous couplings was recently shown at the ICHEP 2020 conference in Prague [8] as ζ_1 <3.7 10^{-13} GeV^{-4} and ζ_2 <7.7 10^{-13} GeV^{-4}.

1.3 Search for Axion like particles at the LHC in the di-photon channel

Looking for exclusive di-photon events with tagged protons can be directly applied to the search for axion-like particles (ALPs) at high mass [9]. The ALP would be produced by $\gamma\gamma$ interactions and would decay into two photons. The sensitivity in the coupling versus ALP mass plane is shown in Fig. 7 and we see the gain of about two orders of magnitude in coupling at high mass using this method with 300 fb^{-1} at the LHC. We also note that this is complementary to looking for exclusive di-photons in pPb, $PbPb$, and $ArAr$ collisions at lower masses of ALPs. This is due to the fact that the cross section is enhanced by a factor Z^4 in heavy ion collisions but the sensitivity at high mass is reduced to a large suppression at small impact parameter due to the size of the heavy ion [10].

1.4 Search for $\gamma\gamma\gamma Z$, $\gamma\gamma ZZ$ and $\gamma\gamma WW$ anomalous couplings

The same methods described above to select potential new beyond standard model signal events appearing via quartic anomalous couplings can be used for $\gamma\gamma\gamma Z$, $\gamma\gamma ZZ$ and $\gamma\gamma WW$. We benefit from the fact that we detect and measure the protons in the final state in order to select exclusive events. The gain of two orders of magnitude on photon anomalous couplings is also true for $\gamma\gamma WW$ and $\gamma\gamma ZZ$ whereas the gain reaches three orders of magnitude for $\gamma\gamma\gamma Z$ [11, 12].

2 Time-of-flight measurements at the LHC and other applications

2.1 Measuring proton time-of-flight at the LHC

In order to reject pile up events, it is also possible to measure precisely the time-of-flight of the protons. Namely we can constrain the protons to originate from the same interaction point as the two

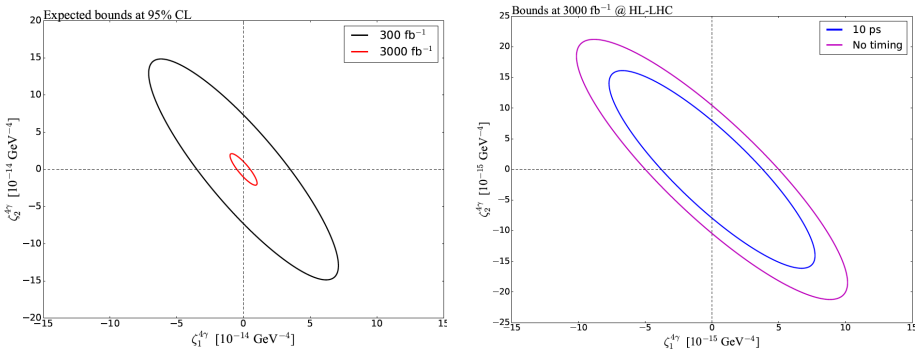

Figure 6: Sensitivity contours on photon quartic anomalous couplings at the LHC with 300 and 3000 fb^{-1}.

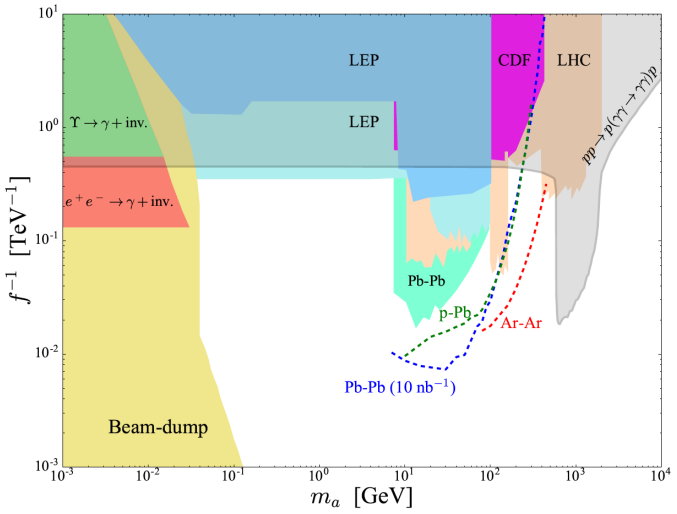

Figure 7: Sensitivity plot on axion like particles in the coupling versus mass plane at the LHC in pp collisions with 300 fb^{-1} (grey band) and in $PbPb$ (blue dashed line), pPb (green dashed line), $ArAr$ (red dashed lines) collisions.

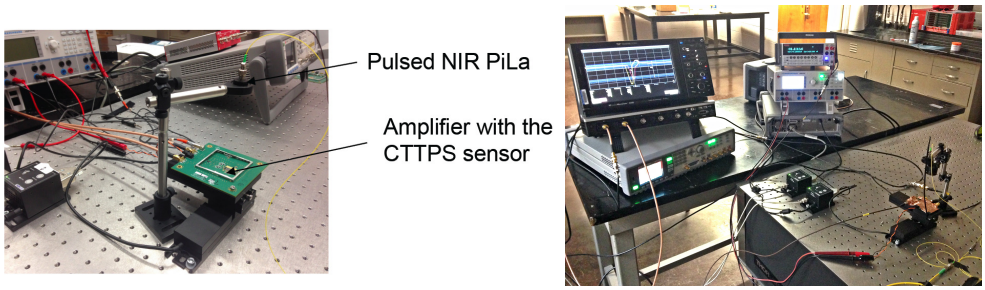

Figure 8: Timing detector test stand at the University of Kansas.

photons or W/Z bosons. Since particles at the LHC travel at the speed of flight, time needs to be measured with high precision, of the order of ten picoseconds, that allows a rejection factor of about 40 for a pile up of 50. This is specially needed when the mass matching cannot work perfectly for instance for the leptonic decays of W pairs where the neutrinos cannot obviously be measured directly in CMS or ATLAS. Fast Silicon detectors together with their readout electronics have been developed in order to achieve this goal.

2.2 Performance of timing detectors at the University of Kansas

At the University of Kansas, we designed a multi-purpose electronics board to read out ultra-fast Silicon or diamond detectors to measure precisely time-of-flight, as well as a test-stand in order to test the full chain from the detector to the read-out electronics. The test-stand is equiped with a laser or a radioactive source in front of the Silicon detectors (see Fig. 8). The system is highly adaptable to different kinds of sensors (diamond or Silicon) and only requires a low voltage power supply as an input. The electronics readout can be performed either directly from the sensor itself or after a signal amplifier via a scope or some waveform signal analyzer such as SAMPIC [13, 14]. The amplifier was designed at the University of Kansas and can be used for a full range of detectors and applications.

The performance of the timing detector and its amplifier is shown in Fig. 9, right. In order to test the full system in real conditions we used a beam test at Fermilab, Batavia, USA. For one layer of Silicon detectors, we obtained a resolution of about 39 picoseconds, which means that a resolution better than 15 picoseconds can be achieved with 8 layers of ultrafast Si detectors. On Fig. 9, left, we can see a photo of the circuit designed and built at the University of Kansas. The idea was to build a “plug-and-play" circuit that can be used to test many possible applications.

2.3 Measuring radiation out of a diamond or ultrafast Si detector

Additional applications that we are going to discuss now rely on the same principle: we can measure the full signal originating from a diamond or ultrafast Si detectors. The applications do not rely too much on timing measurements (as in high energy particle or nuclear physics) but in the understanding of the number of particles or charge that cross the detector. When a particle (for instance a proton) crosses a Si detector, some pairs of ions and electrons are formed and drift slowly for the ions or fast for the electrons towards the electrodes because of the electric field. Detecting the particles passing through the detectors is thus possible by measuring the electron signal, using either an oscilloscope or dedicated electronics. Signals originating directly from a Si or a diamond detector are very often low and need to be amplified. The first step of the KU circuit is then to amplify this signal without destroying its properties such as rise time, signal over noise ratio...

By using different layers of Si detectors as an example, the output signal is characteristic of the kind of particle (proton, light or heavy ions...) that crosses the different layers until it stops and proportional to its energy. In order to measure the signal, a very fast digitization is performed (taking

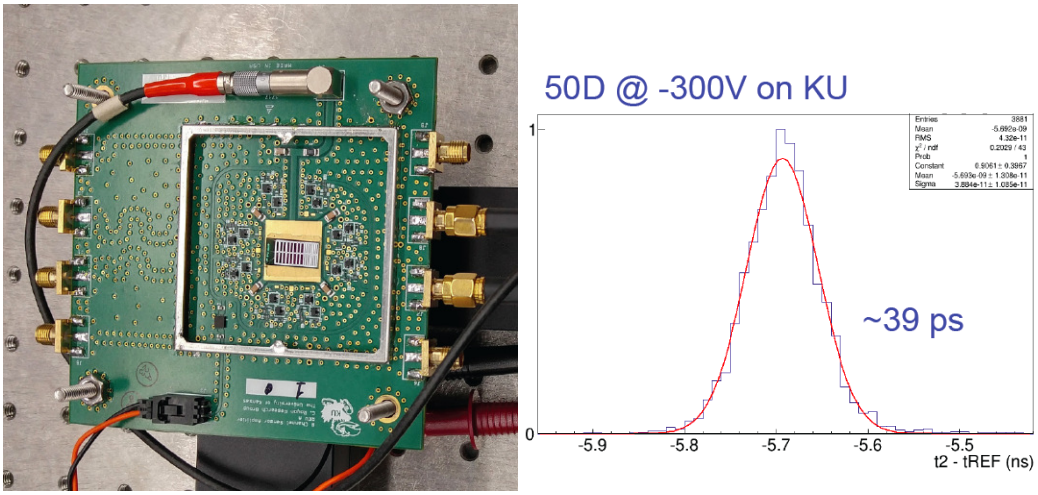

Figure 9: Timing board made at the University of Kansas.

as an example 64 measured points in one nanosecond). A linear interpolation between the different measured points allow then to reconstruct the full signal. The method allows measuring precisely time-of-flight and at the same time the signal amplitude, which will be the basics of all applications.

2.4 Measurement of cosmic rays with NASA

The idea for the project in collaboration with NASA is to measure the type and energy of cosmic ray particles originating from the sun for a range between MeV to GeV as illustrated in Fig. 10, right. In order to do so, it is needed to build a detector made of sandwiches of active layers of Si detectors that allow to measure and contain different kinds of particles with different energies [15]. Using the very fast digitization method described above, it is possible to reconstruct fully the signal in the different Si layers. Since different kinds of particles deposit their energies in the different layers differently, also depending on their energies, it will be possible to reconstruct the full properties of the comic ray radiation, namely the type of particles that are produced, and their energies. This project aims at sending a cube sat in collaboration with NASA (the AGILE project) in the next three years and might also allow later a direct precise measurement of radiation between the earth and Mars needed in order to send astronauts to Mars as an example.

2.5 Measuring radiation in cancer treatment

The second application deals with a precise measurement of radiation accumulated by the human body during cancer treatment during photon or proton therapies [16]. The idea is to measure the amount of radiation with high precision and how its distribution in the human body with millimeter square precision, as well as the beam parameters. In order to achieve this goal, the same technique can be used by counting the number of photons or protons that went through the human body or that originated from the beam.

Another possible medical application deals with PET imaging. Usually, patients absorb radioactive material that interact with electrons inside the tumor. The electron-positron pairs interact emitting photons that can be measured and lead to an image of the tumor. The problem is that the human body emits naturally lots of photons and in average, one pair of photon originates from the tumor out of 10,000. An offline advanced analysis is then needed in order to isolate the interesting photons. In order to preselect the photons originating from the tumor, it is possible to measure the time-of-flight

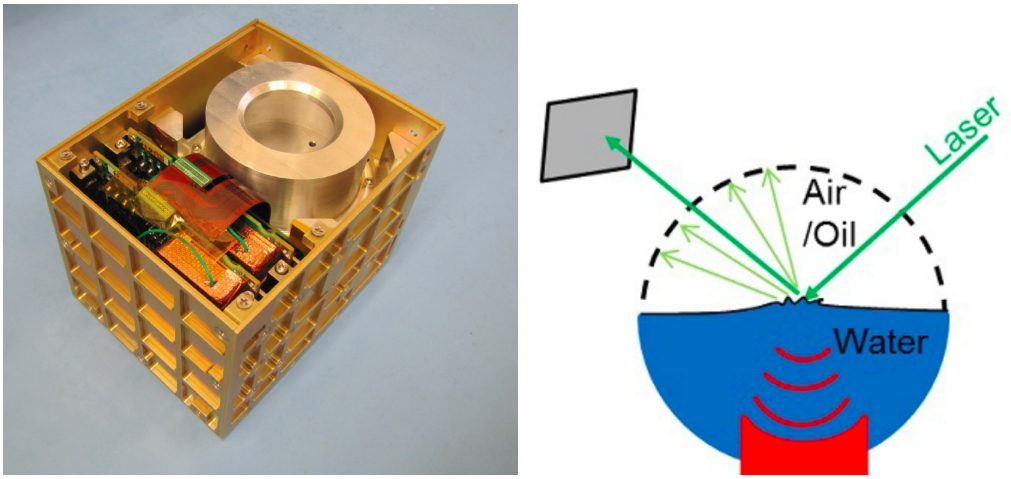

Figure 10: Left: The AGILE project with NASA, Right: Catalysis measurements in chemistry.

of the photons and require them to originate from the tumor itself. This would allow to make an online image of the tumor which will be much more efficient.

2.6 Understanding better catalysis in chemistry

The third application deals with a better understanding of catalysis in chemistry with the application of reaching better methods to desalinize sea water. as illustrated in Fig. 10, right. The idea is to understand better how an interface between two liquids, a solid and a liquid, or a gas and a liquid vary as a function of time when catalysis occurs. Using interferometry technics, we can measure how the interface varies as a function of time by measuring a snapshot every 20 or 30 picoseconds. This will lead to new insights in the mechanism of catalysis and thus in a better understanding of applications where catalysis is needed. This could also have implications on the way medicine is absorbed by human body by improving the interface between human cells and medicine.

3 Conclusions

In this report, we describe the search for quartic anomalous couplings with unprecedented precision at the LHC by measuring intact protons in the final state. We also describe the fast timing detector developments at the University of Kansas in order to measure particle time-of-flights and also applications in medicine, chemistry and cosmic ray detections with NASA.

Acknowledgements

The author acknowledges generous support from the organizers of the workshop and the Guadeloupe Region.

References

[1] CMS and TOTEM Coll., JHEP **1807** (2018) 153; CMS Coll., CERN-LHCC-94-38; TOTEM Coll., JINST **3** (2008) S08007.

[2] TOTEM Coll., JINST **3** (2008) S08007.

[3] ATLAS Coll., CERN-LHCC-99-14, CERN-LHCC-00-15.

[4] V. Khoze, A. Martin, M. Ryskin, Eur. Phys. J. C**23** (2002) 311.

[5] S. Fichet, G. von Gersdorff, B. Lenzi, C. Royon, M. Saimpert, JHEP **1502** (2015) 165; S. Fichet, G. von Gersdorff, O. Kepka, B. Lenzi, C. Royon, M. Saimpert, Phys.Rev. D89 (2014) 114004.

[6] M. Boonekamp, A. Dechambre, V. Juranek, O. Kepka, M. Rangel, C. Royon, R. Staszewski, preprint ArXiv:1102.2631.

[7] S. Fichet, G. von Gersdorff, C. Royon, Phys. Rev. Lett. **116** (2016) no 23, 231801; S. Fichet, G. von Gersdorff, C. Royon, Phys. Rev. D**93** (2016) no 7, 075031;

[8] CMS and TOTEM Coll., CMS-PAS-EXO-18-014, TOTEM-NOTE-2020-003.

[9] C. Baldenegro, S. Fichet, G. von Gersdorff, C. Royon, JHEP **1806** (2018) 131.

[10] C. Baldenegro, S. Hassani, C. Royon, L. Schoeffel, Phys. Lett. B**795** (2019) 339.

[11] E. Chapon, O. Kepka, C. Royon, Phys. Rev. D**81** (2010) 074003; O. Kepka, C. Royon, Phys. Rev. D**78** (2008) 073005.

[12] C. Baldenegro, S. Fichet, G. von Gersdorff, C. Royon, JHEP **1706** (2017) 142.

[13] E. Delagnes, D. Breton, H. Grabas, J. Maalmi, P. Rusquart. Nucl. Instrum. Meth. A**787** (2015) 245.

[14] A. Apresyan *et al.*. Nucl. Instrum. Meth. A**895** (2018) 158.; N. Minafra *et al.*, Nucl. Instrum. Meth. A**867** (2017) 88; D. Breton, V. De Cacqueray, E. Delagnes, H. Grabas, J. Maalmi, N. Minafra, C. Royon, M. Saimpert, Nucl. Instrum. Meth. A**835** (2016) 51.

[15] KU News, https://news.ku.edu/2019/04/25/research-explores-behavior-quarks-and-gluons-large-hadron-collider; A. Novikov, these proceedings.

[16] Physics World, 04 June 2019, https://physicsworld.com/a/particle-telescope-technology-could-help-improve-radiotherapy/ KU News, https://news.ku.edu/2019/05/03/particle-telescope-will-probe-subatomic-makeup-suns-cosmic-rays-and-could-lead-more

The SHiP experiment at CERN

Markus Cristinziani

e-mail: cristinz@uni-bonn.de

Physikalisches Institut, Universität Bonn, Nussallee 12, 53115 Bonn, Germany

Presented at the 3rd World Summit on Exploring the Dark Side of the Universe
Guadeloupe Islands, March 9-13 2020

Abstract

The current status of the proposed SHiP experiment at the CERN Beam Dump Facility is presented. SHiP is a general-purpose fixed-target experiment. The $400\,\mathrm{GeV}/c$ proton beam extracted from the SPS will be dumped on a heavy target to integrate 2×10^{20} protons on target in five years. The detector, based on a long vacuum tank followed by a spectrometer and particle identification detectors, will allow to probe a variety of models with light long-lived exotic particles and masses below $\mathcal{O}(10)\,\mathrm{GeV}/c^2$. The main focus will be the physics of the so-called hidden portals, i.e. the search for dark photons, light scalars and pseudo-scalars, and heavy neutrinos. The sensitivity to heavy neutrinos will allow to probe, in the mass range between the kaon and the charm meson mass, a coupling range for which baryogenesis and active neutrino masses could also be explained. A second dedicated detector will study neutrinos and explore light dark matter.

1 Introduction

SHiP is a general-purpose beam-dump experiment designed to use the high-intensity $400\,\mathrm{GeV}/c$ beam of protons available from the CERN SPS accelerator in order to search for hidden particles. The proposal of the experiment evolved from a first idea [1] to search for Heavy Neutral Leptons (HNLs), whose existence is predicted in the νMSM model [2, 3] with guidance described in Ref. [4], to a more comprehensive programme of new physics searches at the intensity frontier [5], including the option of producing and studying a large sample of ν_τ neutrinos [6], that lead to the SHiP technical proposal [7]. Since then, the detector layout has been continuously optimised and expanded. The most recent results were documented in a progress report [8] and the comprehensive design study report [9].

2 Motivation

While the Higgs boson discovery at the Large Hadron Collider in 2012 marks the triumph of the Standard Model (SM), there are still several shortcomings in particle physics that are waiting to be explained. The SM particles cannot account for the observed matter in the Universe, as there is convincing evidence of dark matter (DM), with unknown mass and couplings. The predominance of matter over antimatter in the Universe calls for additional sources of CP violation, beyond what is known in the SM. The tiny, but non-zero masses of the neutrinos, causing oscillations, could be explained via the see-saw mechanism with right-handed neutrinos with Yukawa couplings to the

Higgs boson and SM leptons. There are also aesthetic shortcomings, like the strong CP problem or the hierarchy/fine-tuning problem of the Higgs mass.

It is thus important to probe new physics beyond the SM in different directions. At the intensity frontier the paradigm is that low-energy, high-intensity experiments could uncover new interactions and particles with very feeble couplings. Popular extensions of the SM proceed through so-called portals, that are generally categorized according to the nature of the mediator: scalar, vector, pseudo-scalar or fermion. Examples for these categories are Dark Higgs, Dark Photon, Axion Like Particles (ALPs), and HNLs, respectively.

3 The SHiP detector at the Beam Dump Facility

The SHiP detector is planned to be installed in the North Area at the CERN SPS 400 GeV/c beam, taking advantage of the Beam Dump Facility (BDF). It features two main sub-detector systems, pursuing complementary physics goals. The hidden sector (HS) decay spectrometer aims at measuring visible decays of HS particles and will reconstruct their decay vertices in a large decay volume. The scattering and neutrino detector (SND) is dedicated to neutrino physics and the search for light dark matter (LDM). The design of the detector underwent several optimisation steps and its current implementation is shown in Figure 1. In particular, there has been a large effort to re-optimize the muon magnetic shield configuration and, as a consequence, the detector layout.

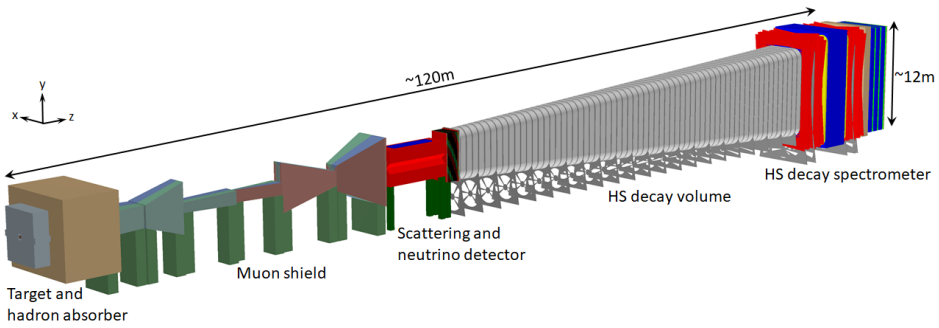

Figure 1: Drawing of the current outline of the SHiP detector [9].

3.1 Beam Dump Facility

The proposed BDF is foreseen to be located at the North Area of the CERN SPS. It is designed to be able to serve both, beam-dump like and fixed-target experiments. The full exploitation of the SPS would allow the delivery of an annual yield of up to 4×10^{19} 400 GeV/c protons on target (pot) while delivering protons to the HL-LHC and the existing SPS facilities. Slow extraction of a de-bunched beam with good uniformity is required to keep the combinatorial background under control and to dilute the large beam power in the proton target. The proposed implementation of the beam dump experimental facility is based on a minimal modification to the SPS complex and maximal use of the existing beamlines. The BDF is described in detail in Ref. [10].

3.2 Target

The SHiP target [11] is designed to maximise the production of hidden sector particles, mainly through the decay of flavoured hadrons produced in the target through primary and secondary (cascade) interactions. At the same time, the target material and density are chosen such to reduce the production of other particles. The longitudinally segmented hybrid target consists of four nuclear interaction

lengths (λ_{INT}) of TZM (titanium-zirconium doped molybdenum) alloy, followed by $6\lambda_{\mathrm{INT}}$ of tungsten, and is interleaved with water cooling spaces, for a cross section of $30 \times 30\,\mathrm{cm}^2$ and a total length of more than 120 cm. Cooling will be essential, as the peak power of the beam during a spill will be 2.56 MW. The target complex will be housed in a $440\,\mathrm{m}^3$ bunker made of remotely handled iron bricks and is additionally cooled, underpressurized, and shielded. A 5 m thick iron shield absorbs hadrons behind the target.

3.3 Active muon shield

After the hadron absorber, penetrating muons are a possible source of undesired occupancy. From simulation, it is expected that 10^{11} muons/s are produced in the collisions of the proton beam on the beam-dump target from the decay of pions, kaons, and other light and charmed mesons. A magnetic muon shield [12] will deflect muons of both polarities and a wide range of transverse momenta and significantly reduce this muon flux. Since the produced hidden sector particles typically exhibit large transverse momenta, the muon shield has to be as compact as possible. The original design has been revised using a Bayesian optimisation algorithm [13], resulting in a total length of 34 m, a weight of 1.5 kt, and a magnetic field of up to 1.8 T. The first part aims at separating muons of opposite polarities and also acts as a hadron absorber, while the rest of the series of magnets is designed to also remove the lower momentum muons that re-enter the acceptance due to the return fields. The muon flux will be reduced to 10^5 muons/s after the muon shield.

3.4 Scattering and neutrino detector

Downstream of the muon shield a detector system consisting of emulsion cloud chamber (ECC) bricks made of lead plates and nuclear emulsion films, interleaved with electronic trackers and followed by a compact emulsion spectrometer (CES) with low-density material, will be immersed in a 1.2 T magnetic field. Behind the magnet, a muon identification system, consisting of several 10 cm thick iron filters and RPC tracking planes, aims at identifying the muons produced in neutrino interactions and τ-decays occurring in the emulsion target. The ECC bricks are composed of stacks of alternating 1 mm lead plates, acting as neutrino targets, and 300 μm emulsion films, where ν_τ interactions and τ-lepton decay vertices can be reconstructed. The CES, a light structure with a long lever arm, will be essential to measure the charge of the τ-lepton daughters. The electronic tracker technologies under study include scintillating fibres (SciFi), and micro-pattern gaseous detectors (μ-RWELL).

3.5 Hidden sector decay volume

The SHiP decay volume has a pyramidal frustum shape with rectangular bases of $2.4 \times 4.5\,\mathrm{m}^2$ at the entrance and $5 \times 10\,\mathrm{m}^2$ at the exit, for a length of 50 m. It has to be sufficiently evacuated from residual air to suppress muon and neutrino interactions. The complete volume is enclosed by the surrounding background tagger (SBT), a veto detector, based on 480 t of linear alkylbenzene liquid scintillators, which will help to identify activity from outside of the detector, like cosmic rays or cavern background. The liquid scintillator is coupled to 3 500 wavelength-shifting optical modules (WOM), already proposed to be used in an extension of the IceCube detector.

3.6 Spectrometer and particle identification

The HS decay volume is followed by a spectrometer with an acceptance of $5 \times 10\,\mathrm{m}^2$. The first sub-detector is the spectrometer straw tracker, designed to accurately reconstruct the momenta and the decay vertex, mass and impact parameter of the hidden particle trajectory at the proton target. The spectrometer dipole magnet is a conventional magnet with a total field integral of 0.65 Tm. The SplitCal electromagnetic calorimeter employs the sampling technology with lead/scintillator planes. To accurately measure the shower transverse profile, the SplitCal is longitudinally segmented and

will contain high-precision layers of MicroMegas chambers, similar to those developed for the ATLAS muon upgrade. This will be important for the reconstruction of decays of axion-like particles to two photons. The muon system consists of four stations interleaved by three muon filters. To reject random crossings, a dedicated timing detector made of scintillator bars is placed at the end of the detector and will match the arrival times of the particles forming vertex candidates with a precision of 100 ps.

4 Physics performance

The SHiP experiment is a unique discovery tool for HS particles. Present constraints on various channels will be improved by several orders of magnitude. SHiP will also distinguish among different models, and measure parameters relevant for cosmology and model building, in a large part of the parameter space. Together with the direct search for LDM and neutrino physics, SHiP is a wide scope general-purpose fixed-target experiment.

The HS detector is designed to fully reconstruct a wide range of decay modes, and identify the particles, to ensure a model-independent search for hidden particles. The SND detector is optimised for scattering signatures of LDM and neutrinos. The sensitivity of the SHiP experiment heavily relies on redundant background suppression. The SHiP physics case was presented in Ref. [5].

4.1 Background studies

Large samples of simulated events have been produced to accurately determined the level of backgrounds, including from the floor, ceiling, walls and detector supports, using Geant4 [14] and the FairRoot framework [15]. Samples of muons produced in 10^{12} pot have been fully simulated. In order to claim discovery of a HS particle, it is of paramount importance to suppress the backgrounds that would mimic the same final states to a negligible level. Signal events feature a vertex pointing back to the target, consisting of at least two charged particles and possibly additional invisible particles.

Three sources of background can mimic the HS signature: random muon combinatorial, muon inelastic scattering and neutrino deep-inelastic scattering. The background from cosmics has been found to be negligible. The three sources of background are reduced by requirements on the track momentum, vertex position and impact parameter with respect to the target. To avoid irreducible background from neutrinos interacting with the air molecules inside the vessel, a level of vacuum below 10^{-2} bar is necessary. The background from neutrino scattering in the floor and the walls of the cavern was studied and found to be negligible. Additionally, information from the timing detector and veto information from the SBT will reduce the backgrounds to less than 0.3 events during the five-year data-taking. Thus, SHiP can be considered a zero-background experiment with a high level of redundancy to efficiently suppress the background for a broad spectrum of searches.

4.2 Signal sensitivities

Hidden sector

To illustrate the physics potential of SHiP to hidden sector particles the sensitivities to HNLs, dark scalars, dark photons and ALPs coupling to photons are shown in Figures 2 and 3. More details can be found in the report of the Physics Beyond Colliders study group [16].

In the case of a discovery, SHiP is capable of measuring parameters and identifying the underlying models. For instance, SHiP may distinguish between Majorana-type and Dirac-type HNLs in a significant fraction of the parameter space by detecting lepton number violating or conserving decays [17], as shown in Figure 2. If the mass splitting between the HNLs is small, it may also be possible to resolve HNL oscillations as a direct measurement of the mass splitting between HNLs.

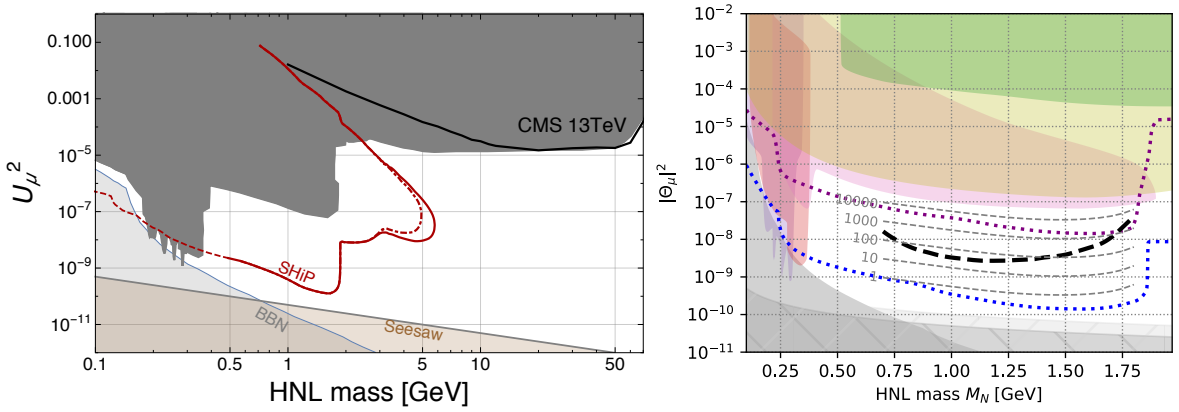

Figure 2: Left: Sensitivity to HNL for the mixing with muon flavour [18]. The dark grey area and the solid line indicate the excluded regions by previous experiments. The solid and dashed-dotted red lines indicate the uncertainty related to the production of B_c mesons. Right: SHiP sensitivity to lepton number violation (thick dashed curve) compared to exclusions by previous experiments (coloured areas). The thin dashed grey lines show the number of fully reconstructible events [17].

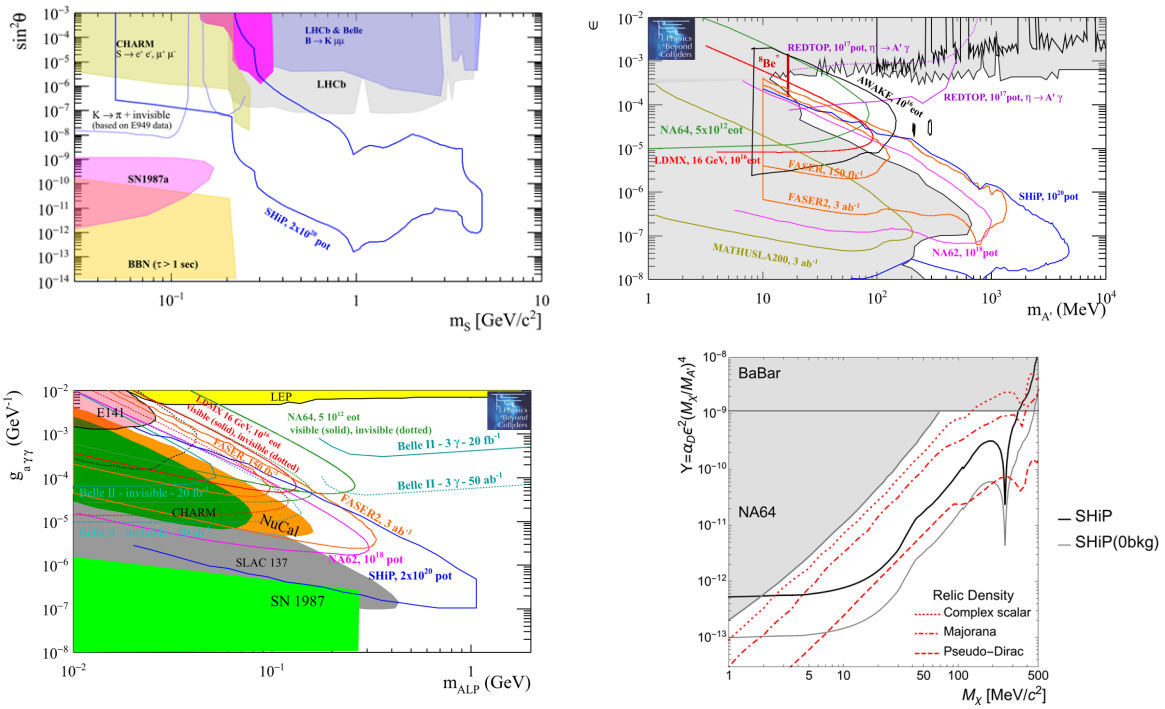

Figure 3: Sensitivity of SHiP to dark scalar [9], dark photon, ALPs [16] and LDM signals [9], compared to existing (coloured or grey areas) and projected (lines) exclusion limits.

Light Dark Matter

If LDM particles undergo elastic scattering ($\chi e^- \to \chi e^-$) in the SND detector material, the electromagnetic shower induced by the recoil electron can be detected in the SND, which would act as a sampling calorimeter. A sufficient portion of the shower can be reconstructed in order to determine the particle angle and energy. The high accuracy of the nuclear emulsions will provide topological discrimination against neutrino-induced background. Figure 3 shows the SHiP sensitivity as a function fo the LDM mass M_χ, along with existing constraints and the thermal relic abundance, for a benchmark scenario with a dark coupling $\alpha_D = 0.1$.

Neutrino physics

The SND detector will be able to determine the neutrino flavour by measuring the flavour of the charged lepton produced in the neutrino charged-current interactions. About 10^4 τ-neutrinos will be detected and the tracking capabilities in the SND will allow distinguishing, for the first time, between ν_τ and $\bar{\nu_\tau}$. In addition, the large sample of neutrino-induced charm production will allow for unprecedented studies in this domain, as for instance double-charmed production or the strange-quark content of nucleons. The samples available at SHiP will also allow to significantly constrain the ν_τ magnetic moment and test lepton flavour violation in the neutrino sector.

5 Measurements

5.1 Muon flux normalisation

In order to validate the Monte-Carlo simulation (Pythia, Geant4) that is being used for the sensitivity studies, the muon flux was measured in a test-beam setup at the CERN SPS [19]. Protons of $400\,\mathrm{GeV}/c$ were directed onto a SHiP target replica with full length. Behind an iron hadron absorber the emanated muons were measured with a spectrometer setup using scintillators, OPERA drift-tubes stations, the Goliath magnet and an RPC-based muon tagger. In three weeks during 2018, about 327 billion pot were recorded, corresponding to 1% of a nominal SHiP spill. Events with muons were recorded at a rate of one in 710.

The relevant physics processes for muon production are foremost the decays of pions and kaons, the production and decay of charm particles and low-mass resonances, and the transportation of the muons through the iron absorber. Data and simulation agree remarkably well (Figure 4), with maximal differences in the absolute rate of 30% for large transverse momenta at high muon momenta.

5.2 Charm production cross-section

The production of charmed hadrons in $400\,\mathrm{GeV}/c$ protons on the SHiP target is expected to be increased by a factor of more than two with respect to the direct production due to the interactions of particles produced in the hadronic cascade showers. The exact normalisation is an important input and will be measured by the SHiP-charm experiment at the CERN SPS [20].

An optimisation run was performed in 2018, collecting about 1.5 million pot, directly after the muon flux measurement, thus using the same magnet, the scintillators, drift tubes and RPCs. To precisely measure the charm production vertices and the tracks, emulsion films were used, along with a tracker built with ATLAS pixel modules and LHCb SciFi. To keep the occupancy to manageable levels, the emulsion detector was moving horizontally during a spill at 2 cm/s and vertically in between spills. This makes the alignment and matching of tracks between the detectors challenging. Preliminary results show that more than 50% of the tracks associated with reconstructed vertices can be matched. Several runs were taken with varying amounts of target material in front of the emulsion detector, to probe the charm content of the different parts of the shower development. Figure 4 shows an event display of a charm candidate in the emulsion detector.

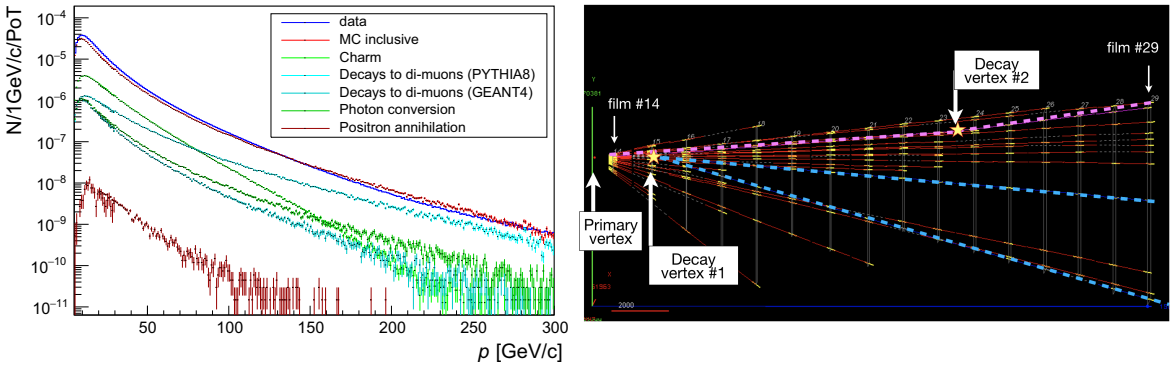

Figure 4: Left: Measured muon momentum distribution compared to simulation [19]. The most important individual sources in simulation are shown, along with the total prediction. Right: A double-charm candidate event produced in proton collisions with the tungsten target recorded at the H4 charm-production measurement [9].

6 Conclusions

With the current status of SHiP and the mature understanding of the continued detector developments, the SHiP project is ready to commence the Technical Design Report phase. First prototypes of all subsystems can be constructed and tested within the next three years. It is estimated that the detector production will require two to three years and that the detector assembly and installation, including infrastructure, will require another two years. The installation of the facility and the SHiP detector could be performed in the Long Shutdown 3, allowing commissioning and starting data-taking early in Run 4.

Acknowledgements

The author would like to thank the organisers of the 3rd World Summit on Exploring the Dark Side of the Universe 2020 for a very enjoyable conference in Guadeloupe and the Physique-Outremer association. The work of the author is funded by the German Science Foundation (DFG) under Grant Agreement MC312/4-1.

References

[1] W. Bonivento et al., *Proposal to Search for Heavy Neutral Leptons at the SPS*, arXiv:1310.1762.

[2] T. Asaka, S. Blanchet, and M. Shaposhnikov, *The νMSM, dark matter and neutrino masses*, *Phys. Lett.* **B631** (2005) 151, [hep-ph/0503065].

[3] T. Asaka and M. Shaposhnikov, *The νMSM, dark matter and baryon asymmetry of the universe*, *Phys. Lett.* **B620** (2005) 17, [hep-ph/0505013].

[4] D. Gorbunov and M. Shaposhnikov, *How to find neutral leptons of the νMSM?*, *JHEP* **10** (2007) 015, [arXiv:0705.1729]., Erratum and Addendum: JHEP **11** (2013) 101.

[5] S. Alekhin et al., *A facility to Search for Hidden Particles at the CERN SPS: the SHiP physics case*, *Rept. Prog. Phys.* **79** (2016) 124201, [arXiv:1504.04855].

[6] G. De Lellis, *Search for Hidden Particles (SHiP): a new experiment proposal*, *Nucl. Part. Phys. Proc.* **263** (2015) 71.

[7] **SHiP** Collaboration, M. Anelli et al., *A facility to Search for Hidden Particles (SHiP) at the CERN SPS*, arXiv:1504.04956.

[8] **SHiP** Collaboration, *SHiP Experiment - Progress Report*, Tech. Rep. CERN-SPSC-2019-010. SPSC-SR-248, CERN, Geneva, Jan, 2019.

[9] **SHiP** Collaboration, *SHiP Experiment - Comprehensive Design Study report*, Tech. Rep. CERN-SPSC-2019-049; SPSC-SR-263, CERN, Geneva, Dec, 2019.

[10] C. Ahdida et al., *SPS Beam Dump Facility - Comprehensive Design Study*, arXiv:1912.06356.

[11] E. Lopez Sola et al., *Design of a high power production target for the Beam Dump Facility at CERN*, *Phys. Rev. Accel. Beams* **22** (2019) 113001, [arXiv:1904.03074].

[12] **SHiP** Collaboration, A. Akmete et al., *The active muon shield in the SHiP experiment*, *JINST* **12** (2017) P05011, [arXiv:1703.03612].

[13] A. Baranov et al., *Optimising the active muon shield for the SHiP experiment at CERN*, *J. Phys. Conf. Ser.* **934** (2017) 012050.

[14] **GEANT4** Collaboration, S. Agostinelli et al., *GEANT4 — A Simulation toolkit*, *Nucl. Instrum. Meth.* **A506** (2003) 250.

[15] M. Al-Turany et al., *The FairRoot framework*, *J. Phys. Conf. Ser.* **396** (2012) 022001.

[16] J. Beacham et al., *Physics Beyond Colliders at CERN: Beyond the Standard Model Working Group Report*, *J. Phys.* **G47** (2020) 010501, [arXiv:1901.09966].

[17] J.-L. Tastet and I. Timiryasov, *Dirac vs. Majorana HNLs (and their oscillations) at SHiP*, *JHEP* **04** (2020) 005, [arXiv:1912.05520].

[18] **SHiP** Collaboration, C. Ahdida et al., *Sensitivity of the SHiP experiment to Heavy Neutral Leptons*, *JHEP* **04** (2019) 077, [arXiv:1811.00930].

[19] **SHiP** Collaboration, C. Ahdida et al., *Measurement of the muon flux from 400 GeV/c protons interacting in a thick molybdenum/tungsten target*, *Eur. Phys. J.* **C80** (2020) 284, [arXiv:2001.04784].

[20] **SHiP** Collaboration, *Measurement of associated charm production induced by 400 GeV/c protons*, Tech. Rep. CERN-SPSC-2017-033; SPSC-EOI-017, CERN, Geneva, Oct, 2017.

Dark sector searches with BABAR

Georges Vasseur

e-mail: georges.vasseur@cea.fr

IRFU, CEA, Université Paris-Saclay, F-91191 Gif-sur-Yvette, France

Presented at the 3rd World Summit on Exploring the Dark Side of the Universe
Guadeloupe Islands, March 9-13 2020

Abstract

The BABAR Collaboration has obtained limits on several dark sector models. Primarily designed for the study of CP violation in B meson decays, the BABAR experiment is also, thanks to its huge data sample and its powerful particle identification, sensitive to many other interesting physics processes. These include topics linked to the dark sector, such as searches for dark photons with either visible or invisible decays, a new Z' boson coupling preferentially to muons, and a stable six-quark state as a dark matter candidate.

1 Introduction

The BABAR experiment was installed at the SLAC PEP-2 high intensity e^+e^- collider. It took a huge quantity of data, more than half an attobarn inverse, over 10 years from 1999 to 2008, running on various Υ resonances and on the nearby quark-antiquark continuum. In fact the bulk of data was taken on the $\Upsilon(4S)$, above the threshold for the production of pairs of B mesons, in order to study heavy flavour physics and CP violation in the quark sector, which were the main physics goals of the experiment. However, at the end of the data taking, substantial data samples were taken on the $\Upsilon(2S)$ and $\Upsilon(3S)$ resonances.

The BABAR detector [1] was made of a silicon vertex detector providing a good reconstruction of displaced vertices, a drift chamber for momentum measurement, a DIRC Cherenkov detector for particle identification with a very good pion-kaon separation, a CsI electromagnetic calorimeter with precise photon detection, all inside a 1.5 T solenoid, and finally muon chambers.

Thanks to its good particle detection and identification, the clean environment in e^+e^- collisions, and the hermetic detector coverage, which together provide a precise reconstruction of the missing energy, thanks to some dedicated triggers and its huge data sample, BABAR was able to search for manifestations of the dark sector in low energy e^+e^- collisions. Even if it was not its original goal.

2 Dark Photon

A simple dark sector scenario is to add a new U(1) gauge symmetry. The associated gauge boson A', the so-called dark photon, provides a portal to the dark sector, mixing to the standard model photon with kinetic mixing strength ϵ. If its mass is in the GeV range, it can be produced at BABAR in e^+e^- collisions with initial state radiation (ISR). It then decays to either dark matter or standard model particles depending on their kinematic accessibility. The BABAR Collaboration performed a search for such a process $e^+e^- \to \gamma A'$ in both cases.

The full BABAR data sample of 516 fb^{-1} was used for the search performed in case of visible decays of the dark photon into two leptons, either two electrons or two muons, $A' \to \ell^+\ell^-$ [2]. We require one ISR photon, with energy greater than 200 MeV, and two leptons with opposite sign in the event. Except in the low di-electron mass region, where the Monte Carlo is known to fail to reproduce the data, the di-lepton mass distribution in the data in the electron and muon cases is well reproduced by all known processes included in the simulation. Apart for a resonant part around 3 GeV corresponding to the J/ψ and $\psi(2S)$ resonances, the background, dominated by radiative Bhabha and radiative dimuon production, is varying smoothly, and there is no sign of a new peak due to a dark photon.

By scanning the dark photon mass, considering more then five thousand mass hypotheses from threshold up to 10.2 GeV, we measure as a function of the dark photon mass the cross section of dark photon production, which fluctuates around 0, and the associated signal significance. No signal evidence is seen. By combining the two di-lepton channels, we put 90% confidence level (C.L.) upper limit on the mixing strength ϵ at the level of 10^{-3} for dark photon mass up to 10.2 GeV, as illustrated in figure 1.

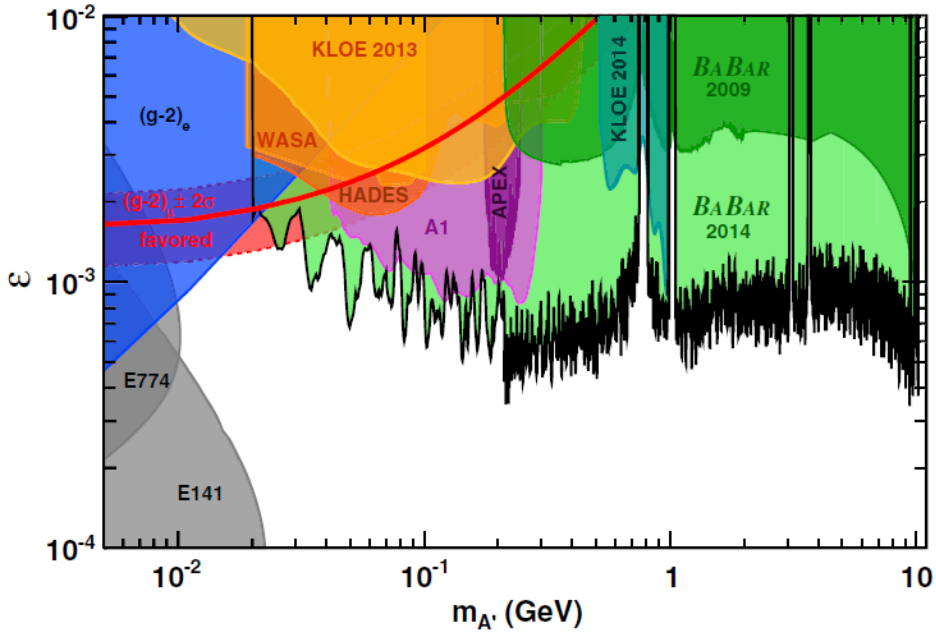

Figure 1: Upper limits (90% C.L.) on the mixing strength ϵ as a function of the dark photon mass (for visible decays). The region excluded by BABAR is shown in green and is compared to previous constraints.

In the case the dark photon may kinematically decay into dark matter particles $A' \to \chi\bar{\chi}$, it would escape detection. This process was also searched for by the BABAR experiment [3]. Here we detect only the photon from initial state radiation and missing energy due to the dark photon. The dark photon mass can be determined from the known beam energy and the measured photon energy.

The analysis was made possible by the introduction of a special trigger during the last months of data taking with the BABAR detector. On the level 1 hardware trigger, a new line was added requiring a calorimeter cluster with energy greater than 0.8 GeV. On the level 3 software trigger, two triggers were introduced requiring no tracks and a photon candidate with a threshold on the centre-of-mass photon energy at 2 GeV and then at 1 GeV, corresponding respectively to the last 53 fb^{-1} and 38 fb^{-1} of the data taking.

The main backgrounds are QED processes with two photons or radiative Bhabha with undetected particles. Thus, in the analysis, we check for additional detector activity and combine several variables providing such information in a boosted decision tree to separate the expected signal from the background.

For each dark photon mass hypothesis from 0 to 8 GeV in 166 steps, the signal yield is extracted from a fit to the photon recoil mass. The signal significance as a function of dark photon mass has a maximum around 6 GeV, corresponding to 3.1 σ local significance, but only 2.6 σ global significance, so not enough to claim any signal evidence. Consequently, we sets 90% C.L. upper limits on the mixing strength ϵ at the level of 10^{-3}, as illustrated in figure 2.

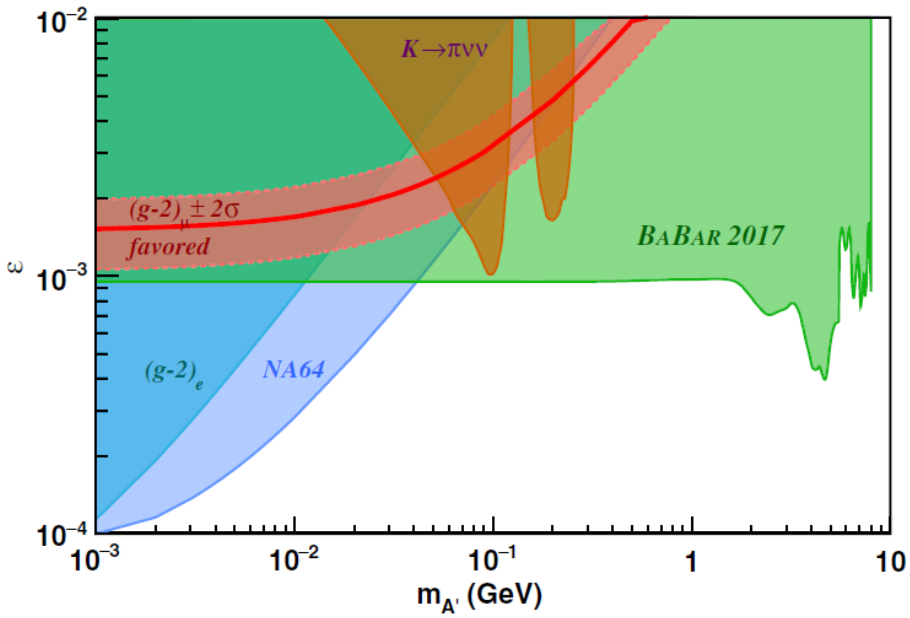

Figure 2: Upper limits (90% C.L.) on the mixing strength ϵ as a function of the dark photon mass (for invisible decays). The region excluded by BABAR is shown in green and is compared to previous constraints.

3 Muonic dark force

A search was also performed for muonic dark force, more precisely a dark boson Z' coupling to the second and third generation of leptons [4]. This can be motivated by various anomalies in the muon sector, such as the discrepancy between the calculated and mesured values for $g-2$. The Z' dark boson could be produced in $e^+e^- \to \mu^+\mu^-$ events and decay to two muons, giving a final state of four muons.

The principle of the analysis, performed on the whole dataset of BABAR (514 fb^{-1}), is to search for a di-muon mass peak in four muon final state events. The main background comes from combinatorial QED process. The dark boson production cross-section and the corresponding signal significance is measured as a function of the Z' mass, probing 2219 mass hypotheses up to 10 GeV. No signal is seen. Consequently we can set 90% C.L. upper limits on the g' coupling parameter down to 10^{-3}, as illustrated in figure 3. Most of the region that would explain the $g-2$ anomaly is excluded.

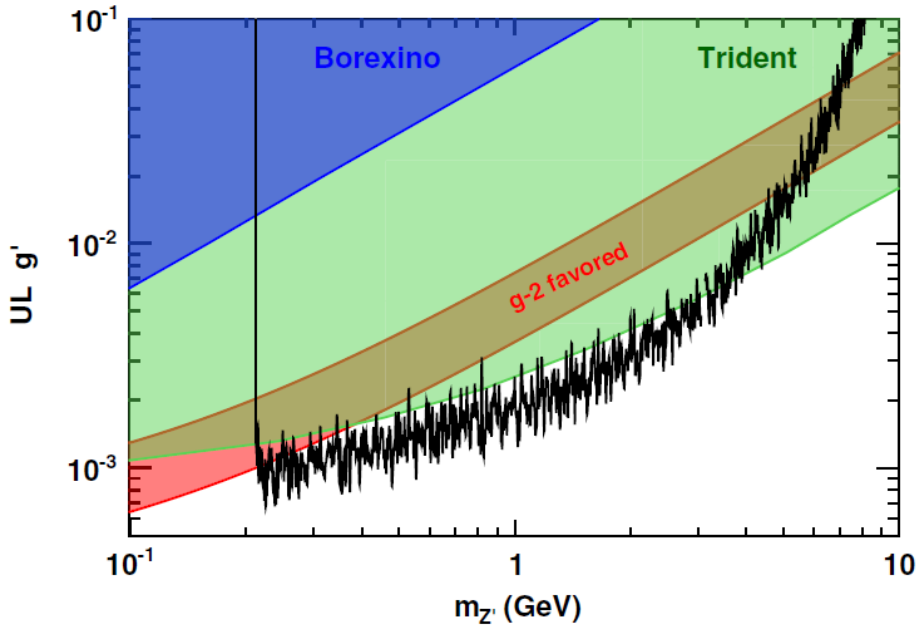

Figure 3: Upper limits (90% C.L.) on the coupling parameter g' as a function of the Z' mass, shown in black and compared to previous experiments. The region to explain the $g-2$ discrepancy is shaded in red.

4 Six-quark state

A six-quark state was proposed by Farrar [5] as a possible dark matter candidate. This state S is a $uuddss$ combination, with charge 0 and baryon number 2. If its mass is smaller than 2.055 GeV, the usual weak decay is forbidden so that it will have a very long lifetime. If it is smaller than 1.878 GeV, the state would be absolutely stable. A six-quark state has never been observed, but is allowed in QCD and not excluded by present experiments.

So BABAR recently performed a first search for such a state [6] which could be produced in the hadronic decays of the $\Upsilon(2S)$ and $\Upsilon(3S)$ in association with two Λ particles. We use the whole data sample taken on these two resonances, corresponding to 90 million $\Upsilon(2S)$ decays and 110 million $\Upsilon(3S)$ decays. We fully reconstruct two Λ candidates in their decay in a proton and a charged pion with a displaced vertex and pointing to the interaction point. The observable is the recoil mass square against the two Λ candidates, which for the signal should be the hexa-quark mass square.

The other main variable used in the analysis is $E_{\rm extra}$ which measures the additional activity in the electromagnetic calorimeter. Figure 4 shows the distribution of the squared recoil mass for the signal region with $E_{\rm extra} < 0.5$ GeV and for the sideband with $E_{\rm extra} > 0.5$ GeV. The signal is expected at low values of the recoil mass squared. The $E_{\rm extra}$ sideband shows that the background is well reproduced in the simulation and that no background event is expected in the signal region. In the $E_{\rm extra}$ signal region, four candidates are kept in the final selection with recoil mass compatible with the background and away from the signal region.

So we have no evidence for a signal and we set a 90% C.L. on the branching fraction of $\Upsilon \to \bar{S}\Lambda\Lambda$, for the $\Upsilon(2S)$ sample, the $\Upsilon(3S)$ sample, and the combined sample assuming the same partial width. The combined limit on the branching fraction varies with the hexaquark mass in the range from 0 to 2.05 GeV between $1.2\,10^{-7}$ and $1.4\,10^{-7}$.

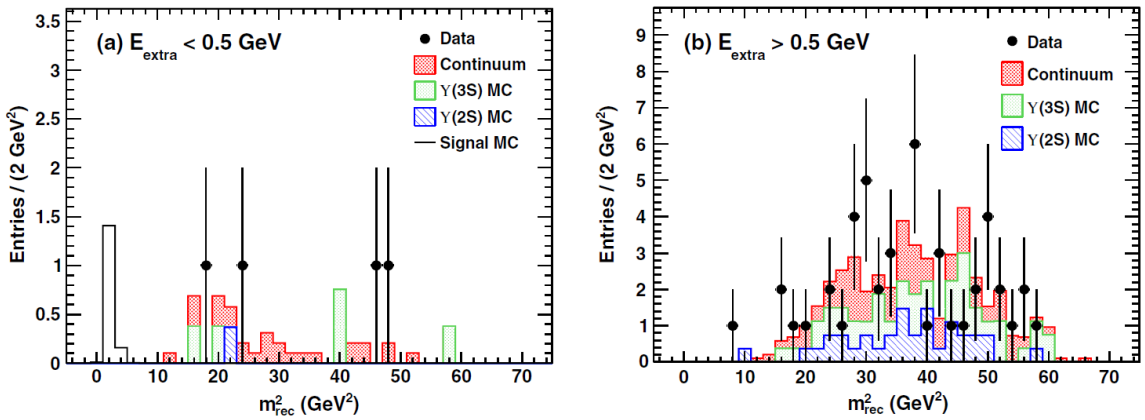

Figure 4: Distribution of the recoil mass squared for (a) the $E_{\rm extra} < 0.5$ GeV signal region and (b) the $E_{\rm extra} > 0.5$ GeV sideband. The data are the black points with error bars. The white histogram shows where the signal is expected. The stacked histograms show background estimates.

5 Conclusions

In summary, the BABAR experiment has performed a number of dark sector searches in low energy e^+e^- annihilations. No signal have been seen and constraints have been set for dark photon with visible or invisible decays, muonic dark force, and recently on a six-quark state as possible dark matter candidate.

References

[1] **BABAR** Collaboration, B. Aubert et al., *The BABAR Detector: Upgrades, Operation and Performance*, *Nucl. Instrum. Methods Phys. Res. A* **729** (2013) 615.

[2] **BABAR** Collaboration, J.-P. Lees et al., *Search for a Dark Photon in e^+e^- Collisions at BABAR*, *Phys. Rev. Lett.* **113** (2014) 201801.

[3] **BABAR** Collaboration, J.-P. Lees et al., *Search for Invisible Decays of a Dark Photon Produced in e^+e^- Collisions at BABAR*, *Phys. Rev. Lett.* **119** (2017) 131804.

[4] **BABAR** Collaboration, J.-P. Lees et al., *Search for a muonic dark force at BABAR*, *Phys. Rev. D* **94** (2016) 011102.

[5] G. R. Farrar, *Stable Sexaquark*, arXiv:1708.08951.

[6] **BABAR** Collaboration, J.-P. Lees et al., *Search for a Stable Six-Quark State at BABAR*, *Phys. Rev. Lett.* **122** (2019) 072002.

Dark Sector Searches at Belle II

Michel Bertemes on behalf of the Belle II collaboration

e-mail: Michel.Bertemes@oeaw.ac.at

Institute of High Energy Physics (HEPHY), Nikolsdorfer Gasse 18, 1050 Vienna

Presented at the 3rd World Summit on Exploring the Dark Side of the Universe
Guadeloupe Islands, March 9-13 2020

The Belle II experiment at the SuperKEKB asymmetric energy e^+e^- collider is a substantial upgrade of the B factory facility at the Japanese KEK laboratory. The design luminosity of the machine is 8×10^{35} cm^{-2}s^{-1} and the Belle II experiment aims to record 50 ab^{-1} of data, a factor of 50 more than its predecessor. During 2018, the machine has completed a commissioning run, recording a data sample corresponding to an integrated luminosity of about 0.5 fb^{-1}. Main operations started in March 2019 with the complete Belle II detector; an integrated luminosity of 60 fb^{-1} has been collected so far. These early data sets, with specifically designed low multiplicity triggers, offer already the possibility to search for a large variety of dark-sector particles in the GeV mass range, complementary to the sensitivities of the LHC and to dedicated low-energy experiments. These proceedings review the status of the dark-sector searches at Belle II, with a focus on the discovery potential with early data, and show the first results.

1 Belle II and SuperKEKB

SuperKEKB is an asymmetric energy e^+e^-collider located in Tsukuba, Japan. The beam energies are chosen such that the resulting centre-of-mass energy is equal to $10.58\,\mathrm{GeV}$, which is the mass of the $\Upsilon(4S)$. As this $b\bar{b}$ resonance decays mostly into a pair of B mesons, SuperKEKB is called a B *factory*. Higher beam currents combined with a smaller beam spot will allow SuperKEKB to reach an instantaneous luminosity of 8×10^{35} cm^{-2}s^{-1}, which is 40 times higher than what its predecessor KEKB achieved.

The Belle II experiment is located at the interaction region of the electron and positron beams of SuperKEKB. It consists of different layers of sub-detectors arranged concentrically with the vertex detectors being closest to the beam pipe. These are surrounded by a central drift chamber, followed by an electromagnetic calorimeter and the outermost detector responsible for K_L and muon reconstruction.

In 2018, the first collisions were recorded at Belle II while collecting a small dataset of $0.5\,\mathrm{fb}^{-1}$ during a commissioning run. Regular operations started in March of 2019. The plan is to collect 50 times more data than the precursor Belle did, $50\,\mathrm{ab}^{-1}$. Belle II has a rich physics program including B and D physics, quarkonium, τ and low mass dark sector [1]. A more detailed description of both SuperKEKB and Belle II is given in [1].

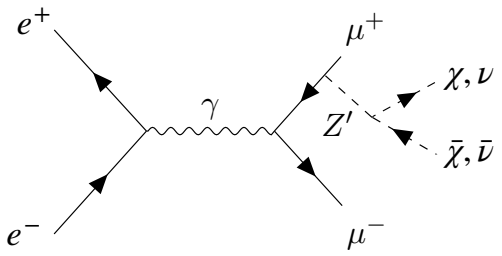

Figure 1: Feynman diagram for Z' production at Belle II and decay into invisible final state.

2 Invisible Z'

One possible way of extending the Standard Model (SM) is by adding a $U(1)'$ gauge group. Along with one of these extensions comes a new massive gauge boson Z' which belongs to an Abelian symmetry indicated as $L_\mu - L_\tau$ and which is charged under the additional $U(1)'$ group. Such a boson may serve as a mediator between the SM and the dark sector (DS), explain the $(g-2)_\mu$ anomaly and address anomalies in $b \to s\mu^+\mu^-$ ([2],[3]). In this scenario, the Z' would only couple to leptons of the 2$^{\text{nd}}$ and 3$^{\text{rd}}$ generation via a new coupling indicated with g'. In the environment of the Belle II experiment, the Z' could be produced in processes such as $e^+e^- \to \mu^+\mu^- Z'$, while being radiated off one of the muons and then further decaying either into a muon or tau pair, or invisibly to neutrinos or dark matter. The associated Feynman diagram is shown in Figure 1.

A search for a visible decay of the Z' into muons was already performed by the BaBar experiment [4]. In the study at Belle II the invisible-decay channel of the Z' was explored for the first time leading to a final state consisting of two muons plus missing energy. Given the experimental signature, one reconstructs the recoiling mass against the two muons and then looks for a peak at the Z' candidate mass in the resulting distribution. This search was performed using the data collected during the 2018 commissioning run. Due to the configuration of the trigger system for low-multiplicity final states, only $276\,\text{pb}^{-1}$ were available for the analysis. The main contributing backgrounds arise from QED processes with two muons in the final state such as $e^+e^- \to \mu^+\mu^-(\gamma)$, $e^+e^- \to \tau^+\tau^-(\gamma)$ (where both tau decays into muons) and $e^+e^- \to e^+e^-\mu^+\mu^-$. Upper limits on the coupling g' at the 90% confidence level (CL) as a function of the candidate Z' mass were extracted and are shown in Figure 2 [5]. No evidence for a Z' was seen with a significance greater than 3σ.

3 ALPs

Axion-like particles (ALPs) are pseudoscalar particles that can couple to SM bosons and appear in different extensions to the SM. Unlike axions, which are originally motivated by the strong CP problem [6], the coupling and the mass of ALPs are taken to be independent. At Belle II the simplest approach to search for ALPs is via the two-photon coupling $g_{a\gamma\gamma}$. Two different processes may be considered for this scenario: photon fusion ($e^+e^- \to e^+e^-a$) and ALP-strahlung ($e^+e^- \to \gamma a$). Whereas photon fusion dominates over ALP-strahlung in terms of production cross section (unless m_a approaches $\sqrt{s}$), the latter is still preferred for experimental searches as the final state of pho-

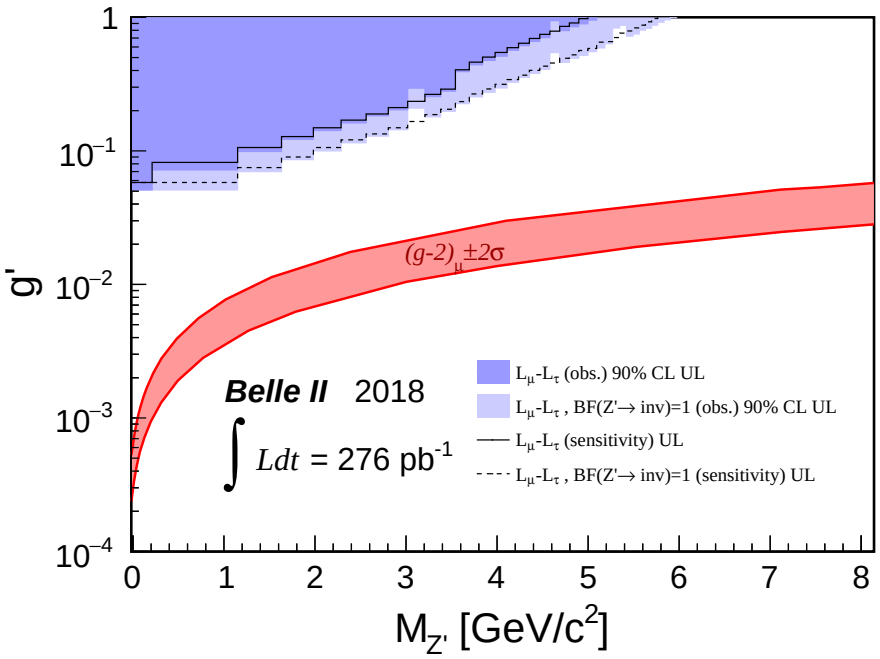

Figure 2: 90% CL upper limits on coupling constant g'. Dark blue filled areas show the exclusion regions for g' at 90% CL, assuming the $L_\mu - L_\tau$ predicted branching fraction (BF) for $Z' \to$ invisible; light blue areas are for BF($Z' \to$ invisible)=1. The solid and dashed lines are the expected sensitivities for the two hypotheses. The red band shows the region that could explain the muon anomalous magnetic moment $(g-2)_\mu \pm 2\sigma$ [5].

ton fusion consists of two soft photons giving rise to large QED backgrounds. The corresponding Feynman diagram for ALP-strahlung is shown in Figure 3.

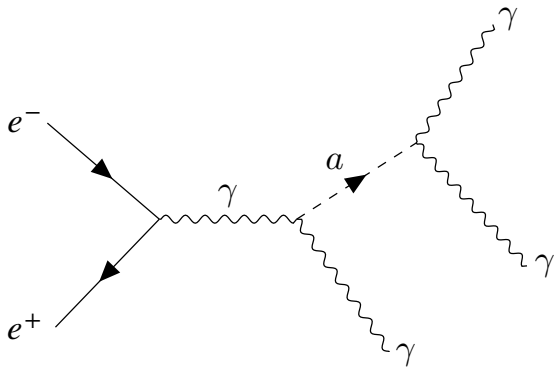

Figure 3: Feynman diagram for ALP-strahlung process.

According to the ALP mass and coupling, there are different topologies that can be observed in the Belle II detector: the three final-state photons being either resolved, two of them overlapping

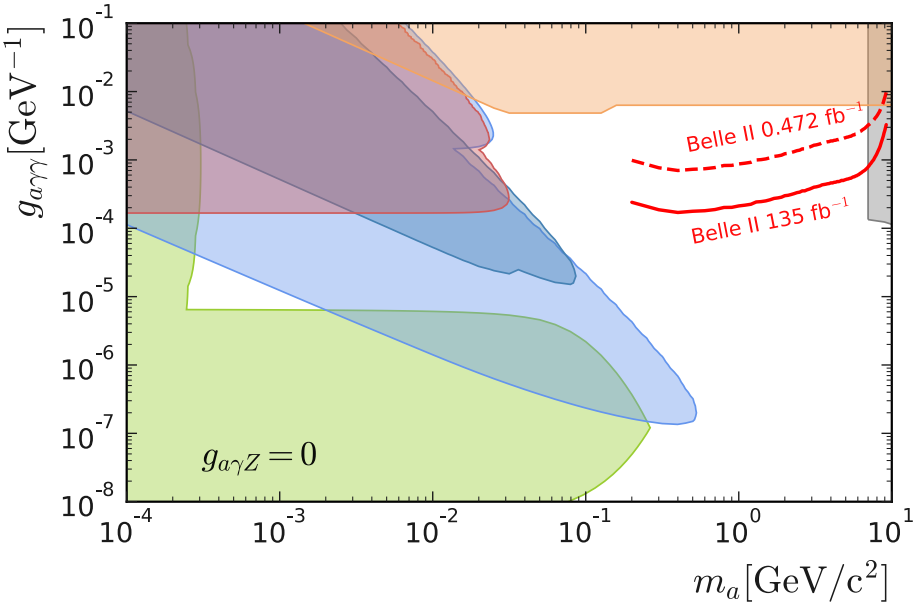

Figure 4: Expected sensitivity (90% CL) for the ALPs search at Belle II with early datasets [7].

(in terms of cluster shape in the electromagnetic calorimeter) or the ALP decaying outside of the detector leading to one single photon in the final state. The general idea of the analysis consists of reconstructing three photon candidates with energies summing up to the beam energy and no charged tracks in the event. The main contributing background processes are $e^+e^- \to \gamma\gamma(\gamma)$, $e^+e^- \to e^+e^-\gamma$ and $e^+e^- \to P\gamma$ with $P = \pi^0, \eta, \eta'$ and $P \to \gamma\gamma$. The expected sensitivity at 90% CL for the ALPs search via the ALP-strahlung process is shown in Figure 4 [7]. The existing limits on the two-photon coupling can already be improved by Belle II with the small dataset of $472\,\mathrm{pb}^{-1}$ collected during the commissioning run.

4 Dark Photon

In a minimal extension of the SM the dark photon A' may serve as the mediator of a hypothetical dark force. It is charged under a $U(1)'$ gauge-symmetry-extension and kinetic mixing with the SM γ is allowed with a strength equal to ϵ, leading to interactions between SM and DS particles. At Belle II we consider on-shell A' decays and differentiate between a number of experimental signatures according to the mass of the dark photon, $m_{A'}$. If A' is the lightest DS particle, it will decay into SM particles and we look for a peak in the invariant mass of the decay products. However, if A' is not the lightest DS particle, it decays into dark matter and it can be searched for in the process $e^+e^- \to \gamma_{ISR}A'$, which is shown in Figure 5.

The first search for the A' at Belle II will be performed in the invisible decay channel whilst looking for monoenergetic initial-state radiation photon with energy $E_\gamma = \frac{s-m^2_{A'}}{2\sqrt{s}}$. This mono-photon final state is mimicked by different QED processes such as $e^+e^- \to \gamma\gamma(\gamma)$ and $e^+e^- \to e^+e^-\gamma(\gamma)$, where different final- state particles go outside of the detector acceptance except one photon. Special low-multiplicity trigger logic has been developed and implemented into the Belle II trigger system,

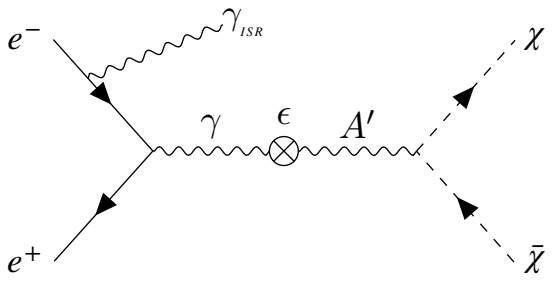

Figure 5: Feynman diagram for the production of A' via kinetic mixing and subsequent invisible decay.

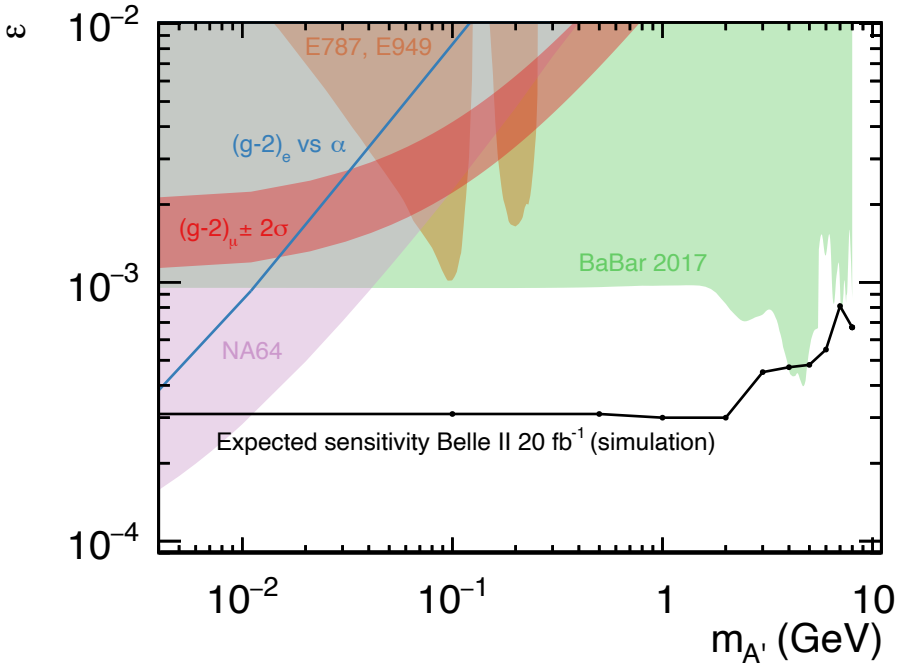

Figure 6: Expected sensitivity for Belle II for measuring the mixing strength ϵ for invisible A' decays [1].

so that these single-photon signatures may be selected. Preliminary estimates on the sensitivity of the kinetic-mixing strength ϵ have been computed and are shown in Figure 6 [1].

5 Conclusion

In these proceedings, the Belle II experiment as well as its capabilities for performing low-mass DS searches have been presented. Indeed there is a broad and active program of DS physics at Belle II including many different models and mediators such as the Dark Photon, ALPS and Z'. First

results have been published and there is much more to come with Belle II ramping up to its design luminosity and collecting much larger data sets.

References

[1] **Belle II Collaboration** Collaboration, E. Kou et al., *The Belle II Physics Book*, *PTEP* **2019** (2019), no. 12 123C01, [arXiv:1808.10567].

[2] W. Altmannshofer, S. Gori, S. Profumo, and F. S. Queiroz, *Explaining dark matter and B decay anomalies with an $L_\mu - L_\tau$ model*, *JHEP* **12** (2016) 106, [arXiv:1609.04026].

[3] B. Shuve and I. Yavin, *Dark matter progenitor: Light vector boson decay into sterile neutrinos*, *Phys. Rev. D* **89** (2014), no. 11 113004, [arXiv:1403.2727].

[4] **BaBar Collaboration** Collaboration, J. Lees et al., *Search for a muonic dark force at BABAR*, *Phys. Rev. D* **94** (2016), no. 1 011102, [arXiv:1606.03501].

[5] **Belle II** Collaboration, I. Adachi et al., *Search for an Invisibly Decaying Z' Boson at Belle II in $e^+e^- \to \mu^+\mu^-(e^\pm\mu^\mp)$ Plus Missing Energy Final States*, *Phys. Rev. Lett.* **124** (2020), no. 14 141801, [arXiv:1912.11276].

[6] R. D. Peccei and H. R. Quinn, CP *conservation in the presence of pseudoparticles*, *Phys. Rev. Lett.* **38** (Jun, 1977) 1440–1443.

[7] M. J. Dolan, T. Ferber, C. Hearty, F. Kahlhoefer, and K. Schmidt-Hoberg, *Revised constraints and Belle II sensitivity for visible and invisible axion-like particles*, *JHEP* **12** (2017) 094, [arXiv:1709.00009].

Axions as Dark Matter and HAYSTAC

Heather Jackson, Alex Droster and Karl van Bibber

hjackson@berkeley.edu

University of California, Berkeley
Berkeley, CA 94720 USA

Presented at the 3rd World Summit on Exploring the Dark Side of the Universe
Guadeloupe Islands, March 9-13, 2020

Abstract

Dark matter is thought to be non-baryonic by nature and composed of yet to be detected subatomic particles. Though several dark matter candidates exist, this paper will focus on the axion, whose detection would also resolve the strong charge-parity (CP) problem of quantum chromodynamics (QCD) [1]. The Haloscope at Yale Sensitive to Axion Cold Dark Matter (HAYSTAC) has made recent improvements to the microwave cavity dark matter axion experiment by circumventing quantum noise using a squeezed state reciever (SSR) and by implementing physical changes to the microwave cavities themselves. HAYSTAC is the first particle physics experiment to circumvent the Standard Quantum Limit of linear amplifiers.

1 The Axion

For many years, the leading candidate for dark matter was the Weakly Interacting Massive Particle (WIMP). However, much of its parameter space has been excluded, thus motivating the search for different dark matter particles [2–4].

The QCD axion is a hypotheical particle that was initially proposed in Peccei-Quinn theory as a solution to the strong CP problem. As WIMP detection has become increasingly difficult in recent years, the axion has become a well-motivated candidate for cold dark matter [5]. The search effort for the axion relies on the inverse Primakoff effect, which would allow an axion in the presence of a DC magnetic field to convert into a detectable photon [6]. A comprehensive review of the particle physics of the axion, its cosmological and astrophysical significance, and experimental searches for it can be found in Ref. [7].

2 The Microwave Cavity Dark Matter Axion Experiment

In the presence of a strong DC magnetic field, the hypothetical axion may convert to a photon via the inverse-Primakoff effect. In 1983, Sikivie proposed that a tuneable microwave cavity permeated by a strong magnetic field, and coupled to a low-noise readout system may be able to resonantly detect this axion-induced photon [8], with expected signal power given in natural units by

$$P_S = \left(g_\gamma^2 \frac{\alpha^2 \rho_a}{\pi^2 \Lambda^4}\right)\left(\omega_c B_0^2 V C_{mnl} Q_L \frac{\beta}{1+\beta}\right) \tag{1}$$

where the first term in parentheses relates the theory parameters out of the experimentalist's control: g_γ and $\rho_a \approx 0.45$ GeV/cm^3 are the dimensionless axion-photon coupling and local dark matter density, respectively, α is the fine structure constant, $\Lambda \approx 77.6$ MeV is the QCD parameter, and $\omega_c = 2\pi m_a$ is the angular frequency associated with the axion.

Within experimental control are the frequency of the cavity's TM_{010}-like mode ω, the applied magnetic field strength B_0, the volume V, the "form factor" $C_{mn\ell}$ of the $mn\ell$ electromagnetic mode, and the loaded quality factor of the cavity Q_L with coupling β.

Because the signal power is expected to be on the order of 10^{-22} Watts [7], the cavity must have a high quality factor (Q) and be immersed in a strong magnetic field. Furthermore, operation at dilution refrigerator temperatures and use of a low noise receiver are necessary.

However, searching for the axion requires detecting a narrow band signal of unknown frequency. Therefore, the figure of merit of microwave cavities is determined by scan rate, the rate at which one may scan frequency space at a given sensitivity. For a given strength magnetic field, the scan rate depends functionally on three parameters of the microwave cavity, i.e. its volume, quality factor and form factor (to be described below) as follows:

$$R \equiv \frac{dv}{dt} \propto QC^2V^2. \tag{2}$$

This shows that the scan rate is dependant on the quality factor of the cavity (Q), the figure of merit (C), and the volume of the cavity. The form factor describes the coupling of the axion to a specific mode, and is calculated from

$$C_{nml} = \frac{(\int E_z dV)^2}{V \int \epsilon_r E^2 dV}. \tag{3}$$

where E the electric field and ϵ_r is the relative permittivity. In order to maximize the scan rate, we seek to maximize these three factors. Microwave simulations can be performed and show ideal cases; however when cavities are manufactured, the quality factor will generally be less than the simulated Q due to imperfections in manufacturing and quality of the copper coating. Typical Q values achieved are $Q_L = 3 \times 10^4$, where Q_L is the loaded quality factor, which accounts for the resonator's connection to an external network.

UF / RBF	**ADMX @ LLNL**	**ADMX @ UW**	**CAPP**	**HAYSTAC I**	**HAYSTAC II**
1985 - 1990	1995 - 2010	2016 - present	2019 - present	2015 - 2018	2019 - present
HEMT	HEMT, SQUID	SQUID	HEMT	JPA	SSR
f $\sim$ 2.5 GHz	$\sim$ 0.6 GHz	$\sim$ 0.7 GHz	$\sim$ 1.6 GHz	$\sim$ 6 GHz	$\sim$ 4 GHz
V $\sim$ 5 L	$\sim$ 200 L	$\sim$ 150 L	$\sim$ 3.5 L	$\sim$ 1.5 L	$\sim$ 1.5 L
$T_{SYS} \sim$ 5 - 20 K	$\sim$ 3 K	$\sim$ 350 mK	$\sim$ 1K	$\sim$ 300 mK	G_{SQ} = -4 dB
$T_{SYS}/T_{SQL} \sim$ 100 - 200	$\sim$ 50 - 100	$\sim$ 10	$\sim$ 12	$\sim$ 2	<1

Table 1: Summary of past and current microwave cavity experiments. Temperatures listed in the HAYSTAC column reflect those when Squeezed-vacuum State Reciever (SSR) is used.

3 HAYSTAC

3.1 The Experiment

HAYSTAC (Haloscope At Yale Sensitive To Axion Cold dark matter) was conceived to serve both as a data pathfinder in the 3-12 GHz (12.5 - 50 μeV) mass range, and an agile innovation testbed for new technologies in resonators and quantum-limited receivers. The HAYSTAC collaboration began operations in 2015 and is composed of three groups: UC Berkeley, CU Boulder/JILA, and Yale. Berkeley is responsible for the cavities, CU Boulder/JILA for the receiver, and Yale for the magnet, dilution

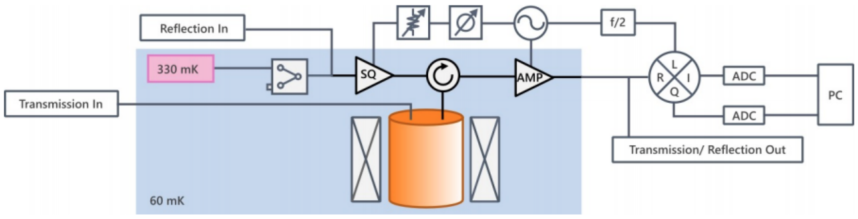

Figure 1: Block diagram of the experiment in Phase II Run 1. The Squeezed State Receiver components are shown in black.

refrigerator, balance of infrastructure and operations. The experiment is composed of the following parts:

1. The CMI magnet, NbTi-superconducting solenoid with a 9.4 T maximum field, 55 cm long, 14.5 cm cold bore.
2. The Blue Fors dilution refrigerator, which has a base temperature 25 mK, although we have run deliberately around 100 mK.
3. Microwave cavity, open volume V = 1.5 L, stainless steel electroplated with OFHC copper and annealed.
4. A receiver, originally using a single JPA (Josphson Parametric Amplifier), whose system noise temperature was 2-3 times the Standard Quantum Limit, more recently with a 2-JPA Squeezed State Reciever.

A block diagram of the experimental setup is shown in Figure 1.

The TM-like modes of the cylindrical cavity may be tuned by the rotation of a copper-plated rod which takes up 25% of the cavity volume. Rotating this rod about an off-center axle provides a continuous tuning range of 3.6-5.8 GHz for the TM_{010}-like mode, which corresponds to the axion mass range 15-24 μeV.

Various potential axion masses can be explored by changing the resonant frequency of the cavity. Only a very small range of axion masses can be explored at a time for each frequency, so the frequency must be manipulated in very small steps, on the order of 10 kHz, to collect data for different masses.

3.2 Phase I

Phase I of HAYSTAC consisted of two runs. Run 1 covered the 5.7-5.8 GHz frequency range and completed in August 2016. Run 2, completed in July 2017, covered the 5.6-5.7 GHz frequency range and featured improved thermal noise reduction over Run 1. The T_{SYS} in Run 1 was about three times T_{SQL}, but only two times T_{SQL} in Run 2, which is consistent with losses in the cables and circulator.

Fig. 3 shows the 90% exclusion limit for g_γ based on the two axion search data runs 1 and 2, labeled "HAYSTAC 2018" [9, 10]. This sensitivity is 2.7 times greater than KSVZ model couplings, a benchmark model for microwave cavity axion searches [11]. This result was the first cosmologically relevant exclusion of a QCD axion of $m_a > 20$ μeV [9].

3.3 Phase II

After a successful Phase I, HAYSTAC improved upon the experiment by implementing quantum squeezing with a squeezed state receiver (SSR) [12]. The SSR is a system of two flux pumped JPAs [13]: the first JPA, called the "squeezer," prepares a the cavity in a squeezed vacuum state and the second, or "amplifier" JPA, amplifies the signal noiselessly.

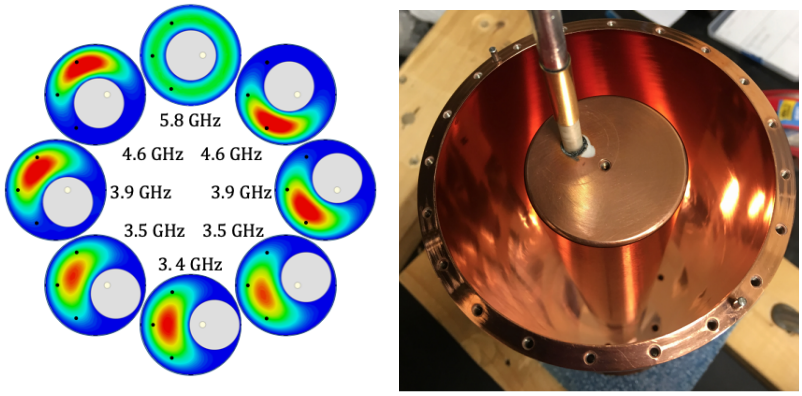

Figure 2: Left: Top view false-color plots of the magnitude of the TM010 electric field of the HAYSTAC cavity for runs I and II. Right: Top view photograph of the HAYSTAC cavity used for runs I and II with the endcap removed to show the tuning rod.

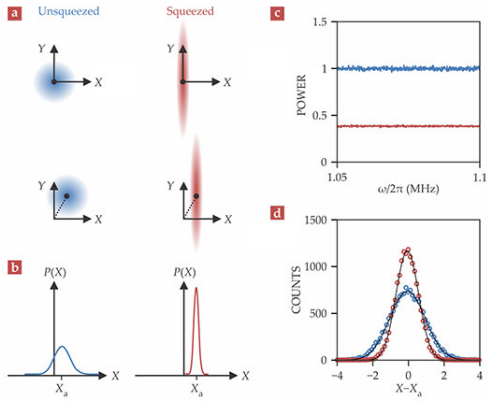

Figure 3: (a) The cavity's field can be described by its cosine (X) and sine (Y) components. These variables define the its phase space. The cavity can be prepared in either an unsqueezed state (blue) or squeezed state (red). The presence of an axion in the cavity will displace this state (represented by the dotted line). (b) Measuring the X component yields a probability density $P(x)$. Because the noise has been squeezed from the X to the Y component, the axion signal is enhanced in the squeezed case. (c) Noise power with (red) and without (blue) squeezing. (d) Measured values of X with (red) and without (blue) squeezing.

The improvement due to the SSR may be understood by considering the three sources of noise which degrade sensitivity. The first source of noise is Johnson-Nyquist sourced by internal losses in the microwave cavity, N_c. The second source of noise is amplifier added noise, which historically dominates over the other two noise sources on resonance. However, this source of noise is eliminated in one quadrature by using the JPAs in phase-sensitive mode. The third source of noise is Johnson-Nyquist noise incident on and reflected from the cavity, N_r, which dominates off cavity resonance. The SSR reduces this third source of noise by preparing the cavity in a squeezed state in one quadrature and reading out the other quadrature, therefore reducing N_r to below the quantum limit for Johnson-Nyquist noise. This technique makes N_c dominant over N_r and increases the bandwidth over which the experiment is sensitive to the axion [14]. The advantage of the SSR is shown schematically in Fig. 4.

The Phase II experiment ran in 2019, and data analysis and rescans were performed in early 2020.

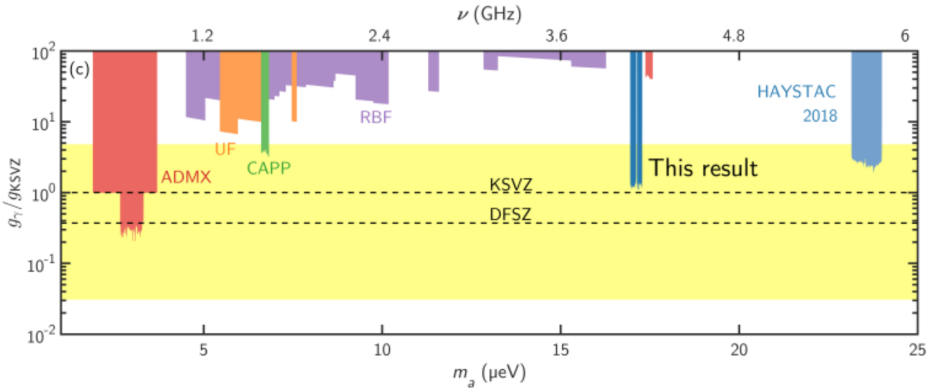

Figure 4: Exclusion plot with results from Phase II Run 1 shown by "this result" as well as results from other axion dark matter searches [8, 16–25]. KSVZ [11, 26] and DFSZ [27, 28] are shown with dotted lines.

The run excluded $g_\gamma \geq 1.38 g_\gamma^{KSVZ}$ for the mass range $16.96 < m_a < 17.12$ and $17.14 < m_a < 17.28$ $\mu eV/c^2$ [15]. This corresponds to the frequency ranges 4.100–4.140 and 4.145–4.178 GHz. These results are shown in Fig. 3, labeled "This result."

3.4 Future Plans

Recent theoretical predictions for the axion mass which would account for the dark matter density of the universe (under the scenario of Peccei-Quinn symmetry breaking after inflation) are converging on the 15-35 μeV mass range [29, 30], well within HAYSTAC's range, and running in the near term will focus on covering as much of this range as possible, with a sensitivity in axion-photon coupling $g_{a\gamma\gamma}$ at or slightly greater than the KSVZ model. Our first run with a squeezed-state receiver already resulted in an improvement in scan rate of 3.6; our next run should provide an additional acceleration of a factor of 4. Half of this is expected by a cavity built by Berkeley of the same design as in Figure 2, but of electroplated copper on aluminum, rather than the stainless steel substrate as has been used to date. Owing to the lower density, much lower specific heat and much greater thermal conductivity of aluminum relative to steel, it is hoped that the last quantum of thermal noise will be eliminated that plagued the first SSR run. The other x2 contribution to the increased rate is due to elimination of dead-time in reading out the data.

Subsequent runs will employ another Berkeley cavity designed for higher frequency operation; it incorporates a tuning mechanism which preserves discrete rotational symmetry, which has been shown to be critical to preserve good figure-of-merit (i.e. maximizes scan rate) over a broad dynamic range in frequency. This multirod cavity has one fixed central rod, and six rods which pivot outward in unison. Figure 4 shows a photograph of the cavity, and plots of the magnitude of the electric field as a function of rotation, or equivalently frequency.

Collaborators from the University of Colorado Joint Institute for Laboratory Astrophysics, and currently designing a much more powerful receiver based on two-mode squeezing (entangling) and state-swapping, which could produce factors of 20-25x greater scan rate for the experiment, the CEASEFIRE project.

4 Conclusions

The QCD axion is an attractive dark matter candidate, and its discovery would solve both the strong CP problem and the identity of 85% of the universe's matter density. HAYSTAC is the first dark

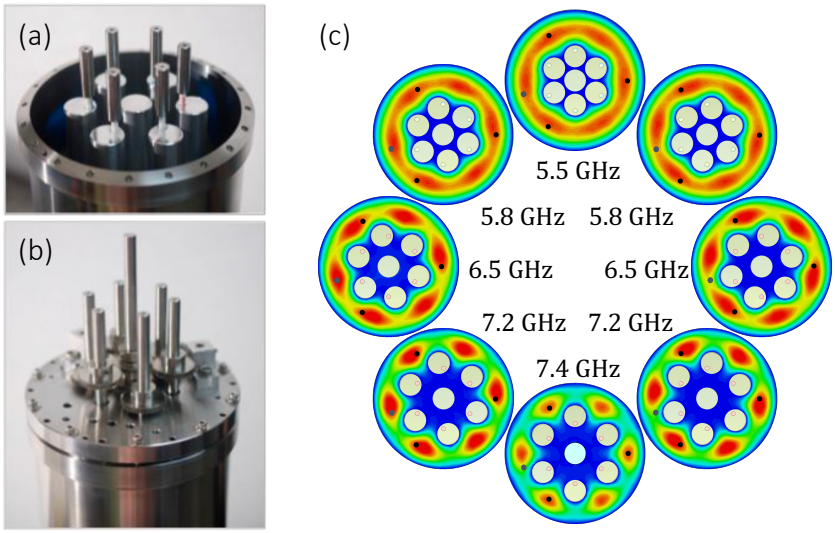

Figure 5: (a) and (b) Photographs of the symmetric tuner multirod cavity, partially disassembled. (c) False-color plots of the magnitude of the electric field of the TM_{010}-like mode [24]. Preserving discrete rotational symmetry maximizes the microwave cavity figure-of-merit over a wide dynamic range of frequencies. [31]

matter experiment to utilize squeezed states to circumvent the Standard Quantum Limit, and along with LIGO are the only experiments to have done so in fundamental physics. With the squeezed-state receiver, we have excluded $g_\gamma \geq 1.38 g_\gamma^{KSVZ}$ in the mass range $16.96 < m_a < 17.12$ and $17.14 < m_a < 17.28$ $\mu\mathrm{eV/c}^2$, which correspond to the frequencies 4.100–4.140 and 4.145–4.178 GHz. Future HAYSTAC runs will deploy new cavity geometries to probe higher mass ranges, and new quantum-enhanced receivers to both improve experimental sensitivity and further accelerate the search.

References

[1] R. D. Peccei and H. R. Quinn. Cp conservation in the presence of pseudoparticles. *Phys. Rev. Lett*, 38(1440), 1977.

[2] Xiangyi Cui et al. Dark Matter Results From 54-Ton-Day Exposure of PandaX-II Experiment. *Phys. Rev. Lett.*, 119(181302), 2017.

[3] E. Aprile et al. First Dark Matter Search Results from the XENON1T Experiment. *Phys. Rev. Lett.*, 119(181301), 2017.

[4] D. S. Akerib et al. Results from a search for dark matter in the complete LUX exposure. *Phys. Rev. Lett.*, 118(021303), 2017.

[5] J. Ipser and P. Sikivie. Can galactic halos be made of axions? *Phys. Rev. Lett.*, 50(925), 1983.

[6] Pierre Sikivie. Experimental Tests of the 'Invisible' Axion. *Physical Review Letters*, 51(685), July 1983.

[7] Peter W. Graham et al. Experimental Searches for the Axion and Axion-Like Particles. *Annu. Rev. Nucl. Part. Sci.*, 65:485–514, August 2015.

[8] C. Hagmann, P. Sikivie, N. S. Sullivan, and D. B. Tanner. Results from a search for cosmic axions. *Phys. Rev. D*, 42(1297(R)), August 1990.

[9] L. Zhong et al. Results from Phase 1 of the HAYSTAC Microwave Cavity Axion Experiment. *Phys. Rev. D*, 97(092001), 2018.

[10] B. M. Brubaker et al. First results from a microwave cavity axion search at 24 μ ev. *PRL*, 118(061302), 2017.

[11] Jihn E. Kim. Weak-Interaction Singlet and Strong CP Invariance. *Phys. Rev. Lett.*, 43(103), July 1979.

[12] Carlton M. Caves. Quantum-mechanical noise in an interferometer. *Phys. Rev. D*, 23(1693), April 1981.

[13] T. Yamamoto et al. Flux-driven josephson parametric amplifier. *Appl. Phys. Lett.*, 93(042510), 2008.

[14] M. Malnou, D. A. Palken, B. M. Brubaker, Leila R. Vale, Gene C. Hilton, and K. W. Lehnert. Squeezed Vacuum Used to Accelerate the Search for a Weak Classical Signal. *Phys. Rev. X*, 9(021023), April 2018.

[15] K. Backes and D. Palken et al. A quantum-enhanced search for dark matter axions. *https://arxiv.org/abs/2008.01853*, 2020. Submitted to *Nature*.

[16] C. Hagmann et al. Results from a High-Sensitivity Search for Cosmic Axions. *Phys. Rev. Lett.*, 80(2043), March 1998.

[17] S. J. Asztalos et al. Experimental Constraints on the Axion Dark Matter Halo Density. *The Astrophysical Journal Letters*, 2002.

[18] S. J. Asztalos et al. Improved RF cavity search for halo axions. *Phys. Rev. D*, 69(011101(R)), January 2004.

[19] S. J. Asztalos et al. SQUID-Based Microwave Cavity Search for Dark-Matter Axions. *Phys. Rev. Lett.*, 104(041301), January 2010.

[20] J. V Sloan et al. Limits on Axion–Photon Coupling or on Local Axion Density: Dependence on Models of the Milky Way's Dark Halo. *Physics of the Dark Universe*, 14:95–102, 2016.

[21] S. DePanfilis et al. Limits on the abundance and coupling of cosmic axions at $4.5 < m_a < 5.0$ μeV. *Phys. Rev. Lett.*, 59(839), August 1987.

[22] W. U. Wuensch et al. Results of a Laboratory Search for Cosmic Axions and Other Weakly Coupled Light Particles. *Phys. Rev. D*, 40(3153), November 1989.

[23] N. Du et al. Search for Invisible Axion Dark Matter with the Axion Dark Matter Experiment. *Phys. Rev. Lett.*, 120(151301), April 2018.

[24] T. Braine et al. Extended Search for the Invisible Axion with the Axion Dark Matter Experiment. *Phys. Rev. Lett.*, 124(101303), March 2020.

[25] S. Lee et al. Axion Dark Matter Search around 6.7 μeV. *Phys. Rev. Lett.*, 124(101802), March 2020.

[26] M. A. Shifman, A. I. Vainshtein, and V. I. Zakharov. Can Confinement Ensure Natural CP Invariance of Strong Interactions? *Nuclear Physics B*, 166(3):493–506, April 1980.

[27] Michael Dine, Willy Fischler, and Mark Srednicki. A simple solution to the strong CP problem with a harmless axion. *Physics Letters B*, 104(3):199–202, August 1981.

[28] A. R. Zhitnitsky. On possible suppression of the axion hadron interactions. (in russian). *Sov. J. Nucl. Phys.*, 31(260), 1980.

[29] V. B. Klaer and G. D. Moore. The dark-matter axion mass. *Journal of Cosmology and Astroparticle Physics*, (049), 2017.

[30] Malte Buschmann et al. Early-universe simulations of the cosmological axion. *PRL*, 124(161103), 2020.

[31] M. Simanovskaia et al. Symmetric multi-rod tunable microwave cavity for the haystac dark matter axion search. *arXiv preprint*, (2006.01248), 2020.

Indirect Detection of Dark Matter in the Galaxy

Rebecca K. Leane[1]

e-mail: rleane@mit.edu

Center for Theoretical Physics
Massachusetts Institute of Technology
Cambridge, MA 02139, USA

Presented at the 3rd World Summit on Exploring the Dark Side of the Universe
Guadeloupe Islands, March 9-13 2020

Abstract

I present a short overview of the latest developments in indirect searches for dark matter using gamma rays, X-rays, charged cosmic rays, micro waves, radio waves, and neutrinos. I briefly outline key past, present, and future experiments and their search strategies. In several searches there are exciting anomalies which could potentially be emerging dark matter signals. I discuss these anomalous signals, and some future prospects to determine their origins.

1 Introduction

Indirect searches for dark matter are incredibly exciting. The Universe has been exploding systems, smashing systems together, and allowing systems to decay since the beginning of time. This provides an enormous advantage in searches for dark matter compared to collider and direct detection efforts – we can access unique lengths and energies using experiments the Universe has been running *for us* over very long time scales. Compared to Earth-based searches, we can probe higher energies, longer particle decay lengths, and weaker particle couplings. Furthermore, we can observe dark matter in its natural habitat. All the evidence to date for dark matter comes from its fingerprints in astrophysics and cosmology. The defining feature of thermal particle dark matter, its annihilation cross section, can be directly compared to its annihilation rate observed in indirect experiments. This provides a clear target for dark matter discovery, or exclusion of particular models.

In this mini-review, I provide a brief overview of searches for dark matter using gamma rays, cosmic rays, and neutrinos. I will discuss the latest developments for hints for dark matter in these observables. I detail future paths enabling the fundamental particle nature of dark matter to potentially be finally revealed.

2 Ingredients for Indirect Dark Matter Searches

Indirect dark matter searches scan the sky for any excess Standard Model (SM) particles or anti-particles produced from dark matter annihilation or decay. The flux Φ of neutral particles[2] arising

[1]ORCID: 0000-0002-1287-8780

[2]Note that for charged particles arising from dark matter annihilation or decay, their flux will contain additional terms relevant for cosmic ray propagation, see e.g. Ref [1]. Also note that redshift (or absorption) effects are not shown here, which can be relevant when particles traverse large distances/times, see e.g. Ref. [2].

from the annihilation ($a = 2$) or decay ($a = 1$) of dark matter with mass m_χ can be described as

$$\Phi(E, \phi) = \frac{\Gamma}{4\pi m_\chi^a} \frac{dN}{dE} \int \rho[r, (\ell, \phi)]^a \, d\ell. \tag{1}$$

This equation encapsulates three important aspects for the dark matter sourced particle rate:

1. The interaction rate of dark matter particles Γ. For annihilating dark matter, the rate is $\Gamma = \langle \sigma v \rangle / 2$, where σ is the cross section for dark matter particles with relative velocity v. For dark matter decay, the interaction rate is $\Gamma = 1/\tau$, where τ is the dark matter lifetime.

2. The energy spectrum of the annihilating/decaying particles (dN/dE). Depending on the mass of the dark matter particles, different amounts of energy can be imparted to the detectable annihilation/decay products. Further, depending on what the products are, their energy spectrum will vary depending on how/if they hadronize, how/if they decay, and how/if they radiate any particles themselves.

3. A piece arising from astrophysics, which relates to the dark matter density in the relevant environment. This factor is the integral over the dark matter density ρ raised to some power a along the line of sight $d\ell$. For annihilating dark matter, this is called the J-factor [3], with $a = 2$. For decaying dark matter, this is called the D-factor [4], with $a = 1$. This relies on information from N-body simulations, which informs of the possible dark matter density profiles present in the system of interest.

While indirect searches for dark matter are advantageous over other searches in many ways, they have a significant difficulty: not-well understood backgrounds. Along with this, can come large systematic errors. To optimize discovery or exclusion, we want to search in a way that maximizes signal over background (or minimizes potential unknown systematics). To do this, we want to exploit the relevant inputs to the dark matter particle flux listed above. This can be optimized by:

1. Looking for scenarios (or times) where the annihilation or decay rate is enhanced. For example, Sommerfeld enhanced annihilation can lead to larger rates today than in the early Universe. Importantly however, for many dark matter models, the annihilation rate will be set by the relic density of dark matter in the Universe today, and as such may not be able to be freely increased or decreased without consequence.

2. Looking in energy bands where the signal energy spectrum is distinct or peaked relative to the shape of the background spectrum. This can happen for example where line or box spectral features arise.

3. Looking in places where the dark matter density is large. A good example here is the galactic center.

Equipped with these points, lets see what we can find throughout the Universe, and what has been potentially found so far!

3 Dark Matter Searches with Neutrinos

3.1 Experiments and Prospects

Searches with neutrinos provide unique opportunities and challenges. The very weak interactions of these ghostly particles provide a window into the deepest and darkest places in the Universe, where no other signals can escape. On the other hand, exactly because they are so weakly interacting, they can then be difficult to detect.

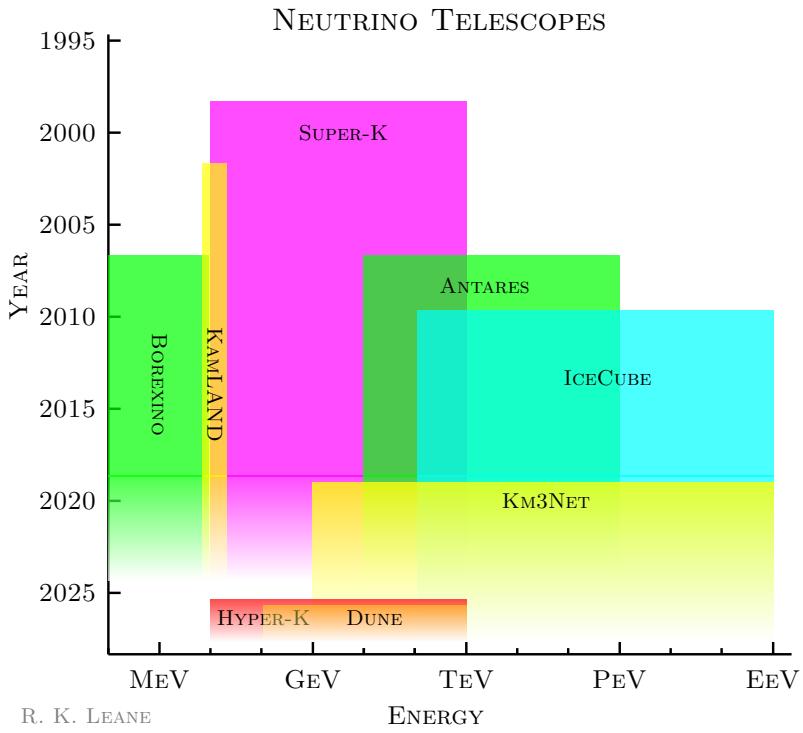

Figure 1: Summary of selected neutrino experiments directly searching for dark matter annihilation, by mission dates and approximate energy sensitivity.

Figure 1 shows a brief overview of selected neutrino experiments searching for dark matter in the last couple of decades, as a function of their approximate energy sensitivity. Just in 2019, KM3Net has come online, and is beginning to provide preliminary results on dark matter annihilation [5, 6]. IceCube-Gen2 (the IceCube upgrade) will substantially improve sensitivity to dark matter masses below around 100 GeV for high-energy solar neutrino searches, by many orders of magnitude [7]. Coming soon is Super-K's successor, Hyper-K. The fiducial volume of the Hyper-K tank is about 10 times larger than the Super-K tank, leading to a large improvement on previous flux sensitivities. This will provide better sensitivities to the dark matter annihilation cross section by about an order of magnitude [8–10]. For solar neutrino searches, Borexino has sensitivity to ∼MeV mass annihilating dark matter [11]. Limits on ∼MeV mass dark matter can also be set using the flux of extraterrestial neutrinos with KamLAND [9, 12]. Dune is a new experiment currently under construction, and compared to Cherenkov detectors such as Super-K, IceCube, and ANTARES, has improved energy resolution to observe neutrinos from dark matter annihilation [13, 14]. Dune can be used in future for several dark matter-neutrino related contexts; behind Hyper-K, it may provide the next best sensitivity to galactic dark matter for ∼GeV dark matter masses, down to annihilation cross sections of $\sim 10^{-24}\text{cm}^3/\text{s}$ [9].

3.2 Dark Matter Annihilation and Decay into Neutrinos

The current leading limits on dark matter annihilation into neutrinos, for most dark matter masses, come from observations of the galactic center, where locally the dark matter density is greatest. However, compared to searches with the same targets using with gamma or cosmic rays, these limits are generally the weakest (and certainly above the thermal relic cross section), as neutrinos are much

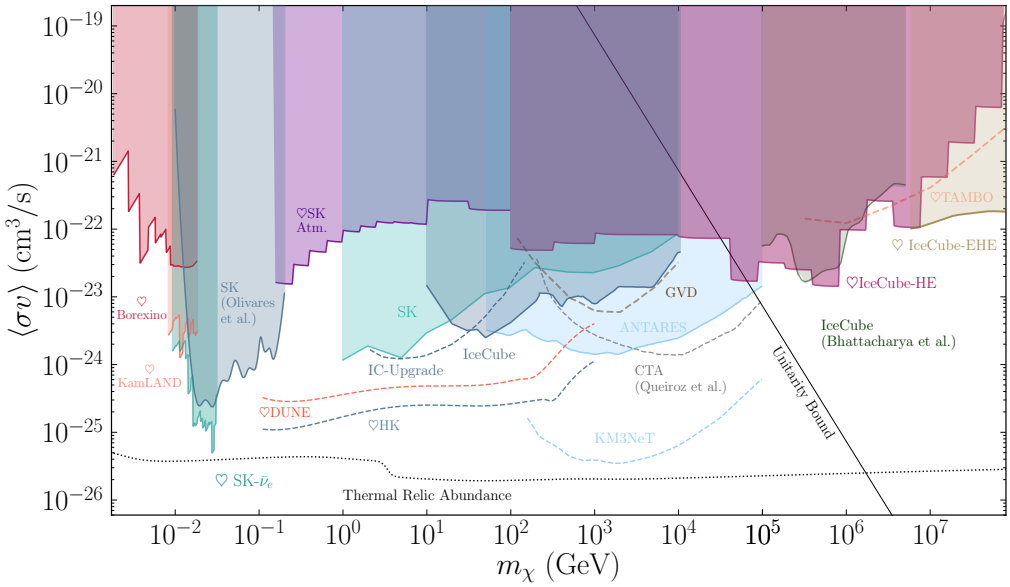

Figure 2: Summary of 90% C.L. limits (shaded) and projected sensitivities (dashed) to the dark matter annihilation cross section, assuming s-wave annihilation. Plot taken from Ref. [9].

more difficult to detect.

Figure 2 shows a recent summary of the landscape of constraints on the dark matter annihilation cross section from neutrinos. See Ref. [9] for further details.

The diffuse neutrino flux in the Milky Way halo can also be used to search for dark matter [15,16]. In fact, a hint of dark matter has been suggested to potentially exist in IceCube's observed TeV-PeV diffuse neutrino flux [17]. The origin of such high-energy neutrinos is not yet understood, so has been purported to potentially contain a component from decaying dark matter (see e.g. [18, 19]). However, this is constrained in part by gamma-ray observations, as decaying dark matter that produces neutrinos should also produce gamma rays – and no such excess gamma rays are observed by the gamma-ray telescope Fermi [20, 21]. Therefore, the current status is that dark matter could still contribute to the diffuse TeV-PeV neutrino flux, though parameters which could give rise to this flux are partly constrained.

3.3 Dark Matter Scattering and Annihilation to Neutrinos in the Sun

Due to their ghostly nature, one of the best things about using neutrinos is peering into environments in which no other particles could escape. Such a way to search with neutrinos is to look for neutrinos escaping stars, like the Sun. Dark matter particles sweeping through the Sun can scatter with the solar matter, lose energy, and become gravitationally captured. Dark matter can then accumulate at the core, and if present with anti-particles, can annihilate to high-energy neutrinos which may escape the Sun and be detected on Earth [23–26]. This provides a complementary probe of both the dark matter scattering cross section (as this determines how much dark matter was captured), as well as the dark matter annihilation cross section. In the scenario that dark matter annihilates to long-lived mediators, the neutrino flux is boosted as the particles are not as attenuated [27, 28] (and in such a scenario, other particles can escape, such as gamma rays or charged particles [22, 27, 29–37]).

Figure 3 shows a comparison of these processes in the Sun. For similar processes but for dark matter in other stars such as neutron stars and white dwarfs, see Refs. [38–65, 65–73].

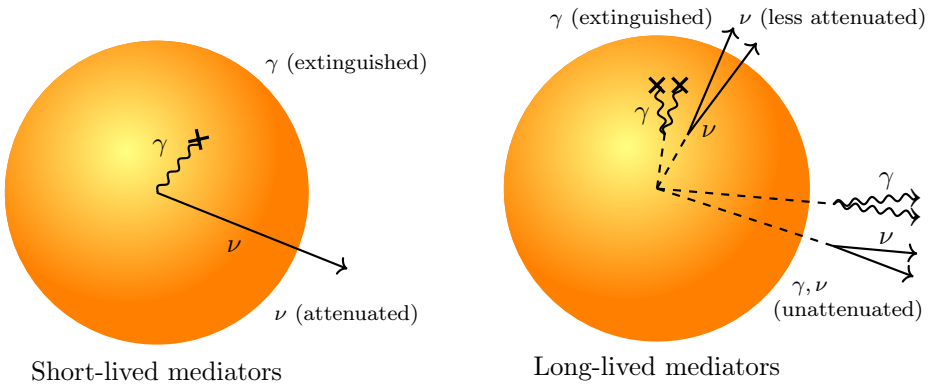

Figure 3: **Left:** Short-lived mediator scenario. Only neutrinos can escape the Sun and they are attenuated. **Right:** Long-lived dark mediator scenario. Gamma rays (and other particles) can escape, and neutrinos are less attenuated. Figure taken from Ref. [22].

4 Dark Matter Searches with X-Rays

4.1 Experiments and Prospects

Like neutrinos, a benefit of X-ray signatures is that, being neutral particles, they are not subject to turbulent astrophysical magnetic fields, and propagate otherwise directly from their source (if not absorbed). Electrically charged dark matter annihilation products can lead to X-ray signatures, through inverse Compton scattering with astrophysical magnetic fields. Alternatively, the X-ray band provides an interesting probe of a keV-mass dark matter candidate, the sterile neutrino. In this case, sterile neutrino can decay into an active neutrino and photon, leading to an X-ray line (see below).

Figure 5 shows a range of experiments searching for dark matter signals in X-ray (and gamma rays, see section below), as an approximate function of energy sensitivity and mission times.

4.2 3.5 keV line

Perhaps the most striking potential dark matter hint in X-ray at the moment is the 3.5 keV line. This may arise from a process $\chi \to \nu + \gamma$, where χ is a 7 keV sterile neutrino decaying to an active neutrino ν and photon γ. This line was first detected in stacked galaxy clusters with XMM-Newton [74, 75]. Intriguingly, it has been shown to be consistent with many complementary observations, though there is at least a slight tension with some other constraints [76].

Figure 4 shows an overview of X-ray constraints on sterile neutrinos; see Refs. [77, 79, 80] for more details on the left figure, and Ref. [76] for more details on the right figure.

It has been recently argued that using blank-sky searches, no 3.5 keV line is detected, allowing a strong constraint to be set on the sterile neutrino dark matter explanation [78]. This is because dark matter should be present everywhere in the halo (including the otherwise "blank sky"), and so the line should have been detected if it were coming from decaying dark matter. However, study of a larger albeit overlapping region by other authors claim the line is indeed found [81]. The discrepancy is claimed to arise due to too small an energy window used in Ref. [78], and claims that other lines and instrument features not being correctly modeled [81–83]. Considering the larger region of study [81–83] which includes other background X-ray lines, the background is more supported and can result in its normalization being pushed down, such that a signal is visible. This is not a feature of the smaller

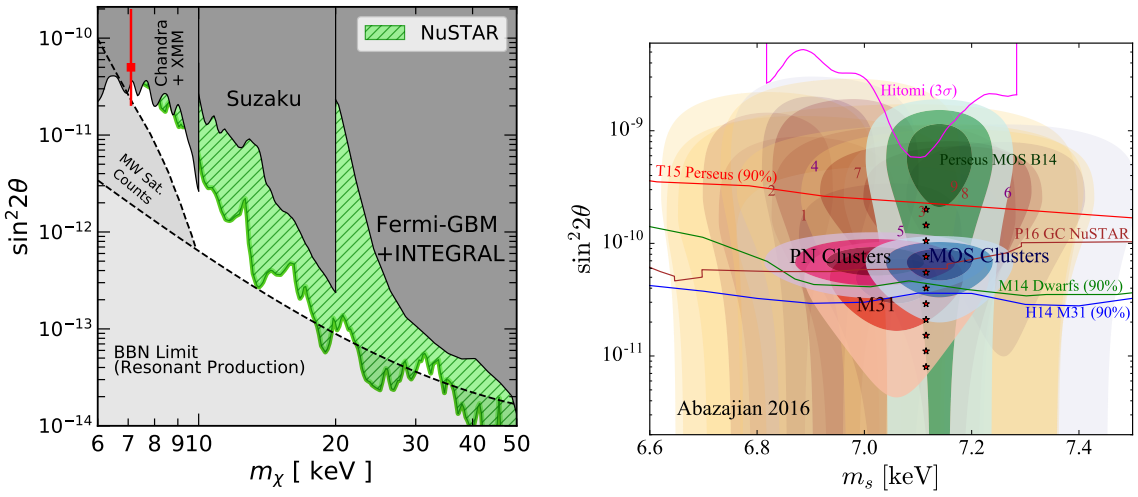

Figure 4: **Left:** Summary of X-ray constraints on the sterile neutrino parameter space, taken from Ref. [77]. The red data point corresponds to an explanation of the 3.5 keV line. **Right:** Summary of best-fits (and some constraints) to the 3.5 keV line for the sterile neutrino model, taken from Ref. [76]. Ref. [78] argues for an additional upper constraint at $\sin^2 2\theta \sim 10^{-12} - 10^{-11}$ in this mass range, which would present strong tension with the signal as dark matter, though there is some debate (see text).

energy window. However, it is interesting to note that in Ref. [78], there does appear to be a large downwards fluctuation of the background in the signal region, such that the data is much lower than the expected background, leading to very strong limits. The treatment of the energy window and backgrounds appears to be the main point that is debated, and leads to bounds on $\sin^2 2\theta$ that vary by a factor of ~ 8.

It is also argued that including additional systematics from uncertainty in the dark matter density profile weakens the limits of Ref. [78] by an additional factor of ~ 3 [83]. This is certainly true, although changing the dark matter profile and associated uncertainties would likely move the parameters corresponding to a signal detection from other Milky Way observations as well.

The origin of this line would have been settled in 2016 by satellite Hitomi, which unfortunately was destroyed only weeks after launching. New telescopes will be required to settle the debate once and for all. This should be possible within the next decade or so, with several X-ray telescopes and observatories to be launched which should be sensitive to an anomalous 3.5 keV line, such as e.g. Micro-X, X-Prism, and Athena. See Ref. [84] for more details.

5 Dark Matter Searches with Gamma Rays

5.1 Experiments and Prospects

Dark matter annihilation can yield gamma rays, by hadronization of the final states, radiating gamma rays, or annihilating directly into pairs of gamma rays (producing a gamma-ray line). Generally, any dark matter model which has hadronic final states, will produce a strong signal in gamma rays. We currently search for dark matter in gamma rays from the Sun, the center of our galaxy, the Milky Way halo, in other galaxies, and in extragalactic environments. Like X-rays and neutrinos, gamma rays also benefit from not being subject to astrophysical magnetic fields, and if not absorbed, propagate directly from their source.

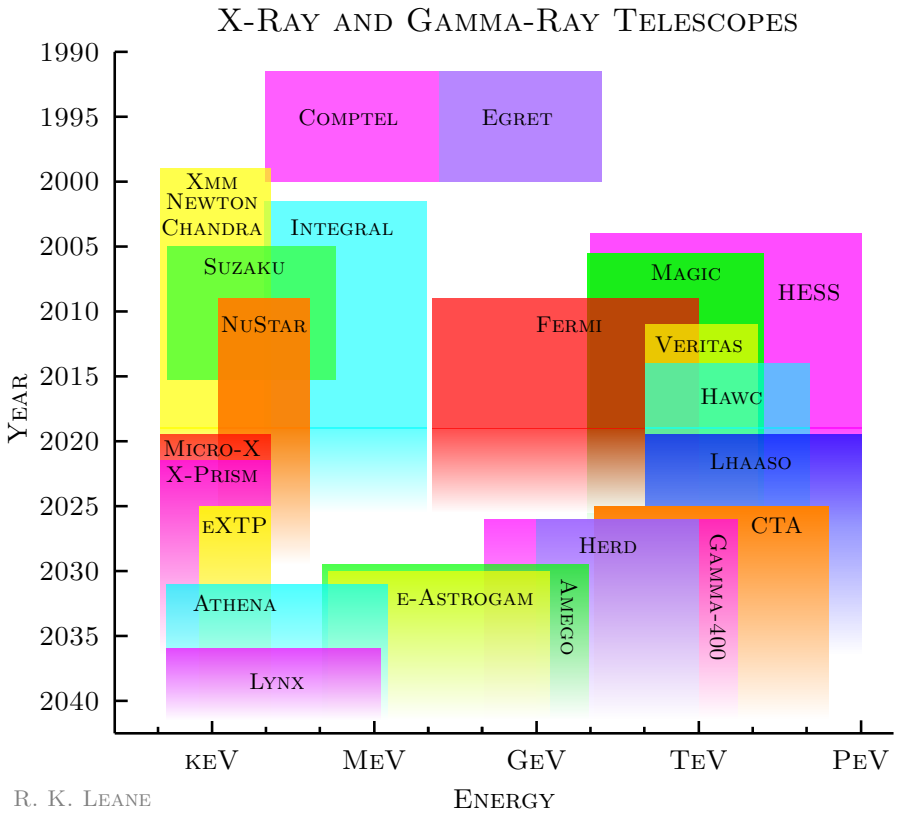

Figure 5: Summary of selected X-ray and gamma-ray experiments by mission dates, and approximate energy sensitivity.

Figure 5 shows a range of experiments searching for dark matter signals in gamma ray (and X-rays, see section above), as a function of the approximate energies they are sensitive to, and their mission times in years. Our searches have been revolutionized by the Fermi Gamma-Ray Telescope (usually referred to as just "Fermi"), which provides leading sensitivity to nearly all GeV gamma-ray targets. It has now collected over 10 years of data, with excellent angular and energy resolution in the GeV range. Above 1 TeV, other telescopes and observatories are superior, with progress rapidly improving. Currently, experiments such as MAGIC, VERITAS, HESS, HAWC, and LHAASO are providing sensitivity to the dark matter annihilation cross section. MAGIC, VERITAS and HESS are Imaging Atmospheric Cherenkov Telescopes (IACTs), and cannot look directly at nearby high-energy sources such as the Sun. They are ideal for e.g. TeV-gamma-ray Galactic Center searches. HAWC and LHAASO are water Cherenkov telescopes, and detect TeV gamma rays created in air-showers in the atmosphere (i.e., they don't measure the original cosmic rays/gamma rays directly). This means they are able to observe bright nearby sources such as the Sun, though they are also able to perform other searches (e.g. TeV-PeV gamma rays from the Galactic Center, dwarf spheroidals, etc). We can expect exciting developments soon with CTA (Cherenkov Telescope Array). CTA is a set of over 100 ground-based telescopes, collectively using large mirrors and high-speed cameras to detect the cherenkov light produced by charged cosmic rays and gamma rays in atmospheric air showers. We can be excited for a significant boost in dark matter search sensitivity soon with CTA, which should extend below the thermal relic cross section at TeV masses [85,86].

5.2 Galactic Center

5.2.1 GeV Excess

The GeV Excess is an anomalous flux of GeV gamma rays peaked at $\sim 2-3$ GeV, detected by the Fermi Gamma-Ray Space Telescope. It was first discovered in 2009 [87], and has led to considerable debate as to its origin ever since. It is quite an exciting anomaly, as it first presented with many features of thermal particle dark matter signal. It features:

- Consistent intensity of a thermal WIMP: the annihilation cross section required to fit the signal is $\langle \sigma v \rangle \sim 10^{-26} \text{cm}^3/\text{s}$ [88, 89], which is of the same order obtained in the standard freezeout scenario.
- Consistent energy spectrum of a dark matter particle with mass $\sim 50-100$ GeV [88, 89], best fit if the annihilation products are hadrons. Furthermore, the energy spectrum appears to be consistent throughout the excess, rather than changing with spatial distance from the center. This implies whatever is creating the excess is likely locally producing it, rather than it coming from some outflow event from the galactic center.
- Consistent morphology: it can be well fit with an NFW^2 dark matter profile [88, 89] (though note that this point has since been debated[3]), and extends well out of the center of the galaxy, to at least 10 degrees. Visible matter, on the other hand, mostly correlates with the disk.

While the signal appears to nicely fit with the dark matter origin, there is a leading alternative: pulsars. Pulsars are rapidly spinning neutron stars. Those with millisecond periods, called millisecond pulsars, appear to be the leading candidate. This is mostly because the millisecond pulsars observed in other environments (specifically globular clusters) have a gamma-ray energy spectrum that also appears to approximately match the GCE [94, 95].

Now, while pulsars are a good candidate for the excess, we still haven't seen any of the pulsars that are contributing GCE (if they are), which is argued to be surprising given the number of low-mass X-ray binaries observed in the GC [95, 96]. Furthermore, there are questions of how it is possible to have the number and distribution of pulsars that are required to explain the excess [95, 97].

The general point is that there are two good leading explanations, and it is difficult to know which is the correct answer. Knowing the answer, however, is of pressing importance. We know dark matter makes up most of the matter in the Universe, yet we still have no information as to its fundamental particle nature. If the GCE turns out to be dark matter, it would be the first evidence of dark matter interacting with the Standard Model, and would have dramatic implications for all of physics.

So let's try to answer the question: what is the best explanation of the data, dark matter, or pulsars? To try to answer this question by searching for evidence for point sources (note pulsars appear as point sources to Fermi), there are two main methods:

- Non-Poissonian Template Fitting (NPTF): This method exploits the difference in photon statistics expected from dark matter vs point sources. Specifically, gamma rays from dark matter are expected to provide smooth diffuse glow. This is because it is spread approximately smoothly through a halo. Gamma rays from point sources, however, look more clumpy. You can imagine a given pixel has no point sources, while another pixel has several, leading to more gamma rays. The variance across pixels in the sky can be much higher, leading to the clumpy image. We can then build up a picture of the gamma-ray sky by modeling individual spatial components which contribute in gamma rays, called "templates", and assign them either the non-Poissonian (clumpy) statistics, or Poisson (smooth) statistics. These templates are then all floated in a fit,

[3] More recently, studies have shown that the morphology may be more like the stellar bulge than NFW^2 [90–93]. Indeed, this would provide strong evidence against the dark matter explanation. However, this has been shown in some analyses to be dependent on modeling choices [90, 91], especially relating to the spatial tails of the excess, where the dark matter and bulge morphologies are most different, and the signal is over background is not large. Furthermore, given even the best current background models lead to very poor chi-squared values, it is not clear if systematic effects have yet been fully bracketed.

which aims to reveal if the preference is for the GCE to look more dark matter like (smooth), or point source like (clumpy) [98,99].

- Wavelets: This method uses a wavelet transform to look for peaks in the data, which could be attributed to point sources. A smooth GCE such as that from dark matter would not be expected to produce peaks. If enough peaks are found with cumulative intensity of the GCE, this would be evidence for the point source origin [100].

In 2015, evidence for clumpy rather than smooth GCE signals was independently found using both these techniques by independent groups [99,100]. This was a seemingly fatal blow to the dark matter interpretation, and had led to the community consensus that the GCE was instead likely due to point sources.

2019 Updates

2019 presented a *double* plot twist for these methods, with the interpretation of both the independent 2015 results challenged by two independent groups.

In Ref. [101], using the NPTF, it was shown that mismodeling of the templates can hide a dark matter signal. In a proof-of-principle scenario, where an unmodeled set of point sources were simulated alongside a dark matter signal, the dark matter signal was misidentified as a new population of GCE point sources. Most importantly, evidence of some mismodeling effect was found in the real data. When injecting a dark matter signal into the data, the dark matter signal was not recovered, and instead was misattributed to the GCE point source template in the fit. Perhaps worse, when allowing the dark matter template to take negative values, the fit preferred deeply negative flux values, which clearly is not physical. The degree in which the dark matter was driven negative varied with Galactic Galactic diffuse emission models, and so it appeared likely this behavior was driven by mismodeling of the poorly-understood Galactic diffuse emission model[4]. More broadly, this paper argued that given that systematics were clearly not under control, no robust evidence using the NPTF could be claimed for (or against) the point source interpretation of the data.

In Ref. [97], the interpretation of the wavelet method results were challenged. It was shown that when updating the wavelet analysis to mask out Fermi's new point source catalog (4FGL), the previously claimed evidence for point sources as the bulk of the excess disappears. That is, the 2015 wavelet result in Ref. [100] was correct in that it detected previously unknown point sources, but now such point sources are known to be mostly part of Fermi's 4FGL point source catalog, which cannot be the bulk of the excess. This is because masking the 4FGL catalog does not change the intensity of the excess, while stacking the spectra of non-excluded potential GCE sources reveals that the non-excluded sources do not produce enough flux to power the excess [97]. This points towards a *smooth* origin for the excess, rather than a bright point source origin. Any remaining point sources, if they exist, must be too faint to be seen, and being so faint, many more of them are required to produce enough flux to explain the excess. This places the number of point sources required in the several to tens of thousands, or potentially up to a few million sources depending on the cutoff on the low flux end of the luminosity function [97]. The upper ends of these estimates are certainly in strong tension with the maximum number of pulsars that could possibly exist in the inner galaxy. In future, better understanding of the total number of pulsars in the Milky Way may set a strong constraint on the potential luminosity function of a new population of pulsars needed to explain the excess.

2020 Updates

In Ref. [102], it was found that the failure of the injection test reported in Ref. [101] was indeed likely due to diffuse mismodeling. This is because simulating a dataset using a newer and improved

[4]Galactic diffuse gamma rays are the largest contribution to the gamma-ray sky, and arise from cosmic rays interacting with the gas and starlight in our Galaxy. Modeling for the diffuse gamma rays is not well understood, and is often the largest source of uncertainty in gamma ray searches.

Galactic diffuse emission model than those used previously, and fitting the data with the older Galactic diffuse emission models, could replicate the negative dark matter fluxes found when fitting the real data (in the scenario the known point sources are masked). In addition, a new way to improve the Galactic diffuse emission model was presented, by breaking the Galactic diffuse emission model into spherical harmonics and floating the pieces separately. In that case, in a 25 degree radius ROI (region of interest) in the sky with a ± 2 degree band mask, it was found that a GCE point source flux was found in all Galactic diffuse emission models. However, compared to the original NPTF paper [99], the point source evidence in this analysis with the new model is now decreased to only around $\sim 3\sigma$. This evidence drops even further for any other radius choice for the ROI other than the 25 degree radius ROI shown in Ref. [102].

Improving the Galactic diffuse emission model, as done in Ref. [102], is an important step forward, as this is currently the least well-understood component of the gamma-ray sky. Indeed, even the best models we currently have, including those used in Ref. [102], still lead to very poor fits to the data. This means there is already another systematic *we know* is present and that *we do not know* the impact of: what happens to the result once there is a correct Galactic diffuse emission model (one that actually matches the data to the level of Poisson noise). As such, it is not clear if systematic effects have yet been fully bracketed.

Indeed, the importance of unidentified systematics, and the implications for attempting to claim any evidence for point sources in the data, were further argued recently in Refs. [103, 104]. There, it was explicitly shown that mismodeling of a smooth signal, and a true point source signal, both lead to increased pixel-to-pixel variance in the data, and that the fit can mistake one for the other. This means that apparent evidence for a point source signal can be misinterpreted, when truly its origin may just be in mismodeling. This argument was mathematically demonstrated in Ref. [104]. Given we already know we are not modeling the gamma-ray sky perfectly, this is a serious concern for claimed evidence using the NPTF.

Strikingly, evidence of this effect has been found in analyses of real data. In a 10 degree ROI (the region where the GCE is brightest), it was shown that the apparent evidence for point sources using the real Fermi gamma-ray data can be instead be directly traced to manifestations of mismodeling, and lack of inclusion of important systematics [103, 104]. It was demonstrated, in the real data and this ROI, that simply allowing the GCE template to float freely in north and south pieces results in an asymmetric smooth excess, and makes the point source evidence disappear. This behavior was reproduced in simulations, which revealed using an overly restrictive model template created a spurious point source population. This has a source count function that is consistent with what is found in all existing NPTF GCE studies of real data, including Refs. [99,102]. Indeed, this is suggestive (but does not prove) that potentially all NPTF studies are finding a spurious point source population as a result of some kind of mismodeling. The asymmetry of the GCE found in Refs. [103,104] is likely a manifestation of *more* unknown systematics, likely transferred from mismodeling the Galactic diffuse emission model[5]. As such, the asymmetry is not argued to be an intrinsic feature of the excess itself. This is because the degree of asymmetry appears to depend on the Galactic diffuse emission model used and ROI. However, if it were shown to actually be the true distribution of the excess, it would strongly disfavor a dark matter interpretation (though it is also not clear how a population of point sources would exist with such a large asymmetry).

The original GCE NPTF study [99] noted that while unaccounted for systematics could potentially affect the reported results, the results appeared robust to the range of systematics tested. Refs. [101, 103, 104], on the other hand, identified large systematic effects which change the interpretation substantially, explicitly showing what can (and does) go wrong when systematics are missed. While improvements certainly could be made in future, given the impact of systematics at the moment, it does not appear that a dominantly smooth GCE (or point source GCE) is in tension with NPTF analyses. At this stage, we just don't know what the answer is!

[5]Note that the GCE smooth asymmetry appears using the latest Galactic diffuse emission model in Ref. [102], as well.

Finally settling the debate

Within the next decade, it should likely be possible to answer the question of the origin of the excess. Steps that can be taken include:

- New measurements with an MeV gamma-ray instrument could allow the low-energy part of the GCE energy spectrum to be measured more precisely. This is because the systematics using the Fermi telescope degrade drastically in the sub-GeV energy band. In this range, Fermi's PSF is a few degrees, while MeV-targeted instruments may allow for the sub-1 degree resolution. Measuring the low-energy part of the spectrum is important as this is where the DM and pulsar energy spectra predictions deviate most substantially.
- Discovery of more dwarf spheroidal galaxies, to increase sensitivity of Fermi to the dark matter annihilation cross section (see sub-section below).
- Observing the candidate pulsars directly in radio, if they exist (see radio waves section below).
- New measurements of the local dark matter density with Gaia. Currently, systematics on the dark matter density profile are a significant source of uncertainty, which when tightened will help corner the dark matter explanation.
- New and better Galactic diffuse emission models. This is key on the theory front, and is certainly the most significant barrier at the moment to obtaining accurate models of the sky. This can be achieved by better understanding cosmic ray propagation, or obtaining better dust maps with Planck. (The dust provides a tracer of the gas distribution.)

5.2.2 Dark Matter Annihilation Limits

Gamma rays from the center of the galaxy can also be used to set limits on dark matter annihilation.

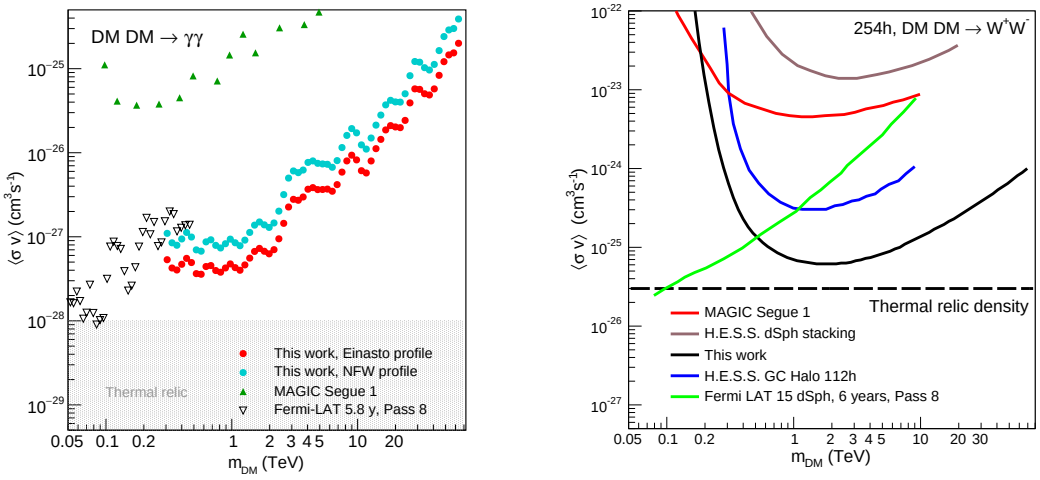

Figure 6: **Left:** Galactic center gamma-ray line limits from H.E.S.S. (with comparison shown to Fermi and MAGIC), figure taken from Ref. [105]. **Right:** Annihilation to WW limits from H.E.S.S., also with comparison with Fermi and MAGIC. Figure taken from Ref. [106], where other final state limits can also be found.

Figure 6 shows bounds on TeV dark matter annihilation in the inner galaxy, from both line searches (direct annihilation into gamma-ray pairs), as well as other various final states. The limits shown are from H.E.S.S. as per Ref [105] and Ref [106, 107], as these are the strongest bounds in the TeV region (though other experiments, Fermi, MAGIC, are compared in the figures). Note that while not shown in the figure, there are also Galactic halo bounds from HAWC [108]). For decay, see e.g. Refs. [85, 108] (and for leading gamma-ray limits on decay from other environments see e.g. Refs. [20, 109]).

In the GeV region, if a bulge morphology rather than dark matter is assumed for the GCE, strong limits can be set on the dark matter annihilation [93].

5.3 Dwarf Spheroidal Galaxies

The dark matter dense satellites of the Milky Way are called dwarf spheroidal galaxies. Having a high signal to background ratio, they are ideal targets for dark matter searches. They yield the strongest limits on dark matter annihilation to any final states which produce copious gamma rays, i.e. hadrons. In the GeV mass range, limits from Fermi are superior. While $\sim 2\sigma$ local excesses have been observed in some dwarfs [110], this is not globally significant at this time.

Figure 9 (middle) shows limits from Fermi observations of gamma rays from dwarf spheroidal galaxies, for various annihilation products. See Ref. [110] for the most recent official Fermi analysis.

More recently, the impact of systematics on dwarf results has been demonstrated to weaken bounds by almost an order of magnitude [111]. The largest source of uncertainty here is the dark matter density profiles, which are modeled based on N-body simulations. This leaves no tension at the moment with dark matter explanations of the GCE.

Moving forward, dwarf spheroidal galaxies are a leading target to corroborate a potential dark matter signal at the galactic center. The Dark Energy Survey (DES) and LSST are expected to locate more dwarf galaxies, which can increase potential sensitivity to the dark matter annihilation cross section by more than an order of magnitude [112]. This may lead to an exclusion, or a corroborated signal with the galactic center.

6 Dark Matter Searches with Micro and Radio Waves

6.1 Experiments and Prospects

Dark matter annihilation can lead to radio waves, by their charged annihilation products producing synchrotron emission as they pass through astrophysical magnetic fields (see e.g. Refs. [114, 115]).

Radio waves are also interesting because they can be used to search for dark matter impostors – pulsars. In terms of the GCE, pulsars potentially present in the galactic center may pulse into radio as well as gamma rays. If so, these could be detected by the upcoming observations of MeerKat or the SKA [113].

Figure 7 shows these prospects. On the left, selected radio and micro wave telescopes are shown, with their approximate frequency sensitivities and mission times. On the right, the prospects to find galactic center pulsars in radio are shown. In principle the GreenBank telescope may already be able to see some of these pulsars if they exist, however no studies have been reported so far.

Dark matter annihilation or decay can also lead to observables in microwaves. Of particular interest is the impact on the cosmic microwave background. Upon annihilating or decaying during the recombination era, charged annihilation products can inject ionizing energy which alters the ionization history of the Universe, and expected features of the CMB [2, 116]. This provides the strongest probe of dark matter annihilation to visible products below about 10 GeV, as shown in Fig. 9 (left). CMB measures of dark matter annihilation are not expected to drastically improve with future measurements, simply because we are cosmic variance limited (we only have one Universe to measure!). However, best improvements can be expected with the upcoming Simons Observatory.

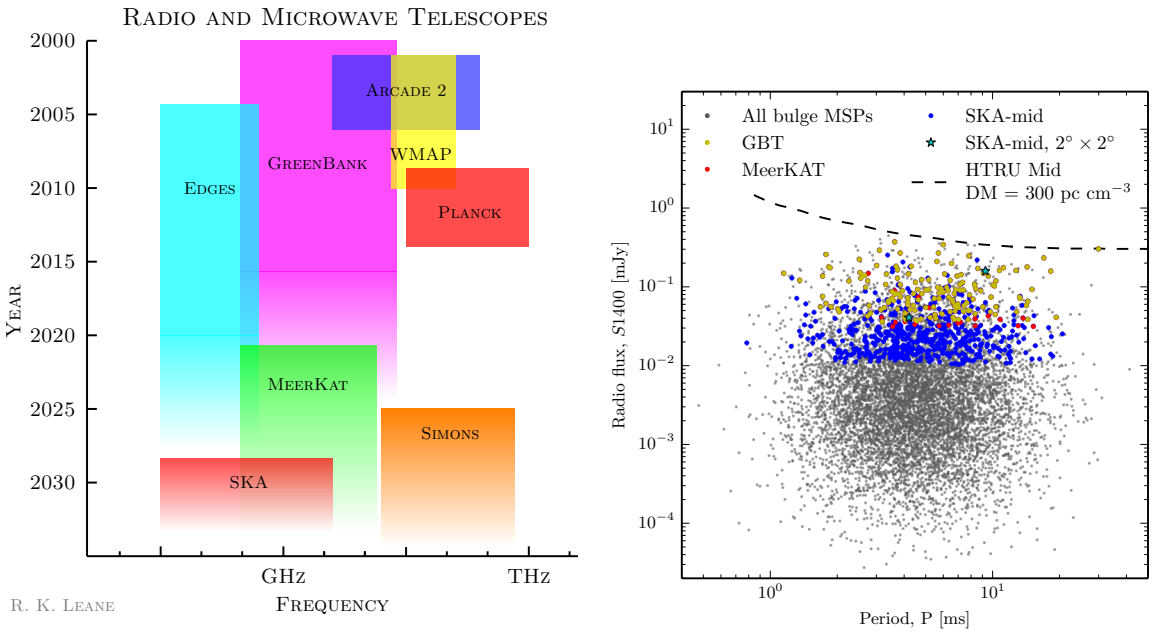

Figure 7: **Left:** Summary of selected micro and radiowave experiments by year operating, and approximate frequency sensitivity. **Right:** Discovery potential for GCE millisecond pulsars in radio. Right figure taken from Ref. [113].

7 Dark Matter Searches with Charged Cosmic Rays

7.1 Experiments and Prospects

For dark matter annihilation into leptonic final states, the best sensitivity is usually obtained by studying charged cosmic rays. One of the exciting aspects of cosmic-ray research is the extreme energies available to probe new physics, which far exceed anything ever made on Earth. We have high-energy cosmic-collider beams just waiting to be studied in new ways. A difficulty in this search is that cosmic ray propagation is not well understood and often induces substantial systematic uncertainties.

Figure 8 summarizes cosmic-ray experiments searching for dark matter interactions, as a function of their mission dates.

7.2 Positrons

An excess in $\sim 10 - 1000$ GeV positrons has been reported by PAMELA [117], AMS-02 [118, 119], and recently DAMPE [120]. If fitting to annihilating dark matter, it is consistent with a mass of $\sim$TeV. The annihilation cross section for this process, however, is $\sim 10^{-23}\text{cm}^3/\text{s}$, which is 3 orders of magnitude above that expected for a vanilla thermal dark matter relic. This excess sparked increased interest in Sommerfeld enhanced dark matter annihilation [121], where the rate of annihilation is much larger in the Universe today than it was at freeze out, due to enhancement from long-range forces. It also sparked interest in leptophilic dark matter models (see e.g. [122–125]), to order to produce the excess with a large branching fraction to leptons, and avoid other hadronic constraints.

This signal was presented also as likely coming from pulsars [126, 127], as they are expected to produce a comparable positron energy spectrum as that observed in the positron excess. An argument against this result was reported by the HAWC collaboration in 2017 [128], claiming that the excess could *not* be due to pulsars, as the diffusion coefficient observed near two of the closest pulsars to us,

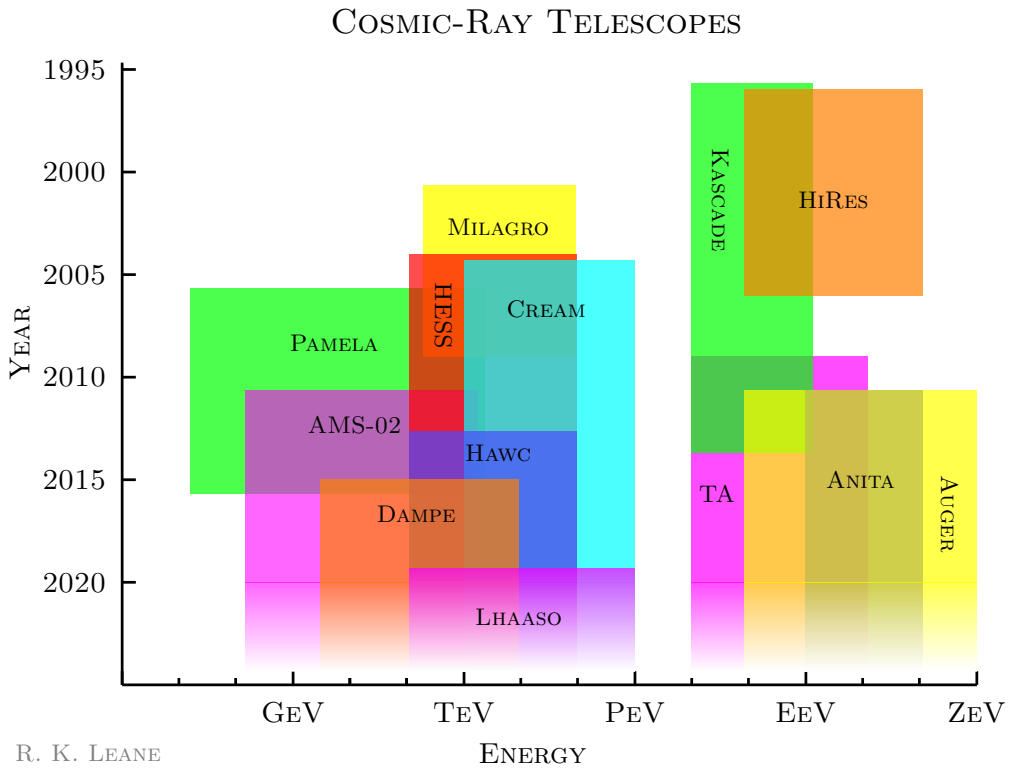

Figure 8: Summary of selected cosmic-ray experiments by year operating, and approximate energy sensitivity. Balloon/transient experiments (e.g. Cream and ANITA) which have discrete missions have been shown as continuous over the time the collaboration is still active.

Geminga and Monogem, appeared to be too low to allow their positrons to escape to reach us at Earth (in fact, it was measured to be about two orders of magnitude lower than expected elsewhere in the Galaxy). However, globally having such a low diffusion coefficient would mean that cosmic rays *in general* would struggle to reach us – and we know that cosmic rays do reach us on Earth, given that we have detected them! So, we know they mustn't be slowed forever by low diffusion. The conclusion to this saga is that the diffusion coefficient is not uniform throughout the Galaxy [129, 130], and they can reach us from these pulsars. Therefore, these pulsars remain the most likely explanation of the positron excess at this stage, rather than annihilating dark matter.

For limits on annihilating DM from positrons from AMS, see Fig. 9 (right).

7.3 Antiprotons

AMS-02 has reported an excess of antiprotons with energies $\sim 5 - 10$ GeV [131]. This can be well fit with an annihilating dark matter candidate of mass $\sim 50 - 100$ GeV [132, 133], particularly if it annihilates to hadronic final states. This excess becomes even more intriguing when noting it is consistent with a common origin with the GCE, as well as the thermal relic cross section, with intensity $\langle \sigma v \rangle \sim 10^{-26} \text{cm}^3/\text{s}$. Both excesses can be fit in a mass range of $50 - 70$ GeV assuming $2 \to 2$ s-wave annihilation to b-quarks [133, 134]. In the scenario dark matter exists in a hidden sector, there are a number of well motivated models that can fit both excesses, and have zero tension with collider, direct detection, dwarf or relic density constraints [135].

To understand the origin of this excess, it would be ideal if AMS would release their uncertainty

correlation matrices. As these are not public, educated guesses need to be made as to the correlated uncertainties between energy bins. One group has argued that the significance of the signal ranges from $3.3 - 7.7\sigma$ depending on cosmic-ray propagation values [133], while another argues it is $\sim 3 - 5.5\sigma$ [132]. On the other hand, it has been shown that this excess might just be consistent with cosmic-ray secondaries (i.e. not dark matter) [136, 137]. Indeed, while all these antiproton studies do consider the sets of systematics, Refs. [136, 137] argue that they should be significantly larger than previously estimated, which is what reduces their calculated significance of the excess. Moving forward, better understanding cosmic-ray propagation will be key to interpret signals as they arise.

For antiproton constraints on dark matter annihilation, see e.g. Refs. [138–140].

8 Outlook

After all this, we can ask, what is the status of indirect dark matter searches?

Figure 9 summarizes the strongest and most robust bounds for GeV dark matter annihilating into various final states; Fermi observations of dwarf spheroidal galaxies provide the strongest bounds on annihilation to hadronic final states, AMS-02 positron fluxes restrict most annihilation to leptons, and the CMB limits are strongest for low dark matter masses.

Figure 10 shows what the limit looks like if we combine *all* this complementary information for each type of visible final state. If one experiment constrains annihilation into a particular final state, the remaining energy at a given mass must go into a different final state, which can be ruled out by a complementary experiment. If no final states can proceed without exclusion, that particular mass is considered ruled out. This plot shows how much progress we have really made in probing the thermal WIMP. It looks like not much so far – just up to 20 GeV! The window up to the unitarity limit of $\sim$100 TeV [141, 142] remains largely open. This window can only be closed by indirect detection experiments, which directly probe the annihilation rate. This motivates many interesting searches and improvements for years to come.

Indeed, indirect detection searches for dark matter are exciting now more than ever. We are exploring unprecedented parameter space, and have a number of persistent hints which could potentially turn out to be dark matter signals.

In the center of our galaxy, the excess of GeV gamma rays reported by Fermi-LAT might be dark matter. The leading alternate explanation is millisecond pulsars. In terms of the non-Poissonian template fitting analyses, as systematics have been shown to not be fully controlled, evidence does not clearly support a smooth nor point source origin at this stage. Recent wavelet analyses have shown that the previous apparent point source detection cannot make up the bulk of the GCE. Dwarf limits have, also due to systematics, recently been shown to be potentially weaker than expected, leaving open the masses and annihilation cross sections that could explain the GCE. Measurements of the excess morphology are actively improving, as recent studies have shown that the morphology may be more like the stellar bulge than a dark matter profile, which would support the non-dark matter interpretation. However, given all models are currently poor fits to the gamma-ray data, it is difficult to know if systematics are truly bracketing all the uncertainties they should be. This will certainly remain an interesting open problem for the next few years, and has many observational prospects on the horizon to help settle the debate.

Antiprotons are observed in excess at AMS-02, and while it is consistent with a dark matter origin (and consistent with the GCE), there are also arguments that it is consistent with cosmic-ray secondaries. Systematic correlation matrices, and better cosmic-ray propagation models, are needed here to definitively confirm or exclude explanations of this excess.

Positrons exist in excess, as observed by PAMELA, AMS-02, and DAMPE. This signal is consistent with a $\sim$TeV dark matter candidate. However, the current consensus is that this is likely due to pulsars, due to nearby known pulsars Geminga and Monogem presenting a comparable positron energy spectrum. Regardless, debate over this signal has led to very interesting developments in

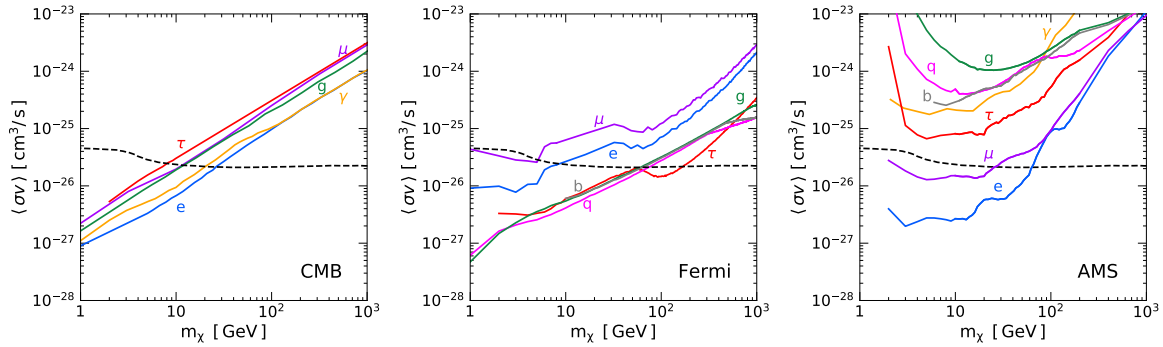

Figure 9: Conservative limits on s-wave $2 \to 2$ GeV dark matter annihilation to various final status as labeled. **Left:** Limits from the CMB. **Middle:** Limits arising from Fermi measurements of gamma rays from dwarf spheriodal galaxies. **Right:** Limits from positron flux measurements with AMS. Relic cross section is the dashed line [143]. Figures taken from Ref. [144].

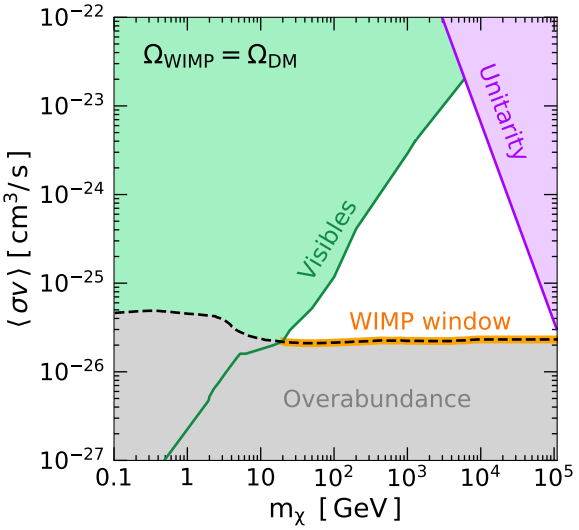

Figure 10: Combined lower limit on the dark matter cross section, for $2 \to 2$ s-wave annihilation to visible final states. Dashed line is thermal relic cross section. Figure taken from Ref. [144].

understanding cosmic-ray propagation. In particular, that the diffusion coefficient is not uniform throughout the Galaxy.

Lastly, the 3.5 keV X-ray line remains the subject of lively debate, as it might be evidence of the decay of a ∼7 keV sterile neutrino dark matter candidate. There are arguments it is ruled out from blank-sky observations, and counter-arguments that it is not, due to particular systematics and modeling issues. Upcoming observations with new X-ray telescopes should answer the question once and for all.

The interplay of all these observations, and corroboration of potential dark matter signals as they arise, will be crucial to understand the nature of dark matter in the years to come.

Acknowledgments

I thank the organizers of the EDSU conference for the invitation and an excellent semi-virtual conference, and John Beacom and Tracy Slatyer for comments on the manuscript. I acknowledge support from the Office of High Energy Physics of the U.S. Department of Energy under Grant No. DE-SC00012567 and DE-SC0013999, as well as the NASA Fermi Guest Investigator Program under Grant No. 80NSSC19K1515.

References

[1] E. Amato and P. Blasi, *Cosmic ray transport in the Galaxy: A review*, *Adv. Space Res.* **62** (2018) 2731–2749, [arXiv:1704.05696].

[2] T. R. Slatyer, *Indirect dark matter signatures in the cosmic dark ages. I. Generalizing the bound on s-wave dark matter annihilation from Planck results*, *Phys. Rev. D* **93** (2016), no. 2 023527, [arXiv:1506.03811].

[3] L. Bergstrom, P. Ullio, and J. H. Buckley, *Observability of gamma-rays from dark matter neutralino annihilations in the Milky Way halo*, *Astropart. Phys.* **9** (1998) 137–162, [astro-ph/9712318].

[4] A. Geringer-Sameth, S. M. Koushiappas, and M. Walker, *Dwarf galaxy annihilation and decay emission profiles for dark matter experiments*, *Astrophys. J.* **801** (2015), no. 2 74, [arXiv:1408.0002].

[5] **KM3NeT** Collaboration, S. Navas, *Dark Matter Searches from the Sun with the KM3NeT-ORCA detector*, *PoS* **ICRC2019** (2020) 536.

[6] **KM3NeT and Antares** Collaboration, S. R. Gozzini and J. de Dios Zornoza Gómez, *Search for dark matter with the ANTARES and KM3NeT neutrino telescopes*, *PoS* **ICRC2019** (2020) 552.

[7] **IceCube** Collaboration, S. In and K. Wiebe, *Latest results and sensitivities for solar dark matter searches with IceCube*, *PoS* **ICRC2017** (2018) 912.

[8] **Hyper-Kamiokande** Collaboration, K. Abe et al., *Hyper-Kamiokande Design Report*, arXiv:1805.04163.

[9] C. A. Argüelles, A. Diaz, A. Kheirandish, A. Olivares-Del-Campo, I. Safa, and A. C. Vincent, *Dark Matter Annihilation to Neutrinos: An Updated, Consistent & Compelling Compendium of Constraints*, arXiv:1912.09486.

[10] N. F. Bell, M. J. Dolan, and S. Robles, *Searching for Sub-GeV Dark Matter in the Galactic Centre using Hyper-Kamiokande*, arXiv:2005.01950.

[11] **Borexino** Collaboration, G. Bellini et al., *Study of solar and other unknown anti-neutrino fluxes with Borexino at LNGS*, *Phys. Lett. B* **696** (2011) 191–196, [arXiv:1010.0029].

[12] **KamLAND** Collaboration, A. Gando et al., *A study of extraterrestrial antineutrino sources with the KamLAND detector*, *Astrophys. J.* **745** (2012) 193, [arXiv:1105.3516].

[13] **DUNE** Collaboration, R. Acciarri et al., *Long-Baseline Neutrino Facility (LBNF) and Deep Underground Neutrino Experiment (DUNE): Conceptual Design Report, Volume 2: The Physics Program for DUNE at LBNF*, arXiv:1512.06148.

[14] F. Capozzi, S. W. Li, G. Zhu, and J. F. Beacom, *DUNE as the Next-Generation Solar Neutrino Experiment*, *Phys. Rev. Lett.* **123** (2019), no. 13 131803, [arXiv:1808.08232].

[15] J. F. Beacom, N. F. Bell, and G. D. Mack, *General Upper Bound on the Dark Matter Total Annihilation Cross Section*, *Phys. Rev. Lett.* **99** (2007) 231301, [astro-ph/0608090].

[16] H. Yuksel, S. Horiuchi, J. F. Beacom, and S. Ando, *Neutrino Constraints on the Dark Matter Total Annihilation Cross Section*, *Phys. Rev. D* **76** (2007) 123506, [arXiv:0707.0196].

[17] **IceCube** Collaboration, M. Aartsen et al., *Evidence for High-Energy Extraterrestrial Neutrinos at the IceCube Detector*, *Science* **342** (2013) 1242856, [arXiv:1311.5238].

[18] A. Esmaili and P. D. Serpico, *Are IceCube neutrinos unveiling PeV-scale decaying dark matter?*, *JCAP* **11** (2013) 054, [arXiv:1308.1105].

[19] B. Feldstein, A. Kusenko, S. Matsumoto, and T. T. Yanagida, *Neutrinos at IceCube from Heavy Decaying Dark Matter*, *Phys. Rev. D* **88** (2013), no. 1 015004, [arXiv:1303.7320].

[20] T. Cohen, K. Murase, N. L. Rodd, B. R. Safdi, and Y. Soreq, *γ -ray Constraints on Decaying Dark Matter and Implications for IceCube*, *Phys. Rev. Lett.* **119** (2017), no. 2 021102, [arXiv:1612.05638].

[21] M. Chianese, D. F. Fiorillo, G. Miele, S. Morisi, and O. Pisanti, *Decaying dark matter at IceCube and its signature on High Energy gamma experiments*, *JCAP* **11** (2019) [arXiv:1907.11222].

[22] R. K. Leane, K. C. Y. Ng, and J. F. Beacom, *Powerful Solar Signatures of Long-Lived Dark Mediators*, *Phys. Rev. D* **95** (2017), no. 12 123016, [arXiv:1703.04629].

[23] W. H. Press and D. N. Spergel, *Capture by the sun of a galactic population of weakly interacting massive particles*, *Astrophys. J.* **296** (1985) 679–684.

[24] L. M. Krauss, K. Freese, W. Press, and D. Spergel, *Cold dark matter candidates and the solar neutrino problem*, *Astrophys. J.* **299** (1985) 1001.

[25] J. Silk, K. Olive, and M. Srednicki, *The photino, the sun, and high-energy neutrinos*, *Phys. Rev. Lett.* **55** (Jul, 1985) 257–259.

[26] A. H. Peter, *Dark matter in the solar system II: WIMP annihilation rates in the Sun*, *Phys. Rev. D* **79** (2009) 103532, [arXiv:0902.1347].

[27] P. Meade, S. Nussinov, M. Papucci, and T. Volansky, *Searches for Long Lived Neutral Particles*, *JHEP* **06** (2010) 029, [arXiv:0910.4160].

[28] N. F. Bell and K. Petraki, *Enhanced neutrino signals from dark matter annihilation in the Sun via metastable mediators*, *JCAP* **04** (2011) 003, [arXiv:1102.2958].

[29] B. Batell, M. Pospelov, A. Ritz, and Y. Shang, *Solar Gamma Rays Powered by Secluded Dark Matter*, *Phys. Rev. D* **81** (2010) 075004, [arXiv:0910.1567].

[30] P. Schuster, N. Toro, and I. Yavin, *Terrestrial and Solar Limits on Long-Lived Particles in a Dark Sector*, *Phys. Rev. D* **81** (2010) 016002, [arXiv:0910.1602].

[31] P. Schuster, N. Toro, N. Weiner, and I. Yavin, *High Energy Electron Signals from Dark Matter Annihilation in the Sun*, *Phys. Rev. D* **82** (2010) 115012, [arXiv:0910.1839].

[32] J. L. Feng, J. Smolinsky, and P. Tanedo, *Dark Photons from the Center of the Earth: Smoking-Gun Signals of Dark Matter*, *Phys. Rev. D* **93** (2016), no. 1 015014, [arXiv:1509.07525]. [Erratum: Phys.Rev.D 96, 099901 (2017)].

[33] J. L. Feng, J. Smolinsky, and P. Tanedo, *Detecting dark matter through dark photons from the Sun: Charged particle signatures*, *Phys. Rev. D* **93** (2016), no. 11 115036, [arXiv:1602.01465]. [Erratum: Phys.Rev.D 96, 099903 (2017)].

[34] M. Nisa, J. Beacom, S. BenZvi, R. Leane, T. Linden, K. Ng, A. Peter, and B. Zhou, *The Sun at GeV–TeV Energies: A New Laboratory for Astroparticle Physics*, arXiv:1903.06349.

[35] **HAWC** Collaboration, A. Albert et al., *First HAWC Observations of the Sun Constrain Steady TeV Gamma-Ray Emission*, *Phys. Rev. D* **98** (2018), no. 12 123011, [arXiv:1808.05620].

[36] **HAWC** Collaboration, A. Albert et al., *Constraints on Spin-Dependent Dark Matter Scattering with Long-Lived Mediators from TeV Observations of the Sun with HAWC*, *Phys. Rev. D* **98** (2018) 123012, [arXiv:1808.05624].

[37] C. Niblaeus, A. Beniwal, and J. Edsjo, *Neutrinos and gamma rays from long-lived mediator decays in the Sun*, *JCAP* **11** (2019) 011, [arXiv:1903.11363].

[38] I. Goldman and S. Nussinov, *Weakly Interacting Massive Particles and Neutron Stars*, *Phys. Rev. D* **40** (1989) 3221–3230.

[39] A. Gould, B. T. Draine, R. W. Romani, and S. Nussinov, *Neutron Stars: Graveyard of Charged Dark Matter*, *Phys. Lett. B* **238** (1990) 337–343.

[40] C. Kouvaris, *WIMP Annihilation and Cooling of Neutron Stars*, *Phys. Rev. D* **77** (2008) 023006, [arXiv:0708.2362].

[41] G. Bertone and M. Fairbairn, *Compact Stars as Dark Matter Probes*, *Phys. Rev. D* **77** (2008) 043515, [arXiv:0709.1485].

[42] A. de Lavallaz and M. Fairbairn, *Neutron Stars as Dark Matter Probes*, *Phys. Rev. D* **81** (2010) 123521, [arXiv:1004.0629].

[43] C. Kouvaris and P. Tinyakov, *Can Neutron stars constrain Dark Matter?*, *Phys. Rev. D* **82** (2010) 063531, [arXiv:1004.0586].

[44] S. D. McDermott, H.-B. Yu, and K. M. Zurek, *Constraints on Scalar Asymmetric Dark Matter from Black Hole Formation in Neutron Stars*, *Phys. Rev.* **D85** (2012) 023519, [arXiv:1103.5472].

[45] C. Kouvaris and P. Tinyakov, *Excluding Light Asymmetric Bosonic Dark Matter*, *Phys. Rev. Lett.* **107** (2011) 091301, [arXiv:1104.0382].

[46] T. Guver, A. E. Erkoca, M. Hall Reno, and I. Sarcevic, *On the capture of dark matter by neutron stars*, *JCAP* **1405** (2014) 013, [arXiv:1201.2400].

[47] J. Bramante, K. Fukushima, and J. Kumar, *Constraints on bosonic dark matter from observation of old neutron stars*, *Phys. Rev.* **D87** (2013), no. 5 055012, [arXiv:1301.0036].

[48] N. F. Bell, A. Melatos, and K. Petraki, *Realistic neutron star constraints on bosonic asymmetric dark matter*, *Phys. Rev.* **D87** (2013), no. 12 123507, [arXiv:1301.6811].

[49] J. Bramante, K. Fukushima, J. Kumar, and E. Stopnitzky, *Bounds on self-interacting fermion dark matter from observations of old neutron stars*, *Phys. Rev.* **D89** (2014), no. 1 015010, [arXiv:1310.3509].

[50] B. Bertoni, A. E. Nelson, and S. Reddy, *Dark Matter Thermalization in Neutron Stars*, *Phys. Rev. D* **88** (2013) 123505, [arXiv:1309.1721].

[51] C. Kouvaris and P. Tinyakov, *Constraining Asymmetric Dark Matter through observations of compact stars*, *Phys. Rev.* **D83** (2011) 083512, [arXiv:1012.2039].

[52] M. McCullough and M. Fairbairn, *Capture of Inelastic Dark Matter in White Dwarves*, *Phys. Rev.* **D81** (2010) 083520, [arXiv:1001.2737].

[53] M. Angeles Perez-Garcia and J. Silk, *Constraining decaying dark matter with neutron stars*, *Phys. Lett.* **B744** (2015) 13–17, [arXiv:1403.6111].

[54] J. Bramante, *Dark matter ignition of type Ia supernovae*, *Phys. Rev. Lett.* **115** (2015), no. 14 141301, [arXiv:1505.07464].

[55] P. W. Graham, S. Rajendran, and J. Varela, *Dark Matter Triggers of Supernovae*, *Phys. Rev.* **D92** (2015), no. 6 063007, [arXiv:1505.04444].

[56] M. Cermeno, M. Perez-Garcia, and J. Silk, *Light dark matter scattering in outer neutron star crusts*, *Phys. Rev.* **D94** (2016), no. 6 063001, [arXiv:1607.06815].

[57] P. W. Graham, R. Janish, V. Narayan, S. Rajendran, and P. Riggins, *White Dwarfs as Dark Matter Detectors*, *Phys. Rev.* **D98** (2018), no. 11 115027, [arXiv:1805.07381].

[58] J. F. Acevedo and J. Bramante, *Supernovae Sparked By Dark Matter in White Dwarfs*, *Phys. Rev.* **D100** (2019), no. 4 043020, [arXiv:1904.11993].

[59] R. Janish, V. Narayan, and P. Riggins, *Type Ia supernovae from dark matter core collapse*, *Phys. Rev.* **D100** (2019), no. 3 035008, [arXiv:1905.00395].

[60] R. Krall and M. Reece, *Last Electroweak WIMP Standing: Pseudo-Dirac Higgsino Status and Compact Stars as Future Probes*, *Chin. Phys.* **C42** (2018), no. 4 043105, [arXiv:1705.04843].

[61] D. McKeen, A. E. Nelson, S. Reddy, and D. Zhou, *Neutron stars exclude light dark baryons*, *Phys. Rev. Lett.* **121** (2018), no. 6 061802, [arXiv:1802.08244].

[62] M. Baryakhtar, J. Bramante, S. W. Li, T. Linden, and N. Raj, *Dark Kinetic Heating of Neutron Stars and An Infrared Window On WIMPs, SIMPs, and Pure Higgsinos*, *Phys. Rev. Lett.* **119** (2017), no. 13 131801, [arXiv:1704.01577].

[63] N. Raj, P. Tanedo, and H.-B. Yu, *Neutron stars at the dark matter direct detection frontier*, *Phys. Rev.* **D97** (2018), no. 4 043006, [arXiv:1707.09442].

[64] N. F. Bell, G. Busoni, and S. Robles, *Heating up Neutron Stars with Inelastic Dark Matter*, *JCAP* **1809** (2018), no. 09 018, [arXiv:1807.02840].

[65] R. Garani, Y. Genolini, and T. Hambye, *New Analysis of Neutron Star Constraints on Asymmetric Dark Matter*, *JCAP* **1905** (2019), no. 05 035, [arXiv:1812.08773].

[66] C.-S. Chen and Y.-H. Lin, *Reheating neutron stars with the annihilation of self-interacting dark matter*, *JHEP* **08** (2018) 069, [arXiv:1804.03409].

[67] K. Hamaguchi, N. Nagata, and K. Yanagi, *Dark Matter Heating vs. Rotochemical Heating in Old Neutron Stars*, *Phys. Lett.* **B795** (2019) 484–489, [arXiv:1905.02991].

[68] D. A. Camargo, F. S. Queiroz, and R. Sturani, *Detecting Dark Matter with Neutron Star Spectroscopy*, *JCAP* **1909** (2019), no. 09 051, [arXiv:1901.05474].

[69] N. F. Bell, G. Busoni, and S. Robles, *Capture of Leptophilic Dark Matter in Neutron Stars*, *JCAP* **1906** (2019), no. 06 054, [arXiv:1904.09803].

[70] J. F. Acevedo, J. Bramante, R. K. Leane, and N. Raj, *Warming Nuclear Pasta with Dark Matter: Kinetic and Annihilation Heating of Neutron Star Crusts*, *JCAP* **03** (2020) 038, [arXiv:1911.06334].

[71] R. Garani and J. Heeck, *Dark matter interactions with muons in neutron stars*, *Phys. Rev.* **D100** (2019), no. 3 035039, [arXiv:1906.10145].

[72] A. Joglekar, N. Raj, P. Tanedo, and H.-B. Yu, *Relativistic capture of dark matter by electrons in neutron stars*, arXiv:1911.13293.

[73] A. Joglekar, N. Raj, P. Tanedo, and H.-B. Yu, *Kinetic Heating from Contact Interactions with Relativistic Targets: Electrons Capture Dark Matter in Neutron Stars*, arXiv:2004.09539.

[74] E. Bulbul, M. Markevitch, A. Foster, R. K. Smith, M. Loewenstein, and S. W. Randall, *Detection of An Unidentified Emission Line in the Stacked X-ray spectrum of Galaxy Clusters*, *Astrophys. J.* **789** (2014) 13, [arXiv:1402.2301].

[75] A. Boyarsky, O. Ruchayskiy, D. Iakubovskyi, and J. Franse, *Unidentified Line in X-Ray Spectra of the Andromeda Galaxy and Perseus Galaxy Cluster*, *Phys. Rev. Lett.* **113** (2014) 251301, [arXiv:1402.4119].

[76] K. N. Abazajian, *Sterile neutrinos in cosmology*, *Phys. Rept.* **711-712** (2017) 1–28, [arXiv:1705.01837].

[77] B. M. Roach, K. C. Ng, K. Perez, J. F. Beacom, S. Horiuchi, R. Krivonos, and D. R. Wik, *NuSTAR Tests of Sterile-Neutrino Dark Matter: New Galactic Bulge Observations and Combined Impact*, arXiv:1908.09037.

[78] C. Dessert, N. L. Rodd, and B. R. Safdi, *The dark matter interpretation of the 3.5-keV line is inconsistent with blank-sky observations*, *Science* **367** (2020) 1465, [arXiv:1812.06976].

[79] K. Perez, K. C. Y. Ng, J. F. Beacom, C. Hersh, S. Horiuchi, and R. Krivonos, *Almost closing the νMSM sterile neutrino dark matter window with NuSTAR*, *Phys. Rev. D* **95** (2017), no. 12 123002, [arXiv:1609.00667].

[80] K. C. Ng, B. M. Roach, K. Perez, J. F. Beacom, S. Horiuchi, R. Krivonos, and D. R. Wik, *New Constraints on Sterile Neutrino Dark Matter from $NuSTAR$ M31 Observations*, *Phys. Rev. D* **99** (2019) 083005, [arXiv:1901.01262].

[81] A. Boyarsky, D. Iakubovskyi, O. Ruchayskiy, and D. Savchenko, *Surface brightness profile of the 3.5 keV line in the Milky Way halo*, arXiv:1812.10488.

[82] A. Boyarsky, D. Malyshev, O. Ruchayskiy, and D. Savchenko, *Technical comment on the paper of Dessert et al. "The dark matter interpretation of the 3.5 keV line is inconsistent with blank-sky observations"*, arXiv:2004.06601.

[83] K. N. Abazajian, *Technical Comment on "The dark matter interpretation of the 3.5-keV line is inconsistent with blank-sky observations"*, arXiv:2004.06170.

[84] A. Boyarsky, M. Drewes, T. Lasserre, S. Mertens, and O. Ruchayskiy, *Sterile Neutrino Dark Matter*, *Prog. Part. Nucl. Phys.* **104** (2019) 1–45, [arXiv:1807.07938].

[85] M. Pierre, J. M. Siegal-Gaskins, and P. Scott, *Sensitivity of CTA to dark matter signals from the Galactic Center*, *JCAP* **06** (2014) 024, [arXiv:1401.7330]. [Erratum: JCAP 10, E01 (2014)].

[86] H. Silverwood, C. Weniger, P. Scott, and G. Bertone, *A realistic assessment of the CTA sensitivity to dark matter annihilation*, *JCAP* **03** (2015) 055, [arXiv:1408.4131].

[87] L. Goodenough and D. Hooper, *Possible Evidence For Dark Matter Annihilation In The Inner Milky Way From The Fermi Gamma Ray Space Telescope*, arXiv:0910.2998.

[88] T. Daylan, D. P. Finkbeiner, D. Hooper, T. Linden, S. K. N. Portillo, N. L. Rodd, and T. R. Slatyer, *The characterization of the gamma-ray signal from the central Milky Way: A case for annihilating dark matter*, *Phys. Dark Univ.* **12** (2016) 1–23, [arXiv:1402.6703].

[89] F. Calore, I. Cholis, and C. Weniger, *Background Model Systematics for the Fermi GeV Excess*, *JCAP* **03** (2015) 038, [arXiv:1409.0042].

[90] O. Macias, C. Gordon, R. M. Crocker, B. Coleman, D. Paterson, S. Horiuchi, and M. Pohl, *Galactic bulge preferred over dark matter for the Galactic centre gamma-ray excess*, *Nat. Astron.* **2** (2018), no. 5 387–392, [arXiv:1611.06644].

[91] R. Bartels, E. Storm, C. Weniger, and F. Calore, *The Fermi-LAT GeV excess as a tracer of stellar mass in the Galactic bulge*, *Nat. Astron.* **2** (2018), no. 10 819–828, [arXiv:1711.04778].

[92] O. Macias, S. Horiuchi, M. Kaplinghat, C. Gordon, R. M. Crocker, and D. M. Nataf, *Strong Evidence that the Galactic Bulge is Shining in Gamma Rays*, *JCAP* **09** (2019) 042, [arXiv:1901.03822].

[93] K. N. Abazajian, S. Horiuchi, M. Kaplinghat, R. E. Keeley, and O. Macias, *Strong constraints on thermal relic dark matter from Fermi-LAT observations of the Galactic Center*, arXiv:2003.10416.

[94] I. Cholis, D. Hooper, and T. Linden, *A New Determination of the Spectra and Luminosity Function of Gamma-Ray Millisecond Pulsars*, arXiv:1407.5583.

[95] I. Cholis, D. Hooper, and T. Linden, *Challenges in Explaining the Galactic Center Gamma-Ray Excess with Millisecond Pulsars*, *JCAP* **06** (2015) 043, [arXiv:1407.5625].

[96] D. Haggard, C. Heinke, D. Hooper, and T. Linden, *Low Mass X-Ray Binaries in the Inner Galaxy: Implications for Millisecond Pulsars and the GeV Excess*, *JCAP* **05** (2017) 056, [arXiv:1701.02726].

[97] Y.-M. Zhong, S. D. McDermott, I. Cholis, and P. J. Fox, *A New Mask for An Old Suspect: Testing the Sensitivity of the Galactic Center Excess to the Point Source Mask*, arXiv:1911.12369.

[98] S. K. Lee, M. Lisanti, and B. R. Safdi, *Distinguishing Dark Matter from Unresolved Point Sources in the Inner Galaxy with Photon Statistics*, *JCAP* **05** (2015) 056, [arXiv:1412.6099].

[99] S. K. Lee, M. Lisanti, B. R. Safdi, T. R. Slatyer, and W. Xue, *Evidence for Unresolved γ-Ray Point Sources in the Inner Galaxy*, *Phys. Rev. Lett.* **116** (2016), no. 5 051103, [arXiv:1506.05124].

[100] R. Bartels, S. Krishnamurthy, and C. Weniger, *Strong support for the millisecond pulsar origin of the Galactic center GeV excess*, *Phys. Rev. Lett.* **116** (2016), no. 5 051102, [arXiv:1506.05104].

[101] R. K. Leane and T. R. Slatyer, *Revival of the Dark Matter Hypothesis for the Galactic Center Gamma-Ray Excess*, *Phys. Rev. Lett.* **123** (2019), no. 24 241101, [arXiv:1904.08430].

[102] M. Buschmann, N. L. Rodd, B. R. Safdi, L. J. Chang, S. Mishra-Sharma, M. Lisanti, and O. Macias, *Foreground Mismodeling and the Point Source Explanation of the Fermi Galactic Center Excess*, arXiv:2002.12373.

[103] R. K. Leane and T. R. Slatyer, *Spurious Point Source Signals in the Galactic Center Excess*, arXiv:2002.12370.

[104] R. K. Leane and T. R. Slatyer, *The Enigmatic Galactic Center Excess: Spurious Point Sources and Signal Mismodeling*, arXiv:2002.12371.

[105] **HESS** Collaboration, H. Abdallah et al., *Search for γ-Ray Line Signals from Dark Matter Annihilations in the Inner Galactic Halo from 10 Years of Observations with H.E.S.S.*, *Phys. Rev. Lett.* **120** (2018), no. 20 201101, [arXiv:1805.05741].

[106] **H.E.S.S.** Collaboration, V. Lefranc and E. Moulin, *Dark matter search in the inner galactic center halo with H.E.S.S*, in *51st Rencontres de Moriond on Cosmology*, pp. 149–152, 8, 2016. arXiv:1608.08453.

[107] **H.E.S.S.** Collaboration, A. Abramowski et al., *Search for a Dark Matter annihilation signal from the Galactic Center halo with H.E.S.S*, *Phys. Rev. Lett.* **106** (2011) 161301, [arXiv:1103.3266].

[108] **HAWC** Collaboration, A. Abeysekara et al., *A Search for Dark Matter in the Galactic Halo with HAWC*, *JCAP* **02** (2018) 049, [arXiv:1710.10288].

[109] R. Essig, E. Kuflik, S. D. McDermott, T. Volansky, and K. M. Zurek, *Constraining Light Dark Matter with Diffuse X-Ray and Gamma-Ray Observations*, *JHEP* **11** (2013) 193, [arXiv:1309.4091].

[110] **Fermi-LAT, DES** Collaboration, A. Albert et al., *Searching for Dark Matter Annihilation in Recently Discovered Milky Way Satellites with Fermi-LAT*, *Astrophys. J.* **834** (2017), no. 2 110, [arXiv:1611.03184].

[111] S. Ando, A. Geringer-Sameth, N. Hiroshima, S. Hoof, R. Trotta, and M. G. Walker, *Structure Formation Models Weaken Limits on WIMP Dark Matter from Dwarf Spheroidal Galaxies*, arXiv:2002.11956.

[112] **Fermi-LAT** Collaboration, E. Charles et al., *Sensitivity Projections for Dark Matter Searches with the Fermi Large Area Telescope*, *Phys. Rept.* **636** (2016) 1–46, [arXiv:1605.02016].

[113] F. Calore, M. Di Mauro, F. Donato, J. W. T. Hessels, and C. Weniger, *Radio detection prospects for a bulge population of millisecond pulsars as suggested by Fermi LAT observations of the inner Galaxy*, *Astrophys. J.* **827** (2016), no. 2 143, [arXiv:1512.06825].

[114] S. Colafrancesco, S. Profumo, and P. Ullio, *Multi-frequency analysis of neutralino dark matter annihilations in the Coma cluster*, *Astron. Astrophys.* **455** (2006) 21, [astro-ph/0507575].

[115] N. Fornengo, R. Lineros, M. Regis, and M. Taoso, *Cosmological Radio Emission induced by WIMP Dark Matter*, *JCAP* **03** (2012) 033, [arXiv:1112.4517].

[116] T. R. Slatyer, N. Padmanabhan, and D. P. Finkbeiner, *CMB Constraints on WIMP Annihilation: Energy Absorption During the Recombination Epoch*, *Phys. Rev. D* **80** (2009) 043526, [arXiv:0906.1197].

[117] **PAMELA** Collaboration, O. Adriani et al., *An anomalous positron abundance in cosmic rays with energies 1.5-100 GeV*, *Nature* **458** (2009) 607–609, [arXiv:0810.4995].

[118] **AMS** Collaboration, M. Aguilar et al., *First Result from the Alpha Magnetic Spectrometer on the International Space Station: Precision Measurement of the Positron Fraction in Primary Cosmic Rays of 0.5–350 GeV*, *Phys. Rev. Lett.* **110** (2013) 141102.

[119] **AMS** Collaboration, L. Accardo et al., *High Statistics Measurement of the Positron Fraction in Primary Cosmic Rays of 0.5–500 GeV with the Alpha Magnetic Spectrometer on the International Space Station*, *Phys. Rev. Lett.* **113** (2014) 121101.

[120] **DAMPE** Collaboration, G. Ambrosi et al., *Direct detection of a break in the teraelectronvolt cosmic-ray spectrum of electrons and positrons*, *Nature* **552** (2017) 63–66, [arXiv:1711.10981].

[121] N. Arkani-Hamed, D. P. Finkbeiner, T. R. Slatyer, and N. Weiner, *A Theory of Dark Matter*, *Phys. Rev. D* **79** (2009) 015014, [arXiv:0810.0713].

[122] P. J. Fox and E. Poppitz, *Leptophilic Dark Matter*, *Phys. Rev. D* **79** (2009) 083528, [arXiv:0811.0399].

[123] J. Kopp, V. Niro, T. Schwetz, and J. Zupan, *DAMA/LIBRA and leptonically interacting Dark Matter*, *Phys. Rev. D* **80** (2009) 083502, [arXiv:0907.3159].

[124] N. F. Bell, Y. Cai, R. K. Leane, and A. D. Medina, *Leptophilic dark matter with Z′ interactions*, *Phys. Rev. D* **90** (2014), no. 3 035027, [arXiv:1407.3001].

[125] F. D'Eramo, B. J. Kavanagh, and P. Panci, *Probing Leptophilic Dark Sectors with Hadronic Processes*, *Phys. Lett. B* **771** (2017) 339–348, [arXiv:1702.00016].

[126] D. Hooper, P. Blasi, and P. D. Serpico, *Pulsars as the Sources of High Energy Cosmic Ray Positrons*, *JCAP* **01** (2009) 025, [arXiv:0810.1527].

[127] D. Hooper, I. Cholis, T. Linden, and K. Fang, *HAWC Observations Strongly Favor Pulsar Interpretations of the Cosmic-Ray Positron Excess*, *Phys. Rev. D* **96** (2017), no. 10 103013, [arXiv:1702.08436].

[128] **HAWC** Collaboration, A. Abeysekara et al., *Extended gamma-ray sources around pulsars constrain the origin of the positron flux at Earth*, *Science* **358** (2017), no. 6365 911–914, [arXiv:1711.06223].

[129] D. Hooper and T. Linden, *Measuring the Local Diffusion Coefficient with H.E.S.S. Observations of Very High-Energy Electrons*, *Phys. Rev. D* **98** (2018), no. 8 083009, [arXiv:1711.07482].

[130] S. Profumo, J. Reynoso-Cordova, N. Kaaz, and M. Silverman, *Lessons from HAWC pulsar wind nebulae observations: The diffusion constant is not a constant; pulsars remain the likeliest sources of the anomalous positron fraction; cosmic rays are trapped for long periods of time in pockets of inefficient diffusion*, *Phys. Rev. D* **97** (2018), no. 12 123008, [arXiv:1803.09731].

[131] **AMS** Collaboration, M. Aguilar et al., *Antiproton Flux, Antiproton-to-Proton Flux Ratio, and Properties of Elementary Particle Fluxes in Primary Cosmic Rays Measured with the Alpha Magnetic Spectrometer on the International Space Station*, *Phys. Rev. Lett.* **117** (2016), no. 9 091103.

[132] A. Cuoco, J. Heisig, L. Klamt, M. Korsmeier, and M. Krämer, *Scrutinizing the evidence for dark matter in cosmic-ray antiprotons*, *Phys. Rev. D* **99** (2019), no. 10 103014, [arXiv:1903.01472].

[133] I. Cholis, T. Linden, and D. Hooper, *A Robust Excess in the Cosmic-Ray Antiproton Spectrum: Implications for Annihilating Dark Matter*, *Phys. Rev. D* **99** (2019), no. 10 103026, [arXiv:1903.02549].

[134] A. Cuoco, J. Heisig, M. Korsmeier, and M. Krämer, *Probing dark matter annihilation in the Galaxy with antiprotons and gamma rays*, *JCAP* **10** (2017) 053, [arXiv:1704.08258].

[135] D. Hooper, R. K. Leane, Y.-D. Tsai, S. Wegsman, and S. J. Witte, *A Systematic Study of Hidden Sector Dark Matter: Application to the Gamma-Ray and Antiproton Excesses*, arXiv:1912.08821.

[136] M. Boudaud, Y. Génolini, L. Derome, J. Lavalle, D. Maurin, P. Salati, and P. D. Serpico, *AMS-02 antiprotons are consistent with a secondary astrophysical origin*, *Phys. Rev. Res.* **2** (2020) 023022, [arXiv:1906.07119].

[137] J. Heisig, M. Korsmeier, and M. W. Winkler, *Dark matter or correlated errors? Systematics of the AMS-02 antiproton excess*, arXiv:2005.04237.

[138] G. Giesen, M. Boudaud, Y. Génolini, V. Poulin, M. Cirelli, P. Salati, and P. D. Serpico, *AMS-02 antiprotons, at last! Secondary astrophysical component and immediate implications for Dark Matter*, *JCAP* **09** (2015) 023, [arXiv:1504.04276].

[139] A. Cuoco, M. Krämer, and M. Korsmeier, *Novel Dark Matter Constraints from Antiprotons in Light of AMS-02*, *Phys. Rev. Lett.* **118** (2017), no. 19 191102, [arXiv:1610.03071].

[140] A. Cuoco, J. Heisig, M. Korsmeier, and M. Krämer, *Constraining heavy dark matter with cosmic-ray antiprotons*, *JCAP* **04** (2018) 004, [arXiv:1711.05274].

[141] K. Griest and M. Kamionkowski, *Unitarity Limits on the Mass and Radius of Dark Matter Particles*, *Phys. Rev. Lett.* **64** (1990) 615.

[142] J. Smirnov and J. F. Beacom, *TeV-Scale Thermal WIMPs: Unitarity and its Consequences*, *Phys. Rev. D* **100** (2019), no. 4 043029, [arXiv:1904.11503].

[143] G. Steigman, B. Dasgupta, and J. F. Beacom, *Precise Relic WIMP Abundance and its Impact on Searches for Dark Matter Annihilation*, *Phys. Rev. D* **86** (2012) 023506, [arXiv:1204.3622].

[144] R. K. Leane, T. R. Slatyer, J. F. Beacom, and K. C. Ng, *GeV-scale thermal WIMPs: Not even slightly ruled out*, *Phys. Rev. D* **98** (2018), no. 2 023016, [arXiv:1805.10305].

Most dwarf spheroidal galaxies surrounding the Milky Way cannot be dark-matter dominated satellites

Francois Hammer, Yanbin Yang, Frederic Arenou, Hefan Li, Jianling Wang, Piercarlo Bonifacio, Carine Babusiaux, Yongjun Jiao

e-mail: francois.hammer@obspm.fr

GEPI, Observatoire de Paris, Université PSL, CNRS, Place Jules Janssen 92195, Meudon, France;
NAOC, Chinese Academy of Sciences, A20 Datun Road, 100012 Beijing, PR China

Presented at the 3rd World Summit on Exploring the Dark Side of the Universe
Guadeloupe Islands, March 9-13 2020

Abstract

Milky Way dwarf spheroidal galaxies are the tiniest observed galaxies and are currently associated with the largest fractions of dark matter, which is revealed by their too large velocity dispersions. However, most of them are found near their orbital pericenters. This leads to a very low probability, $P = 2\ 10^{-7}$, that they could be long-lived satellites such as sub-halos predicted by cosmological simulations. Their proximity to their pericenters suggests instead that they are affected by tidal shocks, which provide sufficient kinematic energy to explain their high velocity dispersions. Dependency of the dark matter properties to their distance to the Milky Way appears to favor tidally shocked and out of equilibrium dSphs instead of self-equilibrium systems dominated by dark matter.

1 Introduction

The Milky Way (MW) halo is populated by many dwarf spheroidal galaxies (dSphs) that show too large stellar velocity dispersions if considered at equilibrium within the gravitational attraction of their stellar mass. The pioneering work of [1] showed the large velocity dispersion for the Draco stars, which requires significant amounts of DM if the Draco system is considered at equilibrium. Further works have provided robust measurements of velocity dispersion along the line of sight ($\sigma_{\rm los}$) for several tens of MW dSphs [2, 3], confirming their large amplitude. In the current ΛCDM scenario, dSphs belong to the population of dark-matter (DM) dominated sub-halos that are very numerous in cosmological simulations. Therefore, the DM content is calculated assuming self-equilibrium [4, 5], which is also necessary to avoid the destruction of long-lived MW satellites by MW tides. Furthermore, three (UMi, Draco and Sculptor) out of the nine classical dSphs, contain only old stars, which supports an early accretion into the MW halo.
Because of their proximity, MW dSphs are the tiniest galactic objects that can be observed and studied, down to stellar mass as small as few hundred of solar masses. This, associated to their kinematics, let the ultra faint dwarfs (UFDs) to be considered the most DM-dominated objects with DM to

baryon mass ratios larger than several hundreds, even up to few thousands. However, [6] showed that knowing the gravitational attraction exerted by the MW together with the dSph scale-length (r_{half}) and stellar mass, one may accurately derive their DM to baryon mass ratios, which appears at odd with the self-equilibrium scenario. Furthermore, it has been shown that tidal shocks exerted by the MW halo may reproduce the kinematics of dSphs as well. Since DM calculations are based on line of sight measurements, one may wonder whether they could have been corrupted by a physical effect expected if dSphs were out of equilibrium because of MW tides [6–8].

2 Consequences of the Gaia 2nd data release (DR2)

Gaia DR2 has provided accurate proper motions allowing for the first time to:

- calculate the circular velocity curve of the MW up to 25 kpc [9, 10];
- derive 3D velocities for most UFDs [3, 11],while they were known only for the nine classical dSphs.

The first result is based on thorough analysis of a very large sample of 26,000 RGB stars in the MW disk [9] resulting into a slightly but robustly determined decline of the circular velocity from 5 to 25 kpc. Such a result is confirmed by [10] using 773 Classical Cepheids with precise distances. Subsequent analyses of these, including accounting for the different types of errors, have lead to MW total mass near or well below $10^{12} M_{\odot}$ [9, 12–14]. This excludes former models with very large MW mass (e.g., from [15] or the "heavy" MW model of [3]), i.e., those which were able to keep bound Leo I dSph or the Large Magellanic Cloud (LMC).

The second result have revealed that a large majority of dSphs have eccentric orbits with eccentricities in excess of 0.66 [3, 7] for two third of them. Even if most dSphs appear to be bound to the MW [3], their 3D velocities are very large and consistent with a recent infall, less than 4 Gyr ago (see Figure 2 of [8]).

Combined together, the two results lead us to further investigate the nature of dSphs on the basis of their orbital motions.

3 Most dSphs lie near their pericenters

Pericenter is one of the orbital quantity that can be robustly determined and that slightly depends on the MW mass profile [16]. Its determination becomes even more precise if heavy MW mass models are excluded. Both [3, 11] noticed that many dSphs lie near their pericenters. This has been further investigated by [8] on the basis of the MW mass model from [17] and using the sample from [3] (see details in [8]). Figure 1 presents results from the same calculations but using instead the MW mass model from [9] that is very similar than that of [17], with a difference of less than 10% for the cumulative mass at all radii.

If dSphs were MW satellites, it would be unlikely to find most of them near their pericenters. To illustrate this, one could remind that comets with eccentric orbits are very rarely found near their pericenter, obeying the second Kepler law. For example, the Halley comet has a period of 77 years and is only seen few months near pericenter. In an extended mass potential such as that of the MW, one has to consider an orbital motion along a rosette instead of an ellipse. Here we estimate the probability that dSphs assumed to be MW satellites could be mostly observed near their pericenters, by performing the following steps:

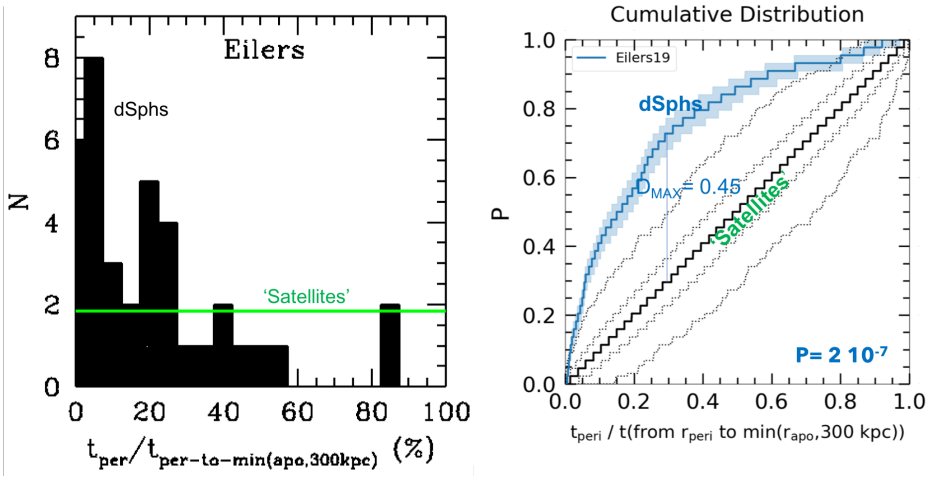

Figure 1: *Left:* histogram of the time ratio distribution of dSphs compared to the expectations if they were MW satellites (horizontal green line). *Right:* Cumulative distribution of time ratios (blue line and area showing the 1σ error) compared to the null hypothesis, i.e., a randomization of locations expected if dSphs are MW satellites (black solid line).

- We first compare two samples: (1) is made by virtual, randomly selected "satellites" of the MW and, (2) corresponds to the observed dSphs (see [8]);
- The time to reach pericenter divided by the total time from pericenter to apocenter provides the chance occurence for a dSph to be at its position within its orbit, which has been calculated using galpy [17] and the mass model from [9];
- Since most dSphs (down to UFD mass, e.g., Coma Berenices) can be seen by the *Dark Energy Survey* (DES) up to 300 kpc [16, 18], we further limit investigations for both samples to a maximal distance equal to min(apocenter, 300 kpc).

The histogram of the time ratio distribution of dSphs (left panel of Figure 1) shows how they concentrate near their pericenters contrary to expectations if they were long-lived satellites of the MW (see the green horizontal line). Right panel shows the cumulative distribution to which we have applied a Kolmogorov Smirnov test, which leads to a very low probability (P= 2 10^{-7} from D_{MAX}=0.45 for 35 objects, see also [8]) that dSphs could be satellites orbiting around the MW. In other words a scenario of long-lived satellites for which DM is shielding dSphs from MW tides is very unlikely.

4 Are dSphs tidally shocked near their pericenters?

The proximity of dSphs to their pericenters suggest that MW tides are at work. However, [19] have excluded that dSphs could be tidally disrupted DM free galaxies because of their observed internal kinematics and structural properties. This conclusion is based on modeling [20–23] that accounts for tidal stripping, which is the dominant process when the satellite is only made of stars and DM (see [7, 8]). In particular, most dSphs do not show tidal disturbance such as tails as it would be expected for tidally stripped galaxies.

The above conclusion could be different if most dSphs were affected by tidal shocks instead of tidal stripping. Let us consider the global instantaneous energy change ΔE caused by MW tidal forces on an individual dSph star with velocity $\mathbf{v}$, which is:

$$\Delta E = \mathbf{v} \cdot \mathbf{\Delta v} + 1/2(\Delta v)^2. \tag{4.1}$$

Tidal shocks may dominate the energy exchange if the first term vanishes because of spherical symmetry. This had been verified by [24] for globular clusters affected by the galactic bulge or disk. In such a case, the latter term (called "tidal shocking" or "heating") is approximated to $1/2(\Delta\sigma^2_{los})$[1], i.e., tidal shocks bring an increase of the kinetic energy for, e.g., stars at r=r_{half}, which follows [8]:

$$1/2\Delta\sigma^2_{\rm los} = \Delta\Phi_{\rm MW} = \sqrt{2} \times g_{\rm MW} \times r_{\rm half} \times f_{\rm MWshocks}, \tag{4.2}$$

where $g_{\rm MW}$ is the gravitational acceleration of the MW and $f_{\rm MWshocks}$ represents the fraction of the system that is affected by tidal shocks [25]. The main discoveries of [7, 8] are:

- That tidal shocks may also apply on DM-free dSph galaxies under the impulse and distant-tide approximations, in particular if dSphs are at first infall; in such a case it is expected that the main initial component, the gas, has been stripped before the pericenter passage, letting residual stars expanding in a spherical geometry due to the subsequent lack of gravity;
- That the kinetic energy change by $1/2\ \Delta\sigma^2_{\rm los}$ along the direction to the Galactic center coinciding to that of the line of sight is precisely what has been assumed to calculate the DM content in dSphs by [4, 5].

Calculation of the DM mass is based on a line of sight measurement, and only the projected mass density ($M_{DM}/r^2_{\rm half}$) is known from observations of $\sigma_{\rm los}$. When multiplied by the gravitational constant G, it leads to the gravitational attraction of the DM exerted on a star at r=r_{half}, which is:

$$a_{\rm DM} = GM_{\rm DM} \times r^{-2}_{\rm half} = \Delta\sigma^2_{\rm los} \times r^{-1}_{\rm half} \tag{4.3}$$

. If the DM is responsible of the velocity dispersion excess of dSphs, $a_{\rm DM}$ does not depends on the distance to the MW, because it is caused by the gravity of the dSph DM mass, and also because DM is expected to shield the dSph mass content against MW tides (see also predictions from *Via Lactea* simulations [26] in Figure 8 of [7]). If tidal shocks are responsible of the velocity dispersion increase (see right panel of Figure 2), the gravitational attraction $a_{\rm DM}$ attributed to the DM is in fact equal to $2\sqrt{2} \times g_{\rm MW} \times f_{\rm MWshocks}$ (see Eq. 4.2), in which $g_{\rm MW}$ induces a strong dependency to the distance to the MW center (D_{MW}).

Left panel of Figure 2 shows that $a_{\rm DM}$=$\Delta\sigma^2_{\rm los} \times r^{-1}_{\rm half}$ anti-correlates with the MW distance for most dSphs having a robust measurement of their internal velocity dispersion (σ_{los}). The result is not dependent on a specific MW mass model because all quantities are observed. Correlation strength is ρ= 0.76 for 21 dSph galaxies, leading to a probability of an occurrence at random to be as low as P= 3 10^{-4} (see all details in [7]).

5 Conclusions

The tidal shock scenario for most MW dSphs appears to be a serious competitor to the usually adopted DM-dominated satellites/subhalos scenario. This is because:

[1] $\Delta\sigma^2_{los}$=σ^2_{los}-σ^2_{stars} [7], where σ_{los} and σ_{stars} are the measured velocity dispersion and the 1D los velocity dispersion associated to the sole stellar component, respectively.

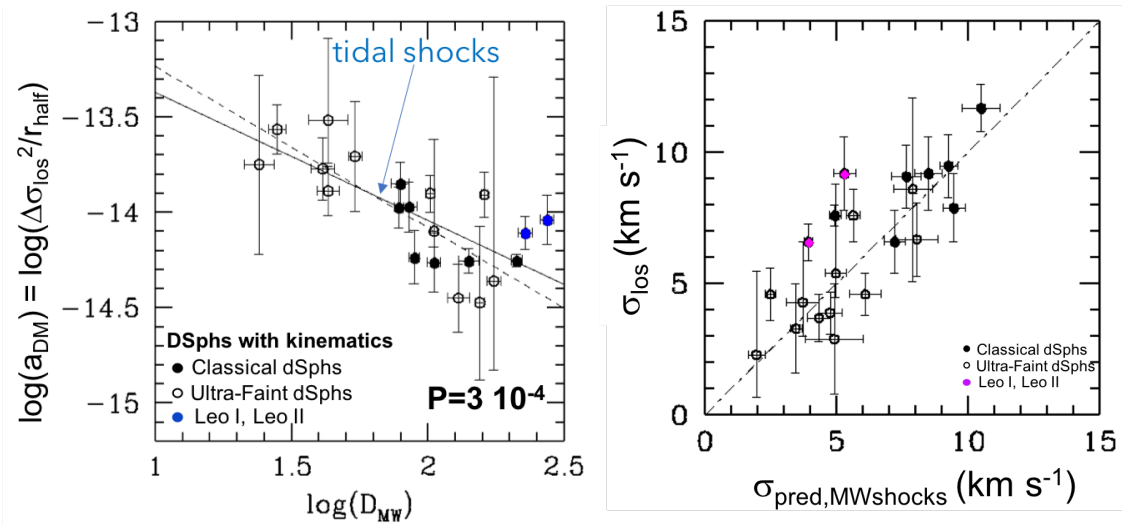

Figure 2: *Left:* Tidal shocks (or DM) acceleration (in km s^{-2}) based on dSph kinematics ($\Delta\sigma^2_{los} \times r^{-1}_{\rm half}$) versus MW distance (in kpc). Data ($\sigma_{\rm los}$, $L_{\rm V}$, $r_{\rm half}$) are coming from [7, 8] and the amplitude of $\Delta\sigma^2_{los} \times r^{-1}_{\rm half}$ assumes $f_{\rm MWshocks} \approx 0.25$. The later value is also supported when comparing tidal shocks caused by a MW potential based on [17] or [9] mass distribution. *Right:* Correlation between the observed $\sigma_{\rm los}$ and that predicted from Eq. 4.2, i.e., $\sigma_{\rm pred,MWshocks} = \sqrt{\Delta\sigma^2_{\rm los} + \sigma^2_{\rm stars}}$, assuming the MW mass model from [9].

- Most MW dSphs are found near their pericenters, which exclude long-lived, DM-dominated satellites (sub-haloes) with an associated probability P=2 10^{-7}; this cannot be circumvented by adapting the MW total mass towards high values that are not consistent with the MW rotation curve.
- The anti-correlation between $a_{\rm DM}$= $\Delta\sigma^2_{\rm los} \times r^{-1}_{\rm half}$ and D_{MW} (left panel of Figure 2, probability that it is fortuitous, P=3 10^{-4}) is a natural prediction if dSphs are tidally shocked, while it cannot be reproduced if dSphs were DM-dominated.
- MW tidal shocks bring sufficient kinetic energy to generate the high velocity dispersions ($\sigma_{\rm los}$) of dSphs (see right panel of Figure 2), and former DM mass determinations might be a misinterpretation of such a physical process on DM-free dSphs.
- Tidal shocks are less destructive than tidal stripping since they bring energy to the dSph stellar content that is partly in resonance with the MW gravitational potential; important mass losses are expected but without tails, and this may correspond to the stars in the dSphs outskirts discovered in wide field observations of classical dSphs (see [27] and references therein).
- After the first passage at pericenter, tides become increasingly dominated by stripping and it is why, e.g., Sagittarius, Bootes I and Crater II escape the anti-correlation (see Figure 6 of [8]).

The MW dSphs are either exceptional or ΛCDM predictions at the low mass end need to be revisited. Star formation histories of few classical dSphs showing neither young nor intermediate-age stars may

appear at odd with a first infall. However, such counter argument deserves to be re-investigated because gas-rich dwarfs having stellar mass equal or lower than that of Sculptor mass may have had their star formation stopped by several mechanisms [28], and the absence of DM would let stellar winds more efficient in removing the gas and stopping the star formation.

The tidal shock scenario may also apply to the infall of gas-rich stellar systems into a massive body, galaxy, group or cluster of galaxies. A gas-rich galactic system is first stripped of most of its gas leading to a spherical expansion of the residual stars, which leads to tidal shocks when it is reaching its orbital pericenter.

References

[1] M. Aaronson, *Accurate radial velocities for carbon stars in Draco and Ursa Minor :the first hint of a dwarf spheroidal mass-to-light ratio.*, *The Astrophysical Journal Letters* **266** (Mar., 1983) L11–L15.

[2] R. R. Muñoz, P. Côté, F. A. Santana, M. Geha, J. D. Simon, G. A. Oyarzún, P. B. Stetson, and S. G. Djorgovski, *A MegaCam Survey of Outer Halo Satellites. III. Photometric and Structural Parameters*, *The Astrophysical Journal* **860** (June, 2018) 66.

[3] T. K. Fritz, G. Battaglia, M. S. Pawlowski, N. Kallivayalil, R. van der Marel, S. T. Sohn, C. Brook, and G. Besla, *Gaia DR2 proper motions of dwarf galaxies within 420 kpc. Orbits, Milky Way mass, tidal influences, planar alignments, and group infall*, *Astronomy and Astrophysics* **619** (Nov., 2018) A103, [arXiv:1805.00908].

[4] M. G. Walker, M. Mateo, E. W. Olszewski, J. Peñarrubia, N. W. Evans, and G. Gilmore, *A Universal Mass Profile for Dwarf Spheroidal Galaxies?*, *The Astrophysical Journal* **704** (Oct., 2009) 1274–1287, [arXiv:0906.0341].

[5] J. Wolf, G. D. Martinez, J. S. Bullock, M. Kaplinghat, M. Geha, R. R. Muñoz, J. D. Simon, and F. F. Avedo, *Accurate masses for dispersion-supported galaxies*, *MNRAS* **406** (Aug., 2010) 1220, [arXiv:0908.2995].

[6] F. Hammer, Y. Yang, F. Arenou, C. Babusiaux, J. Wang, M. Puech, and H. Flores, *Galactic forces rule the dynamics of milky way dwarf galaxies*, *The Astrophysical Journal* **860** (2018), no. 1 76.

[7] F. Hammer, Y. Yang, J. Wang, F. Arenou, M. Puech, H. Flores, and C. Babusiaux, *On the Absence of Dark Matter in Dwarf Galaxies Surrounding the Milky Way*, *The Astrophysical Journal* **883** (Oct., 2019) 171, [arXiv:1812.10714].

[8] F. Hammer, Y. Yang, F. Arenou, J. Wang, H. Li, P. Bonifacio, and C. Babusiaux, *Orbital Evidences for Dark-matter-free Milky Way Dwarf Spheroidal Galaxies*, *The Astrophysical Journal* **892** (Mar., 2020) 3, [arXiv:2002.09493].

[9] A.-C. Eilers, D. W. Hogg, H.-W. Rix, and M. K. Ness, *The Circular Velocity Curve of the Milky Way from 5 to 25 kpc*, *The Astrophysical Journal* **871** (Jan., 2019) 120, [arXiv:1810.09466].

[10] P. Mróz, A. Udalski, D. M. Skowron, J. Skowron, I. Soszyński, P. Pietrukowicz, M. K. Szymański, R. Poleski, S. Kozłowski, and K. Ulaczyk, *Rotation Curve of the Milky Way from Classical Cepheids*, *The Astrophysical Journal Letters* **870** (Jan., 2019) L10, [arXiv:1810.02131].

[11] J. D. Simon, *Gaia Proper Motions and Orbits of the Ultra-faint Milky Way Satellites*, *The Astrophysical Journal* **863** (Aug., 2018) 89, [arXiv:1804.10230].

[12] P. F. de Salas, K. Malhan, K. Freese, K. Hattori, and M. Valluri, *On the estimation of the local dark matter density using the rotation curve of the Milky Way*, *Journal of Cosmology and Astroparticle Physics* **2019** (Oct., 2019) 037, [arXiv:1906.06133].

[13] R. J. J. Grand, A. J. Deason, S. D. M. White, C. M. Simpson, F. A. Gómez, F. Marinacci, and R. Pakmor, *The effects of dynamical substructure on Milky Way mass estimates from the high-velocity tail of the local stellar halo*, *MNRAS* **487** (July, 2019) L72–L76, [arXiv:1905.09834].

[14] E. V. Karukes, M. Benito, F. Iocco, R. Trotta, and A. Geringer-Sameth, *A robust estimate of the Milky Way mass from rotation curve data*, *Journal of Cosmology and Astroparticle Physics* **2020** (May, 2020) 033, [arXiv:1912.04296].

[15] P. J. McMillan, *The mass distribution and gravitational potential of the Milky Way*, *MNRAS* **465** (Feb., 2017) 76–94, [arXiv:1608.00971].

[16] J. D. Simon, *The Faintest Dwarf Galaxies*, *Annual Review of Astronomy and Astrophysics* **57** (Aug., 2019) 375–415, [arXiv:1901.05465].

[17] J. Bovy, *galpy: A python Library for Galactic Dynamics*, *The Astrophysical Journal Suppl.* **216** (Feb., 2015) 29, [arXiv:1412.3451].

[18] A. Drlica-Wagner, K. Bechtol, S. Mau, M. McNanna, E. O. Nadler, A. B. Pace, T. S. Li, A. Pieres, E. Rozo, J. D. Simon, A. R. Walker, R. H. Wechsler, T. M. C. Abbott, S. Allam, J. Annis, E. Bertin, D. Brooks, D. L. Burke, A. C. Rosell, M. Carrasco Kind, J. Carretero, M. Costanzi, L. N. da Costa, J. De Vicente, S. Desai, H. T. Diehl, P. Doel, T. F. Eifler, S. Everett, B. Flaugher, J. Frieman, J. García-Bellido, E. Gaztanaga, D. Gruen, R. A. Gruendl, J. Gschwend, G. Gutierrez, K. Honscheid, D. J. James, E. Krause, K. Kuehn, N. Kuropatkin, O. Lahav, M. A. G. Maia, J. L. Marshall, P. Melchior, F. Menanteau, R. Miquel, A. Palmese, A. A. Plazas, E. Sanchez, V. Scarpine, M. Schubnell, S. Serrano, I. Sevilla-Noarbe, M. Smith, E. Suchyta, G. Tarle, and DES Collaboration, *Milky Way Satellite Census. I. The Observational Selection Function for Milky Way Satellites in DES Y3 and Pan-STARRS DR1*, *The Astrophysical Journal* **893** (Apr., 2020) 47, [arXiv:1912.03302].

[19] G. Battaglia, A. Helmi, and M. Breddels, *Internal kinematics and dynamical models of dwarf spheroidal galaxies around the Milky Way*, *New Astronomy Reviews* **57** (Sept., 2013) 52–79, [arXiv:1305.5965].

[20] S. Piatek and C. Pryor, *The Effect of Galactic Tides on the Apparent Mass-To-Light Ratios in Dwarf Spheroidal Galaxies*, *The Astronomical Journal* **109** (Mar., 1995) 1071.

[21] P. Kroupa, *Dwarf spheroidal satellite galaxies without dark matter*, *New Astronomy* **2** (July, 1997) 139–164.

[22] J. I. Read, M. I. Wilkinson, N. W. Evans, G. Gilmore, and J. T. Kleyna, *The importance of tides for the Local Group dwarf spheroidals*, *MNRAS* **367** (Mar., 2006) 387–399, [astro-ph/0511759].

[23] G. Iorio, C. Nipoti, G. Battaglia, and A. Sollima, *The effect of tides on the Sculptor dwarf spheroidal galaxy*, *MNRAS* **487** (Aug., 2019) 5692–5710, [arXiv:1904.10461].

[24] L. A. Aguilar and S. D. M. White, *Tidal interactions between spherical galaxies.*, *The Astrophysical Journal* **295** (Aug., 1985) 374.

[25] M. D. Weinberg, *Adiobatic Invariants in Stellar Dynamics. II. Gravitational Shocking*, *The Astropnomical Journal* **108** (Oct., 1994) 1403, [astro-ph/9404016].

[26] J. Diemand, M. Kuhlen, P. Madau, M. Zemp, B. Moore, D. Potter, and J. Stadel, *Clumps and streams in the local dark matter distribution*, *Nature* **454** (Aug., 2008) 735–738, [arXiv:0805.1244].

[27] B. McMonigal, N. F. Bate, G. F. Lewis, M. J. Irwin, G. Battaglia, R. A. Ibata, N. F. Martin, A. W. McConnachie, M. Guglielmo, and A. R. Conn, *Sailing under the Magellanic Clouds: a DECam view of the Carina dwarf*, *MNRAS* **444** (Nov., 2014) 3139–3149, [arXiv:1408.2907].

[28] S. Garrison-Kimmel, A. Wetzel, P. F. Hopkins, R. Sanderson, K. El-Badry, A. Graus, T. K. Chan, R. Feldmann, M. Boylan-Kolchin, C. C. Hayward, J. S. Bullock, A. Fitts, J. Samuel, C. Wheeler, D. Kereš, and C.-A. Faucher-Giguère, *Star formation histories of dwarf galaxies in the FIRE simulations: dependence on mass and Local Group environment*, *MNRAS* **489** (Nov., 2019) 4574–4588, [arXiv:1903.10515].

These Proceedings include research presented at the 3rd World Summit on Exploring the Dark Side of the Universe (EDSU2020), one of the major venues of interaction between cosmologists and particle physicists. Topics include Cosmological Microwave Background, Large Scale Structure, Inflation and Early Universe, Particle Astrophysics, Dark Matter and Dark Energy, and Particle Physics. The 3rd World Summit on Exploring the Dark Side of the Universe took place from March 9 to 13 in the Guadeloupe Islands, a picturesque French archipelago in the Caribbean. This was the 3rd meeting in this series of workshops, with previous editions held in the Galapagos Islands and Guadeloupe.